Microstructure and Modelling of Shear Forming

Karla Daniela Vazquez Valdez

Department of Engineering Materials

The University of Sheffield

Thesis submitted for the degree of
Doctor of Philosophy
September 2019

Supervisors:
Prof. Brad P. Wynne
Dr. Martin Jackson

ABSTRACT

The advent of multiaxial CNC machines has generated renewed interest in flexible incremental forming manufacturing methodologies, such as shear forming. These processes use rotating tools in constant local contact with the workpiece, which is often also rotating, to generate shape. As a consequence, much lower loads than conventional forming are needed to produce components with no need for expensive special tooling. Potential has already been established by demonstrating manufacture of high-value products, e.g. turbine and satellite parts, with high dimensional accuracy from difficult to manufacture materials. Thus, huge opportunities exist for these processes to replace the current method of manufacture for a range of high value components, e.g. eliminating lengthy machining, reducing material waste and process times; or the manufacture of a complicated shape without the development of expensive tooling. However, little is known about the exact deformation conditions during processing and why certain materials are better than others for shear forming, leading to significant trial and error before production.

Three alloys were used for this project: Timetal 54M, Jethete M154 and Inconel 718. General microscopy and Electron Backscatter Diffraction were used to measure strains and orientation maps during shear forming and compared with finite element simulations of the process. It was found that in all cases simple shear deformation was dominate but its extent varied through the thickness, with greater levels of deformation at the roller side. A Design of Experiments analysis was also conducted in order to understand the impact of process parameters in the properties of the final workpieces. Such information was the key to develop a reliable Finite Element Model (FEM) that closely resembles the deformation paths of this process. Three methods of damage calculations were embedded in the finite element model and it was found that the forming limit diagram approach had most potential to identify ultimate failure in shear forming, however its use was still not entirely adequate for this process and a different approach was suggested based on previous works found in the literature. Finally, a methodology to test the potential of materials to be shear spun is proposed based on the finite element model developed and these findings.

TABLE OF CONTENTS

Nomenclature

SEM	Scanning Electron Microscopy
EBSD	Electron Backscatter Diffraction
FEM	Finite Element Method
$\propto$	Mandrel Angle
t_1	Final workpiece thickness
t_O	Initial workpiece thickness
θ	Shear plane angle
θ_r	Deformation angle
θ_s	Principal strains' angle
γ	Shear strain
D	Damage
CL	Cockcroft & Latham
FLD	Forming Limit Diagram
ε_1	Maximum principal strain
ε_2	Minimum principal strain
ε_{1Limit}	Limiting maximum principal strain
HCP	Hexagonal Closed Packed
BCC	Body Centred Cubic
BCT	Body Centred Tetragonal
FCC	Face Centred Cubic
DOE	Design of Experiments
σ	Flow stress
$\bar{\varepsilon}$	Effective plastic strain
$\dot{\bar{\varepsilon}}$	Effective strain rate
$\dot{\varepsilon}_{ij}$	Strain rate tensor
ANOVA	Analysis of Variance
FFLD	Fracture Forming Limit Diagram
SFFLD	Shear Fracture Forming Limit Diagram
FLC	Forming Limit Curve

Acknowledgments

First of all, I would like to thank my supervisor Brad Wynne for giving me a chance to work with him and for all his guidance throughout this project. I would also like to thank my second supervisor Dr Martin Jackson who also helped me a lot, at times I was feeling lost in my research.

I also want to thank the members of the STAR research group for their constant support and help, especially to Dr Ben Thomas and Dr Nick Weston for their patience and guidance with Deform, and to Beatriz Fernandez whose help in this final year was essential for the completion of this thesis.

Especial thanks to Mickael Cappelli, who spent long hours helping me with Deform and my model and to Dr Matt Thomas and to Dr Steven Halliday who provided key resources for my research and who were always willing and available to help me. Without their support this project would have not been possible.

I would also like to thank Michael Lee and Jan Safranek who helped me with important aspects of this research even when they were dealing with their own deadlines.

I want to thank all my family and friends that have stayed by my side throughout this journey. I will always be grateful for my parents, my aunts Conchis, Lupita and Zena, my cousins Sthepany and Rocio, my brother Enrique, and my dear friend Silvia, because they always believed in me even at times I didn’t believe in myself. I also want to express my gratitude to my friend Roxana who was there for me at one of the darkest times of this journey and who helped me to not give up. Finally, I would like to thank Emilio, for his immense patience and emotional support, he definitely made this final year a lot more bearable.

Chapter 1 Introduction

1.1 The importance of the study of Shear Forming

In recent years manufacturing needs have been changing, especially in areas such as the automotive and aerospace industries. Whilst in the past, manufacturers focused mainly in mass production and low-cost tooling, nowadays the need for producing products with high mechanical properties and complex shapes have increased. This has led to the development of other manufacturing techniques that were less favoured in comparison to conventional processes; such is the case of incremental forming techniques.

Incremental forming processes work through a series of small local deformations. In general, these processes use rotating tools in constant local contact with the workpiece to generate shape (See Figure 1). This means much lower loads to forge large parts and no need for expensive special tooling.

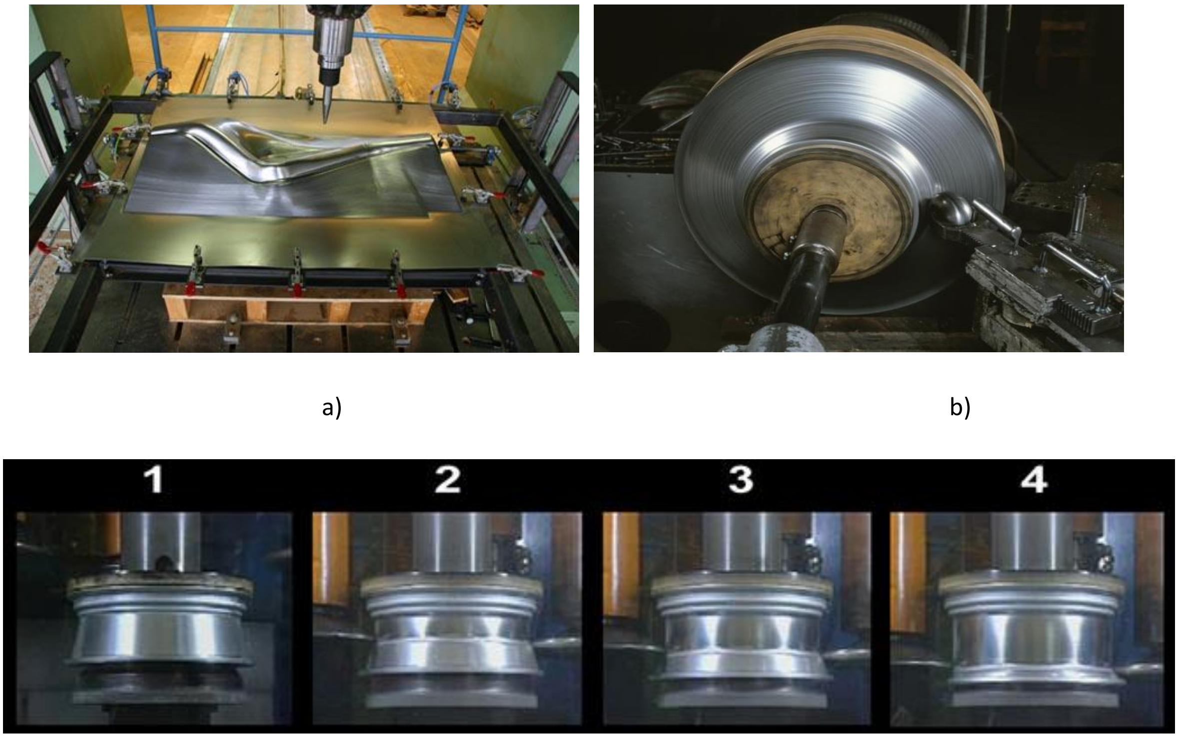

a) b)

c)

Figure 1: Examples of incremental forming processes. a) Incremental sheet forming [1]. b) Shear forming [2]. c) Flow forming [3].

This research is focused on a process called shear forming. This process has the capability of generating axisymmetric forms using basic tooling and much lower forming forces. Its potential has already been established by demonstrating manufacture of high-value products, e. g. jet engine and turbine parts, with high dimensional accuracy from difficult to work materials, which are not viable to be made through conventional processes.

Some of the main advantages of this process are [4]:

- The forces required during shear forming are lower compared to conventional processes given that the tool is in constant local contact with the workpiece.
- Greater reductions and shape modifications can be achieved using simple tooling.
- Machinery costs are reduced.
- The pieces obtained by this process generally have high mechanical properties (caused by work hardening of the material during the deformation) and high-quality surface finish.
- Given that during spinning operations the metal can flow in different paths, it is possible to fabricate parts with complicated shapes that would have to be an assembly of more basic pieces if a conventional process was used.

However, little is known about the exact deformation conditions during processing and why certain materials are better than others for shear forming, leading to a lot of trial and error before production. This has caused this process to have a slow growth in the industrial sector during the last decades despite its great potential. For this reason, this project aims to identify the deformation conditions using advanced microscopy and modelling and, from this information, develop a test method to evaluate a material's potential to be incrementally formed. Thus, significantly reducing lead times and fast tracking the development of this process into industry.

1.2 Project Aim

The main goal of this research is to produce the underlying science and engineering tools to translate shear metal forming into UK industry. In order to reach this goal, the development of a testing strategy for identifying the shear spinnability of materials has been set as a major priority of this project.

1.3 Project Objectives

- Understand the deformation conditions along shear spun workpieces by analysing the microstructural and crystallographic texture evolution using Scanning Electron Microscopy (SEM) and Electron Backscatter Diffraction (EBSD).
- Develop a reliable forming model based on finite element modelling of a basic shear forming process which will closely resemble the deformation conditions observed in the shear spun workpieces.
- Select and implement a damage criterion into the finite element model in order to evaluate various material's potential to be shear spun.

1.4 Thesis Outline

This thesis will be divided in the following chapters:

- **Chapter 2 – Literature Review:** All theoretical background will be found in this section, including technical information about shear forming and conventional spinning processes, as well as experimental methodologies used during this project and general information about damage and failure in metals.
- **Chapter 3 – Experimental Procedure:** This chapter will describe extensively the preparation of the materials selected, the experimental techniques used to analyse their microstructure and texture and the general results and conclusions reached from this information.
- **Chapter 4 – Modelling:** In this chapter, a summary of all the modelling work conducted will be found. This includes a description of the initial shear forming model developed and all the further analysis and changes carried out to validate it and improve it until a damage criterion was selected.
- **Chapter 5 – Conclusions and Future Work:** This chapter will summarise the conclusions drawn from the general results obtained and a methodology for testing the shear spinnability of materials will be proposed. A summary of the areas that could be continued in future research projects will also be included.

Chapter 2: Literature Review

2.1 Introduction

This chapter will be focused on the theoretical background needed for the understanding and development of this research project. This includes key information about shear forming and spinning processes as well as information about the experimental techniques and modelling data used. The chapter can be divided in four big sections:

1. Shear forming background: This section will contain any information regarding analysis performed to shear forming and spinning operations, including; strain and stress states analysis, influence of process parameters, modelling of spinning operations and microstructural studies.
2. Texture Analysis Background: A brief description of important terms needed for the texture analysis in the FEM model and the experimental technique used for the determination of a metal’s texture will be given, as well as examples of typical textures found in metals undergoing shear deformation.
3. Failure Mechanisms in Metals: The main failure mechanisms in ductile metals will be described in this section.
4. Damage models in metals: In this section, three damage models used for ductile materials will be explained and examples of previous works done with each model will be given.

2.2 Shear Forming Background

One of the main incremental forming techniques is the shear forming process, also known as spin forming and power spinning. This is used for fabricating axisymmetric pieces that can vary from a simple cone to a more complex shape. In shear forming a flat sheet blank is pressed against a rotating mandrel by a rotating tool to generate the final shape (See Figure 2). As a result, the thickness of the blank is reduced to a final thickness that should follow the sine law [4] [5];

$$t_1 = t_O \sin(\propto)$$

Equation 1

Where t_1 represents the final wall thickness, t_0 is the initial thickness and α is the angle of the mandrel.

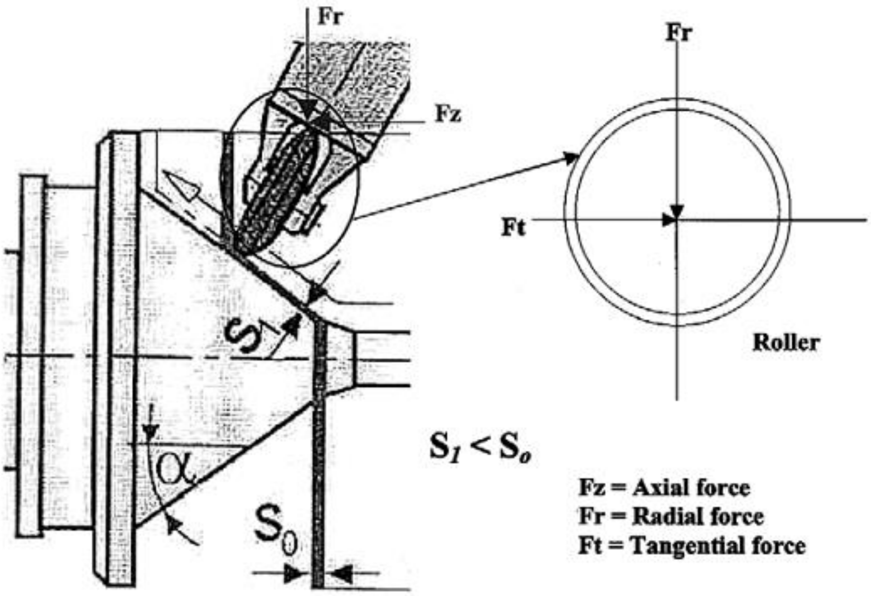

Figure 2: Shear forming arrangement.[4] [5]

The name “shear forming” comes from the main deformation mechanism that occurs during the process, which is simple shear [6]. In simple shear, the deformation unit can be represented with the diagram shown in Figure 3. Three main angles interact in simple shear deformation: the shear plane angle θ, the deformation angle θ_r and the principal strains angle θ_s [7]. The relation between these angles can be described by Equation 2 and Equation 3.

$$\theta_r = \cot^{-1}[2\cot(\theta)]$$

Equation 2

$$\theta_s = \tan^{-1}[\csc(\theta) - \cot(\theta)] = \frac{\theta}{2}$$

Equation 3

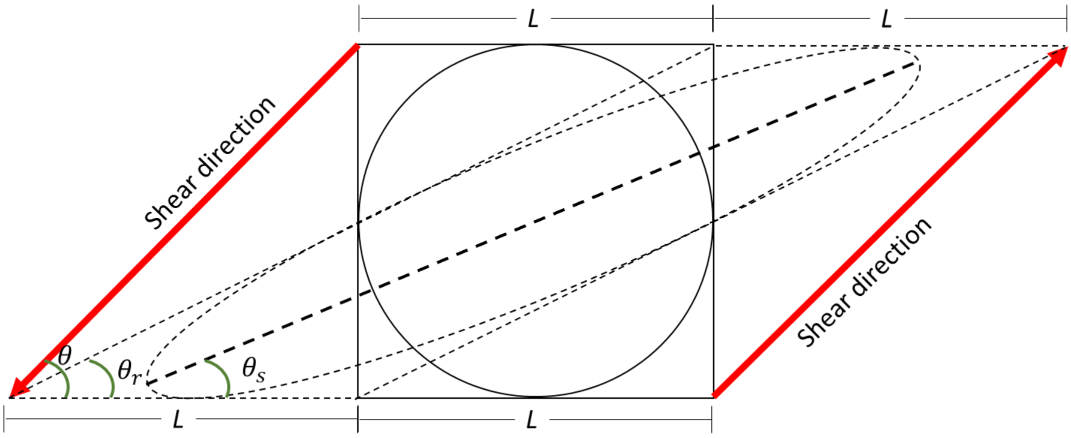

Figure 3: Geometrical representation of deformation mechanism in simple shear. The initial deformation unit is represented by a square. The inner circle is the Mohr's circle for principal strains and stresses calculations. The final state after deformation is drawn with dashed lines. [7]

2.2.1 Deformation Conditions: Strain and Stress States

The first attempt to characterise the deformation behaviour in shear forming was conducted by Kalpakciouglu [6] using the grid lines technique, which consisted in inscribing a grid pattern in the cross sectional area of the blank prior the spinning, to observe the flow pattern of the piece (See Figure 4b). Three main observations were described after the experiment:

1. The centre lines in the plane of the grid became curved.
2. The surface where the grid was inscribed was not a plane surface anymore, which means there was slight circumferential flow.
3. The grid lines were more distorted near the mandrel, but in the rest of the section the lines parallel to the rotation axis kept the same direction.

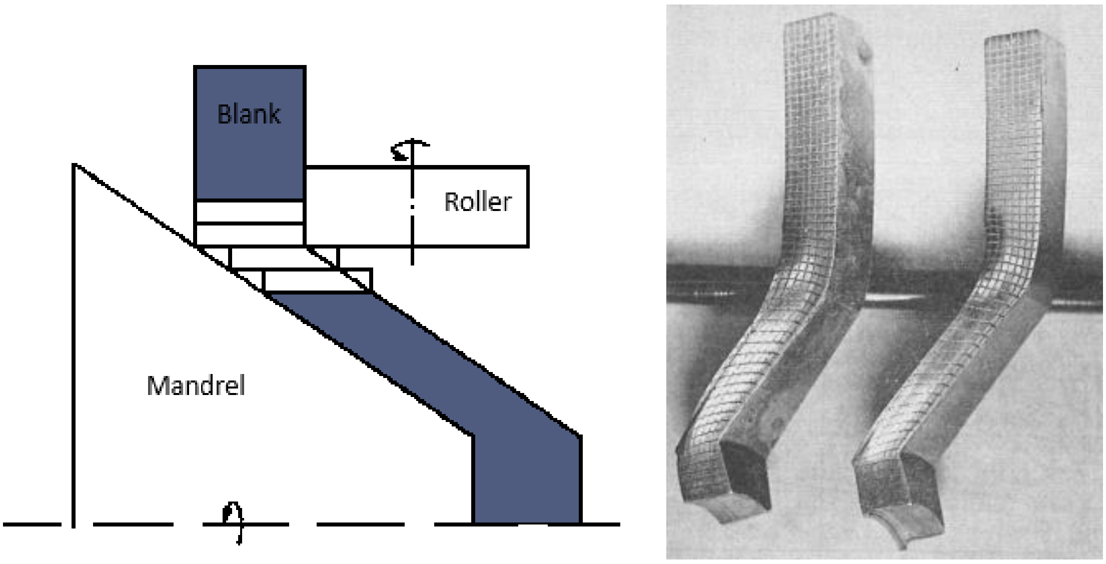

a) b)

Figure 4: a) Representation of the idealised shear forming process. Adapted from Kalpakciouglu [6]. b) Cross section of spun part studied by grid lines technique [6]

A different method to study strains evolution in the process was proposed by Avitzur and Yang [8]. This involves drilling holes along the radius of the blank and in a spiral pattern along the surface, then filling them with a different material so that a three dimensional picture of the deformation could be constructed. With this method, it was concluded that the deformation process varies from pure bending to simple shear depending on the angle of the mandrel; for larger mandrel angles the deformation mechanism is closer to pure bending rather than shearing.

Other studies have been carried out to try to understand the deformation mechanism in conventional spinning operations, such as the one performed by Quigley and Monaghan [9] in which a pattern of circles was inscribed along the surface and then measured after the spinning, as shown in Figure 6. They concluded that the first pass in a multiple pass spinning process is closer to shear forming after observing that the radial strain is much larger than the circumferential strain. Additionally, towards the middle of the workpiece the strain values have almost the same behaviour as the shear forming strain curves. These observations can be seen in Figure 7.

Beni et al. [10] conducted a similar study where the circumferential flow in conventional spinning was observed by inscribing circles along the blank before the process. They found that the circles became ellipses in the longitudinal direction but were not deformed in the circumferential direction (See Figure 8).

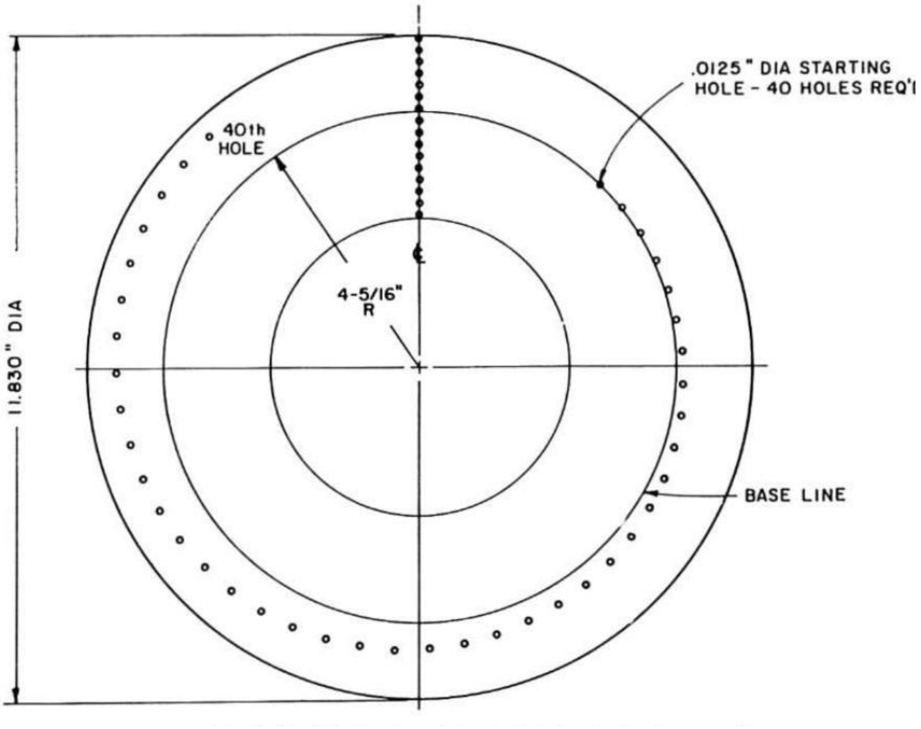

Figure 5: Visualization of hole-drilling method used to study the deformation in shear forming [8].

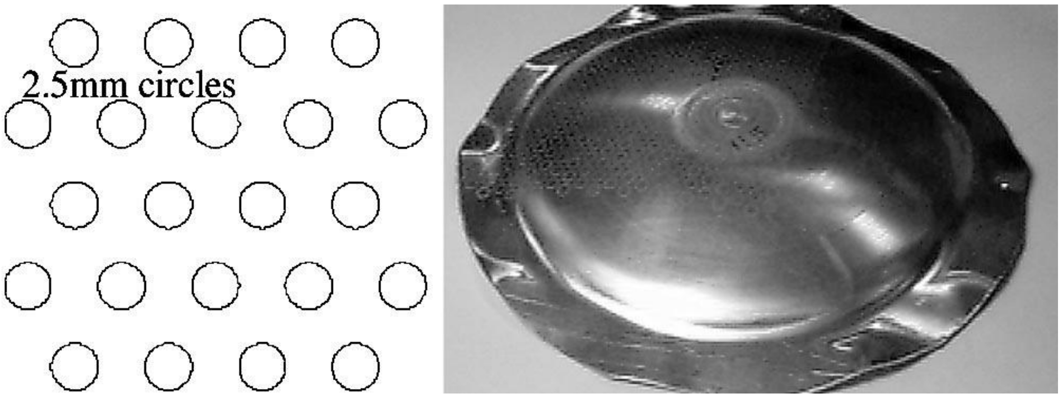

Figure 6: Pattern used by Quigley & Monaghan [9] and an example of an etched blank.

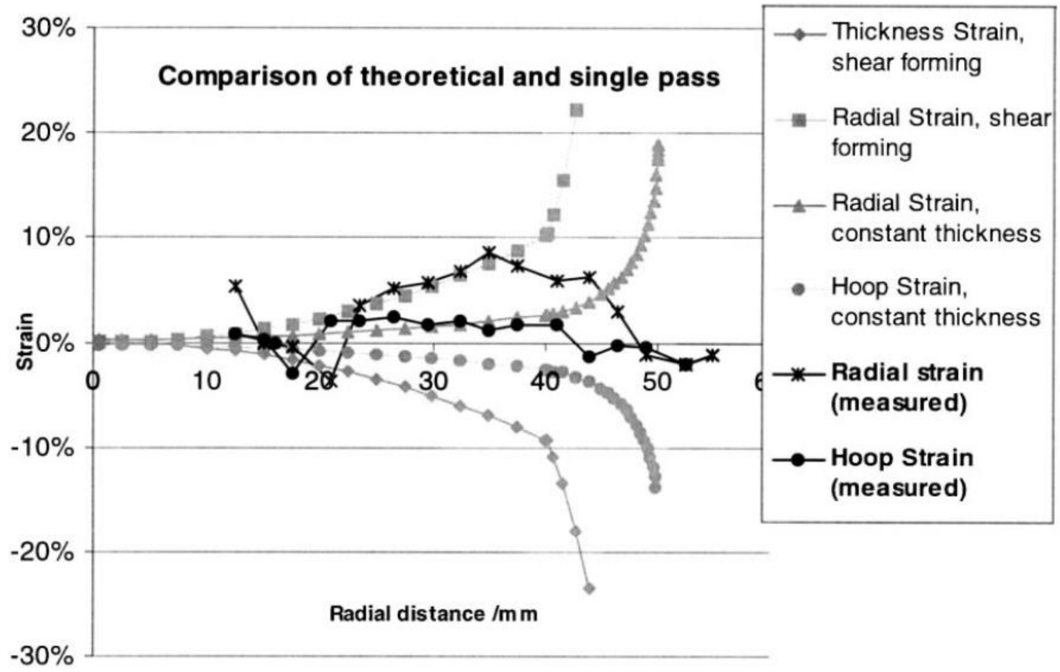

Figure 7: Strain curves obtained by Quigley & Monaghan [9] after a single pass of a spinning operation against theoretical values.

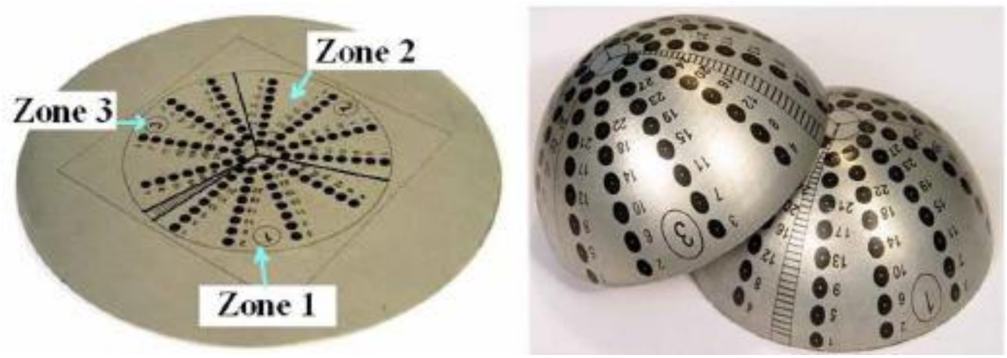

a) b)

Figure 8: Experimental blank used to study the circumferential flow in conventional spinning. a) Before deformation. b) After deformation. [10]

Other authors have suggested that the deformation mechanism in spinning operations vary throughout the process [11] [12]. Sellin [12] proposed that the process should be divided in three stages: initial deformation and contact with the mandrel, rotation of the blank and progressive deformation of the blank and the final forming of the flange.

However, it is still not clear how the deformation mechanism varies along the thickness and the surface of the blank. Considering Kalpakcioglu [6] observations mentioned before, it is possible to conclude that the deformation along the centre of the sheet is very close to simple shear, but as he mentions the lines become more distorted close to the mandrel and the centre lines got curved after the experiment, so it is not correct to assume that ideal simple shear is present throughout the whole thickness. Knowing this, one of the objectives of this research is to understand the deformation process along the zones of the sheet in contact with the mandrel and the roller.

Another important point to be considered are the stresses along the workpiece due to its relation to the final mechanical properties of the workpiece and the possible failure during the shear forming process. Even so, according to Music et al. [13] several experimental studies have been conducted to understand other features of shear forming (such as final strains, forming forces, failure mechanisms, among others), but no studies were found where stresses were experimentally investigated and all the knowledge had regarding stresses is based on theoretical works.

When referring to stresses during the shear forming process, the sine law plays a very important role. Any deviation from the sine law would produce a different and complex stress and strain state, which can affect certain properties like the ductility of the materials; when the workpiece is over-reduced, the unprocessed zone suffers circumferential tensile stresses which generate radial compressive stresses in the zone being deformed (See Figure 9) and these compressive stresses causes the material's ductility to increase, but also in the case of under-reduction the opposite happens and the ductility is decreased [14].

It is also important to mention that later Kalpakcioglu noted that for materials with a fracture strain of 0.5 or larger in the tensile test the maximum spinning reduction was not influenced by the changes in the material's ductility due to over-reduction while the contrary happened for the materials with a fracture strain of 0.5 or less [15]. Another important observation made by Kegg [14] is that materials that fractured at smaller angles and achieved higher strains presented a stress state similar to pure tension (See Figure 10).

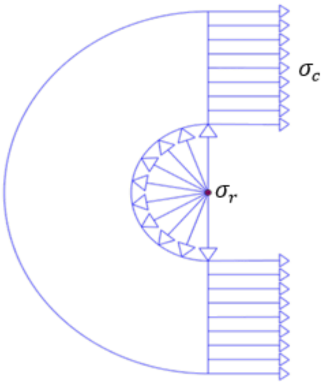

Figure 9: Representation of stresses in the case of over-reduction. Adapted from Kegg [14]

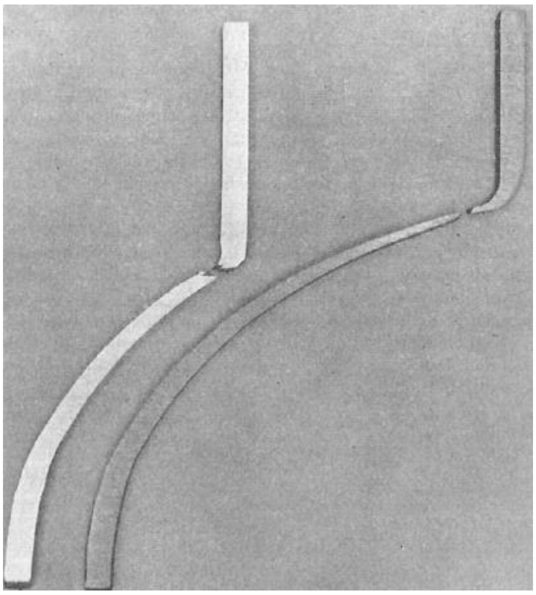

Figure 10: Fracture cases observed by Kegg [14]. First case corresponds to a material that failed at a lower mandrel angle due to other a deformation state different to tension. The second case corresponds to a material that failed due to high tension at a higher mandrel angle.

Finally, Kalpakcioglu [4] mentioned that if this law is not complied with, the final workpiece will not stay stress-free after the spinning, given that the stresses generated during the operation will not be restricted to the area undergoing the deformation and this would cause two main types of failure: bending of the unspun end of the workpiece caused by over-spinning, and wrinkling caused by under-spinning. An example of these defects is shown in the following figure.

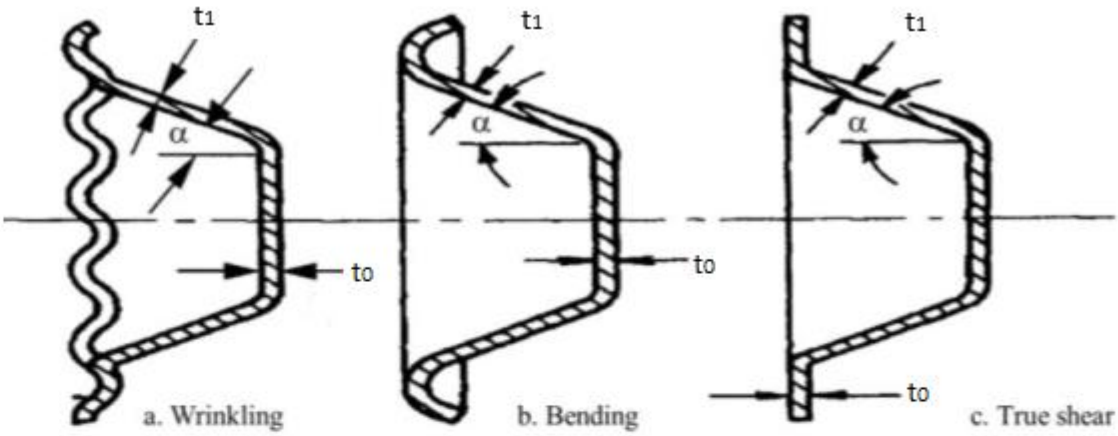

Figure 11: Defects caused by deviation from sine law: a) Wrinkling caused by under-spinning, b) Bending caused by over-spinning and c) True shear spinning. [16]

2.2.2 Microstructure Evolution

The study of microstructure and microtexture is a key point for the understanding of the deformation mechanism experienced during this forming process. However very few works were found regarding the microstructure and none about microtexture of materials at the time this thesis was written.

In general, the microstructure along the workpiece does not evolve uniformly. In Figure 12 results obtained by Mori et al. [17] are shown, in which it is possible to observe that in the longitudinal cross section the microstructure near the outer surface showed greater shear deformation compared to the area near inner surface while in the circumferential direction the final microstructure was homogenous along the thickness.

Later Radović [18] studied the microstructure of aluminium alloy AlMg6Mn spun parts and demonstrated that grain size does not influence the microstructure evolution behaviour of the workpiece and that in general the grains became elongated in the longitudinal direction and stretched in the circumferential section. Also, large particles (>10µm) existing in the microstructure fragmented during the spinning operation. They concluded that certain properties of the workpiece like strength and hardness improved by reducing the grain size and that grain refinement and particle strengthening cause greater thickness reductions which could improve these properties too.

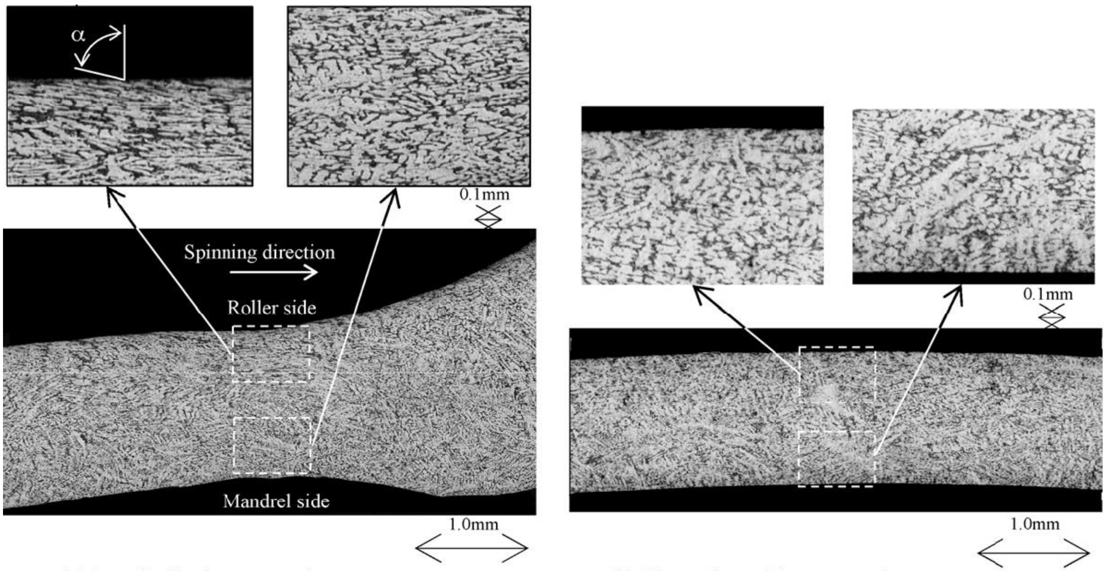

(a) Longitudinal cross-section (b) Circumferential cross-section

Figure 12: Microstructures of an aluminium alloy after shear spinning with 40% thickness reduction [17]

Zhan et al. [19] also demonstrated that the deformation along the thickness of the workpiece is not uniform by studying a titanium alloy in three cases of shear spinning (standard case, under-reduction and over-reduction). In all the cases an elongated microstructure along the longitudinal and circumferential cross section was obtained and the grain size varied along the thickness (it was larger near the inner surface). They attributed this behaviour to three factors: the friction variation along the blank and the deformation and temperature variation along the thickness. These results were more evident in the case of over-reduction and a more uniform microstructure was obtained in the standard case. (See Figure 13 and Figure 14).

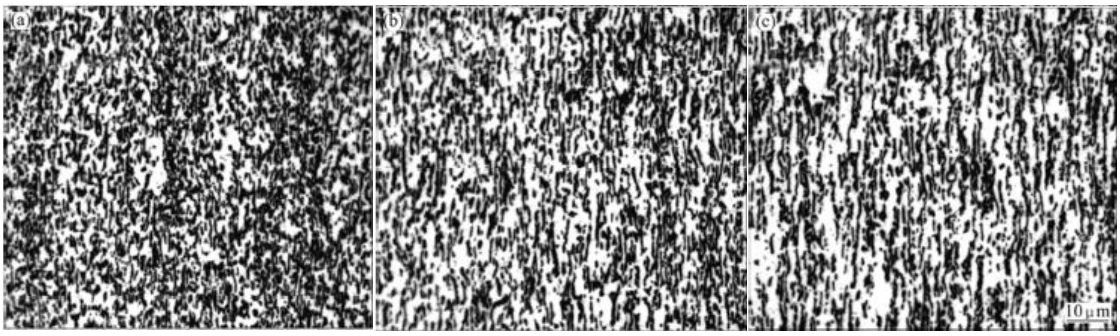

a) b) c)

Figure 13: Microstructure along the circumferential cross section in over-reduction case: a) Near outer surface, b) Centre, c) Near inner surface. [19]

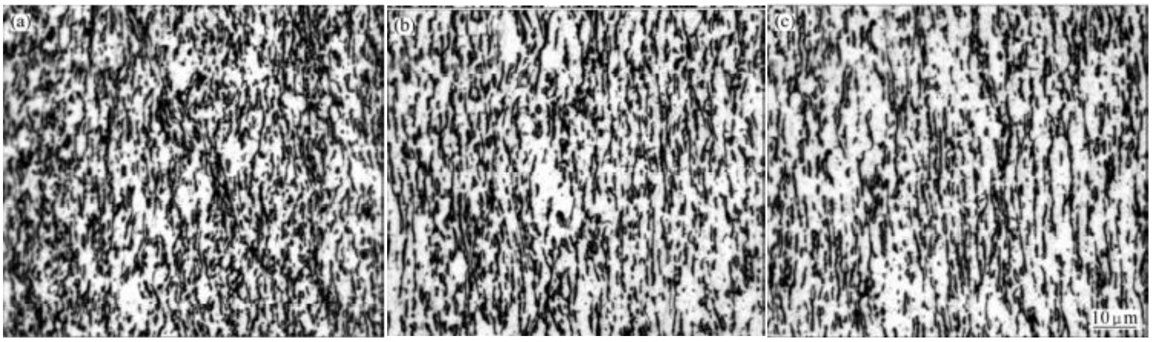

a) b) c)

Figure 14: Microstructure along the longitudinal cross section in over-reduction case: a) Near outer surface, b) Centre, c) Near inner surface. [19]

2.2.3 Shear Spinnability of Materials

The term shear spinnability refers to the limit of deformation that a material can undergo during a shear spinning operation without presenting any type of failure. The first attempt to develop a spinnability test was carried out by Kegg [14], who tested several materials by using an ellipsoid shape mandrel (See Figure 15) to determine the maximum percentage of reduction during the shear forming process. With this mandrel it was possible to vary the percentage of thickness reduction from 0 to 100%. Kegg compared the results from the spinning experiments against the maximum area reduction obtained in the tensile test and concluded that the following relationship exists between these two data:

$$R = \frac{q}{0.17 + \frac{q}{100}}$$

Equation 4

Where, R is the maximum thickness reduction achieved in spinning and q is the maximum area reduction achieved in tensile test.

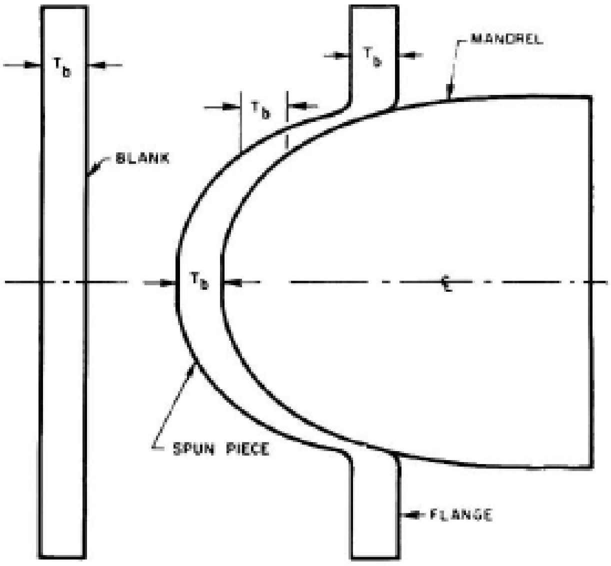

Figure 15: Representation of the ellipsoidal mandrel used by Kegg [14]

However, the results obtained by Kegg were later questioned by Hayama and Tago [20] and concluded that this method could not be applied for the study of spinning of cones because the forces involved in the process were not being considered.

More recently, Mori and Nonaka [21] developed a finite element model and defined the forming limit based on the accumulation of material of the workpiece in front of the roller during the spinning operation. They called this parameter pileup rate and concluded that in general materials cannot be spun when the pileup rate is larger than 35% given that it hinders the material from flowing and increases the forming load.

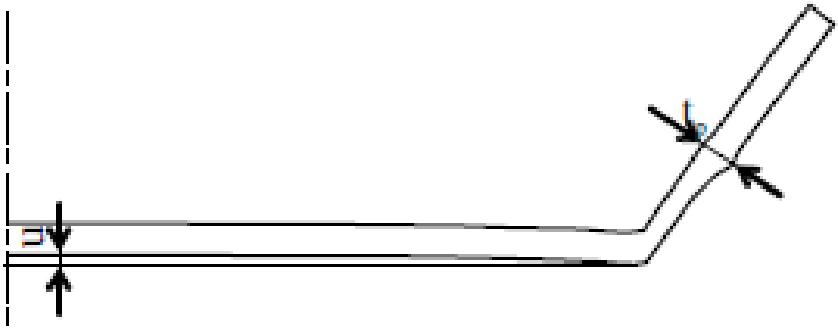

Figure 16: Cross section of the workpiece in Mori and Nonaka's work. A representation of the pileup can be seen on the right side as t_p [21]

2.2.4 Influence of Process Parameters

In shear forming and conventional spinning, process parameters such as feed rate and dies' geometries can have a great influence in the final workpiece. For this reason, several studies like the one conducted by El-Khabeery et al. [22] have been focused on this topic. In their work, several observations were made regarding the effect of the geometry of roller and the feed rate had on the final workpiece dimensional characteristics and the forming forces in conventional spinning; some key points are mentioned below:

- The contact area between the roller and the workpiece is directly influenced by the roller nose radius. Large contact areas caused by large nose radius result in the work material to pile up during the process. This is because the roller cannot easily penetrate the material due to low stress concentration in the deformation area.
- Feed rate also affects the contact area. Higher feed rates cause larger contact areas resulting in low stress concentrations which finally prevent the material to be easily deformed. The relation between the feed rate and the contact area is represented in Figure 17.

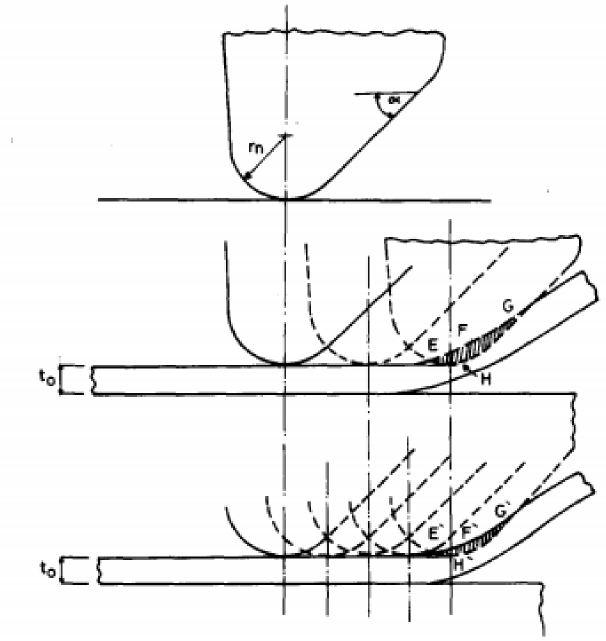

Figure 17: Effect of feed rate on the contact area between the workpiece and the roller. High feed rate represented in the middle cause the contact area EFGH to increase, while low feed rate decrease it. [22]

Another important finding in the topic was introduced by Kegg [14], who concluded that the mandrel shape has a great influence in the bending of the workpiece. Kegg explained that mandrel with sharp corners cause a deviation from the sine law provoking bending and while an ellipsoidal corner is ideal to avoid bending at all, a rounder corner is enough to reduce this effect as shown in Figure 18.

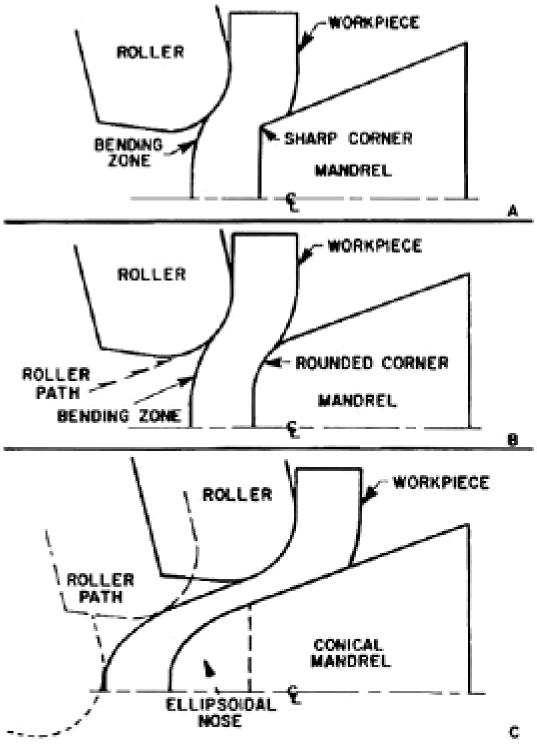

Figure 18: Effect of mandrel geometry. a) Sharp corner, b) Rounded corner and c) Ellipsoidal corner. [14]

Later Kalpakcioglu [15] analysed the influence of the process parameters on the spinnability of the materials based on Kegg's spinnability test mentioned in section 2.2.3. Kalpakciouglu concluded that the minimum angle at which the shear spinning operation is possible for any metal is 15º and that the roller's shape, swivel and speed and the mandrel rotational speed did not influence the spinnability of the materials studied but that the deviation of the sine law did have a great impact on it.

More recently, Tschaetsch and Koth [23] investigated the effect of feed rate and spinning ratio on wrinkling and bending defects during shear forming. They defined the spinning ratio as the ratio between the diameter of the workpiece divided by the diameter of the mandrel after a given revolution. They found that excessively high spinning ratio and feed rate cause wrinkling, while bending can be avoided by reducing the spinning ratio and increasing the feed rate.

Finally, Guillot et al. [24] evaluated how the feed rate, spindle speed, coolant and lubricant affected the final average thickness, angle of shear, first diameter formed and surface finish with a Design of Experiments Analysis. In all cases it was found that the feed rate and the use of lubricant were the most significant parameters having a much higher impact than the others.

2.2.5 Modelling of Spinning Processes

Finite element modelling is a technique commonly used for the analysis of pieces and processes that can provide various type of data depending on the setup and information required. The data that can be extracted vary from thermal, electromagnetical, microstructural, mechanical and many other properties and variables. FEM models are characterised by the division of workpieces in small elements (mesh) and the division of the process in steps for their calculations.

As mentioned by Quigley and Monaghan [25], the modelling of spinning processes can be considerably challenging due to its incremental forming nature for two main reasons:

1. A fine mesh is required for the workpiece because the contact with the roller only happens in a very small area. If the mesh is too big, there will be no contact continuity between elements but if it is too fine large solution times are expected.
2. The step size of the process needs to consider the rotational speed of the workpiece to avoid convergence problems caused by numerous nodes touching and separating from the roller during a single step, if this is too large.

In Quigley and Monaghan’s model, a 4200-element brick mesh was used, and the time step was set at 0.00091 sec/step. The friction coefficient between the roller and the workpiece was 0.02 considering that in real spinning process the contact is so small and so brief that low friction coefficients are expected. In order to reduce the solving times of the model and to increase the quality of results, adaptive meshing was used to have finer mesh areas where the contact is undergoing without increasing the number of elements (See Figure 19). They compared their results to the ones obtained by Qiang and Wang [26] and concluded that the forming forces in their FEM model had the same behaviour as in this study, where the axial force is a considerably bigger that the radial and tangential force.

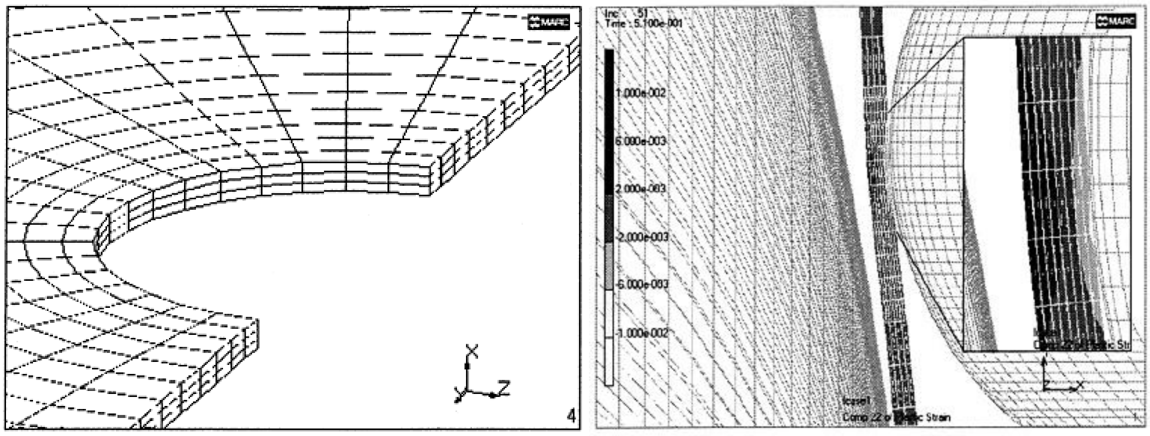

a) b)

Figure 19: Mesh geometry used for Quigley and Monaghan's [25] model. a) General geometry of mesh with brick elements. b) Example of adaptive mesh; an area with smaller mesh is shown in the square, where the roller is touching the blank.

In a similar study, Quigley and Monaghan [27] concluded that the power of new computers is facilitating the modelling of incremental forming processes, reducing greatly the solving times thanks to tools like parallel processing.

More recently, Mori and Nonaka [21] were able to simulate the shear forming process of a real wheel disk for trucks by using an axisymmetric model, where instead of rotating the mandrel and simultaneously pressing the roller to generate the final form, the incremental nature of the deformation was simulated by feeding the roller one revolution at a time and pressing it against the blank only for the corresponding contact time (See Figure 20). The results obtained showed good agreement with the real-life data provided.

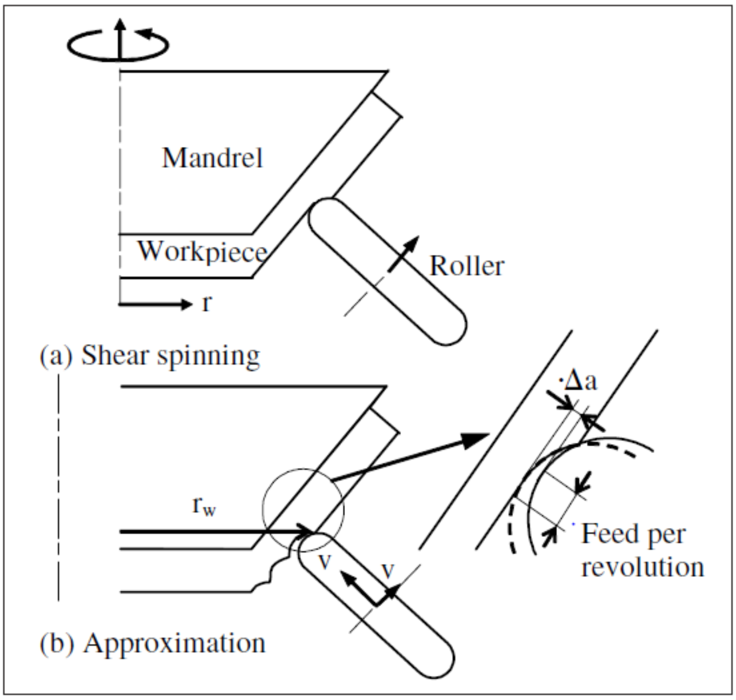

Figure 20: Representation of deformation behaviour using in Mori et al. model. a) Real shear spinning behaviour. b) Approximation used in model. [21]

2.2.6 Important Remarks

Throughout this section a summary of what is already known regarding the deformation conditions in shear forming has been described and even though it has already been established in the past that the main deformation mechanism in shear forming is in fact very close to simple shear, it has also been demonstrated that deviations from this mechanism exists in some areas of the workpieces (where the tools are in contact) [6]. Additionally, other authors have studied several factors that could influence the mechanics of the process and the shear spinnability of materials [8, 13, 14, 22, 24], as well as the microstructural evolution of materials that have undergone this process [17-19], and even though the knowledge regarding the mechanics of shear forming has increased greatly, there is still not a clear shear spinnability test method that is currently used and available in industry despite some attempts conducted in the past [14, 21]. Knowing this, it is clear that establishing the resemblance of the mechanics in shear forming and simple shear experimentally is not a novel aspect of this research, however, its study is still essential for the development of a reliable test methodology, especially if FE modelling is expected to be part of said methodology.

2.3 Microtexture Analysis Background

As explained by Bunge [28], most engineering materials like metals are polycrystalline and the set of orientations of each crystal is called texture. Bunge also mentions that polycrystalline materials usually suffer changes in their texture during working processes, which can give key information about the deformation mechanisms undergoing.

By analysing the texture of samples taken from shear spun materials and comparing them to typical simple shear textures it is possible to have a better understanding of the deformation behaviour throughout the process. This information is also important to validate the FEM model developed in this project.

In this section, a brief explanation of the experimental technique used for the determination of the samples' textures will be given, as well as examples of simple shear textures and key terms needed for the simulation of textures in the FEM model.

2.3.1 Electron Backscatter Diffraction

One of the most popular techniques used for the determination of the texture of materials is the Electron Backscatter Diffraction (EBSD), which is performed in a Scanning Electron Microscope (SEM) and was selected for the analysis conducted throughout this project.

In this technique an electron beam is directed to the sample, so the electrons are scattered, and the diffraction pattern is used to determine the texture of the material. In order to understand how EBSD works it is important to define the following terms:

Bragg's Law: Like Engler and Randle [29] explain, this refers to the phenomenon that occurs when waves are diffracted. When this law is satisfied, reinforced waves will be obtained when the waves being reflected in different crystallographic planes are in phase with each other which happens when they travel an entire number of wavelengths. This is represented in the following equation and figure:

$$n\lambda = 2d\sin\theta$$

Equation 5

Where,

n = order of diffraction

λ = wavelength

d = distance between crystallographic planes

θ = diffraction angle

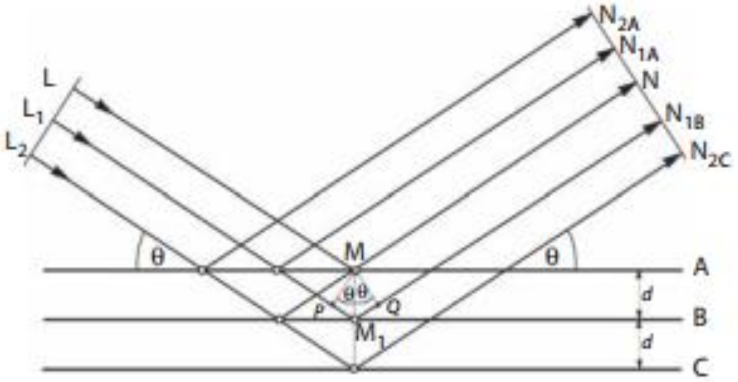

Figure 21: Representation of diffraction of waves and the Bragg's Law. [29]

Kikuchi Pattern: This is used for the determination of the texture in a material. The Kikuchi pattern is formed as follows [29]:

1. The waves enter the surface and are scattered in all directions
2. Some of the scattered waves are reflected following the Bragg's Law (This means they were reflected in what is called the Bragg's angle)
3. The diffracted waves form two cones which are called Kossel cones and whose source is located between crystallographic planes.
4. A camera captures the Kossel cones and two almost parallel lines (which are called Kikuchi lines) are obtained with a distance between them of $2\theta_B$. (See Figure 22)
5. Several Kikuchi lines are obtained corresponding to the different crystallographic planes present in the sample.

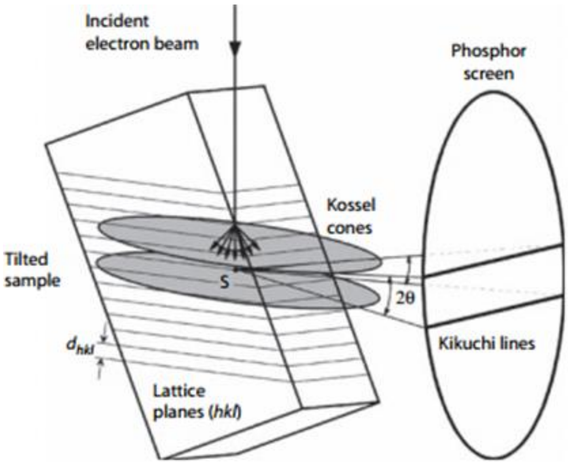

Figure 22: Schematic of the formation of Kikuchi lines in ESBD. [29]

When the Kikuchi pattern is obtained the next step is to identify the crystallographic planes that each line represents. Nowadays, this can be performed automatically using different softwares. An example of this is shown in the following figure.

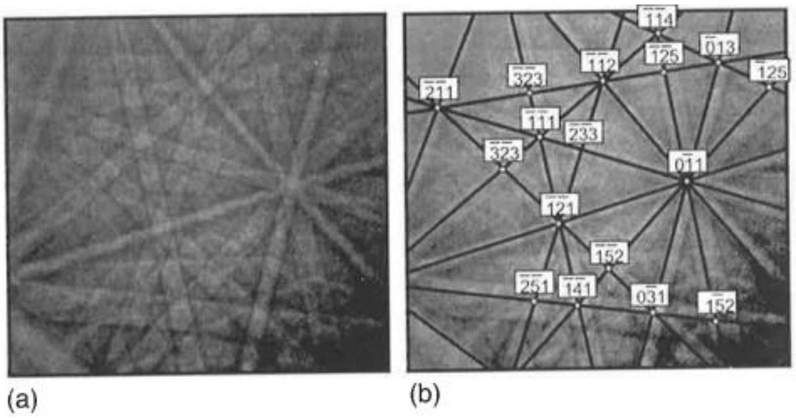

Figure 23: EBSD of a nickel allow. a) Kikuchi pattern obtained. b) Identification of crystallographic planes. [30]

Finally, these results can be represented in a pole figure or an inversed pole figure (See Figure 24) and also density distribution representations are commonly used when a large amount of individual measurements are given (See Figure 25) [29]. It is also important to note that pole figures represent the crystallographic planes normal direction based on the sample's surface normal, while inverse pole figures work the other way around.

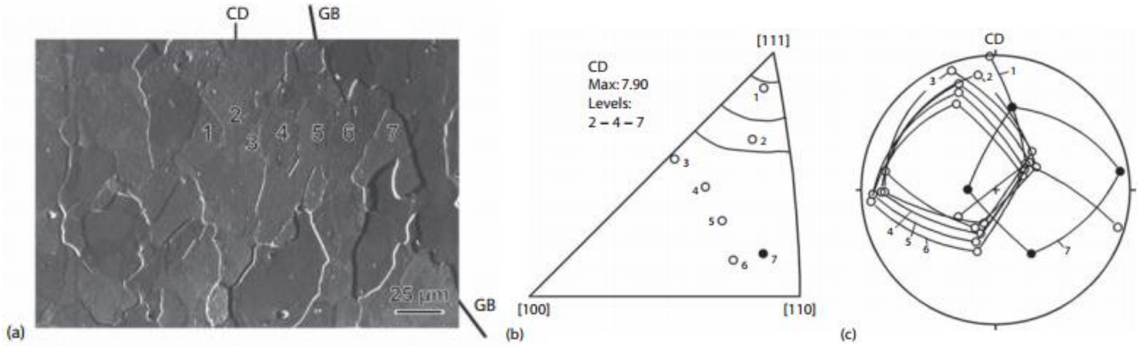

Figure 24: Example of crystallographic texture measurements. a) Microtexture of the analysed sample. b) Inverse pole figure showing the orientation of the grains marked in a. c) Same data shown in b but in a pole figure. [29]

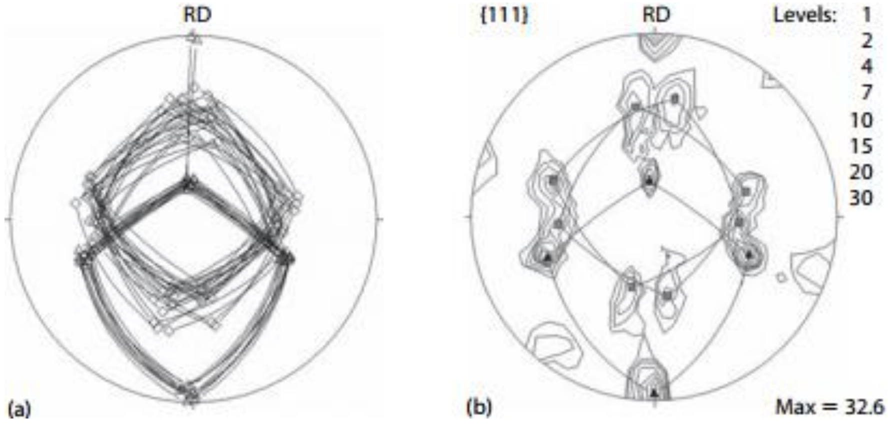

Figure 25: Example of density distribution representation in pole figure against the representation of single measurements. [29]

2.3.2 Texture Simulation of BCC and FCC metals

Several works have been conducted regarding the prediction of a materials texture after a given forming process [7] [31]. MTMTAY is a software developed by Van Houtte [32] to simulate texture changes in FCC and BCC metals, in three main steps:

1. Generating a randomized initial texture by converting a large Orientation Distribution Function (ODF) into a set of discrete orientations using the statistical method STAT [33].
2. Simulating the deformation using an extended version of the Taylor theory [34].
3. Converting the final set of orientations into texture coefficients, which represent the texture of a given plane and can be read by other programs to visualize the final pole figures.

The Taylor-Bishop-Hill theory used in MTMTAY describes the plastic deformation of polycrystals by analysing each crystal individually to identify the active slip systems of each one at a certain moment during the deformation, combining two main theories [34]:

- The Taylor theory, where only the slip combinations that minimize the external work and reach the specified strain are selected.
- The Bishop-Hill theory, where the stress state that maximises the plastic work and the shear stress of any slip systems in such state never exceeds the critical shear stress is selected.

An important remark from this theory is that it assumes that all crystals undergo the same plastic strain [34]. The final mathematical model can be resumed it in the following equations.

Bishop-Hill Theory:

$$W_{BH}^{*} = \boldsymbol{s} \cdot \boldsymbol{a_0} = Max$$

Equation 6

$$\boldsymbol{s} \cdot \boldsymbol{a_{hk}} \leq t_{hk}$$

Equation 7

Taylor Theory:

$$W_T^k = t_{hk} g_{hk}$$

Equation 8

$$g_{hk} \geq 0$$

Equation 9

$$\boldsymbol{a}_{hk} g_{hk} = \boldsymbol{a}_0$$

Equation 10

Where, W_{BH}^{*} is the plastic work in Bishop-Hill theory, W_T^k is the external work in Taylor theory, t_{hk} is the absolute values of the critical shear stresses of a given slip system k, g_{hk} is the ratio between the slip rate on the given system k and the microscopic strain rate, $\boldsymbol{a}_{hk}$ represents the vector representation of the symmetric part of the tensor K of a given slip system k, $\boldsymbol{a}_0$ is the vector representation of the symmetric part of the tensor K of the sample reference system and $\boldsymbol{s}$ is the vector representation of the deviatoric stress tensor.

In a posterior work, Tóth and Van Houtte [33] explained that having a large amount of initial texture coefficients, i.e. a large ODF, for texture simulation is impractical. They studied several discretization methods (including the Cumulative ODF Statistical Technique or STAT implemented in MTMTAY) and used them to reduce the input data of the initial texture in order to compare the final simulated textures to the one obtained against the original data.

As shown in Figure 26, the results obtained with the STAT method, using low and high number of orientations, showed good agreement with the ones obtained using the original ODF.

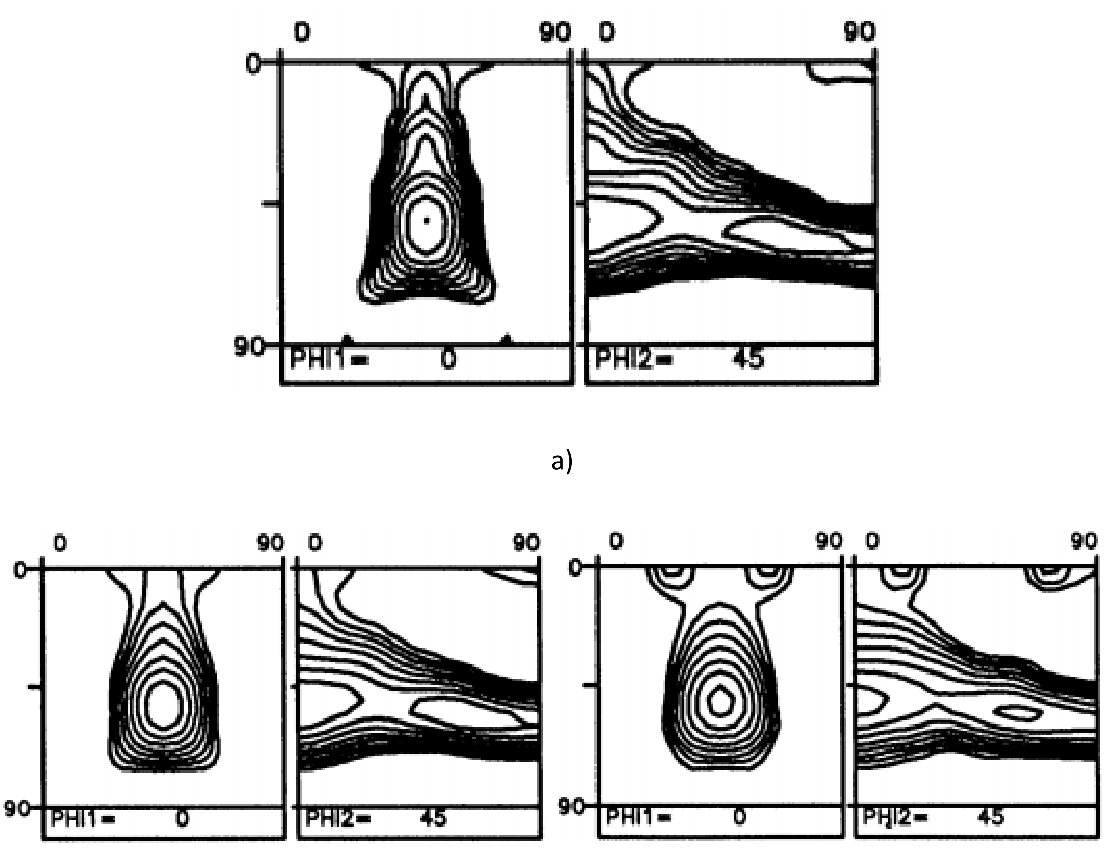

a)

b)

c)

Figure 26: Textures simulation conducted by Tóth and Van Houtte [33]. In all cases initial texture is on the left and final on the right side. a) Original ODF with 6859 orientations. b) Discretised distribution by STAT method with 354 orientations. c) Discretised distribution by STAT method with 1970 orientations.

2.3.3 Texture behaviour during simple shear deformation

2.3.3.2 Ideal orientations for FCC structures

As shown in Figure 27 and explained by Beyerlein and Tóth [7], the simple shear texture in FCC metals is characterised by two main fibres:

- A fibre: It represents the plane $\{1\ 1\ 1\}$ parallel to the shear plane and contains the components A, $\bar{A}$, A_1^* and A_2^*.
- B fibre: It represents the direction $\langle 1\ 1\ 0\rangle$ parallel to the shear direction and it contains the components A, $\bar{A}$, B, $\bar{B}$ and C.

They also explain that, due to the two-fold symmetry nature of the simple shear deformation around the axis perpendicular to the shear plane normal and the shear direction, the A and B components have the same intensity as $\bar{A}$ and $\bar{B}$ respectively. This is not the case for A_1^* and A_2^*, which can have different since they are not symmetric with respect to this axis and C, that is self-symmetric.

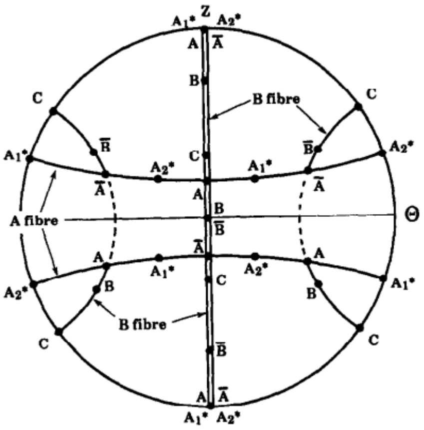

Figure 27: Ideal Orientations for simple shear textures in FCC metals represented in $\{1\ 1\ 1\}$ pole figure. [35]

2.3.3.3 Ideal orientations for BCC structures

In the case of BCC structures, a very similar behaviour is expected. Figure 28 shows the two main fibres described by Beyerlein and Tóth [7] which follow the same patterns as in FCC structures but with the slip planes and directions inverted. These fibres are:

- Fibre $\{1\ 1\ 0\}$ parallel to the shear plane. It contains the components F, J, $\bar{J}$, E and $\bar{E}$.
- Fibre $\langle 1\ 1\ 1\rangle$ parallel to the shear direction. It contains the components D_1, D_2, E and $\bar{E}$.

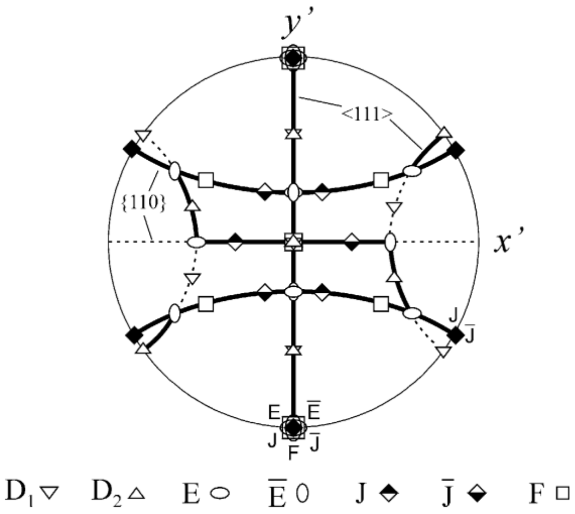

Figure 28: Ideal Orientations for simple shear textures in BCC metals represented in $\{1\ 1\ 0\}$ *pole figure. [36]*

2.3.3.4 Examples of Textures obtained in Simple Shear Deformation

Simple shear is a deformation mechanism present not only shear forming, but also in many other forming processes. By seeing examples of textures obtained by simple shear, even if the process is not shear forming itself, it will be possible to have a better understanding of the expected texture behaviour of the materials studied in this project.

A very common example of a simple shear process is Equal Channel Angular Extrusion (ECAE). In this process the workpiece is extruded through a die formed by two equal channels that intersect each other causing it to deform uniformly by simple shear [37] (See Figure 29). After analysing the changes in the microstructure of a Nickel alloy after a few passes in ECAE following different processing routes, Segal [37] concluded that the deformation mechanism along the workpiece is in fact simple shear. Two examples of textures obtained during ECAE are shown in Figure 30 and Figure 31. The first example corresponds to FCC Pure Copper and the second to a BCC Interstitial-Free Steel.

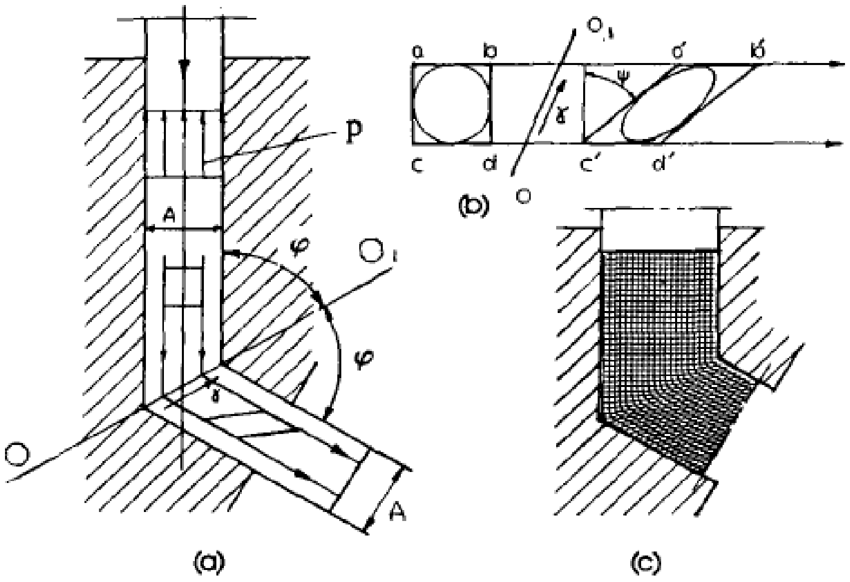

Figure 29: a) Diagram of Equal Channel Angular Extrusion. b) Deformation by simple shear. c) Representation of deformation of elements during ECAE operation. [37]

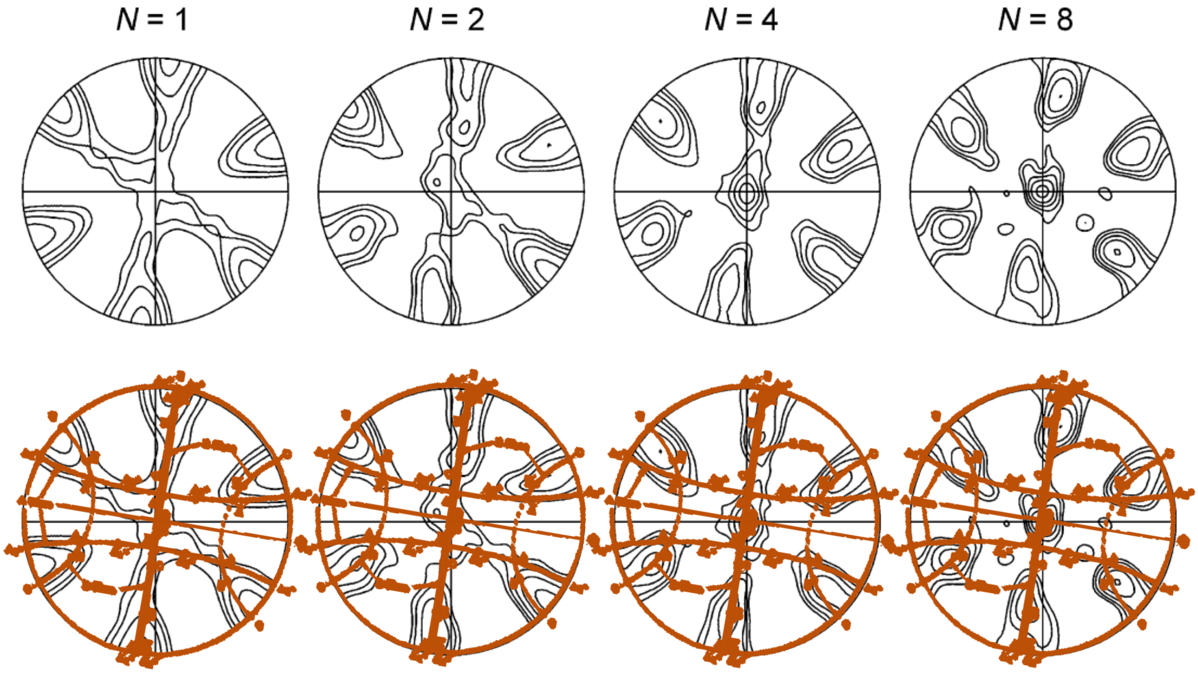

Figure 30: Textures obtained in Cu after 1, 2, 4 and 8 ECAE passes compared against the ideal texture in simple shear. Pole figure (1 1 1)*. [35, 38]*

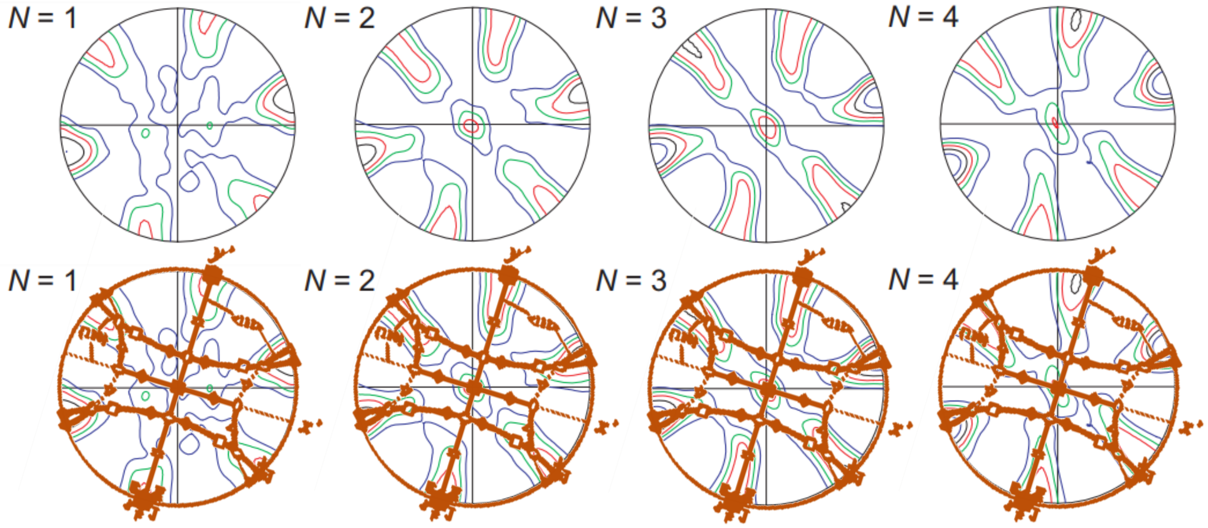

Figure 31: Textures obtained in IF-Steel after four ECAE passes compared against the ideal texture in simple shear. Pole figure $(1\ 1\ 0)$. *[36, 39]*

Simple shear deformation can also be studied using a Split Hopkinson Pressure Bar (SHPB) [40]. Wong et al. [40] used flat Inconel 718 specimens with the shape shown in Figure 32b, and compressed them between two bars to induce shear deformation in the red zone seen in Figure 32a. An example of the textures they obtained is shown in Figure 33, where the presence of adiabatic shear bands (ASB)[1] is very clear in the grain orientation map.

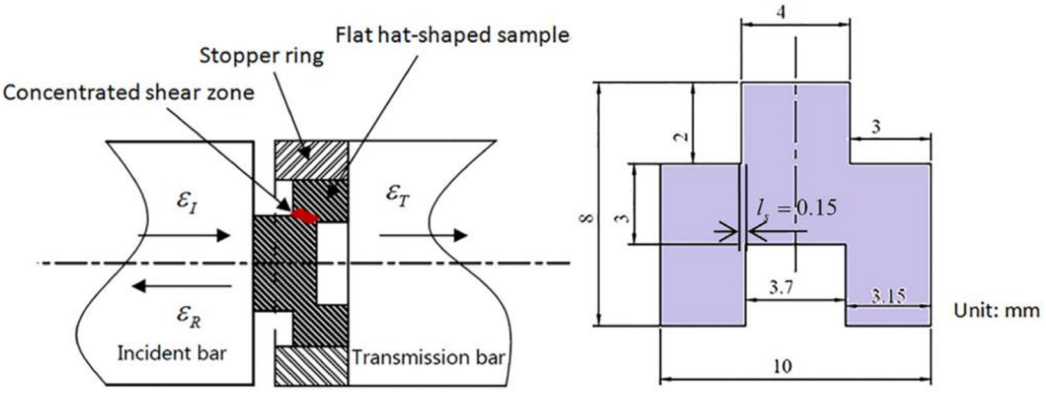

(a) (b)

Figure 32: SHPB test specifications. a) Test layout. b) Specimen shape and dimensions. [40]

---

[1] Adiabatic Shear Bands: Narrow bands, typically between 1 and 100 microns, of localised shearing formed during high strain-rate deformation. They reduce the material's load carrying capacity and other properties.

[41] L. Jiang, Y. Yang, Z. Wang, and H. Hu, "Microstructure evolution within adiabatic shear band in peak aged ZK60 magnesium alloy," *Materials Science & Engineering A,* vol. 711, pp. 317-324, 2018, doi: 10.1016/j.msea.2017.10.111.

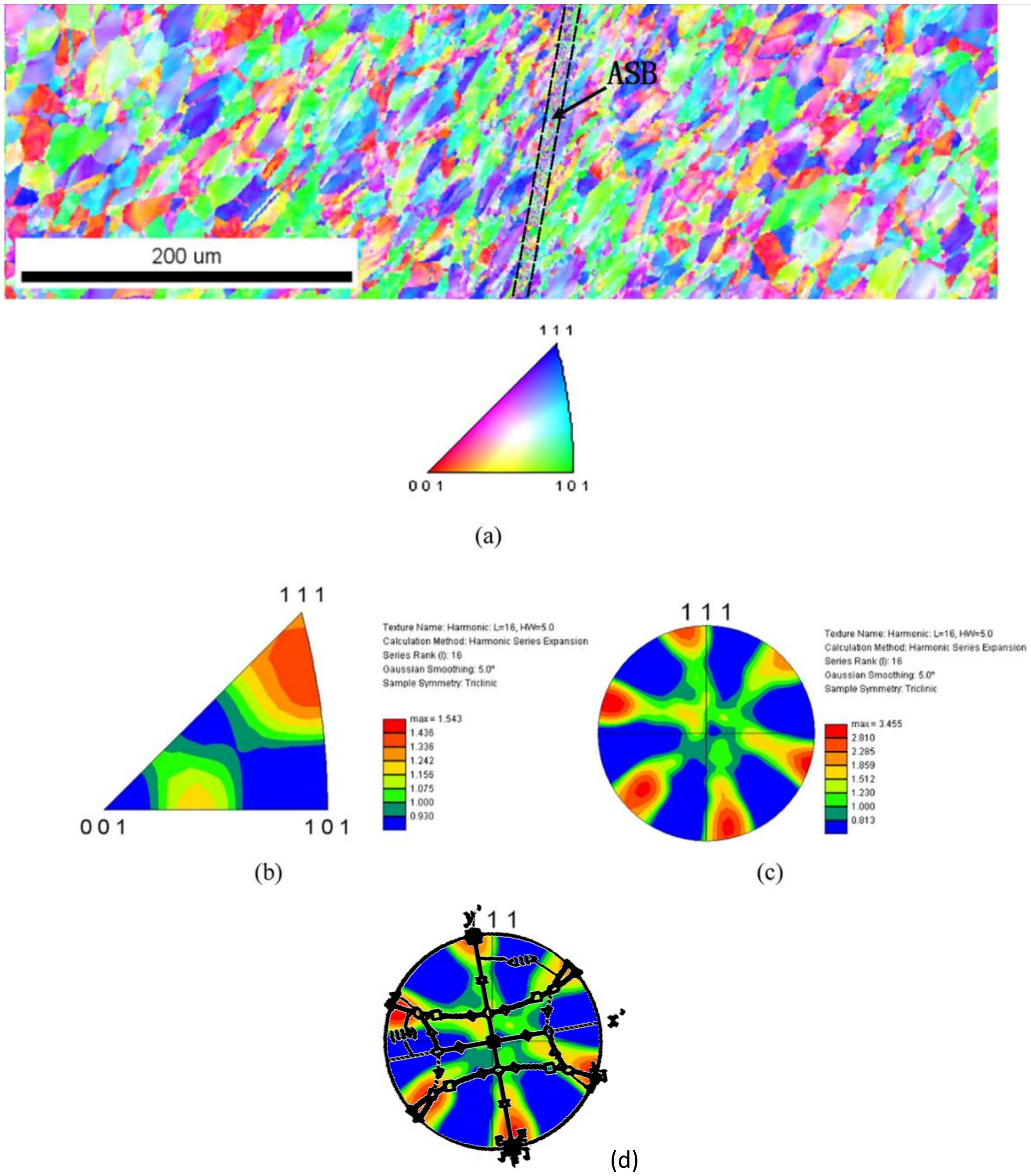

Figure 33: Textures in FCC Inconel 718 sample after SHPB Test. a) Gran orientation Map. b) Inverse Pole figure of shear zone. c) Texture corresponding to the map shown in a), pole figure (1 1 1). D) Texture obtained compared to texture in ideal simple shear. [36, 40]

2.4 Failure Mechanisms in Metals

One of the main objectives of this project is to be able to evaluate the potential of a material to be shear spun. To do this, it is important to understand failure mechanisms in metals. There are two main type of fractures in metals: brittle and ductile. The first type is characterised by little to no plastic deformation before failure, while ductile fracture occurs when there is previous significant plastic deformation[42]. An example of both fractures is shown in Figure 34. Due to the nature of this project and the materials studied in Chapter 3 and 4, only ductile fracture will be of interest.

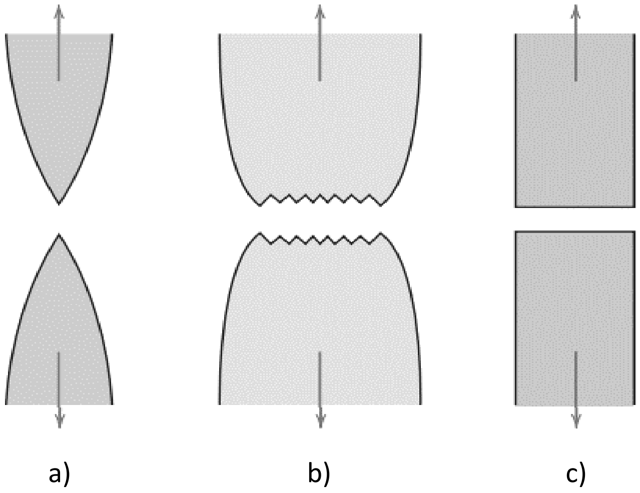

Figure 34: Visualisation of types of fracture: a) Ductile fracture with severe necking, b) Less ductile fracture with some necking, c) Brittle fracture. [43]

The two main mechanisms present in ductile fracture are void coalescence and mechanical instability (See Figure 35). In void coalescence, voids originate at the inclusions present in the material (void nucleation) and then grow and combine with neighbouring voids until a crack is formed. Mechanical instability is characterised by the formation of instabilities like shear bands (narrow bands of high shear strain) or necking[2] where the void coalescence process eventually happens. [44]

---

[2] Necking: When a material reaches the maximum stress that can sustain and starts to form a neck or area where all the following deformation occurs until fracture takes place.

[43] W. D. Callister, *Materials science and engineering : an introduction*, 8th ed., SI version / William D. Callister, Jr., David G. Rethwisch. ed. Hoboken, N.J.: Hoboken, N.J. : Wiley, c2011, 2011.

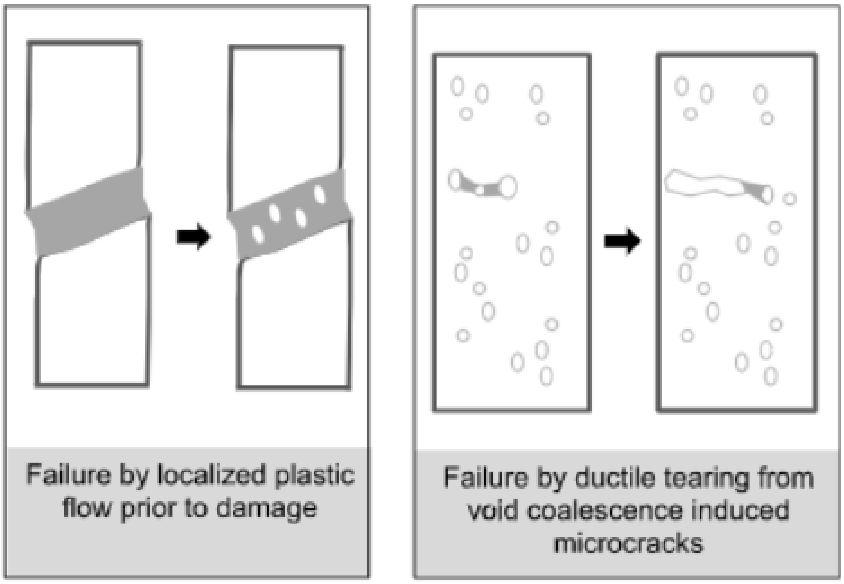

a) b)

Figure 35: Ductile fracture mechanisms: a) Mechanical instability, b) Void Coalescence. [44]

It is important to note that in both failure mechanisms, void coalescence is the cause of the final fracture of the workpiece. There are three basic modes of void coalescence depending on the direction of the forces applied: tension, shear and tensile tearing. These three modes generate different shapes of dimples in the fracture surface which are the result of the cavities formed in the failure process. In tension equiaxed dimples are formed, while in shear and tensile tearing the dimples are elongated. In the case of the tensile tearing the dimples become more elongated the closer they are to the region where the force was applied. An example of the three modes is shown in Figure 36. [42]

The deformation process in uniaxial tension and simple shear has been studied in the past to try and understand the fracture mechanisms in both processes [45] [46]. Gerstein et al. [45] concluded that the test configuration had little effect on the plastic deformation behaviour of the materials studied while the crystal structure did had a great effect on this. Additionally Isakov et al. [46] found a correlation between the tensile and simple shear results (see Figure 37) and concluded that in simple shear higher levels of strain can be achieved due to the lack of necking, which results in a more complex final fracture due to the heavy distortion of the material’s structure and the multiaxial loading in simple shear.

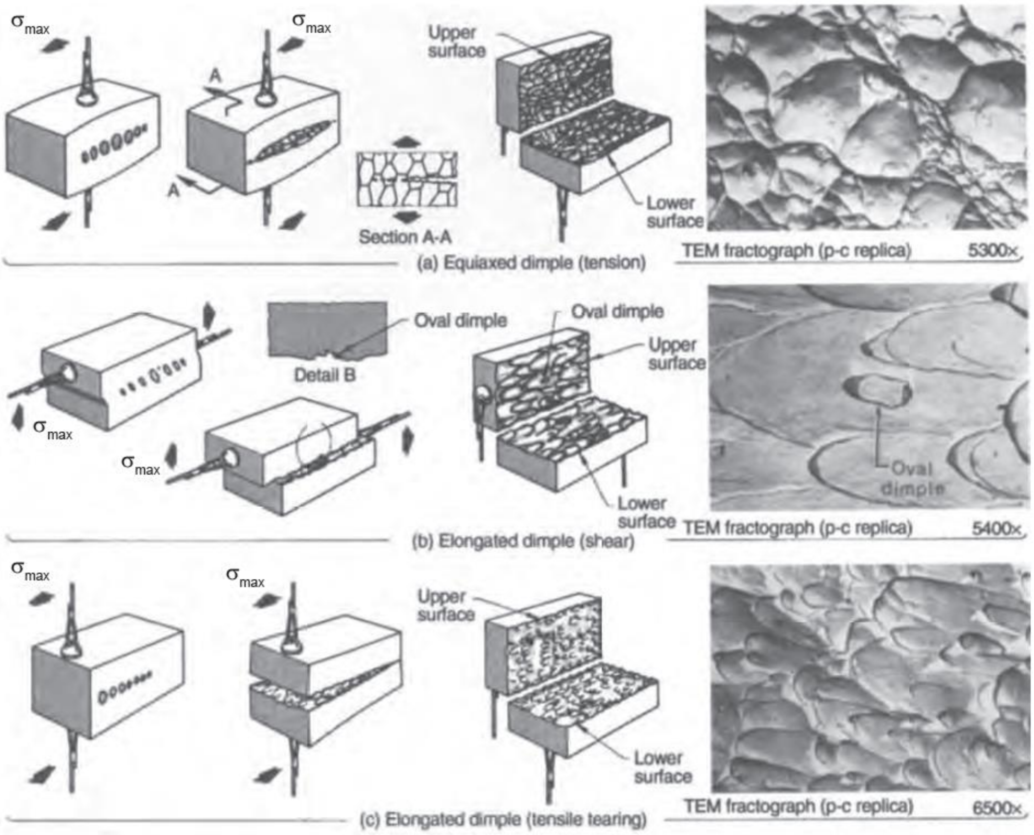

Figure 36: Visualisation of the three modes of void coalescence and the dimples generated in each case. a) Tension, b) Shear, c) Tensile tearing. [42]

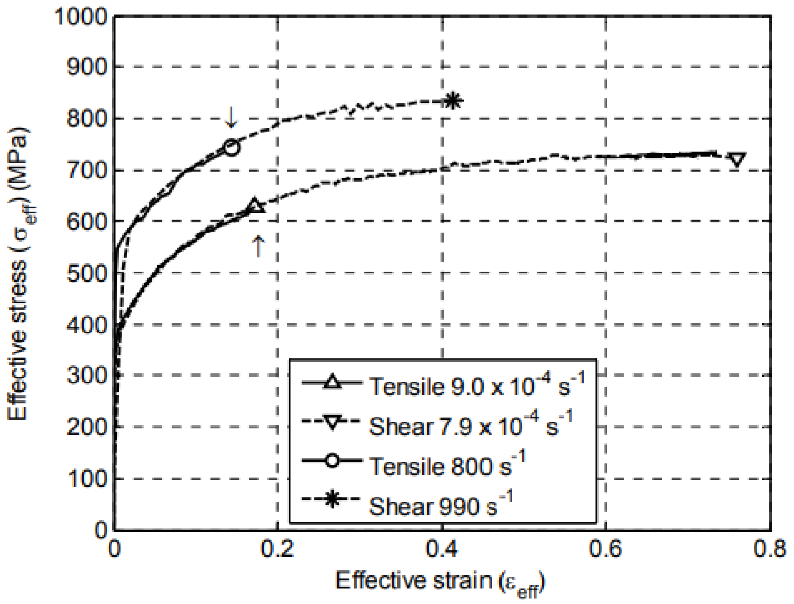

Figure 37: Effective stress-strain curves of a ferritic stainless steel at different strain rates under tensile and simple shear testing. [46]

2.5 Damage Models in Metals

Three uncoupled damage models integrated in Deform were selected for their analysis in order to implement an adequate damage criterion in the final FEM model. The models selected were:

1. Ayada Model
2. Normalised Cockcroft & Latham Model
3. Forming Limit Diagram Model

Uncoupled damage models are the ones that does not consider the effects of damage on the properties of the materials during the process [47]. Even though it would be ideal to take this into consideration, various studies have shown that uncoupled models can accurately predict ductile fracture [48], [47].

2.5.1 Ayada Damage Model

This model was introduced by Ayada [49] to predict fracture in ductile materials based on the stress triaxiality and the effective strain. Stress triaxiality (T) is a way to measure how much of the stress tensor is approaching an hydrostatic stress state (when the principal stresses are equal) [50]. Components with high stress triaxiality are likely to show fractures caused by void growth [50].

The mathematical definitions of stress triaxiality and the Ayada damage factor are shown in equations Equation 11 and Equation 12 in terms of effective stress ($\bar{\sigma}$), mean stress (σ_m) and effective strain ($\bar{\varepsilon}$). When the damage factor reaches a value of 1, fracture is expected.

$$T = \frac{\sigma_m}{\bar{\sigma}}$$

Equation 11

$$D = \int_0^{\bar{\varepsilon}_f} \frac{\sigma_m}{\bar{\sigma}} d\bar{\varepsilon}$$

Equation 12

2.5.2 Normalised Cockcroft & Latham Model

This damage criterion is used to predict fracture in ductile materials and it is based on the Cockcroft & Latham model [51] in which the damage is calculated with the maximum principal stress (σ_{1max}) and the effective strain as shown in Equation 13. Each material has a constant that needs to be determined before using this criterion, and when the damage (D) reaches that value, then fracture is expected.

$$D = \int_0^{\bar{\varepsilon}_f} \sigma_{1max}\, d\bar{\varepsilon}$$

Equation 13

Later, this criterion was modified by normalising the damage value with the effective stress (as show in the equation below [52]), eliminating the need to calculate the constant mentioned before. In this modified criterion, the material is expected to fail if the damage reaches a value of 1.

$$D = \int_0^{\bar{\varepsilon}_f} \frac{\sigma_{1max}}{\bar{\sigma}}\, d\bar{\varepsilon}$$

Equation 14

2.5.3 Forming Limit Diagram Model

Forming limit diagrams (FLD) are a graphical representation of the possible strain states of sheet metals based on the principal strains of the material. A Forming Limit Curve (FLC) indicates which strain states are safe (below the FLC) and which predict failure (above the FLC). A graphical representation of this concept is shown in Figure 38.

Isik et al [53], also clarify that the right side of the diagram represents the tension-tension region and was developed by Keeler [54], while the left side was later developed by Goodwin [55] and represents the tension-compression region.

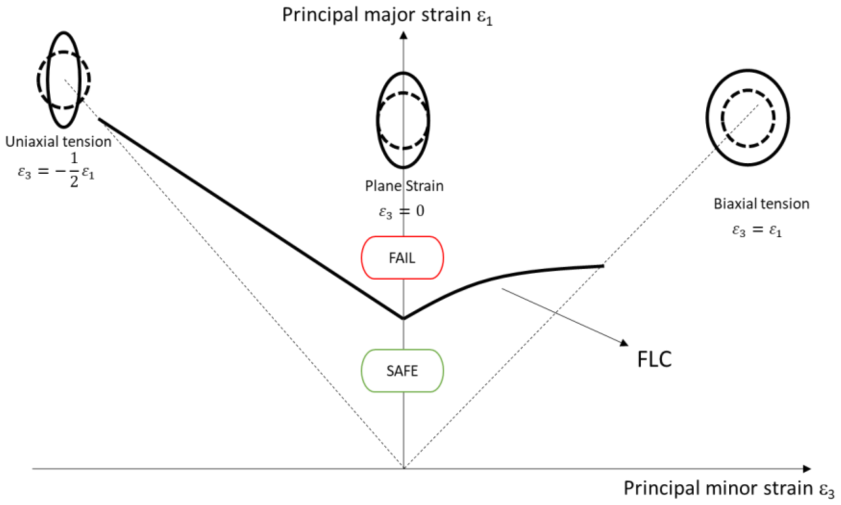

Figure 38: Example of Forming Limit Diagram [56].

In Deform, the damage factor is calculated by dividing the actual major strain obtained (ε_{1Limit}) by the limiting maximum principal strain (ε_1) corresponding to the minimum principal strain (ε_2) of a given deformed element. See equation Equation 15 and Figure 39. Failure is expected when the damage value reaches 1.

$$D = \frac{\varepsilon_{1Limit}}{\varepsilon_1}$$

Equation 15

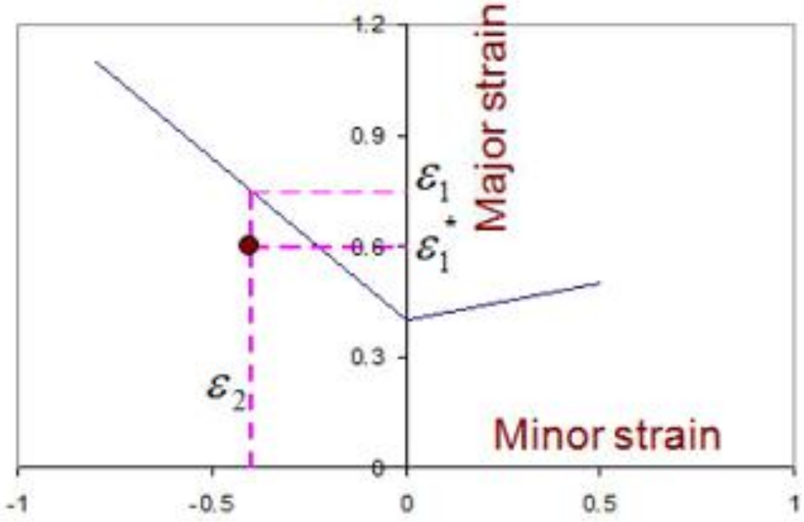

Figure 39: Visualisation of Principal Strains' values used for damage calculations in Deform. [57]

Chapter 3: Experimental Procedure

3.1 Introduction

In order to understand the deformation behaviour of workpieces during shear forming, the microstructure and microtexture of some materials that have already undergone this process were analysed. Such information will be also the key to the validation of FEM model that was developed and will be described in Chapter 4.

Three materials were used in this stage: titanium alloy Timetal 54M, Jethete M152 alloy and nickel alloy Inconel 718. The last two materials have already been successfully shear formed in the past and specimens were provided by external suppliers. In the case of Timetal 54M a fractured sample was provided given that no successful shear spun parts were achieved by the supplier. A summary of the shear forming processes parameters used for these trials is shown in the following table. The as received materials consisted of hot rolled plates and no additional information was provided by the supplier for Timetal 54M regarding heat treatments conducted prior or after the shear forming process. The Jethete M152 plate was hot rolled and annealed at 780 ˚C plus air cooled, while the Inconel 718 plate was hot rolled and solution treated between 950 and 990 ˚C plus water quenched before the shear spinning process. The shear forming process parameters of all samples are shown in the following table.

Table 1: Process parameters of shear spun specimens provided.

Material	Mandrel angle (α)	Blank Thickness (mm)	Feed Rate (mm/rev)	Rotational Speed (m/min)	Overall Result
Timetal 54M	31.5°	4.50	0.50	300	Fractured after 4 revolutions
Inconel 718	40°	6.00	0.50	300	Successful
Jethete M152	50°	5.00	0.50	300	Successful

Micrographs of the transversal section were taken for all samples; however, it was not possible to obtain orientation maps of the Timetal 54M sample because its fine grain size and the heavy deformation that had undergone caused the indexing during the EBSD analysis to be very poor. The results obtained in this chapter, not only provided a better insight of the deformation paths along the workpiece in shear spinning but also allowed to validate the FEM model developed in Chapter 4.

3.2 Experimental Details

3.2.1 Materials

3.2.1.1 Timetal 54M

Timetal 54M, also called Ti54M, is a double phase titanium alloy recently developed by TIMET. The general microstructure consists of a HCP alpha phase matrix with lamellar grains of BCC beta phase [58]. The chemical composition is shown in Table 2. This alloy is very similar to the common alloy Ti6Al4V but with slightly better mechanical properties and higher machinability, which could potentially lead to lower production costs [59]. One important difference is that Timetal 54M presents lower beta transus temperature due to its chemical composition [59] (See Figure 40).

Armendia et al. [60] compared Ti6Al4V and Timetal 54M alloys with various heat treatments and observed that even though mechanical properties remain very similar between both alloys, a much finer grain size was achieved in the Timetal 54M samples which could explain the higher machinability of this alloy.

Table 2: Chemical composition of Timetal 54M. [61]

Element	Al	V	Mo	Zr	Si	Fe	N	O	C	Ti
Ti-54 M	5.03	3.95	0.57	0.005	0.11	0.506	0.05	0.06	0.10	Rest

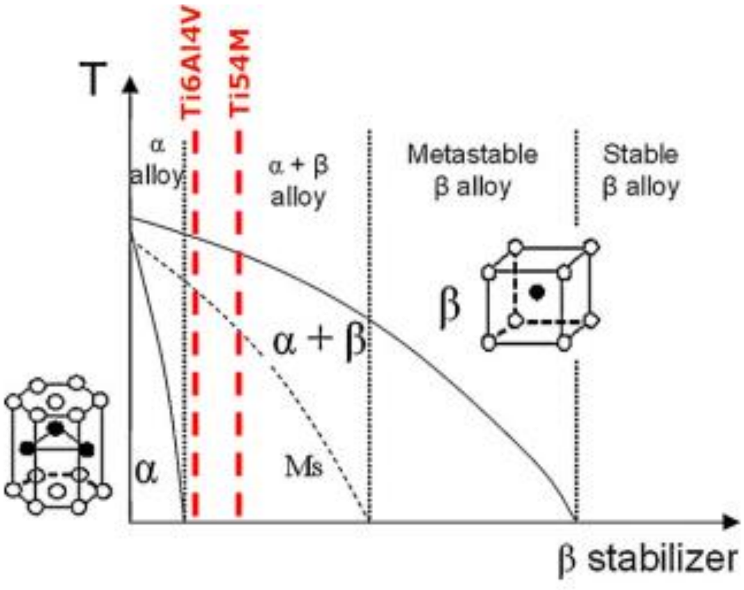

Figure 40: Beta-Isomorphus phase diagram of Titanium Alloys. The position of Ti6Al4V and Ti54M alloys is shown. [59]

Like in many other alloys, the microstructure of Timetal 54M components depends greatly on the heat treatment and processing given to it. Yang [62] studied the impact of various heat treatments, such as full and beta annealing plus either water quenching or air cooling on final the microstructure and the following was observed:

1. Water quenching after both full and beta annealing produced martensitic transformation of both phases in the case of full annealing and of the beta phase after beta annealing.
2. Air cooling produced lamellar microstructures.
3. The annealing temperature directly affects the percentage of alpha phase. Higher annealing temperatures resulted in less percentage of alpha phase.
4. Fully equiaxed microstructures were achieved after 800 ˚C annealing plus either air cooling or water quenching.

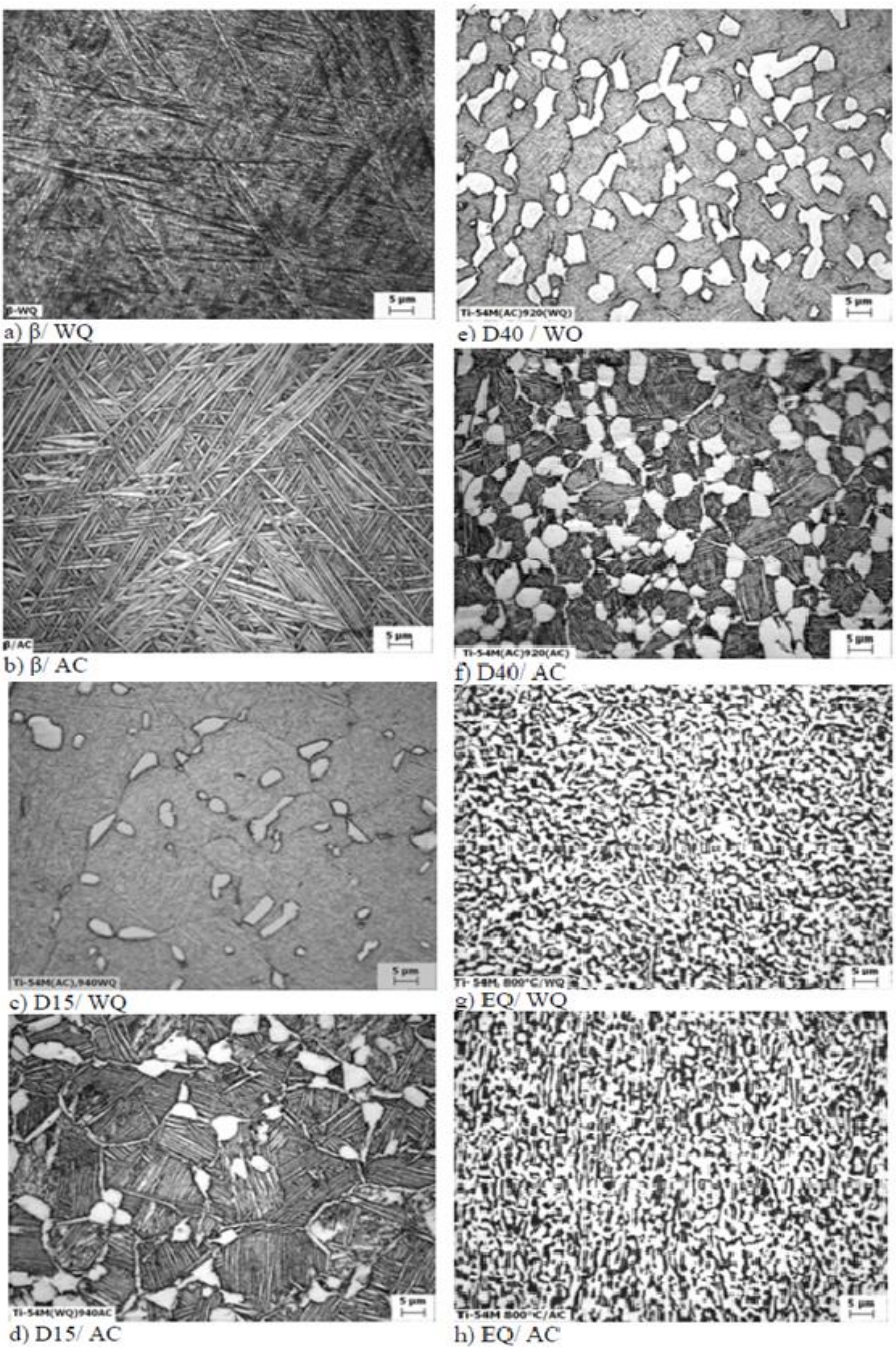

a) β/ WQ

e) D40 / WO

b) β/ AC

f) D40/ AC

c) D15/ WQ

g) EQ/ WQ

d) D15/ AC

h) EQ/ AC

Figure 41: Microstructures obtained by Yang [62] after various heat treatments: a) Beta annealing + water quenching (WQ), b) Beta annealing + air cooling (AC), c) Annealing at 940 ˚C + WQ, d) Annealing at 940 ˚C + AC, e) Annealing at 920 ˚C + WQ, f) Annealing at 920 ˚C + AC, g) Annealing at 800 ˚C + WQ and h) Annealing at 800 ˚C + AC.

3.2.1.2 Jethete M152

Jethete M152 is a low-carbon martensitic stainless steel with high strength, fracture toughness and good weldability after forging [63]. It also has great creep and corrosion resistance properties, which makes it perfect for turbine applications with high stress requirements [64]. The chemical composition of the Jethete M152 sample used for these experiments is shown in the Table 3.

In steels, each phase has a different crystal structure. Figure 42, shows that martensite is a BCT phase, which is very similar to BCC ferrite but with an interstitial carbon atom in the crystal unit, i.e. BCT is basically distorted BCC structure [65]. Since both crystal structures are very similar and to avoid further complications in the analysis, BCT martensite was treated as BCC for the texture studies and predictions conducted throughout the work described in this chapter and chapter 4.

Table 3: Chemical composition of Jethete M152 [66]

Element	C	Si	Mn	P	S	Cr	Ni	Mo	V	N	Fe
Jethete M152	0.167	0.45	0.82	0.018	0.0010	10.68	0.73	0.90	0.20	0.012	Rest

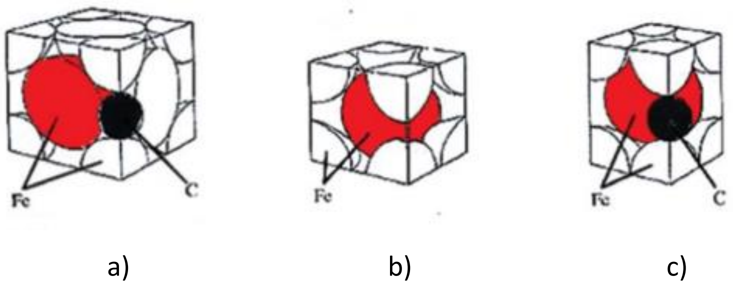

a) b) c)

Figure 42: Crystal structures present in the different phases of steel. a) FCC structure of austenite, b) BCC structure of ferrite and c) BCT structure of martensite. Modified from [65]

Martensite can appear in different forms depending on the steel's chemical composition, which can be lath, butterfly, lenticular and thin plates [67]. In low carbon steels, the typical morphology found is lath martensite divided into single-oriented blocks, which also form packets [68]. Figure 43 shows a diagram of the typical morphology of lath martensite grains and Figure 44 shows an example of this structure found in an Interstitial Free (IF) steel with 0.26 wt% carbon.

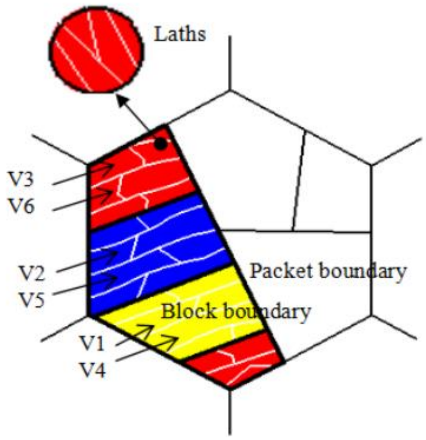

Figure 43: Lath martensite structure. [67]

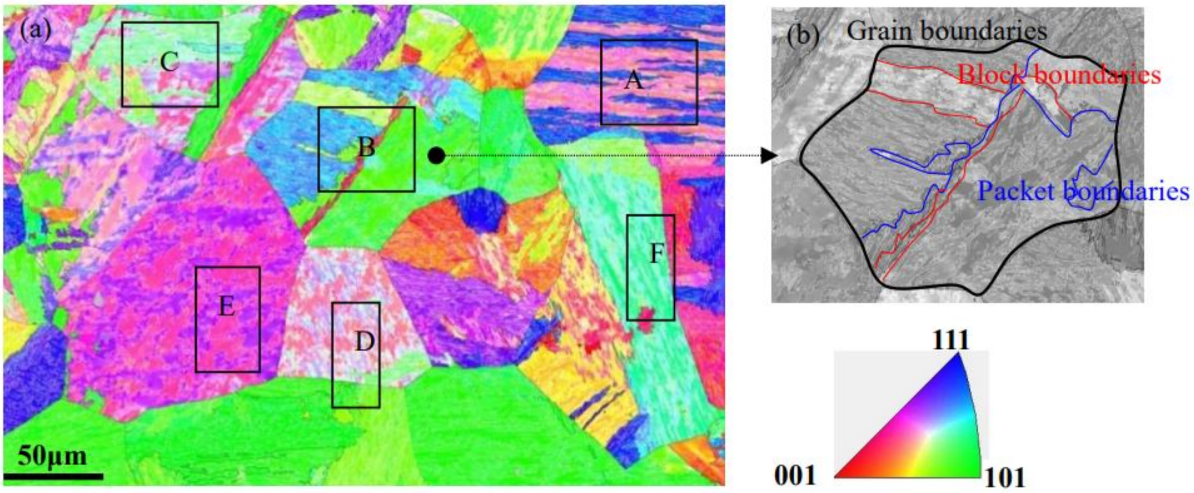

Figure 44: a) EBSD map of martensitic structure found in an IF steel. b) Example of blocks and packets boundaries found in this structure. [67]

The Jethete steel plate used for the shear forming process analysed in this chapter was previously hot rolled and softened by annealing at 780 ˚C plus air cooling. This type of processing and heat treatment has been proved to affect greatly the microstructure of martensitic steels. Ghosh et al. [69] analysed the microstructural changes of a low carbon martensitic steel (0.17 wt% C) after cold rolling and annealing. They found that high thickness reduction cold rolling (50% and 80% thickness reduction) plus annealing at 700 ˚C resulted in the partial recrystallisation of martensite forming ferritic grains and carbide precipitates. The microstructural changes observed in this research are shown in Figure 45 and Figure 46.

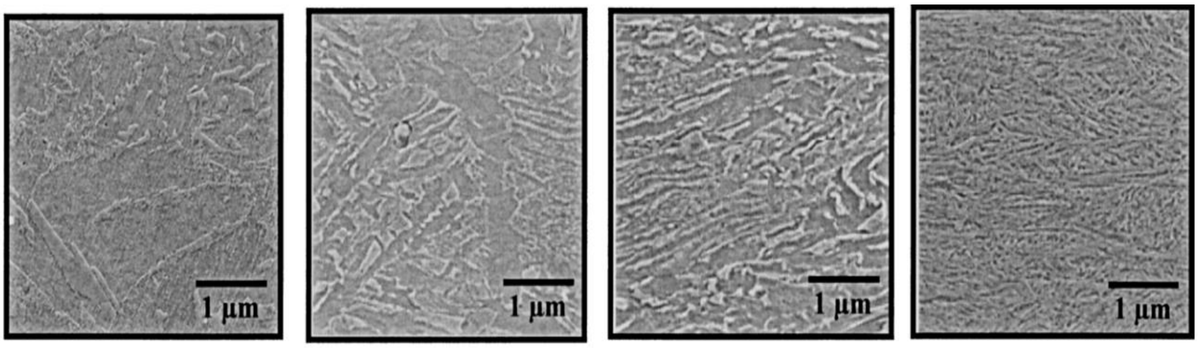

a) b) c) d)

Figure 45: Micrographs of low carbon martensitic steel after: a) No processing (Initial microstructure), b) 30% reduction cold rolling, c) 50% reduction cold rolling and d) 80% reduction cold rolling. [69]

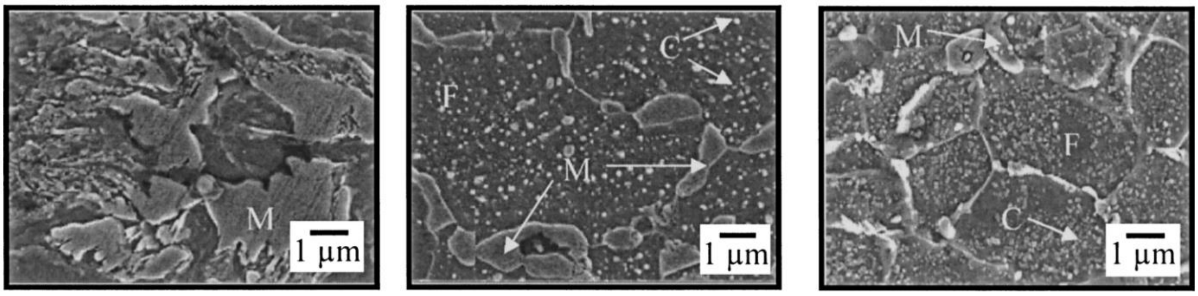

a) b) c)

Figure 46: Micrographs of low carbon martensitic steel after 700 ˚C annealing. a) 30% reduction cold rolling, b) 50% reduction cold rolling and c) 80% reduction cold rolling. M – Martensite, F – Ferrite and C – Carbide. [69]

3.2.1.3 Inconel 718

Inconel 718 (IN718) is a nickel base alloy with high content of chromium (Cr), iron (Fe), niobium (Nb) and molybdenum (Mo) [70]. It is well known for its age hardening behaviour, high corrosion resistance and good workability, as well as good performance at high temperatures [71].

Due to its high strength and toughness at elevated temperatures, IN718 is widely used in high temperature applications, such as turbine parts and heat treatment components [72].

The typical microstructure of IN718 consists of an FCC matrix (γ) made of a solid solution of various alloying elements such as Cr, Fe and Mo in Nickel, and other precipitates and carbides. The main strengthening phases in this alloy at high temperature are BCT Ni_3Nb gamma double prime (γ”) and FCC $Ni_3(Al, Ti)$ gamma prime (γ’) which precipitate between 600 and 900 ˚C [73] [74] [75]. In Table 4, the typical chemical composition of this alloy is shown.

Table 4: Chemical composition of Inconel 718 sample. [76]

Element	**Al**	**C**	**Co**	**Cr**	**Cu**	**Fe**	**Mo**	**Ti**	**Nb**	**Ni**
Inconel 718	0.52	0.021	0.11	19.06	0.02	18.15	3.04	0.93	5.08	Rest

The as-received Inconel 718 plate used in this project was solution heat treated prior shear forming. This heat treatment consists in the heating of an alloy to a certain temperature and maintain it for an adequate period of time, so the precipitates in it dissolute and form a homogenous solid solution structure [77]. Some examples of microstructures obtained in Inconel 718 after solution treatment at different temperatures are shown in Figure 47. In all examples, twins are present throughout the microstructure. Annealing twins are typically formed during the recrystallisation of FCC metals with medium to low stacking fault energy, like Nickel alloys [78].

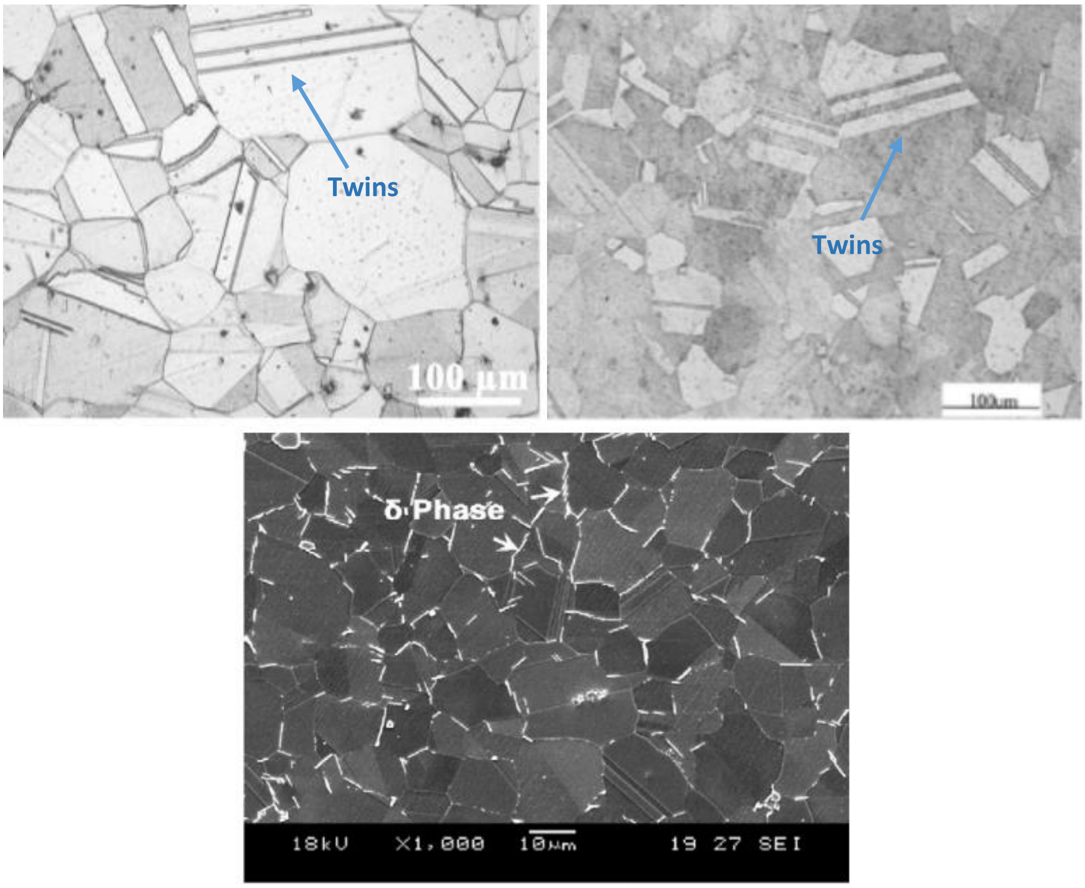

Figure 47: a) Solution treated at 1050 ˚C + air cooled [79], b) Solution treated at 1050 ˚C for 1 h + water quenched [80], c) Solution treated at 968 ˚C + water quenched [81]

3.2.2 Sample Sectioning

Small samples were cut from the Jethete M152 and Inconel 718 specimens provided. Every sample was taken from the transition area of the workpiece, as shown in Figure 48. In this way it was ensured that all specimens had fully deformed and undeformed areas included. All samples had a total length and height of no more than 10 mm and a width of 5 mm. In Figure 49a, a schematic of the geometry of these samples is shown.

For Timetal 54M, a prepared sample of the fractured zone was already provided so no further sectioning was needed (See Figure 49b).

Figure 48: Visualization of the Inconel 718 and Jethete M152 samples provided. These samples consisted of a large section of the original shear spun blank. The red circle indicated the area where the specimens were cut from.

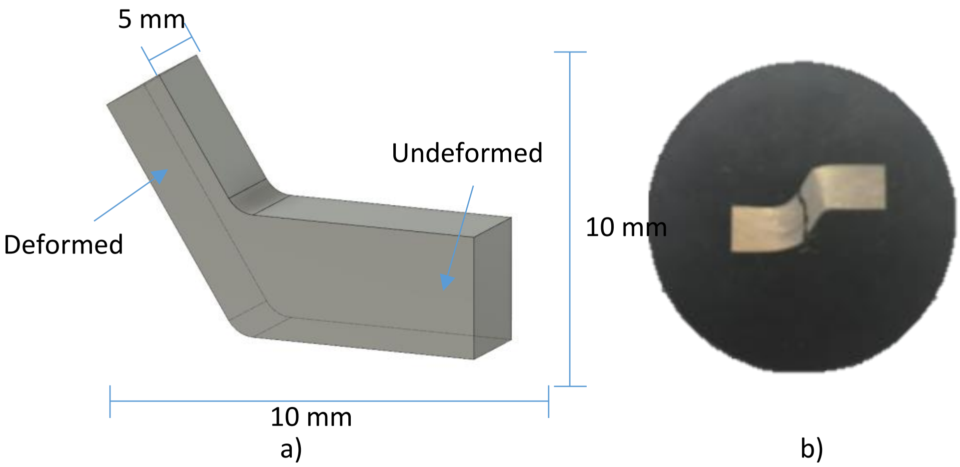

Figure 49: a) Geometry of IN718 and Jethete M152 samples. b) Ti54M sample already mounted in Bakelite provided by TIMET.

3.2.3 Metallographic Preparation

In order to conduct chemical etching and EBSD analysis, a clean flat surface is needed. This was achieved by grinding and polishing the samples following the corresponding methods to each material shown in Table 5, Table 6 and Table 7.

Table 5: Grinding and Polishing method for Jethete M152 alloy.

Surface	Abrasive/Size	Load (N)	Base Speed (RPM, Direction)	Time (min:sec)
CarbiMet 2 abrasive discs	P240 grit SiC	27	240, Comp	Until Plane
CarbiMet 2 abrasive discs	P800 grit SiC	27	240, Comp	1:00
UltraPol polishing cloth	9µm MetaDi diamond suspension	20	120, Comp	5:00
TriDent	3µm MetaDi diamond suspension	20	120, Comp	5:00
ChemoMet cloths	90% Silica / 10% H_2O_2	20	120, Contra	10:00

Table 6: Grinding and polishing method for Inconel 718 alloy.

Surface	Abrasive/Size	Load (N)	Base Speed (RPM, Direction)	Time (min:sec)
CarbiMet 2 abrasive discs	P240 grit SiC	27	240, Comp	Until Plane
CarbiMet 2 abrasive discs	P800 grit SiC	27	240, Comp	1:00
CarbiMet 2 abrasive discs	P1200 grit SiC	27	240, Comp	2:00
CarbiMet 2 abrasive discs	P2500 grit SiC	27	240, Comp	4:00
ChemoMet cloths	90% Silica / 10% H_2O_2	20	120, Contra	25:00

Table 7: Grinding and polishing method for Ti54M alloy.

Surface	Abrasive/Size	Load (N)	Base Speed (RPM, Direction)	Time (min:sec)
CarbiMet 2 abrasive discs	P800 grit SiC	5	300, Comp	2:00
MD-LARGO	9µm MetaDi diamond suspension	5	150, Comp	10:00
ChemoMet cloths	90% Silica / 10% H2O2	5	150, Comp	15:00

3.2.4 Etching and Scanning Electron Microscopy

Chemical etching was performed to the samples to reveal their microstructure and inspect it using Scanning Electron Microscopy (SEM) with the secondary electrons (SE) mode in an Inspect F50 microscope. However, etching was unsuccessful for Inconel 718. This was caused by the drastic changes in the microstructure experienced during the shear forming process, which meant that it was not possible to achieve a regular etching throughout all the surface because of its non-uniform grain size. It was still possible to generate maps of the deformed zones using back scattered electrons (BSE mode). The parameters used for each material in the Inspect F50 SEM are shown in the following table.

Table 8: SEM parameters used in Inspect F50 SEM for all materials.

Parameter	Timetal 54M	Jethete M152	Inconel 718
Beam Spot Size	4.0	3.5	3.5 – 5.0
Beam Accelerating Voltage	15.0 KV	20.0 KV	10.0 – 20.0 KV

In Table 9 a summary of the etching times and etchant used for Jethete M152 and Timetal 54M is shown. In both cases the etching was performed by submerging the samples in the etchant for the time specified, then removing them and submerging them in water for 60 s. To ensure that etching was successful, optical microscopy was used to observe the sample immediately after the procedure. If needed, samples were re-polished and etching was repeated until results were satisfactory.

Table 9: Etchant and etching times used for Jethete M152 and Timetal 54M alloys.

Material	Etchant	Etching Time
Jethete M152	50 ml of Methanol 50 ml of Hydrochloric Acid (HCl) 2.5 gm of Copper II Chloride (Cu2Cl)	10 s
Timetal 54M	10 ml of Hydrofluoric Acid (HF) 10 ml of Nitric Acid (HNO3) 180 ml of water	15 s

Finally, three main areas were studied for all three materials: undeformed zone, deformed area near the mandrel surface and deformed area near the roller surface. From the micrographs taken, the average grain size in the zones of interest was calculated using the following equation.

$$Average\ grain\ diameter = \frac{Length\ of\ lines\ drawn}{Number\ of\ grains\ intercepted}$$

Equation 16

3.2.5 Texture Analysis - EBSD

In order to validate the simple shear deformation mechanism expected during the process, the texture of two of the materials was analysed. This test was not conducted on Timetal 54M because the grain size of the sample provided was so small that it was not possible to see the grains with the microscopes available for this project and this is needed for any EBSD analysis. For both, Jethete M152 and Inconel 718, maps were generated for all three areas of interest defined in section 3.2.6 using the parameters indicated in Table 10 with the Inspect F50 SEM. This would make possible to see if there is any variation of the texture along the thickness of the workpiece and hence evaluate the deformation mechanism present in the workpiece.

All maps studied in this chapter have been subjected to noise reduction. Using the software Channel 5, any points that were not indexed automatically during the EBSD analysis have been indexed by interpolating the results of its neighbouring points. An example is shown in Figure 50. By doing this the microstructural maps obtained remains unaltered but there is better grain definition. Since in all EBSD analysis conducted in this project clear maps with high indexing percentages were obtained, it is not believed that performing noise reduction affected the final results accuracy.

Table 10: EBSD parameters used in Inspect F50 SEM for all materials.

Parameter	Jethete M152	Inconel 718
Magnification	400x	500x
Beam Spot Size	5.0	5.0
Beam Accelerating Voltage	20.0 KV	20.0 KV
Step Size	0.1 µm	0.5 µm
Camera Binning	4x4 pixels	4x4 pixels
Timing per Frame	30-50 ms	30-50 ms
Averaged Frames	2-5	2-5

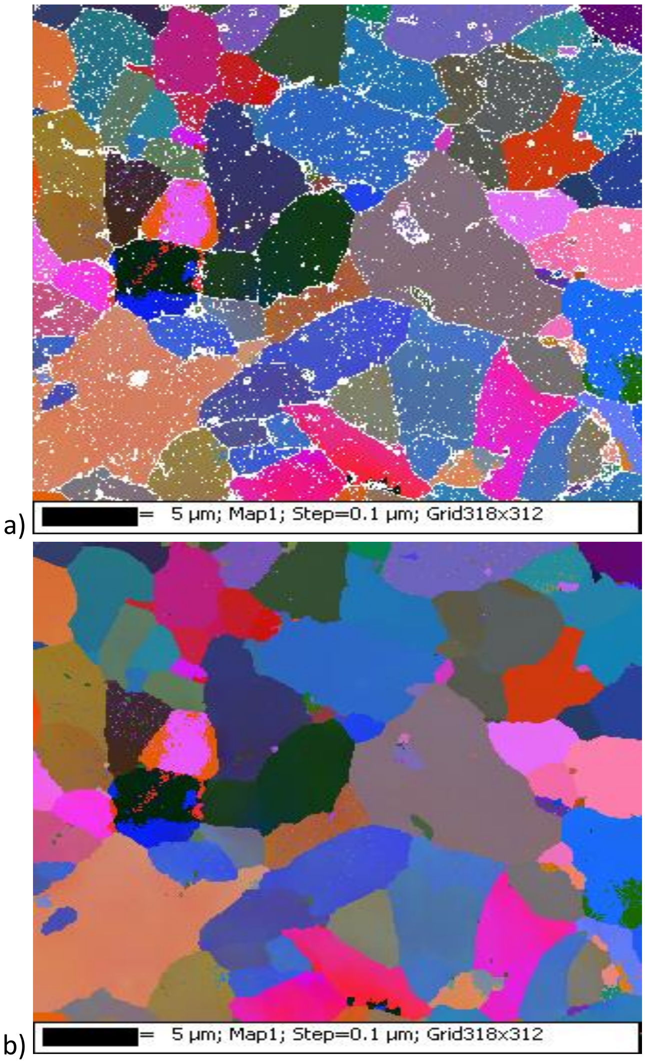

Figure 50: Noise Reduction Example. a) EBSD Map before Noise Reduction with 90.7% Indexing, b) EBSD Map after Noise Reduction with 100% Indexing.

3.3 Results

3.3.1 Timetal 54M

Even though several etching and EBSD attempts were made, it was not possible to reveal the full microstructure of the Timetal 54M sample. This was due to the small gran size of the material even before the deformation process was conducted. However, with the etching method carried out, it was possible to reveal beta phase grains of the alloy. The morphology changes in the beta phase grains were used to study the fracture in the sample, which can be seen in Figure 51. The main fracture occurred across the perpendicular direction of the workpiece thickness, however smaller cracks propagated from the main fracture in the longitudinal direction resulting in delamination of the material.

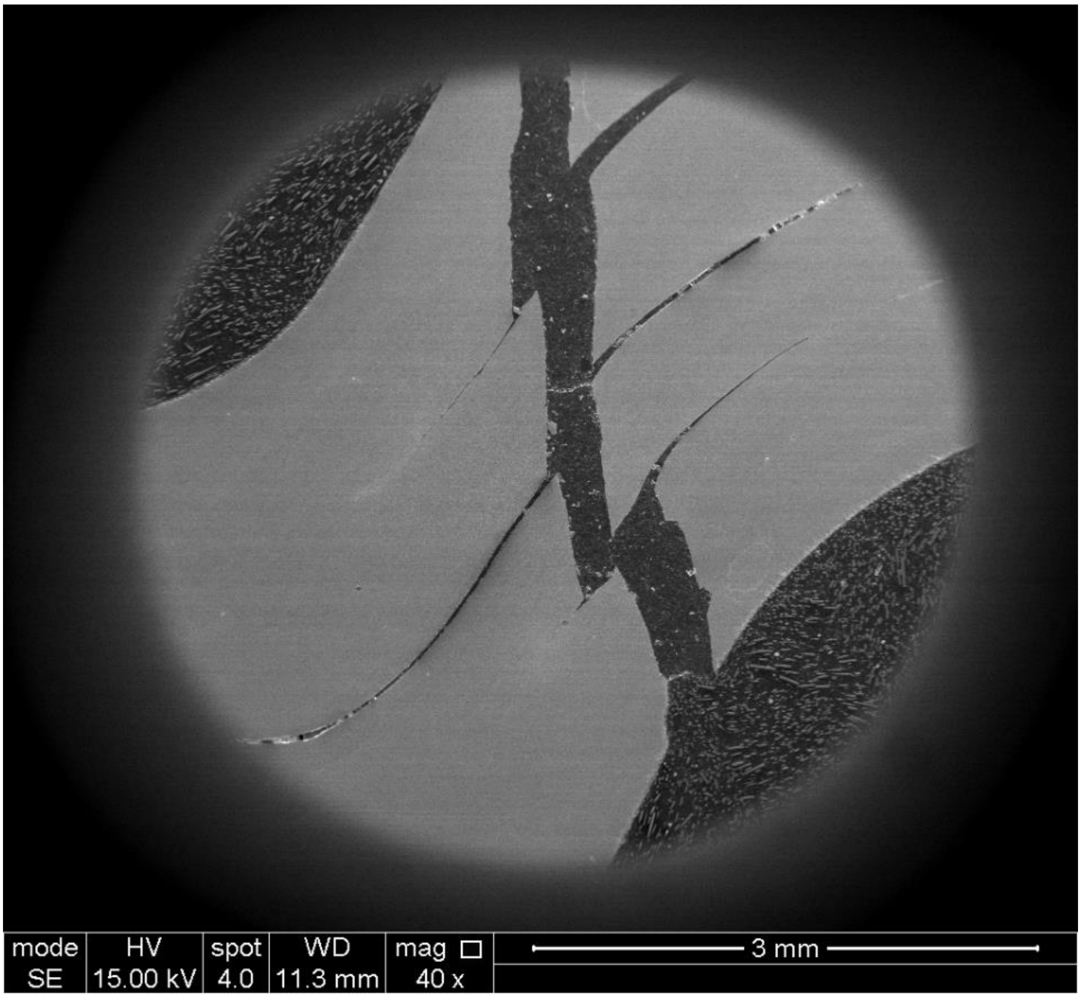

Figure 51: Fracture in Timetal 54M sample analysed. HV

The initial microstructure of the Timetal 54M blank used is shown in Figure 52, which consisted of long thin beta grains in a α matrix. This suggests that the original plate used for shear forming had been previously full annealed resulting in an equiaxed microstructure (refer to section 3.2.1.1) and then hot rolled, deforming the beta grains and giving them this longitudinal morphology. The beta grains observed had various longitudes with an average length of 7 µm and a height of around 1 µm.

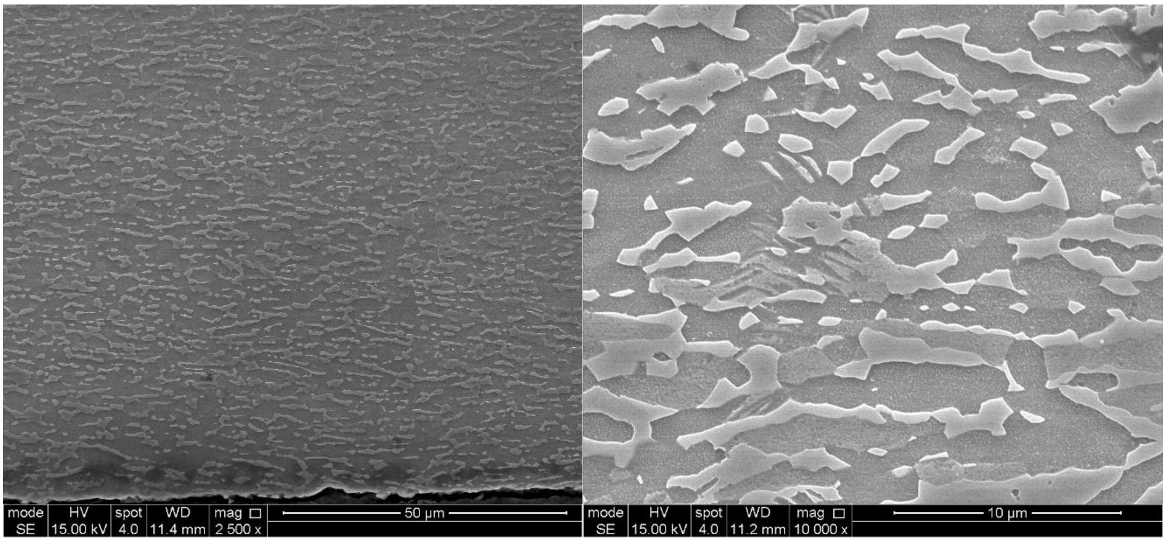

a) b)

Figure 52: Initial microstructure of Timetal 54M workpiece. a) Magnification 2500x. b) Magnification 10000x.

Figure 53 shows a micrograph taken from the transition area of the workpiece, i.e. where the material is already experiencing deformation but it has not achieved the final form of the workpiece yet. The edge that was in contact with the roller during the process is shown on the right. The beta phase grains became more elongated and thinner the closer they were to this edge, suggesting that the deformation experienced here is higher than in the rest of the thickness.

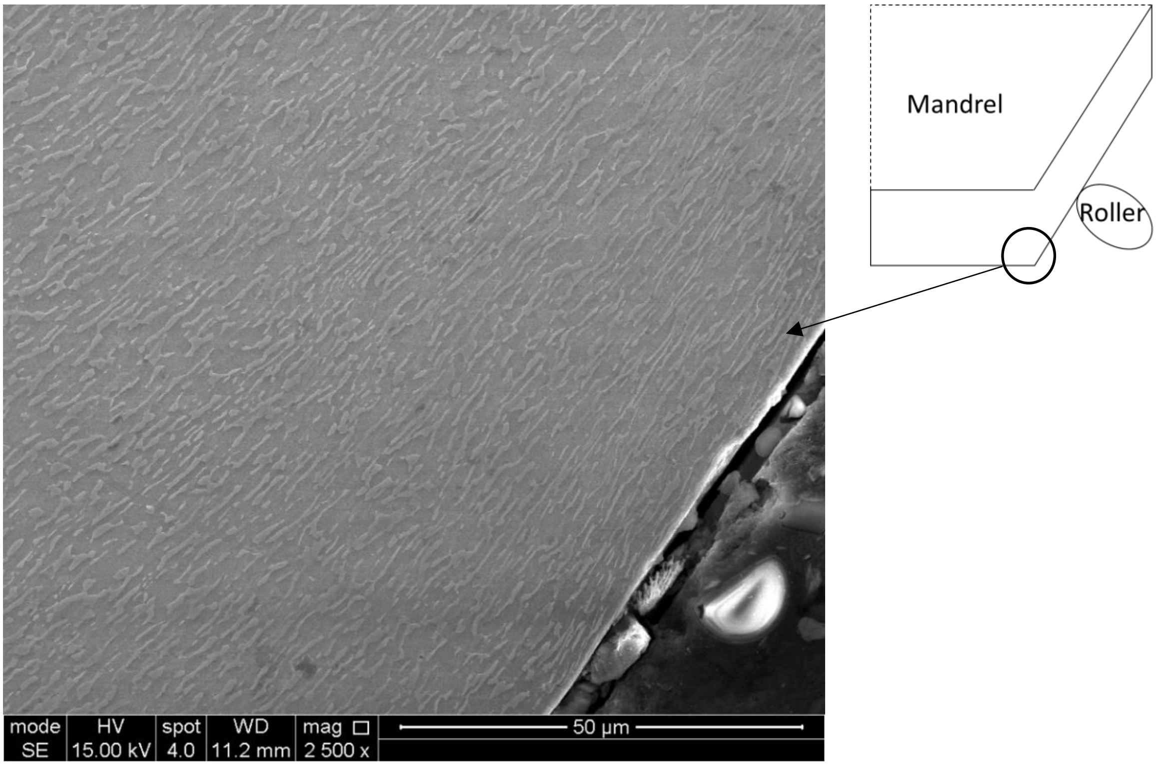

Figure 53: Transition area of Timetal 54M workpiece in the workpiece-roller interface.

When observing the micrographs taken from the main fracture shown in Figure 54, it is possible to see that the beta phase grains are more distorted in both the mandrel and roller edges as a result of the friction between the dies and the workpiece, however more distortion is observed in the roller edge. The morphology of the beta grains is still more elongated and refined in the areas closer to the roller edge, where the average length and height of the structures were 16 µm and 0.4 µm respectively, compared to the mandrel area where these were 9 µm and 0.7 µm on average. This is in accordance with the observations of the transition area and suggesting that the main fracture may have started on this side of the workpiece.

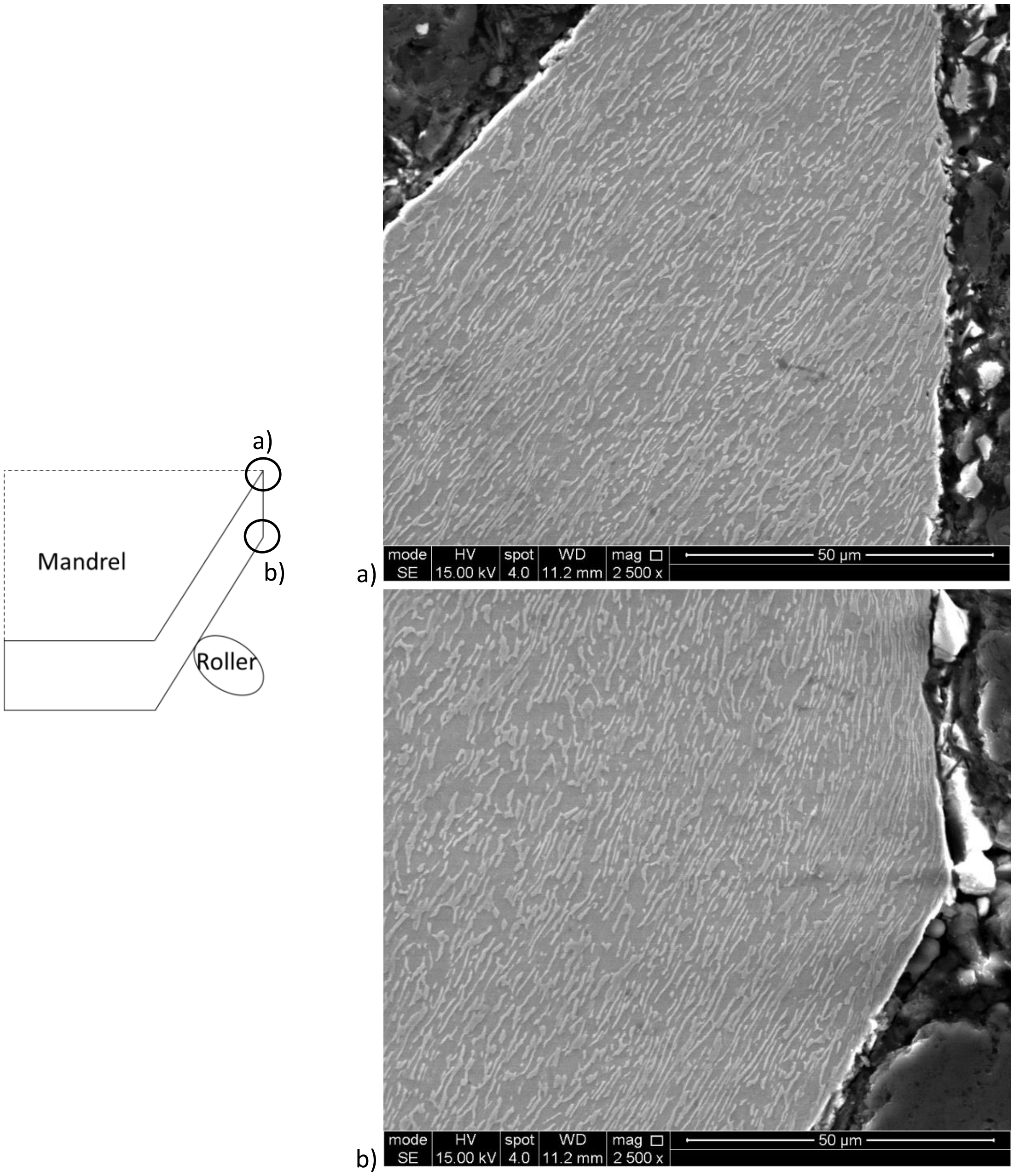

Figure 54: Micrographs of main fracture at: a) Mandrel Edge and b) Roller Edge at 2500x.

3.2.2 Jethete M152

3.2.2.1 Microstructural Inspection

The microstructure of the Jethete M152 plate before shear spinning deformation is shown in Figure 55. As expected, ferrite and martensite phases were found along with dispersed carbides (Refer to section 3.2.1.2). This was the result of the annealing heat treatment conducted. The average grain diameter of the ferritic and martensitic grains was 5.84 µm and these were homogenously distributed along all the surface with an equiaxed morphology.

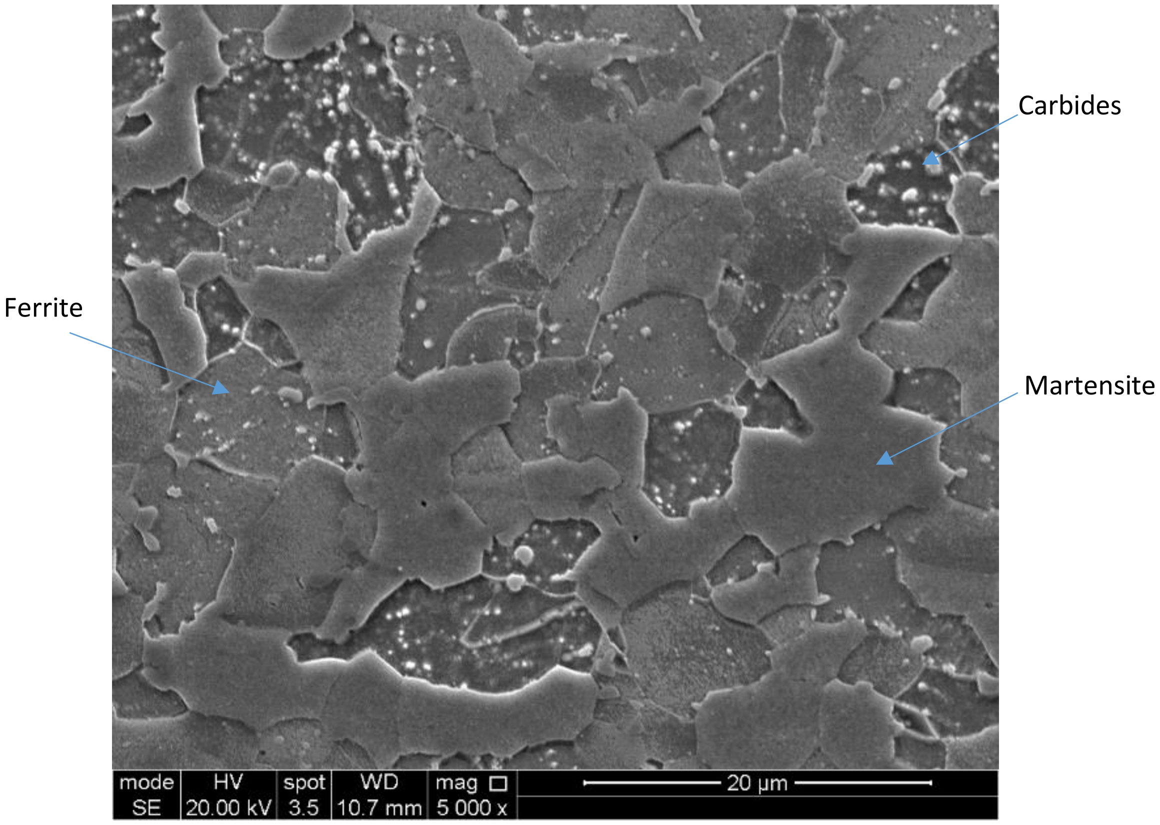

Figure 55: Initial Microstructure of Jethete M152 sample.

Figure 56, shows micrographs of the undeformed, transition and fully formed zones of the shear formed sample. All three micrographs were taken from the middle section of the thickness, so the effect from the roller and mandrel could be neglected and a fair comparison of all three sections could be made. In this case, it is clear that the grains were experiencing heavy morphological changes due to plastic deformation and no recrystallisation seems to be happening. After full deformation, the grains were no longer equiaxed and instead became elongated and distorted. The new grain size could not be calculated with the SEM maps due to the heavy distortion of the grains, however a better analysis could be performed with the EBSD results shown in section 3.2.2.2

Figure 57 shows maps of the fully deformed zone in; a) area near the mandrel contact edge, b) middle area and c) area near the roller contact edge. As it can be seen, the deformation was not uniform across all the thickness and instead the grains were gradually less distorted the further away they are from the roller contact edge. This suggests that the roller had a greater effect during the shear forming process than the mandrel and that much heavier shear deformation happened in this area.

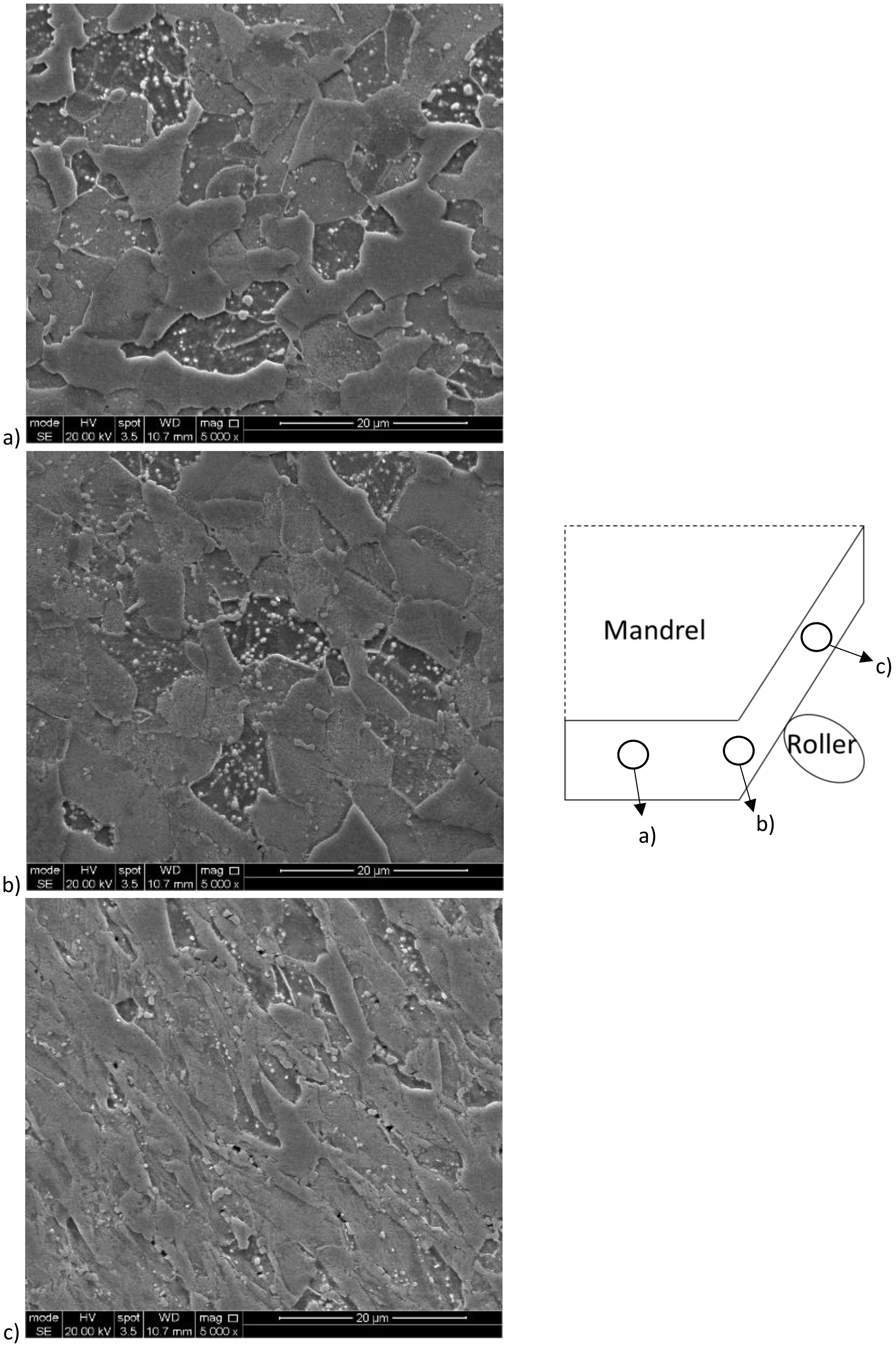

Figure 56: Micrographs of Jethete M152 sample at different areas of the workpiece in the middle section of the thickness. a) Undeformed material, b) Transition area, and c) Fully formed area.

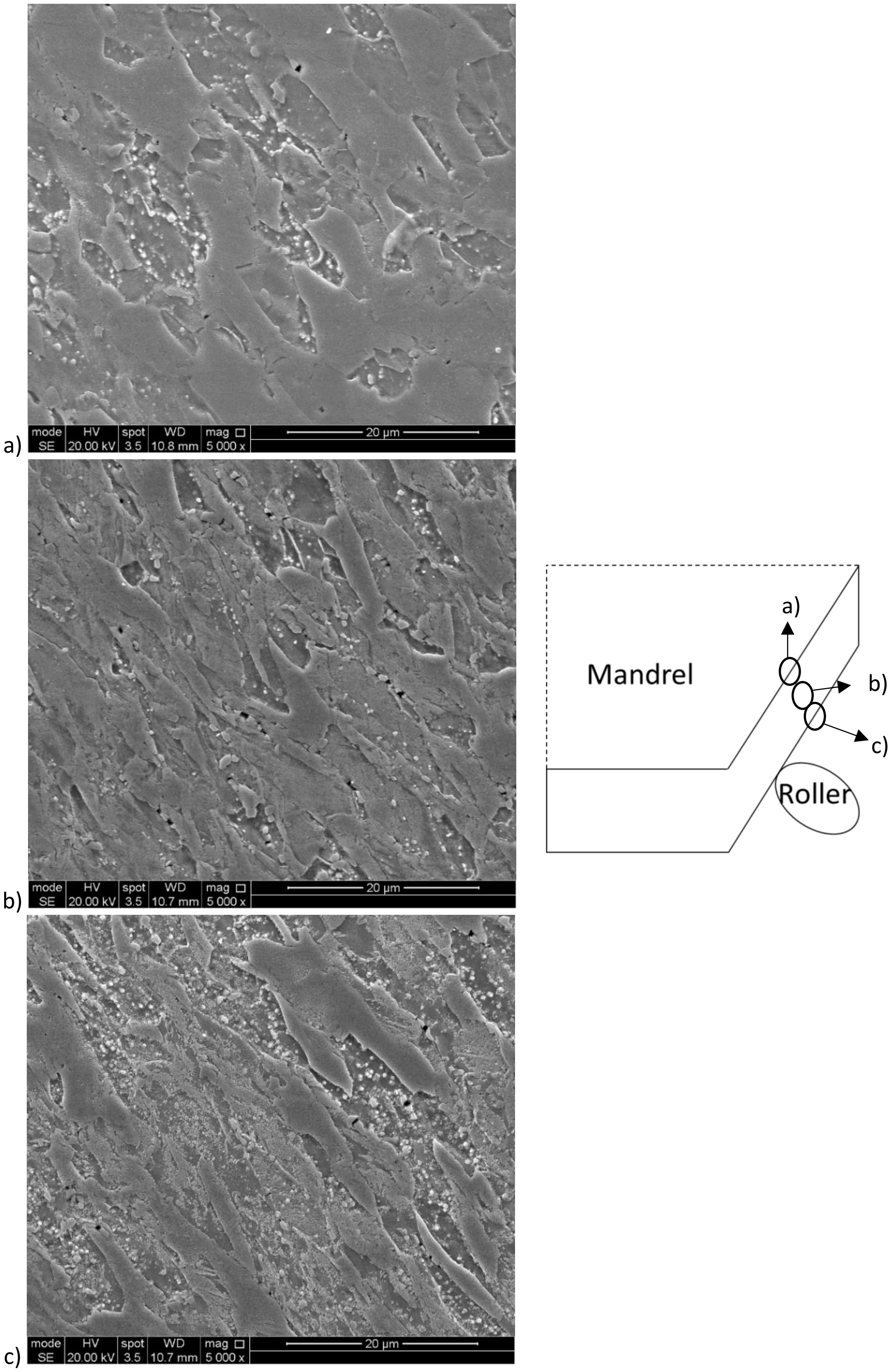

Figure 57: Micrographs of Jethete M152 across the thickness of the deformed workpiece. a) Mandrel zone, b) Middle zone and c) Roller zone

3.2.2.2 Texture Analysis

The initial texture of the Jethete M152 plate used is shown in Figure 59. The orientation map obtained for this sample shows the same results described in section 3.2.2.1; a double phase martensitic and ferritic structure with equiaxed grains and dispersed carbides. Even though this plate was hot rolled, the pole figures obtained (Figure 59b) are not consistent with the texture expected for BCC metals after this kind of processing [29]. This was due to the sample taken for the EBSD analysis not being cut following the rolling direction of the plate, so the normal direction of the sample's face where the EBSD test was performed was not perpendicular to the rolling direction (See Figure 58), and this is a condition needed to be able to see the correct pole figure patterns. The texture obtained under these conditions was still useful for its comparison against the shear formed zones to evaluate the texture changes after processing.

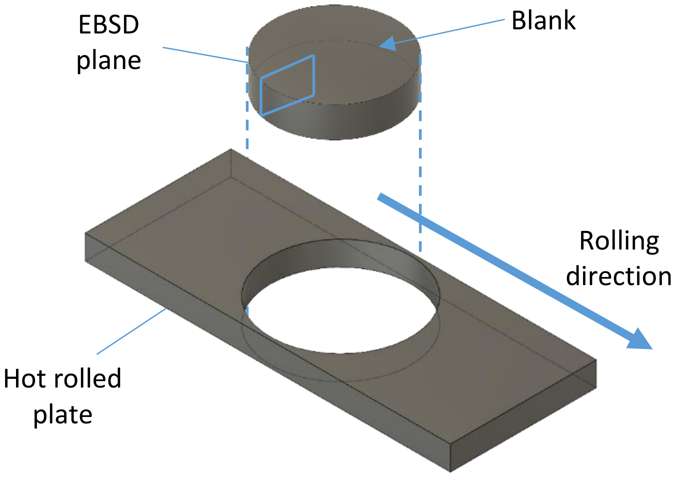

Figure 58: Schematic of the EBSD surface position regarding the rolling direction of the original plate. Note: The position of the EBSD plane was random and it was not the exact position showed in this example, this image is for visualisation purposes only.

Figure 60 and Figure 61 show the orientation maps and pole figures obtained for the deformed zone at the mandrel and roller edge respectively. Both zones have clearly distorted grains due to the shear forming process, but like in section 3.2.2.1 results, the roller zone shows considerably more distortion in its microstructure.

The average dimension of the grains in all three zones was calculated using the orientation maps and is shown in Table 11. Since the microstructure after shear forming is no longer equiaxed, the height and length of the grains in the mandrel and roller zones were measured instead of just a diameter like in the undeformed zone. By comparing the calculated average grain area, it is possible to see that no significant changes in the grain size were found, suggesting that the grains were only deformed and no recrystallisation happened during the process.

Table 11: Average Grain Size measured in undeformed, roller and mandrel zones.

Undeformed	Mandrel	Roller
Diameter: 5.84 µm *Area:* 34.15 µm^2	*Height:* 4.59 µm *Length* 8.13 µm *Area:* 37.3 µm^2	*Height:* 2.93 µm *Length:* 12.23 µm *Area:* 35.83 µm^2

Regarding the pole figures obtained, both deformed zones show a completely different texture to the one obtained in the undeformed zone. They both have a similar pattern typical of simple shear deformation but this is more defined and stronger in the roller zone where the maximum density obtained was 3.41, which is higher than the 2.68 maximum density of the mandrel side.

The Misorientation angle distributions of all three zones are shown in Figure 62. It can be seen that while the undeformed zone have a more even distribution of low and high angle grain boundaries, the mandrel and roller zone have a drastic increase of low angle boundaries. The peaks observed at the 30˚ orientation are the result of an error called pseudo-symmetry (PS). This occurs when the indexing algorithm in the EBSD process selects the wrong orientation due to different crystal orientations having similar kikuchi patterns [82]. These PS errors can also be seen in the orientation maps as isolated random points with a different colour inside a crystal (See Figure 59a). Since the amount of points with this error is minimal compared to the size of the map generated, they do not affect the overall EBSD results and can be dismissed.

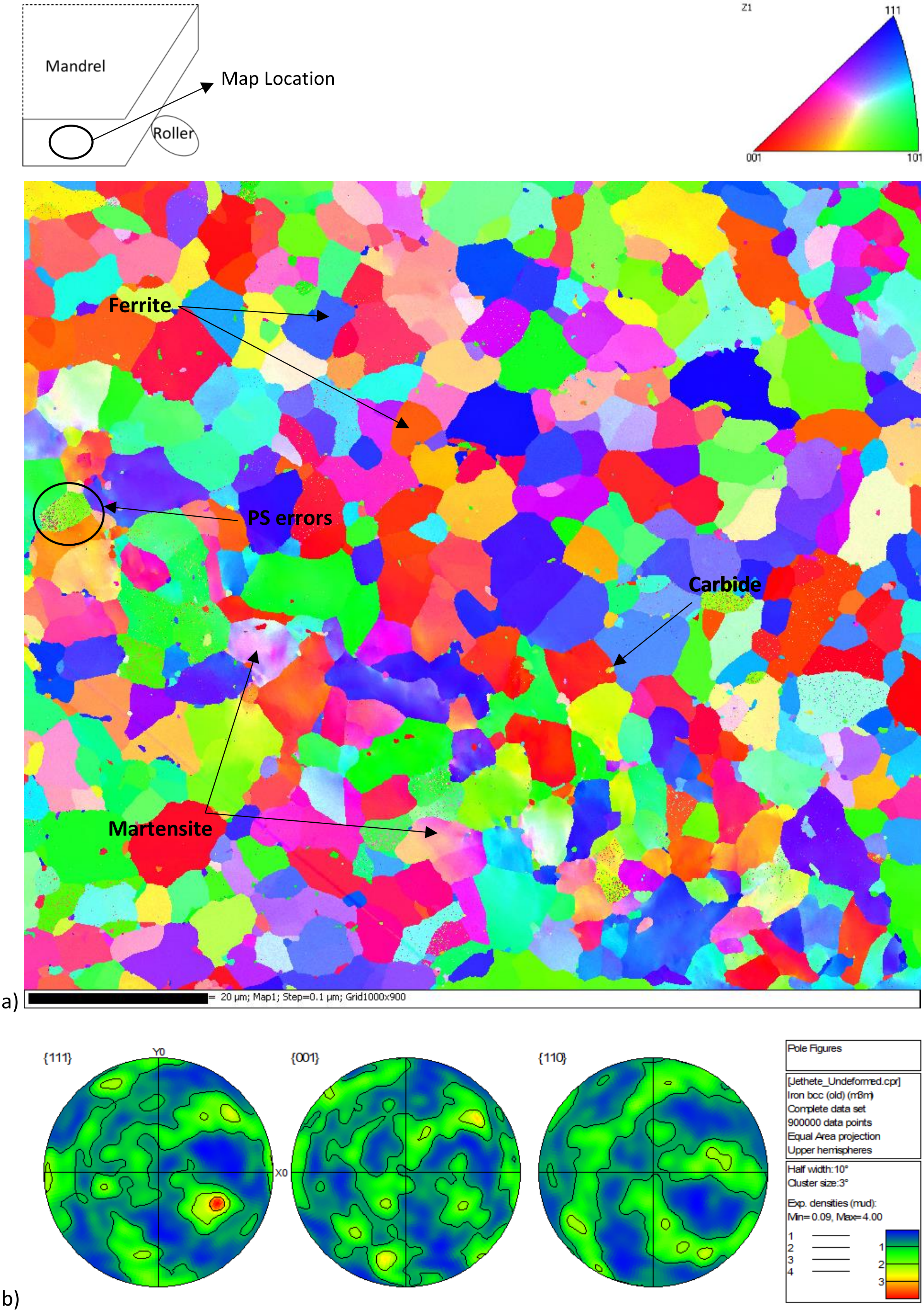

Figure 59: Initial texture of Jethete M152 sample (Undeformed zone). a) Orientation Map, b) Pole figures.

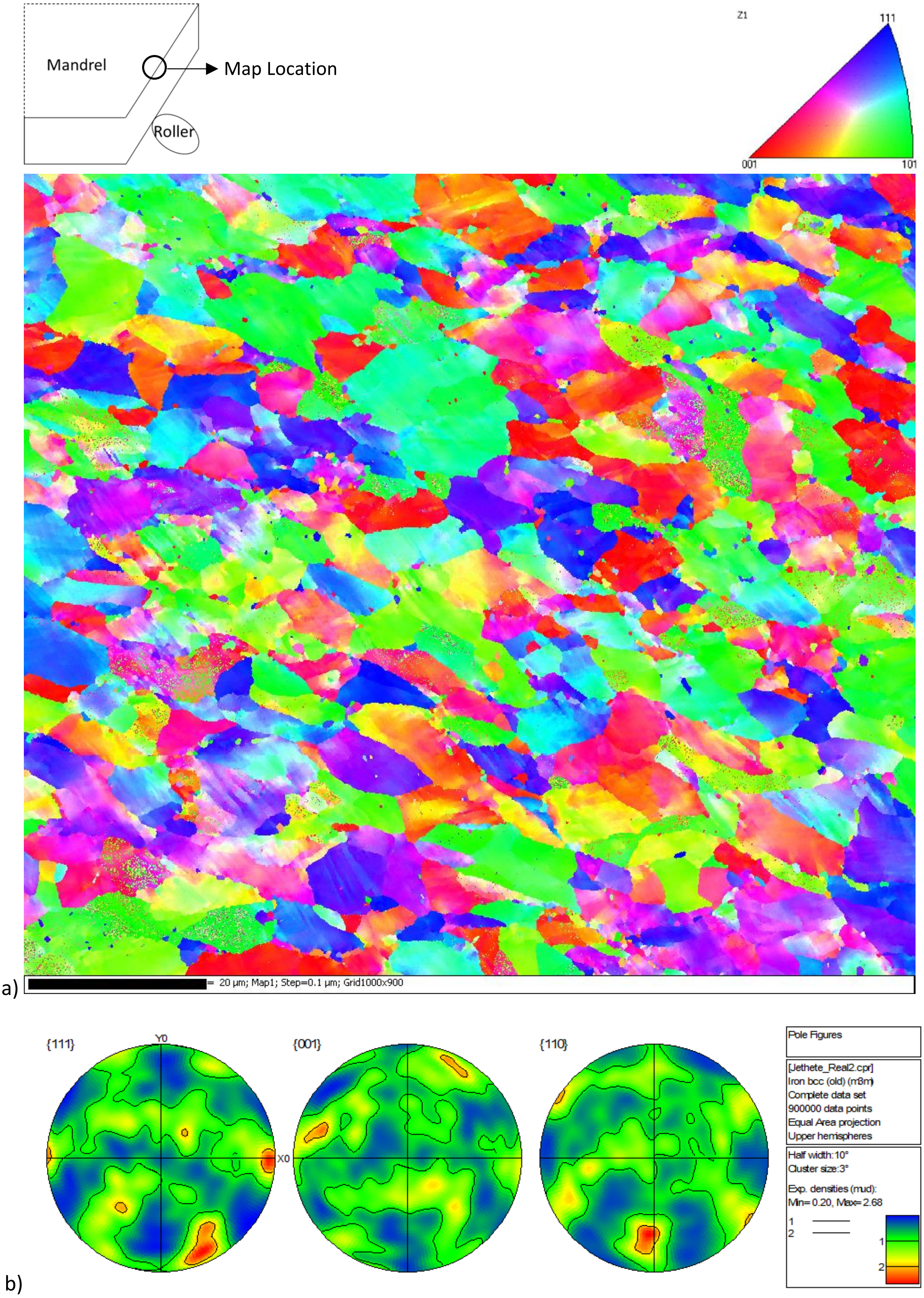

Figure 60: Texture of shear formed Jethete sample at Mandrel zone. a) Orientation Map, b) Pole figures.

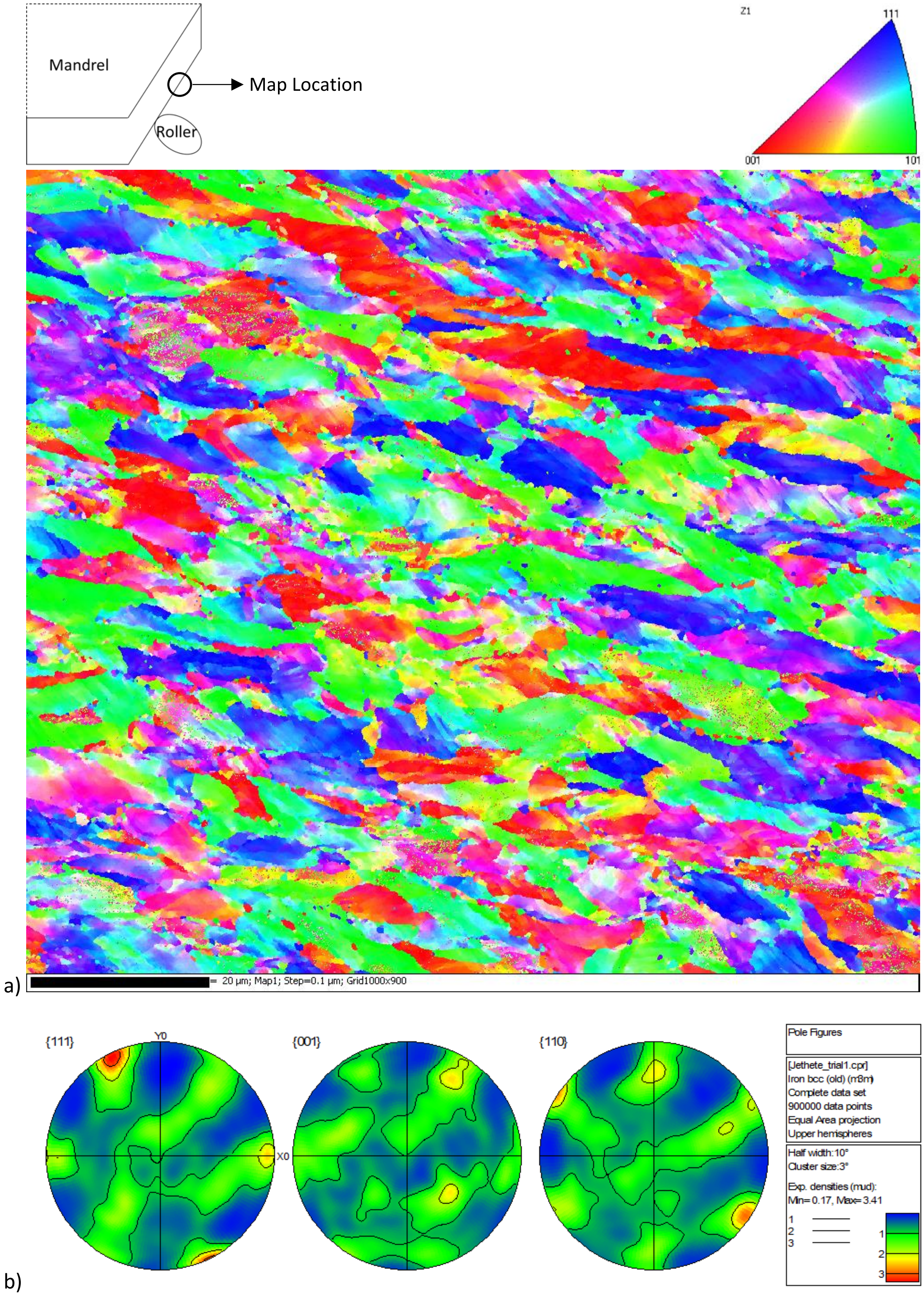

Figure 61: Texture of shear formed Jethete sample at Roller zone. a) Orientation Map, b) Pole figures.

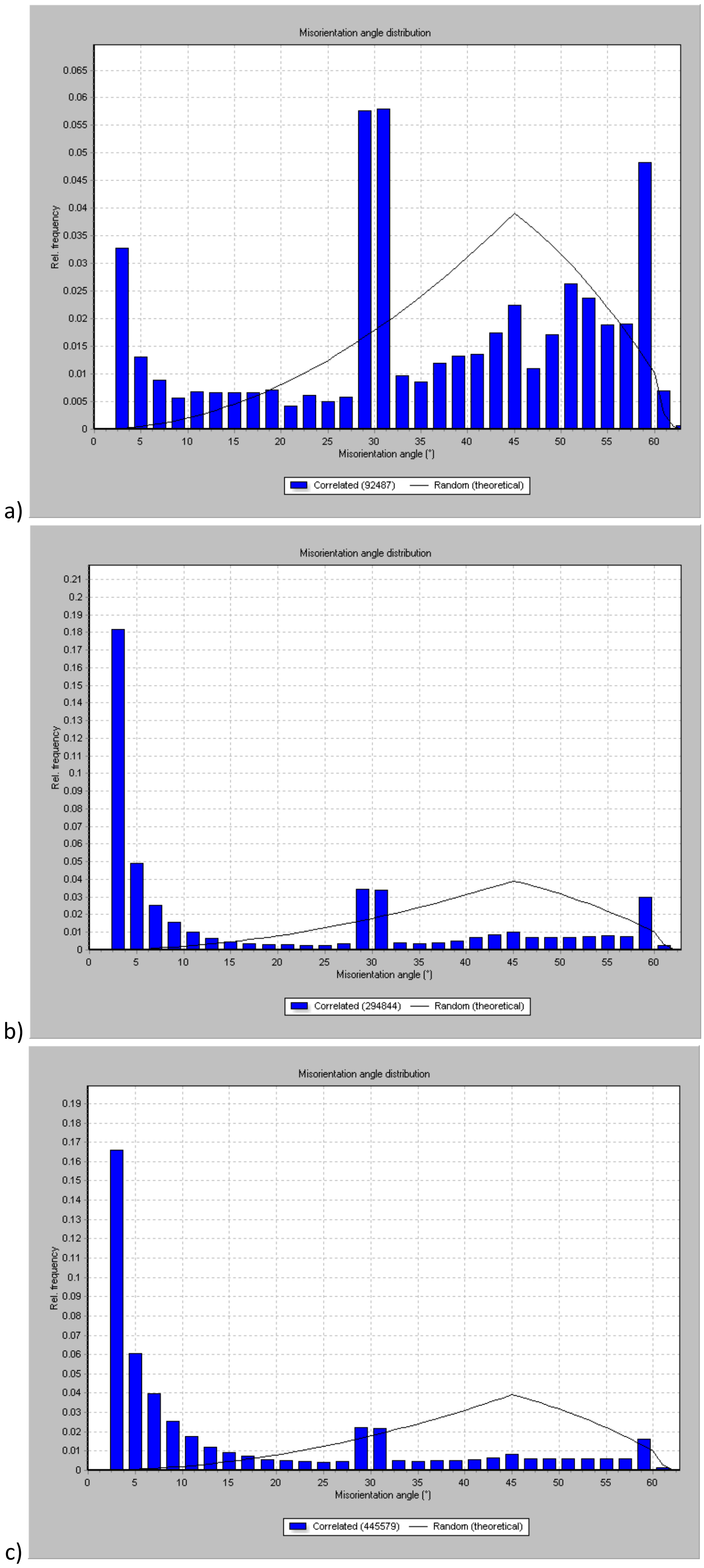

Figure 62: Misorientation Angle Distribution of Jethete M152 at: a) Undeformed zone, b) Mandrel zone and c) Roller zone

3.3.2 Inconel 718

3.3.2.1 Microstructural Inspection

The initial microstructure of the Inconel 718 sample is shown in Figure 63. Overall, it consisted of large equiaxed grains with bands of small equiaxed grains in between them. Twinning can be observed in most of the larger grains but not in the smaller ones. This microstructure is typical in Inconel 718 after hot rolling and recrystallisation due to heat treatments like the one applied to this plate (Refer to sections 3.2.1.3 and 3.4.5). The smaller grains were probably a result of the dynamic recrystallization happening during the hot deformation, which explains why they are only present in bands in between the larger grains. The twinning was originated during the solution heat treatment. The average grain diameter calculated was 43.3 µm, not considering the twins and the recrystallised grain bands.

It is important to mention that all grain sizes calculated in this section (3.3.2) were done based on several micrographs taken and the orientation maps obtained in the texture analysis to reduce the errors that the recrystallised small grains and twins could cause.

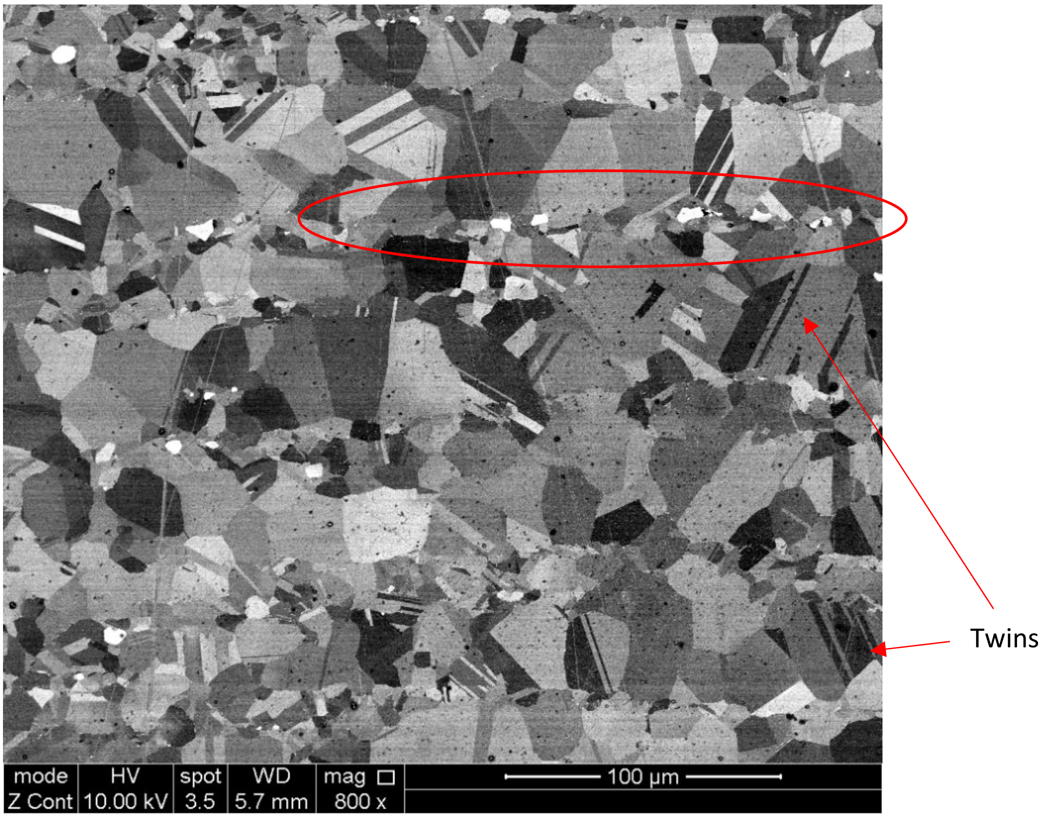

Figure 63: Initial microstructure of Inconel 718 workpiece. An example of areas with recrystallised grains is marked with a red circle.

Figure 64 shows the microstructure of the Inconel 718 sample at the undeformed, transition and fully formed zones. Unlike the Jethete M152 sample described in section 3.2.2, the microstructure observed in this material even after being fully shear formed still consisted of equiaxed grains and no distortion of the grains is seen at all. Additionally twins are still visible within the grains in all three zones.

A slight variation in the grain size between the undeformed and transition zones can be observed (43.3 µm and 29.9 µm respectively), and a much smaller grain size is visible in the fully formed zone (12.9 µm). This grain refinement and the lack of distorted grains suggest that the microstructure has experienced recrystallisation. Figure 65 and Figure 66 offer a better visualisation of the grain refinement found in the sample.

Micrographs of the fully deformed zone in the areas near the mandrel, near the roller and the middle are available in Figure 67. Again, no distorted grains were found but a variation of the grain size was found across the thickness. The average grain diameter in the roller zone was 8.11 µm while in the mandrel zone was 18.2 µm.

The observations in the microstructural changes mentioned above are unexpected given that twinning and grain refinement due to recrystallization usually take place after a heat treatment like annealing and not just plastic deformation, however no post-processing heat treatment was reported by the supplier. A more detailed analysis of these findings is available in the Discussion section.

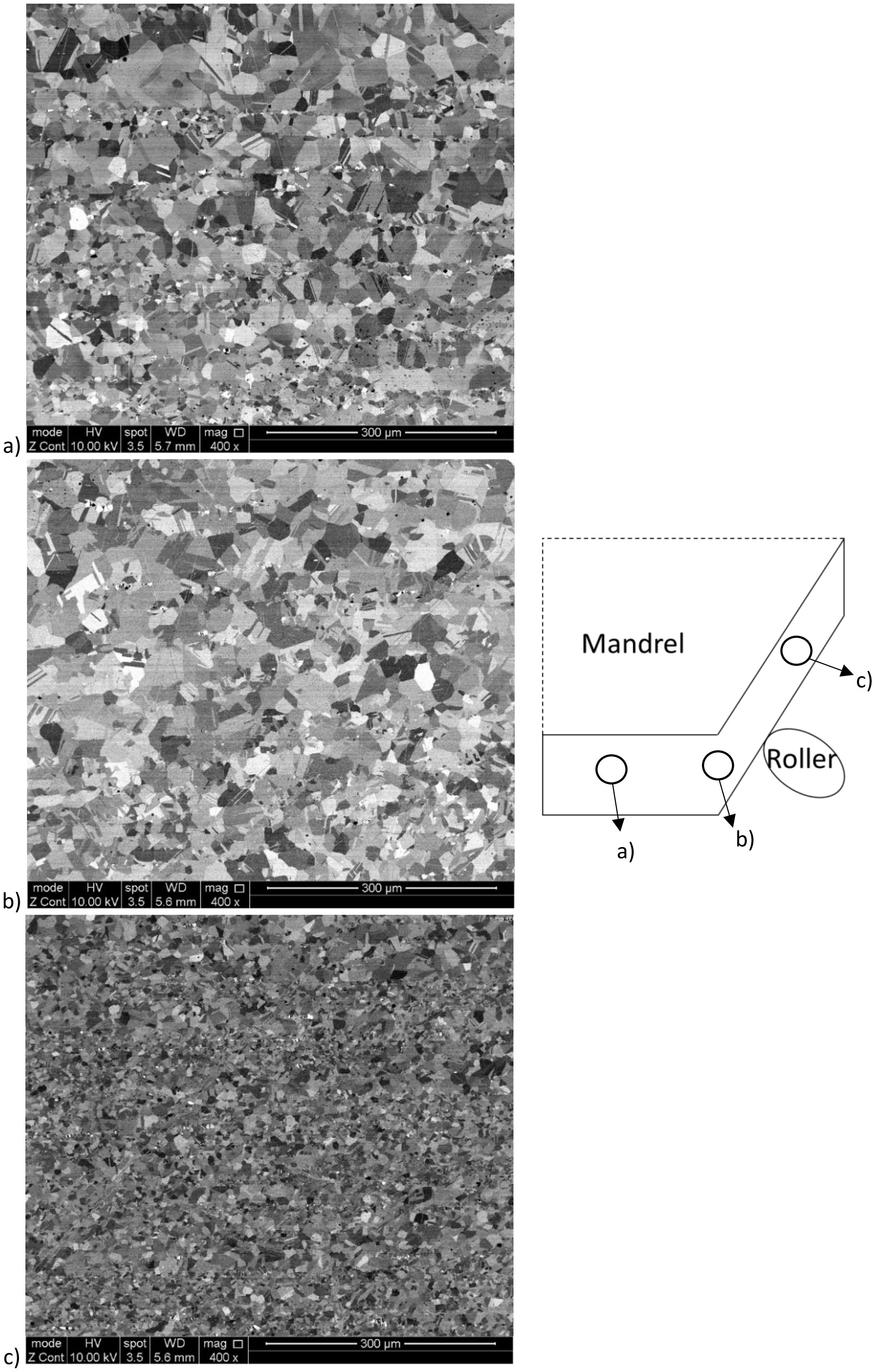

Figure 64: Micrographs of Inconel 718 sample at different areas of the workpiece in the middle section of the thickness. a) Undeformed material, b) Transition area, and c) Fully formed area.

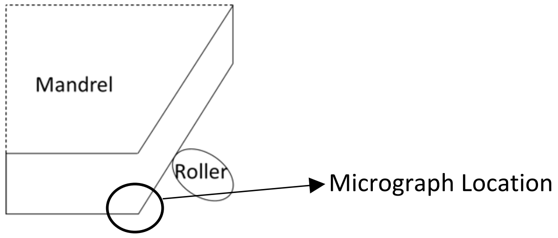

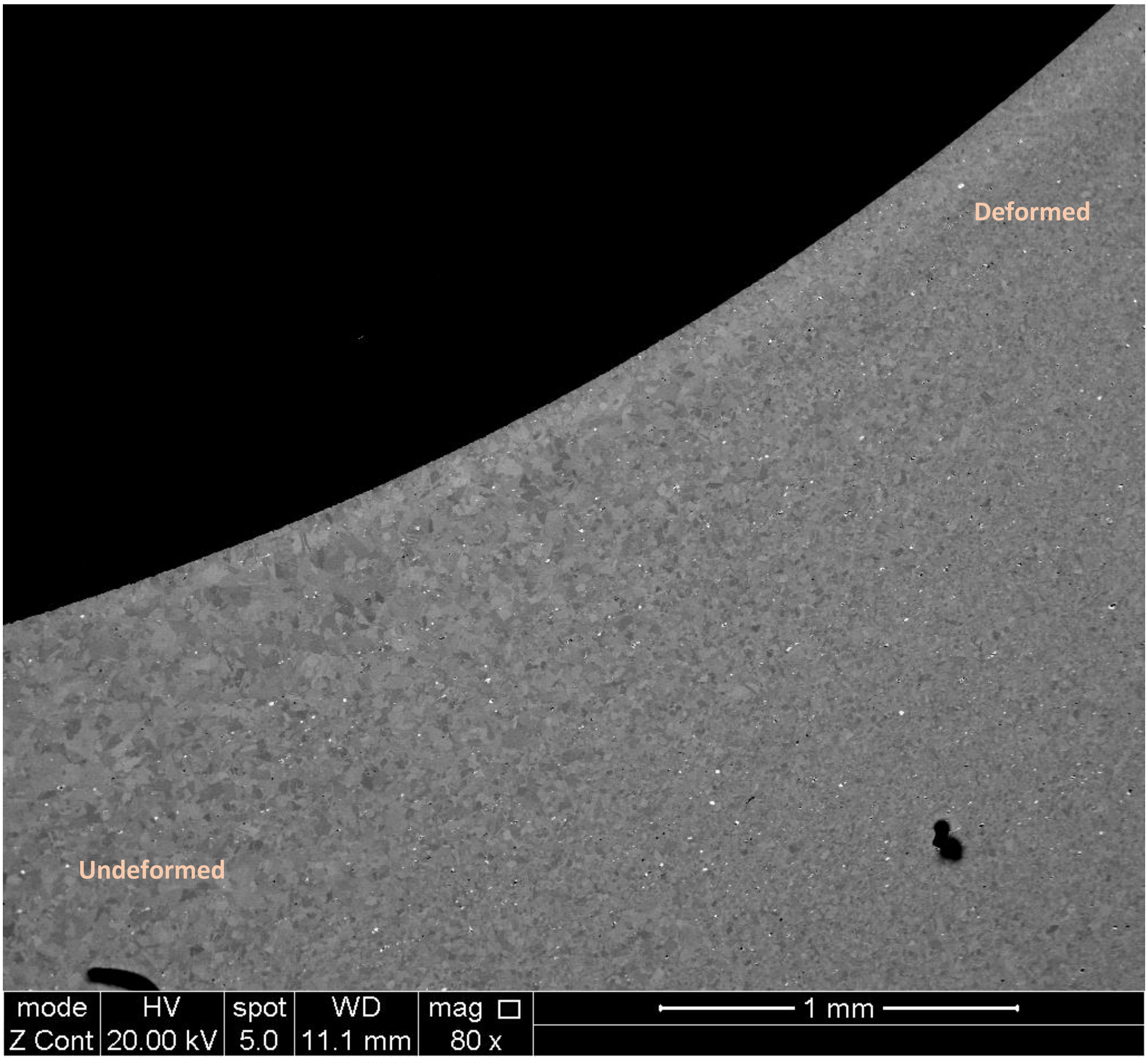

Figure 65: Micrograph of the roller edge of the Inconel 718 sample, covering undeformed, transition and fully formed areas. Note: The black shadows in the image are dirt spots that can be ignored.

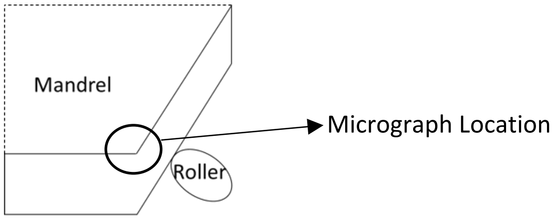

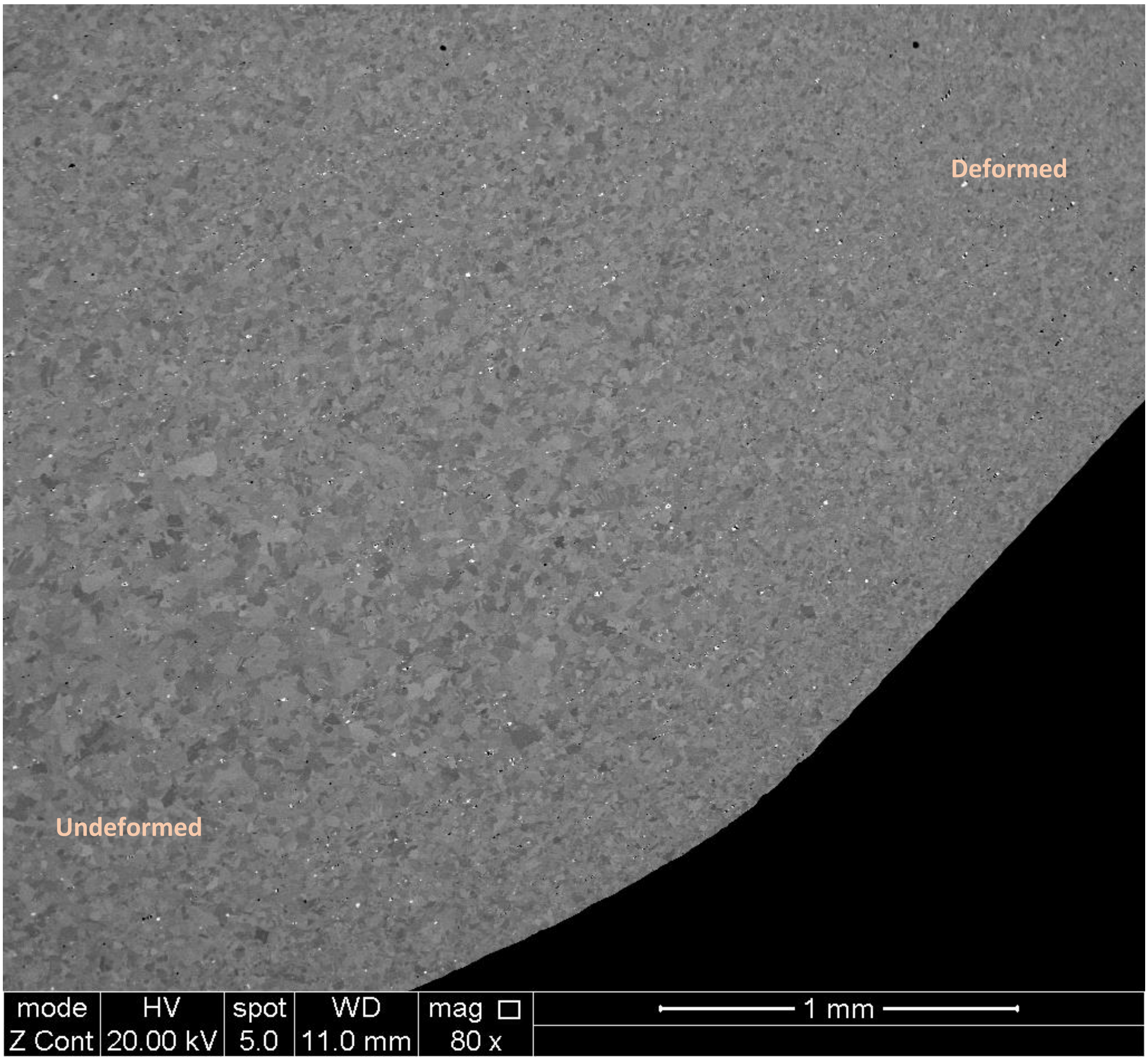

Figure 66: Micrograph of the mandrel edge of the Inconel 718 sample, covering undeformed, transition and fully formed areas. Note: The black spots in the image are dirt spots that can be ignored.

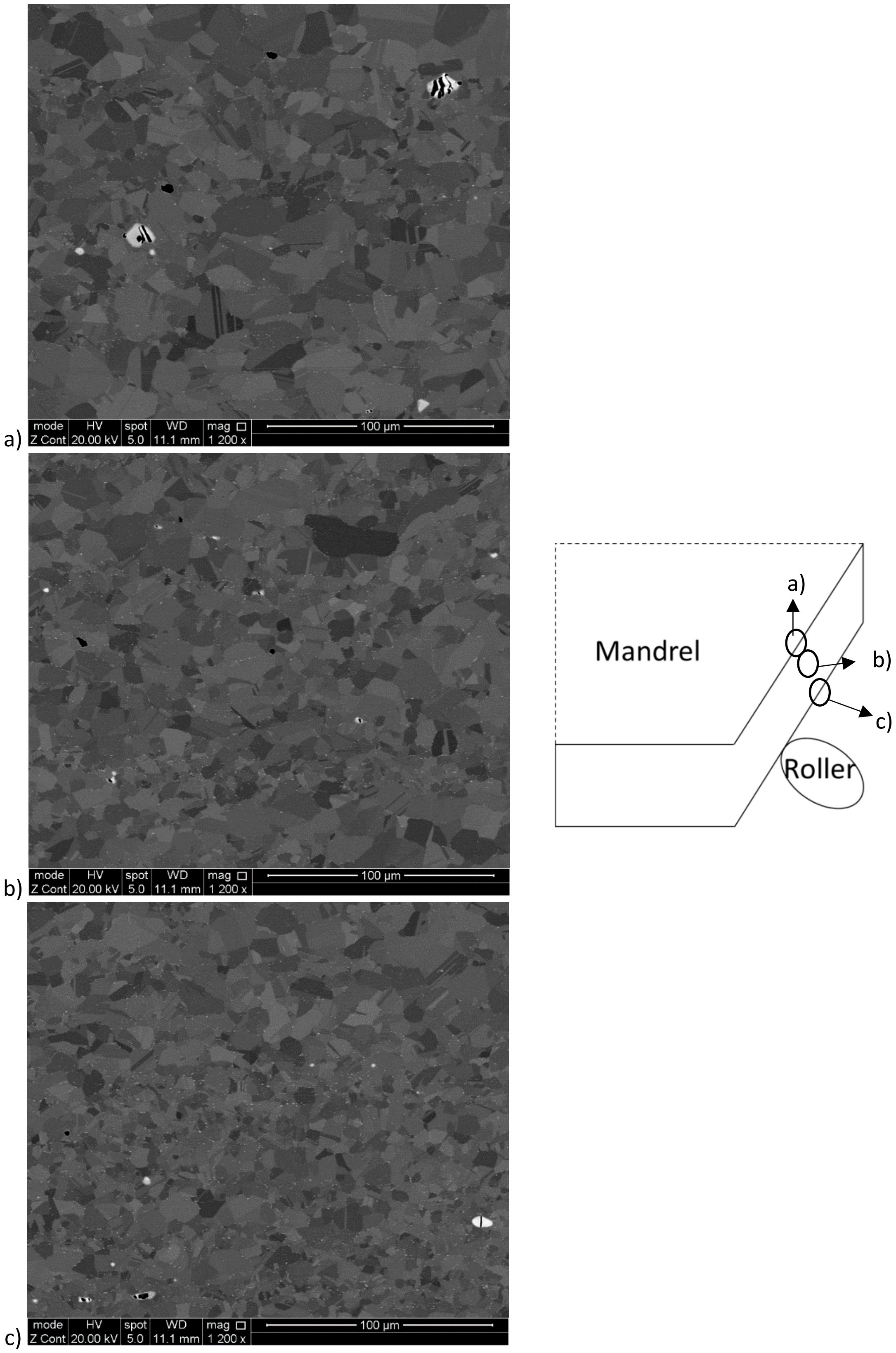

Figure 67: Micrographs of Inconel 718 across the thickness of the deformed workpiece. a) Mandrel zone, b) Middle zone and c) Roller zone. Note: Dirt white spots can be seen in some areas of the micrographs, these do not affect the microstructural analysis so they can be ignored.

3.3.2.2 Texture Analysis

The orientation maps and pole figures of the undeformed, mandrel and roller zones are shown in Figure 68, Figure 69 and Figure 70 respectively. The same observations mentioned in section 3.3.2.1 are visible in the orientation maps.

The texture of the undeformed zone is consistent with the expected after hot rolling and heat treatment. The equiaxed grains and twinning observed in the orientation map (Figure 68a) are the result of the solution heat treatment applied. Even after the recrystallisation, the texture shown in the pole figures available in Figure 68b still show evidence of the initial hot rolling [29].

The grain morphology in the mandrel and roller zones is basically the same as in the undeformed zone but again significant changes in the grain size can be seen (Refer to section 3.3.2.1 for more details). The pole figures of both zones have the same pattern with typical form expected from a simple sheared material, however in the mandrel zone (Figure 69b) the pattern is less defined than in the roller zone (Figure 70b).

The misorientation angle distributions of all three zones shown in Figure 71, follow the same trend. In all cases, there is a uniform distribution of low and high angle boundaries with a high peak in the 60 degrees boundaries due to all the twins in the microstructure.

All the findings described in this section and section 3.3.2.2 suggest that the shear formed sample was heat treated after the process, even though the supplier cannot confirm this information. A more detailed analysis can be found in the discussion section.

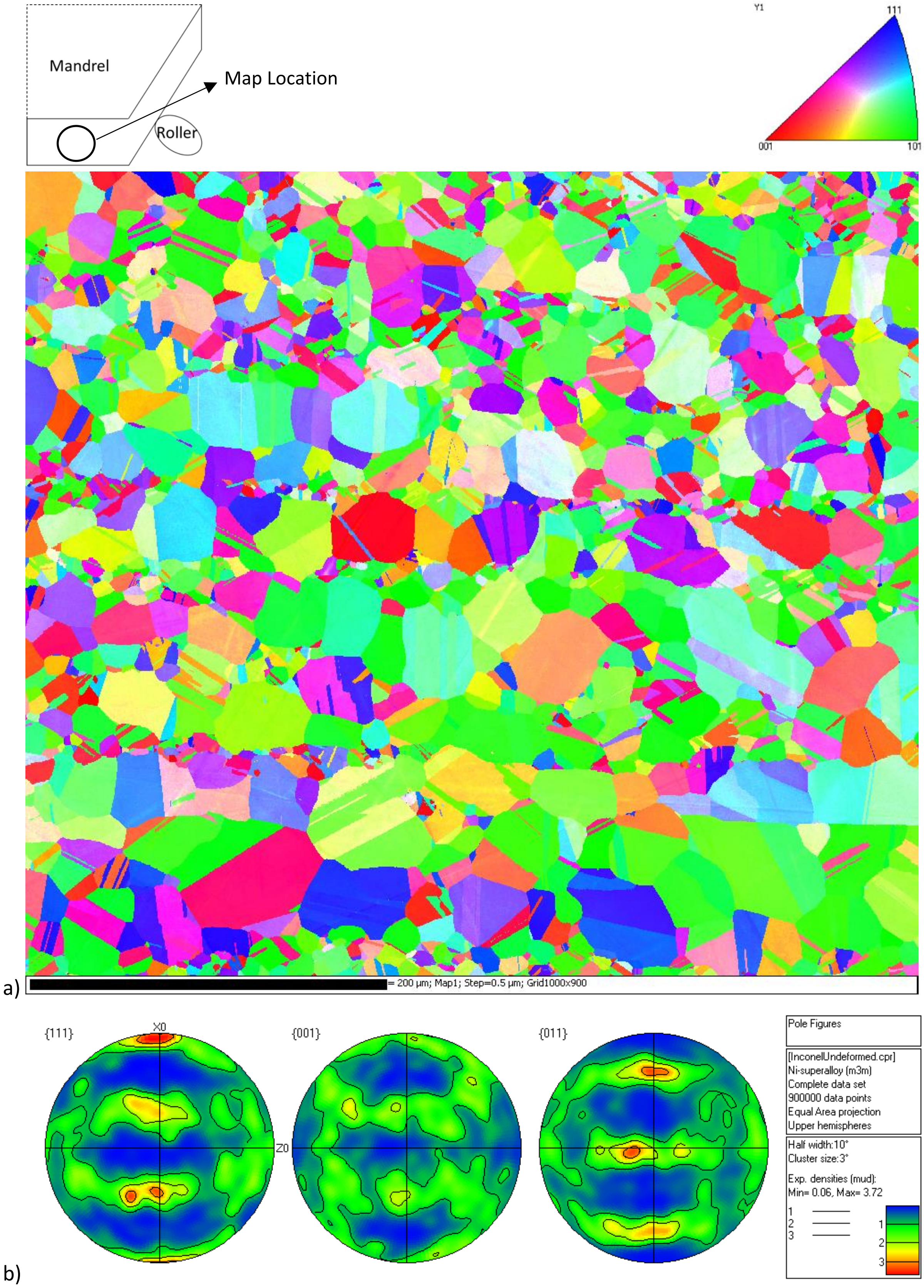

Figure 68: Initial texture of Inconel 718 sample (Undeformed zone). a) Orientation Map, b) Pole figures.

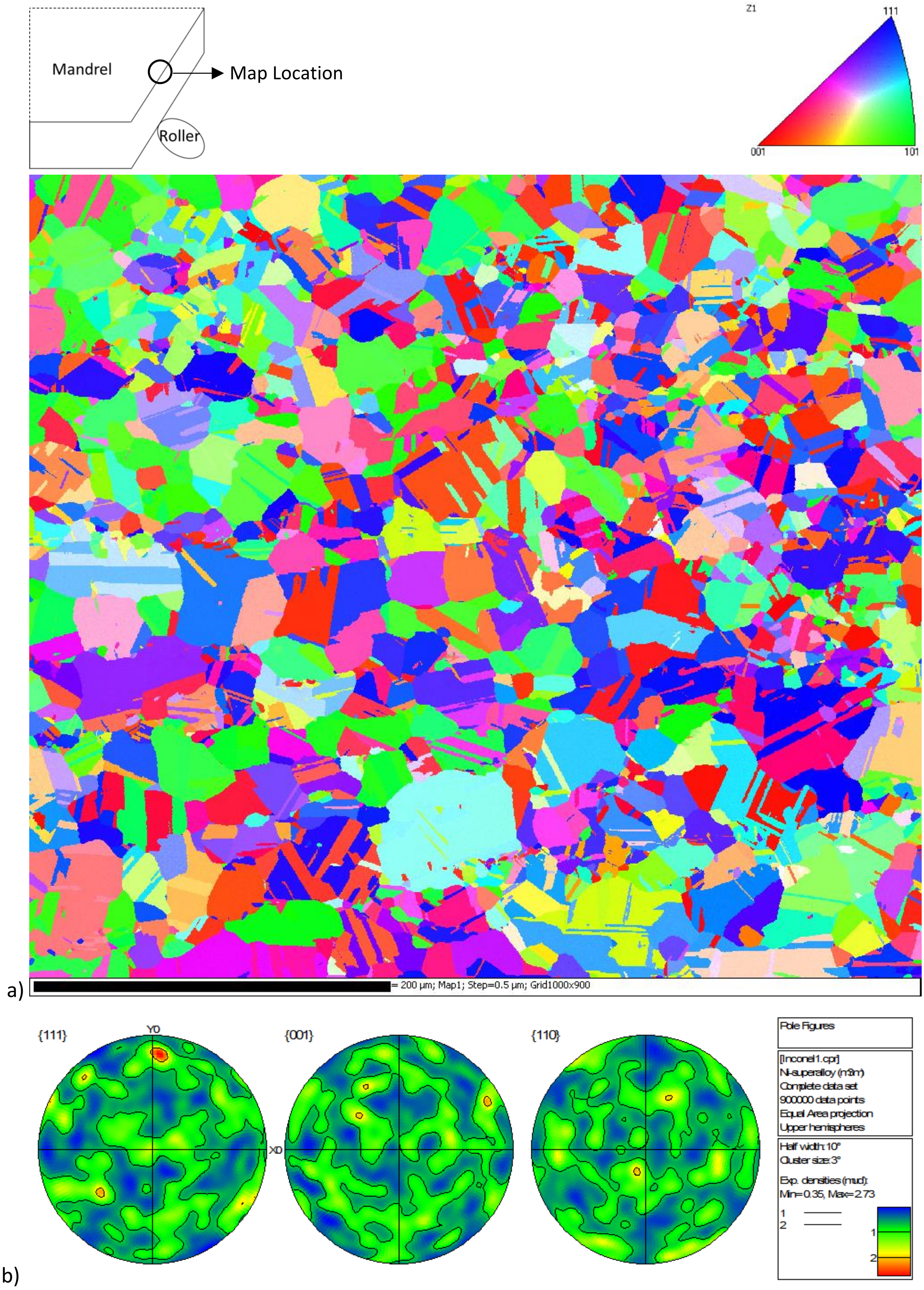

Figure 69: Texture of shear formed Inconel 718 sample at Mandrel zone. a) Orientation Map, b) Pole figures.

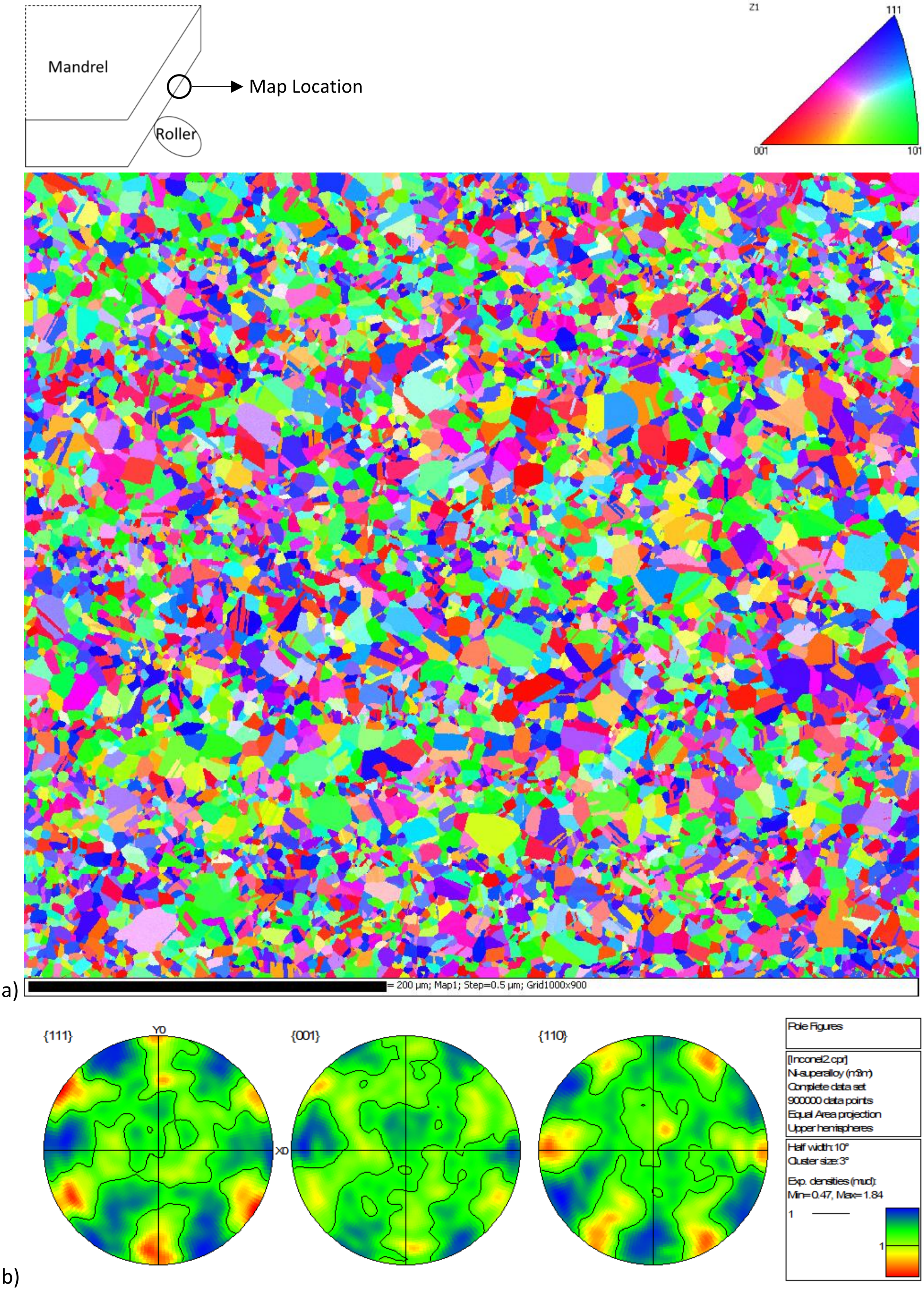

Figure 70: Texture of shear formed Inconel 718 sample at Roller zone. a) Orientation Map, b) Pole figures.

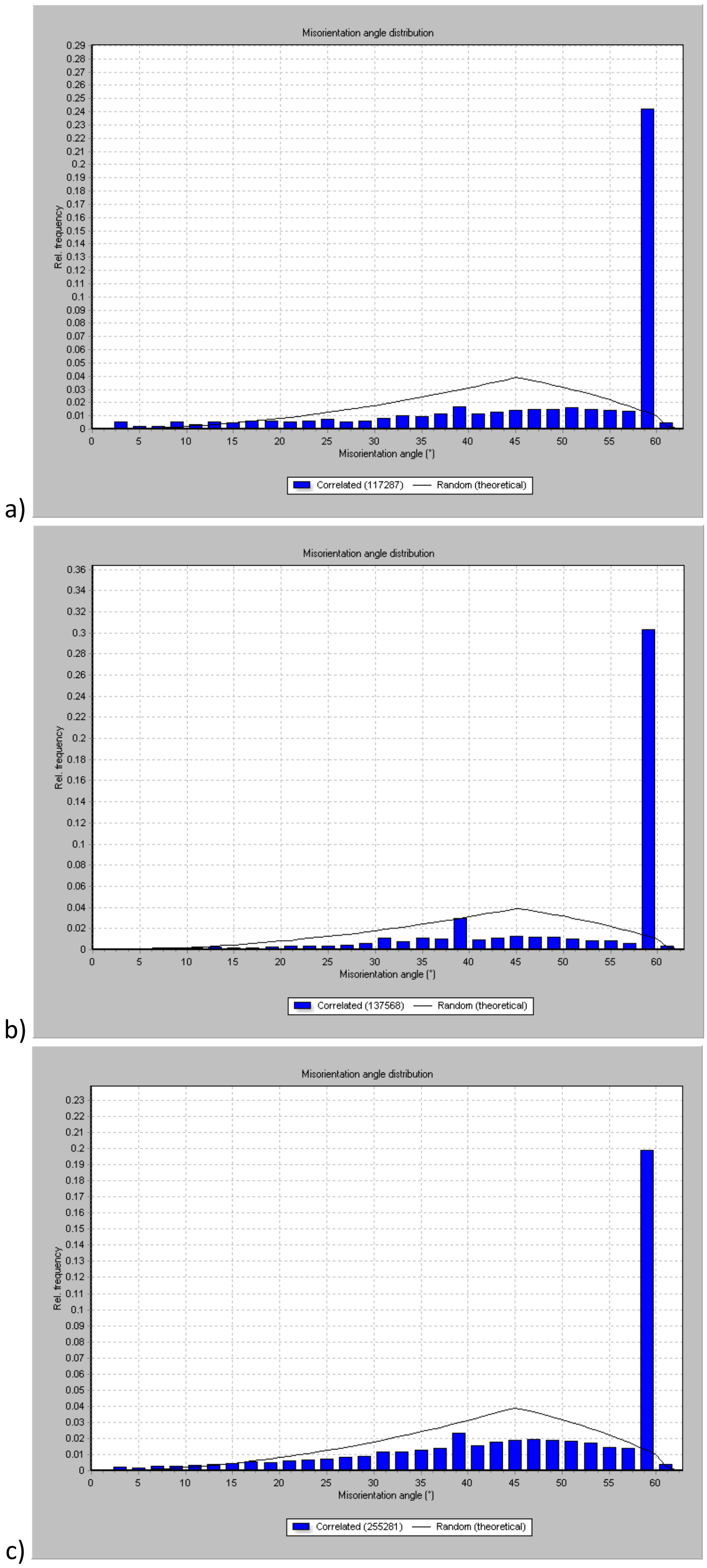

Figure 71: Misorientation Angle Distribution of Inconel 718 at: a) Undeformed zone, b) Mandrel zone and c) Roller zone

3.4 Discussion

By analysing and comparing the microstructural and texture results obtained in all three materials studied in this chapter, two key points can be remarked:

1. In all cases, the microstructure was not uniform across the thickness of the shear formed workpieces. Heavier grain distortion was found in Timetal 54M and Jethete M152 samples in the roller areas of the fully deformed zone. In the case of Inconel 718, finer grains were found in this zone.
2. The texture analysis of Inconel 718 and Jethete M152 proves that the main deformation mechanism during the process is in fact simple shear, since the patterns in the pole figures after deformation are consistent with the expected for simple sheared materials. However this deformation is not uniform and less intense in the areas closer to the mandrel.

Other important remarks of each material studied in this chapter are discussed below.

3.4.1 Timetal 54M

In the case of Timetal 54M, the fracture seems to have originated in the roller zone and propagated across the thickness from there. The presence of intergranular secondary cracks originating from the main fracture and the significant level of deformation that the material was able to undergo before failure suggest that the main fracture was initially ductile and then experienced a ductile-brittle transition [44]. To understand more about the nature of this fracture, it is important to know that titanium alloys with two phase lamellar microstructure usually have poor ductility but high fracture toughness and while higher lamellar grain size increase fracture toughness, it also decreases ductility resulting in unbalanced and deficient mechanical properties [83].

A way to reduce this problem is by refining the lamellar grain size using heat treatments before the deformation process. Even though the lamellar grain size in the Timetal 54M sample was very refined, the large elongation of the lamellar beta grains experienced during the shear forming process could have caused the workpiece ductility to decrease considerably in the perpendicular direction causing it to fail very early during the process. The small cracks in the longitudinal directions indicate that apart from the main fracture originated in the roller side, there was delamination along the workpiece, this can be seen in Figure 72. This type of failure is common in two-phase lamellar titanium alloys because fractures can propagate easily across the alpha/beta interface with almost no resistance so when the main fracture encounters a large misorientation twist of the lamellar grains, it is forced to deflect [84].

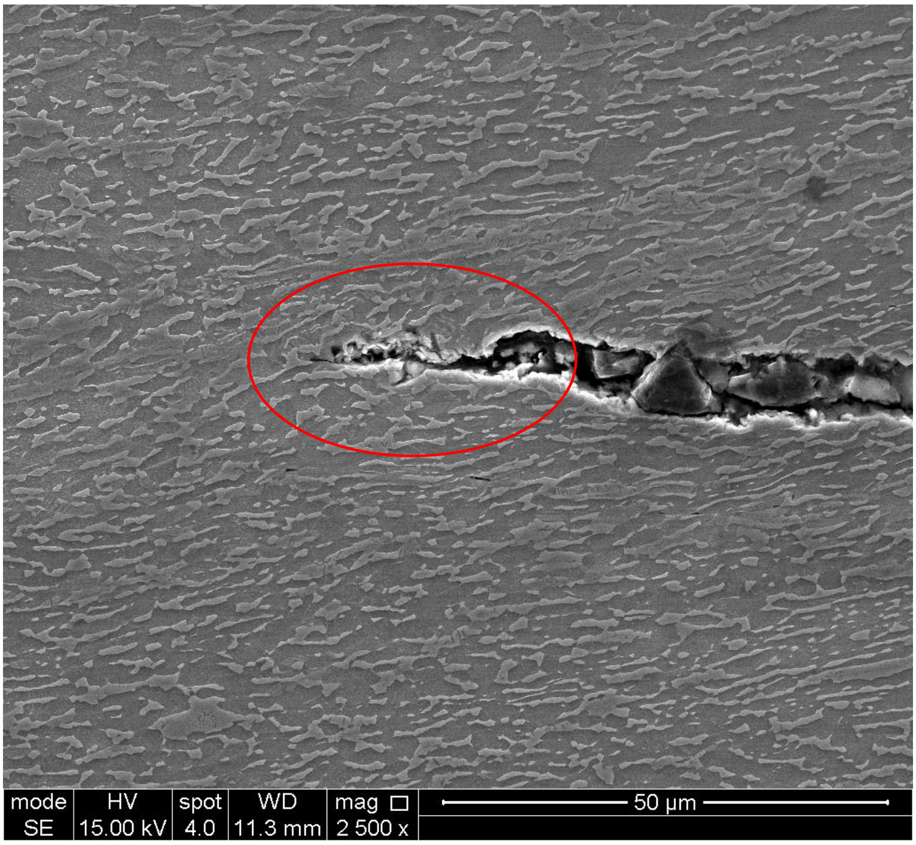

Figure 72: Longitudinal crack on Timetal 54M sample. In the red circle it is possible to see how the fracture is propagating in the alpha/beta interface, around the beta grains.

3.4.2 Jethete M152

The micrographs and orientation maps obtained from this sample, show clearly the microstructural evolution of the material during shear forming. Since the final shear spun workpiece did not experience any kind of heat treatment, it is possible to see how due to shear deformation the grains gradually become elongated. No significant changes in the average grain area after between the undeformed and deformed areas were found, suggesting that no recrystallisation occurred during the process. Greater grain distortion across the workpiece thickness was found closer to the roller contact edge, where the grains were clearly more elongated and thinner than in the mandrel zone. These results are consistent with the found in the literature [17] [18].

A comparison of the ideal texture of BCC metals after simple shear deformation against the experimental texture of the mandrel and roller zones is shown in Figure 73. In both experimental pole figures, the characteristic fibres $\{1\ 1\ 0\}$ and $\langle 1\ 1\ 1 \rangle$ expected for a simple shear texture can be seen, and they follow the expected behaviour described in chapter 2, section 2.3.3.2. However, the mandrel pole figure is less intense and clear than the roller one.

Considering the observations in the grain morphology and the pole figures, it is clear that even though the deformation mechanism that this material experienced during the process is in fact very close to simple shear, the deformation is more intense in the areas closer to the roller contact zone.

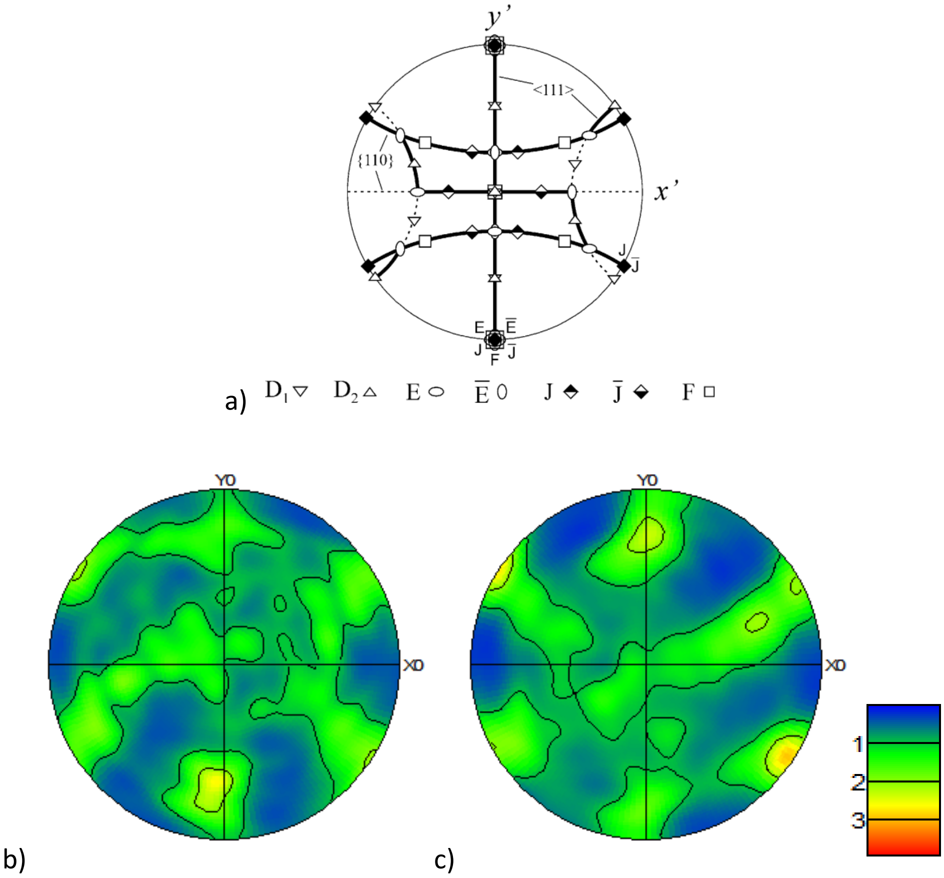

Figure 73: $\{1\ 1\ 0\}$ Pole figures of: a) Ideal orientation of simple shear in BCC metals [33], b) Mandrel zone of Jethete M152 sample and c) Roller zone of Jethete M152 sample

Finally, the change in the misorientation angles distribution between the initial and deformed zones is a strong evidence of the heavy deformation taking place during the shear forming process. To explain this, an example of microstructures and misorientation angle distributions after plastic deformation and a heat treatment of a BCC metal is shown in Figure 74. In this example, the microstructure of the as-rolled material is composed by distorted grains and the misorientation angle distribution shows that the grain boundaries in the sample are mainly low-angle (<15˚). A different behaviour is observed after the material was annealed causing recrystallisation of the microstructure and grain refinement. After the heat treatment low angle boundaries almost disappear and are replaced by high angle boundaries (> 15˚). [85]

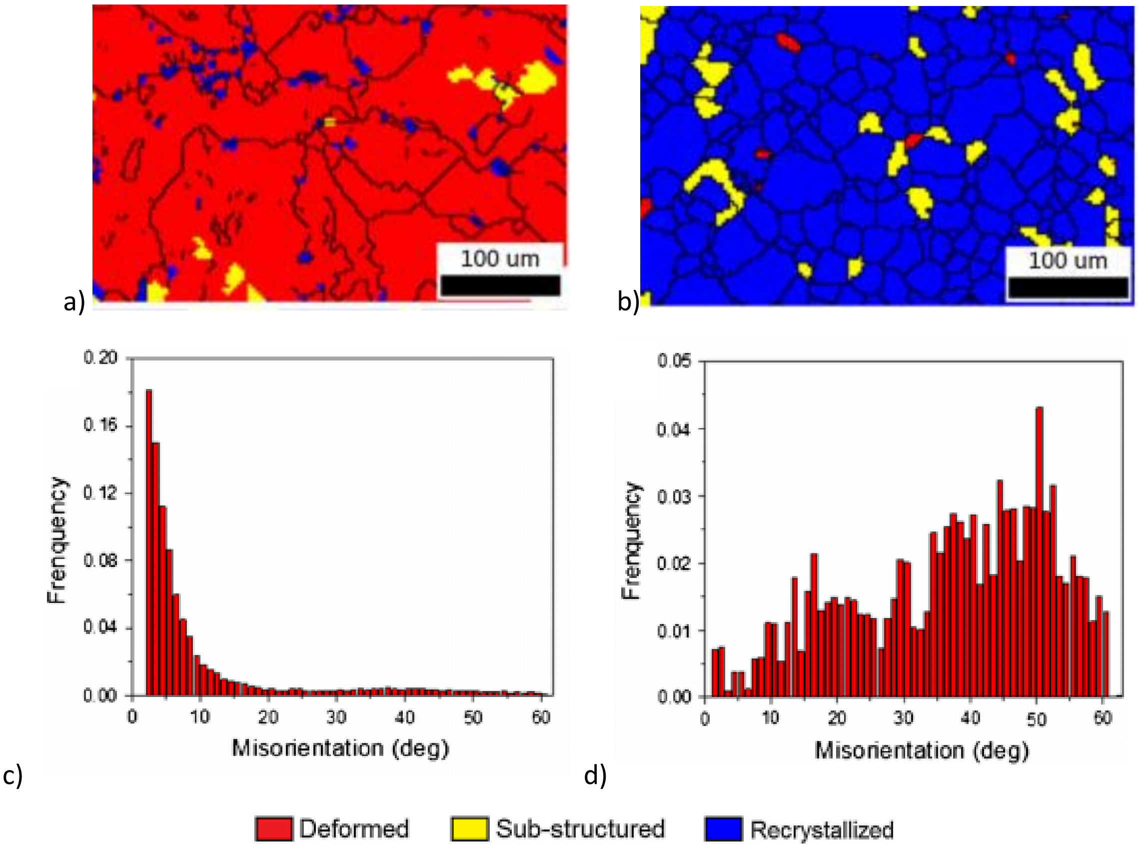

Figure 74: Microstructure of $(Fe_{81}Ga_{19})_{98}B_2$ *sheets after a) Hot rolling and b) HR + annealing at 625 ˚C for 1 hour. Misorientation Angle Distribution of* $(Fe_{81}Ga_{19})_{98}B_2$ *sheets after c) Hot rolling and d) HR + annealing.[85]*

By comparing the results described above and the Jethete M152 results, it is possible to conclude that the initial microstructure of the sample was consistent with a recrystallised heat treated plate, because no grain distortion was observed and a high angle boundaries were predominant in microstructure. On the other hand, the microstructure of the mandrel and roller zones present typical characteristics of a metal subjected to plastic deformation like heavy grain distortion, no apparent recrystallisation and a drastic increase of low angle boundaries.

3.4.5 Inconel 718

Before any analysis of the microstructure and texture found in the shear formed Inconel 718 sample can be made, it is important to note that temperature at which the deformation takes place and any post-process heat treatment applied to this alloy will have an important impact on the microstructure and texture developed. According to the information provided by the supplier, no post-process heat treatment was applied to the sample and the shear forming operation was conducted at room-temperature. However, all the findings in this chapter suggest otherwise. To back up this assumption, some examples found in the literature are described below.

In a previous research it was found that the microstructure obtained directly after cold rolling changed from uniform equiaxed grains to elongated distorted grains. Grain refinement and recrystallisation only occurred when the post process heat treatment temperature was high enough (950 ˚C). Greater grain refinement was also observed in the samples with larger levels of cold rolling. Figure 75, Figure 76 and Figure 77 show the microstructural changes observed in this investigation. [80].

It has also been demonstrated that twinning can increase during cold rolling in Inconel 718, however this behaviour is accompanied by grain distortion (See Figure 78) [79].

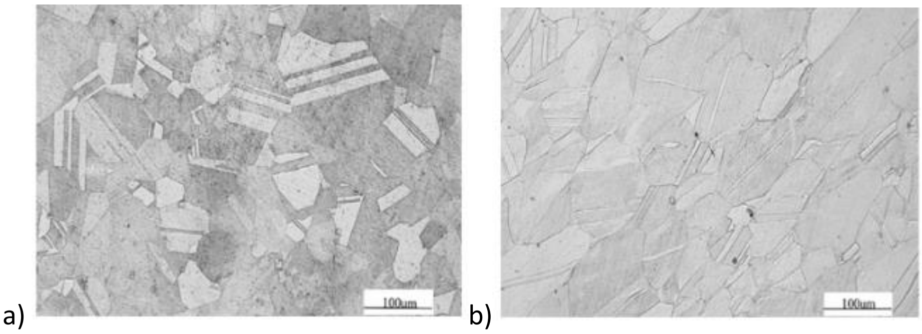

Figure 75: Microstructure of Inconel 718 after: a) Solution treatment at 1050 ˚C, b) ST + Cold Rolling [80]

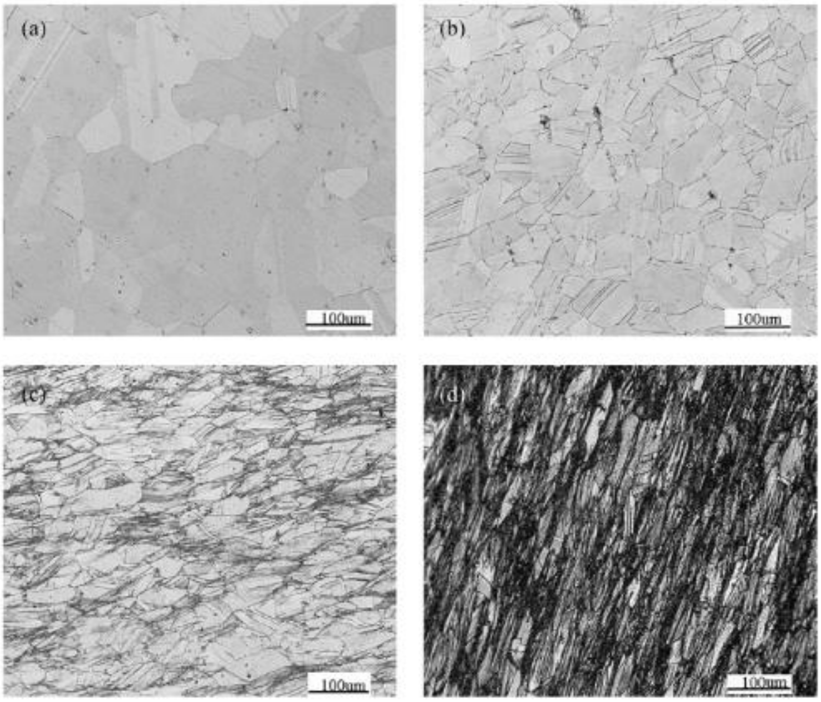

Figure 76: Microstructure of Inconel 718 after different levels of cold rolling + isothermal heat treatment at 800 ˚C : a) No cold rolling, b) 25% thickness reduction, c) 55% and d) 70%. [80]

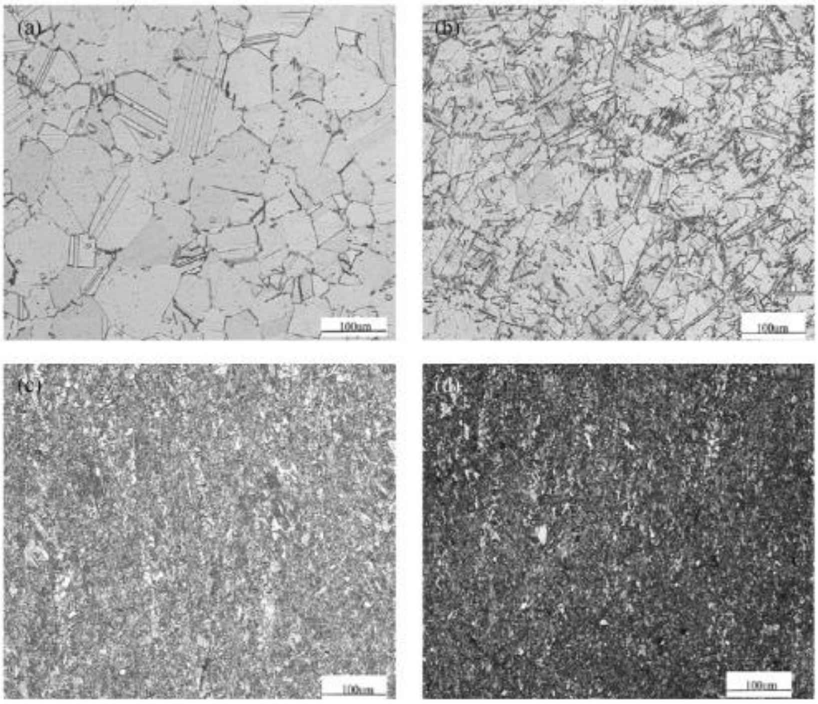

Figure 77: Microstructure of Inconel 718 after different levels of cold rolling + isothermal heat treatment at 950 ˚C : a) No cold rolling, b) 25% thickness reduction, c) 55% and d) 70%. [80]

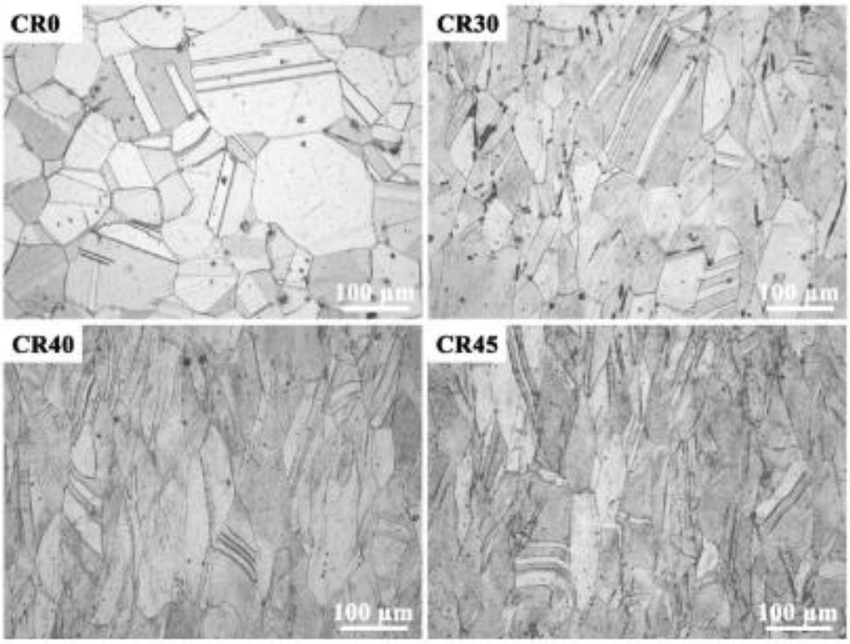

Figure 78 Microstructure of Inconel 718 after different levels of cold rolling. [79]

While recrystallisation does not happen during cold deformation, this is typical in hot processing. Figure 79 shows the microstructures of three different samples deformed at different temperatures inspected in a previous work [86]. In all cases partial recrystallisation of the microstructure occurred, however in higher temperatures a larger portion of the grains recrystallised. It was also observed that twinning occurred in the recrystallised grains at 1050 ˚C, increasing the twining proportion in the microstructure greatly. This was not the case for lower temperatures, where twins almost disappear. This can be seen in the misorientation angle distributions shown in Figure 80. The sample deformed at 1050 ˚C shows a peak of the 60˚ misorientation angles apart from the characteristic increase of low angle boundaries due to the deformation of the grains. This peak is caused by the twins' formation and it is not seen in the 1000 ˚C sample.

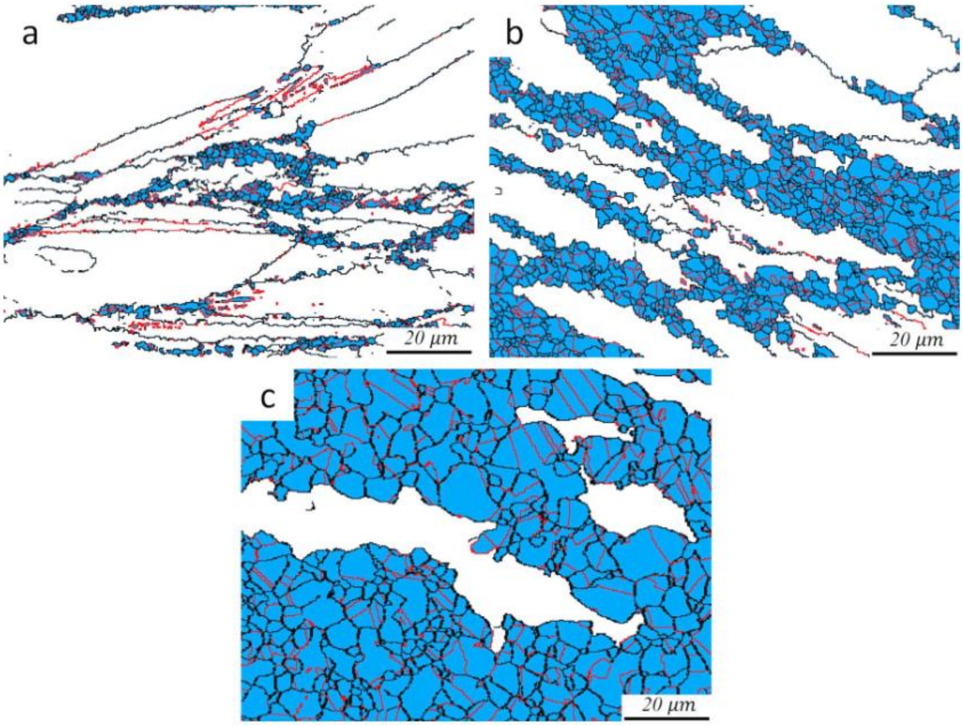

Figure 79: Microstructure of Inconel 718 after cylindrical compression at strain rate of 0.1 s-1 at: 950 ˚C, b) 1000˚ and c) 1050 ˚C. The recrystallised grains are marked in blue and twins in red. [86]

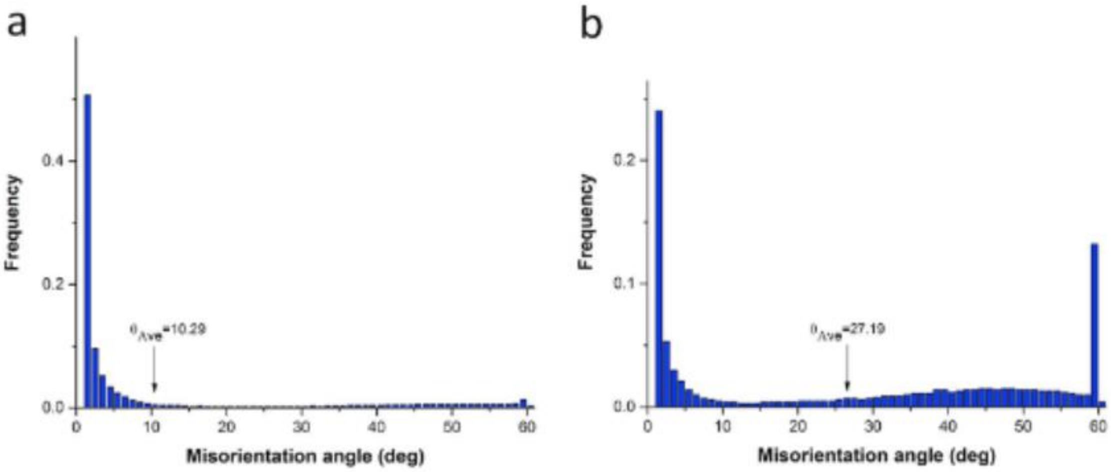

Figure 80: Misorientation angle distributions of Inconel 718 deformed at 1 s-1 strain rate and: a) 1000 ˚C and b) 1050 ˚C. [86]

After comparing the results obtained and shown in section 3.3.2 to the found in the literature, it can be concluded that the shear spun sample provided for this project was presumably cold processed and then heat treated due to the following reasons:

1. There are no morphological changes in the microstructure before and after the shear forming process. Additionally, grain size is considerably smaller in the fully deformed zones and since no grain distortion is observed, this suggest full recrystallisation of the microstructure occurred. During hot deformation, only partial recrystallisation of the microstructure occurs. This means that a heat treatment must have been applied for the microstructure to be this uniform after deformation.
2. The heavier grain refinement observed in fully the formed zones, especially in the roller areas, is consistent with the microstructures obtained in previous works after different levels of cold deformation and heat treatment. Heavier grain refinement is expected in zones with larger plastic deformation
3. The misorientation angle distributions of the roller and mandrel zone show the 60˚ boundary angle peak characteristic of microstructures with twins. Also, no increase of low angle boundaries is observed in neither zone. Again, this suggests that the microstructure has been fully recrystallised due to the heat treatment applied.

Even though the microstructures has been fully recrystallised and there are no apparent traces of the shear deformation in the grain morphology due to the heat treatment applied, the pole figures obtained for the mandrel and roller zones still show some evidence of deformation mechanism experienced during the process. Figure 81 shows a comparison between the $\{1\ 1\ 1\}$ ideal pole figure for simple shear deformed FCC metals against the experimental pole figures obtained. The simple shear pattern is not as clear and intense as in the Jethete M152 samples due to recrystallisation occurred, however the $\{1\ 1\ 1\}$ and $\langle 1\ 1\ 0\rangle$ fibres still follow the expected behaviour and the roller zone exhibits a more defined pattern.

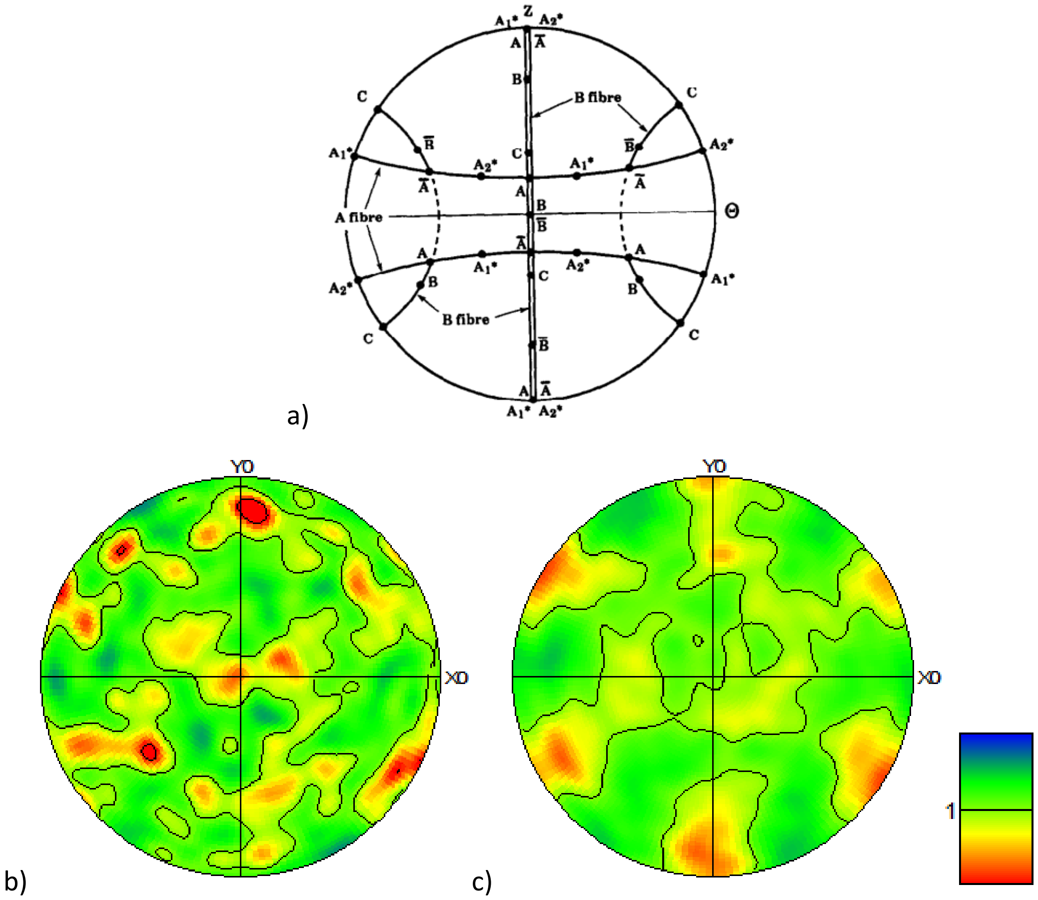

Figure 81: $\{1\ 1\ 1\}$*Pole figures of: a) Ideal orientation of simple shear in FCC metals [33], b) Mandrel zone of Inconel 718 sample and c) Roller zone of Inconel 718 sample.*

3.5 Conclusions

Throughout this chapter, the microstructural evolution of three materials that were subjected to shear forming was studied. In two of the materials it was also possible to study their texture variation. The following conclusions can be drawn from these analysis:

1. The deformation across the shear spun workpieces was not uniform. Heavier deformation was found in the areas near the roller contact surface for all three materials. Timetal 54M and Jethete M152 samples had more distorted and elongated grains in the roller zone. In the case of Inconel 718, the heavier deformation caused higher grain refinement in this zone during the post process heat treatment.
2. The fracture found in Timetal 54M seems to have started as ductile and the suffered a transition to brittle as the material failed. This important for the attempts made in Chapter 4 to predict fracture in the FEM model.
3. The texture of Inconel 718 and Jethete M152 presented some changes after being shear formed. The ideal texture expected after simple shear deformation was observed in the pole figures of both materials in the mandrel and roller zones. In both cases, the roller zone exhibited a clearer and stronger shear pattern than the mandrel. The pole figures obtained for Inconel 718 were not as intense as for Jethete M152 because this material was subjected to a heat treatment after the process.

In general, all the findings mentioned in this chapter are in accordance with the literature and back up the assumption that the main deformation mechanism in the transversal section of the blank during this spinning operation is simple shear. However, the further away the material is from the roller contact edge, the less resemblance exists between its deformation and simple shearing.

Finally, the results obtained in this chapter will help to validate the finite element model developed in chapter 4 since it will be possible to compare the level of shear deformation across the thickness in real life against the simulations.

Chapter 4: General Finite Element Model of Shear Forming Operations

4.1 Introduction

In this chapter a summary of all the modelling work done throughout this project will be presented. The main objective of this section was to develop a reliable Finite Element Model (FEM) for basic Shear Forming operations that closely resembles the deformation conditions that materials suffer during the process. Also, the study of different damage models and the integration of a damage criterion was set as another important objective.

The software Deform was selected for this task for two main reasons: one of the main focuses of this software is the simulation of metal forming operations and its Design of Experiments (DOE) module.

All the modelling work was divided in five main stages, which were:

- Stage 1 – Initial Shear Forming FEM Model: A very basic model was developed using an alloy that is known to have good general formability, in order to avoid further complication in such an early stage.
- Stage 2 – Analysis of Process Parameters: A Design of Experiments analysis was carried out to determine the influence of some of the process parameters on the damage calculations and thickness values of the model.
- Stage 3 – FEM Model for Texture Prediction: A material, that had been successfully shear formed, was selected so texture could be predicted using the FEM model. These results were later compared to the experimental data.
- Stage 4 – Selection of Damage Model: Using a new material that constantly fails during shear forming, different damage models were evaluated, and one was selected for further studies.
- Stage 5 – Evaluation of Damage Criterion: The damage criterion selected in stage 4 was tested using other materials that are expected to be successfully shear formed.

4.2 Stage 1: Initial Shear Forming FEM Model

4.2.1 General Layout

For this stage a very basic shear forming process was modelled and the layout is shown in Figure 82. The geometry of the mandrel and the roller were based on dies seen in industry; the roller nose radius selected for the model was 5 mm after taking into consideration the findings mentioned in Chapter 2 [22].

For this initial model, stainless steel AISI 316 was selected as the material of the workpiece. This alloy is well-known for its good formability and other properties like corrosion resistance, toughness and weldability which makes it ideal for a wide range of applications in the aerospace and engineering fields [87-89]. The good formability of this alloy also means that it should be easily shear formed in real life and not represent a challenge for this FE model. A summary of the process parameters appears in Table 12. The mandrel geometry was based on a study conducted where a very similar alloy was used (stainless steel AISI 304) for this angle [24].

Table 12: Shear forming model parameters.

Input Parameters	Name/Value
Material	Stainless Steel AISI 316
Workpiece Rotational Speed	5 rad/s
Feed rate	1 mm/s
Mandrel Angle	31.5 degrees
Material Thickness	6 mm

The workpiece in the model is set to be an elasto-plastic object while the dies are rigid objects. This will prevent the dies from suffering any deformation (since in real life it is so small, it can be dismissed) and will reduce solving times. A hexahedral mesh with 10440 elements and 14400 nodes was selected for the workpiece (See Figure 83) after conducting several trials with both tetrahedral and hexahedral. It was observed that high element distortion was a constant issue in the tetrahedral meshes due to the high level of deformation experienced in this process, which caused certain elements in the mesh to have disproportionally high strain values. An example of these distorted elements can be seen in Figure 84.

The initial temperature of dies and workpiece was set at 25 ˚C since this process is conducted at room temperature in real life. Heat transfer was disabled for this simulation given that at low temperatures (up to 550 ˚C) the effect of the temperature on the flow stress behaviour of this material can be considered negligible [90].

The friction coefficient between the mandrel and the blank was 0.12, which is around the typical values found in cold metal forming [57, 91, 92], and 0.02 between the roller and the blank since in it has been found in the literature that in metal spinning the roller friction is negligibly small due to the brief contact times and small contact area [21]. No friction sensitivity analysis was conducted for this model due to the time limitations of this project, however it is suggested that for more accurate results the friction to be used in any future models is determined experimentally.

There were several complications regarding the solving times of the model since the constant rotation of the workpiece and the constant changing local deformation conditions in the model meant no axisymmetric symmetry conditions could be used, leading to long initial solving times. This was later solved by rotating the roller around the workpiece, rather than the workpiece itself which reduced the typical solving times to around 17 hours.

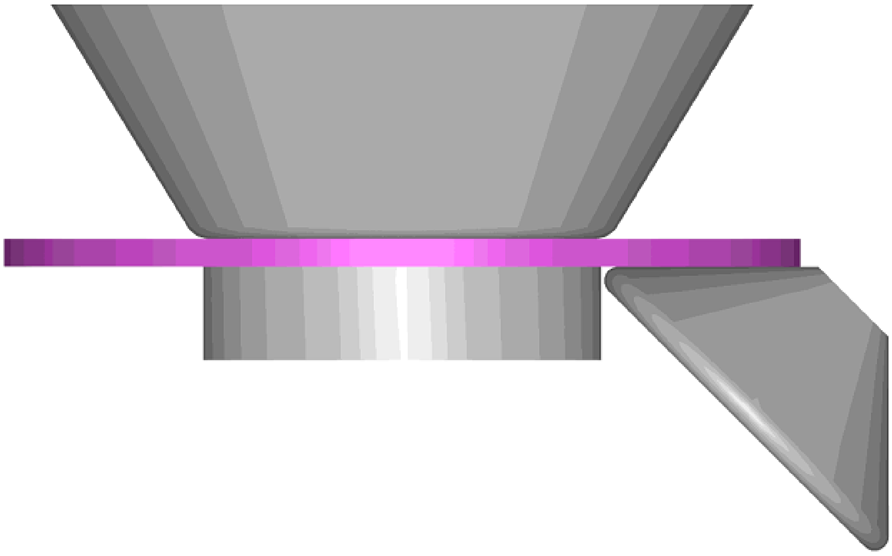

Figure 82: Shear forming model in Deform.

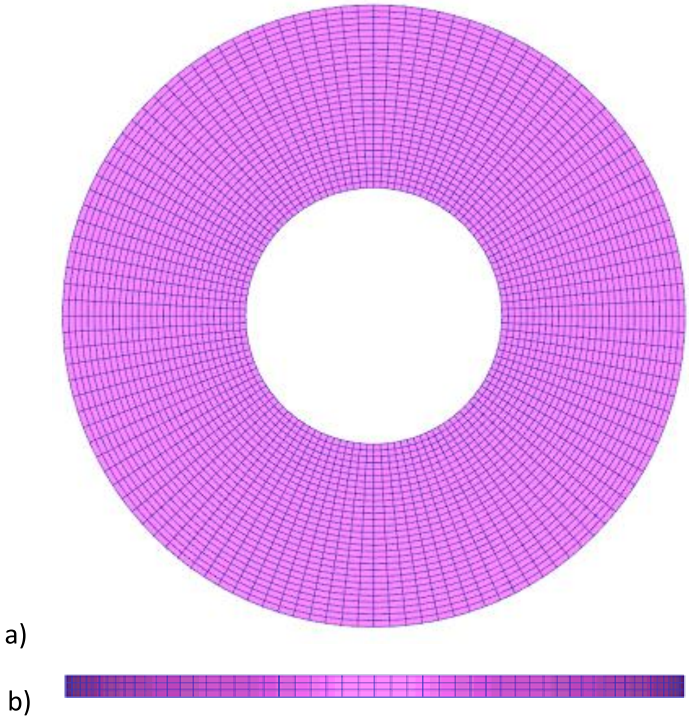

Figure 83: Brick mesh used for the workpiece. a) Circumferential cross section. b) Transversal cross section.

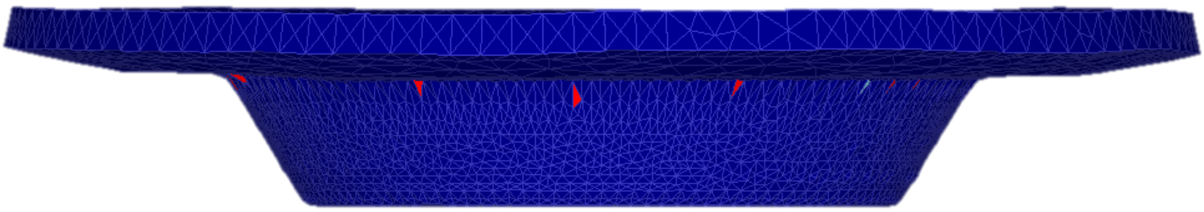

Figure 84: Example of deformed tetrahedral mesh with distorted elements (marked in red).

4.2.2 Material Definition

One of the key points of this model is to have the right material data added to the database, this will allow the material to flow correctly and to establish an accurate damage criterion later. The software Deform provides several methods for the definition of flow stress for the plastic data. In this case the power law was selected, which is represented by the following equation:

$$\sigma = k\bar{\varepsilon}^{n}\dot{\bar{\varepsilon}}^{m} + y$$

Equation 17

Where

$\sigma =$ Flow stress

$k =$ Material strength coefficient

$\bar{\varepsilon} =$ Effective plastic strain

$\dot{\bar{\varepsilon}} =$ Effective strain rate

$n =$ Strain exponent or work-hardening exponent

$m =$ Strain rate sensitivity exponent

$y =$Yield stress

This equation is a combination of the power law for strain hardening ($\sigma = k\varepsilon^n$) [93] and the strain rate sensitivity power law ($\sigma = k\dot{\varepsilon}^m$). From all the options provided by Deform, it was decided that this was the most accurate method to represent the flow stress because, most engineering metals (and especially ferrous alloys) follow this behaviour [93] and like Wagoner [94] mentions some materials are more difficult to deform at higher rates i.e. they are strain-rate sensitive.

Like in most engineering alloys, the flow stress behaviour of this material is greatly influenced by a wide range of factors, like heat treatment applied, previous mechanical processing, test conditions (like temperature and speed), among others. An example of these variations is shown in Figure 85. Knowing this, it was decided that the variables that would affect the flow curves of the material should be minimised so that no further complications would arise at such an early stage of the FE model. A detailed investigation regarding how heat treatments and previous cold working would affect the flow stress behaviour of this material was conducted by Fahr [90] and it was found that when annealing at 1050 ˚C for 1 hour no significant changes can be found in the flow stress curves obtained from tensile tests conducted at different temperatures up to 550 ˚C (See Figure 86). Since this is a very simple and common heat treatment and seeking to neglect the effect of the temperature in this early model, it was decided to search for flow stress data of this alloy under these conditions at room temperature.

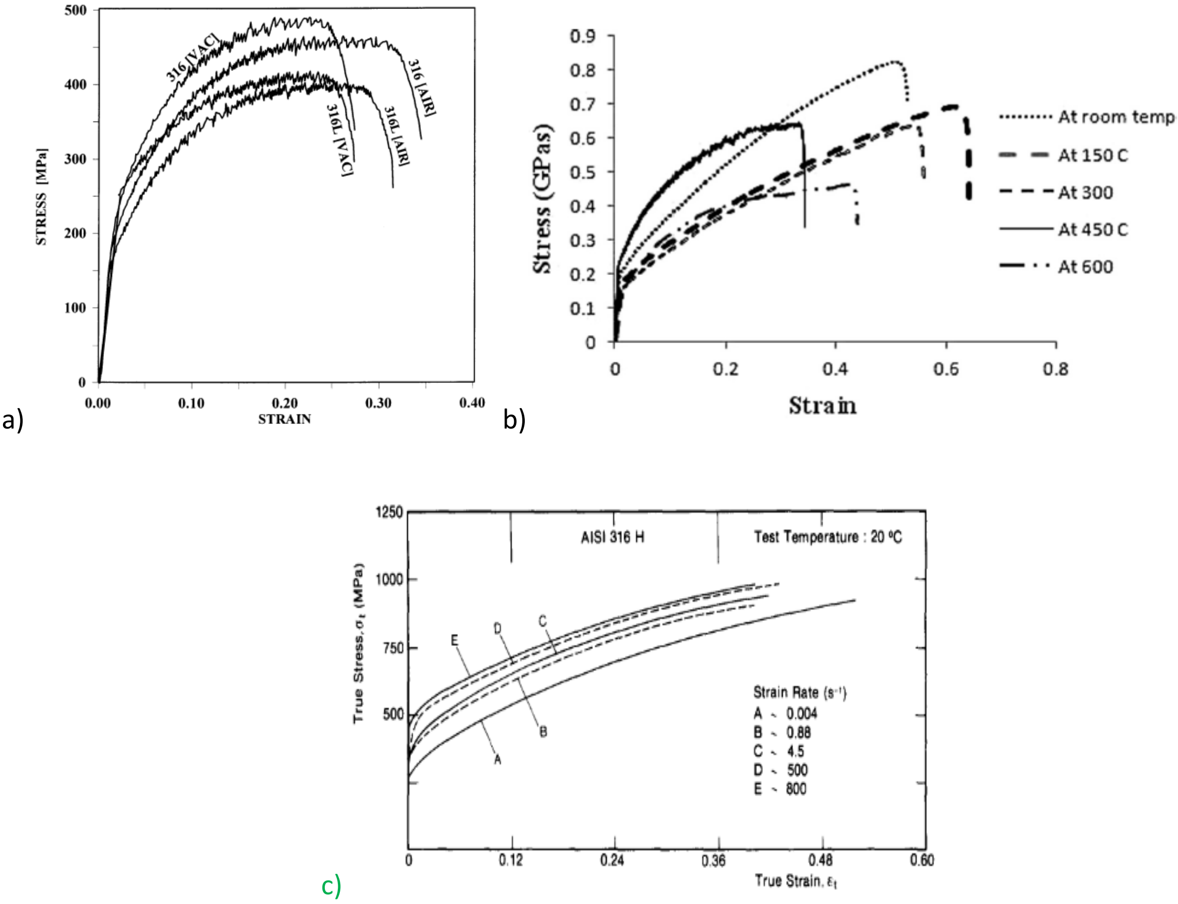

Figure 85: Flow stress curves of stainless steel AISI 316 under different conditions. a) Tensile test conducted at 500 ˚C in air and vacuum conditions of recrystallised AISI 316 [95]. b) Tensile test conducted at different temperatures, no further specifications of the material were found [87]. c) Tensile test conducted at room temperature and various strain rates of cold rolled AISI 316 [96]

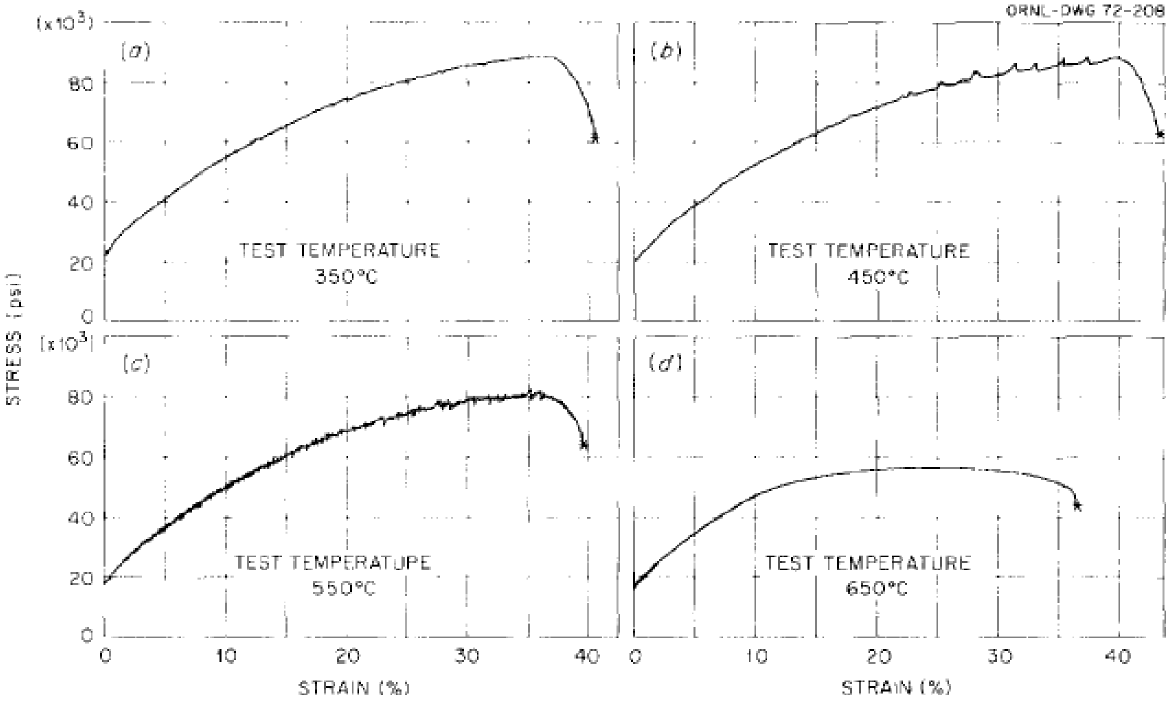

Figure 86: Flow stress curves of annealed Stainless Steel AISI 316 at different temperatures obtained by Fahr [90].

Finally, the material data was taken from a prior study conducted by Palengat et al. [97], where the AISI 316 samples were subjected to annealing heat treatment at 1050˚C before the tensile tests, which were conducted at room temperature and different strain rates (Figure 87). In Table 13, there is a summary of the material data introduced to Deform. Since Deform only supports kinematic hardening for elasto-plastic objects this was used as the hardening model [57]. The main difference between the isotropic and kinematic hardening models is that in the latter the yield surface keeps the same size but moves across the stress space during plastic deformation while in the isotropic model, this expands uniformly (See Figure 88) [98]. By using the kinematic model, the Baushinger effect is included in FEM calculations (this is when a material exhibits lower yield stress after reloading on the opposite direction) [99].

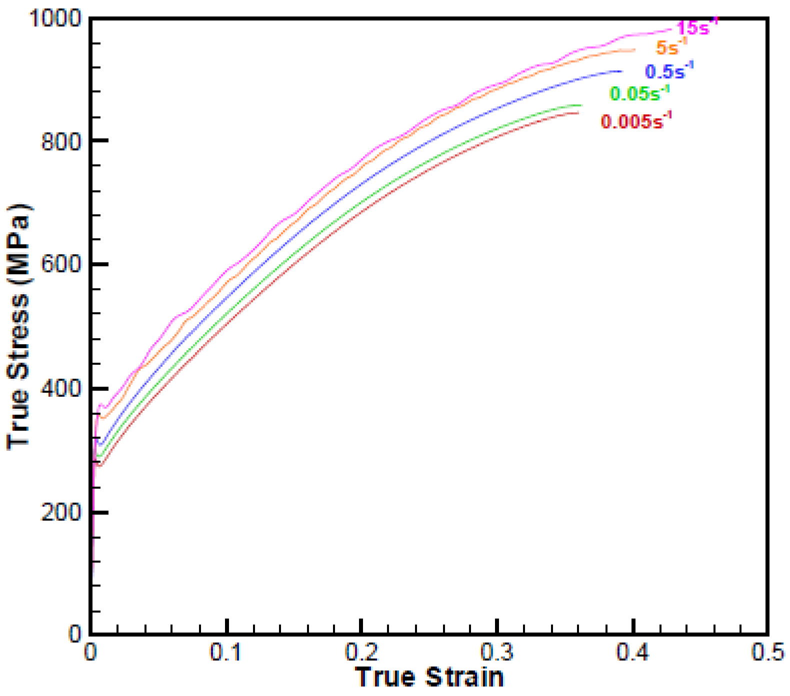

Figure 87: Flow stress curves of annealed AISI 316 alloy at different strain rates [97].

Table 13: Material data used in the model. Data taken from Palengat et al. [97]

		Value
Elastic Data	Young's Modulus	192 GPa
Plastic Data	Yield stress (y)	242 MPa
	Strength Coefficient (k)	1295 MPa
	Work-hardening exponent (n)	0.61
	Strain rate sensitivity exponent (m)	0.02

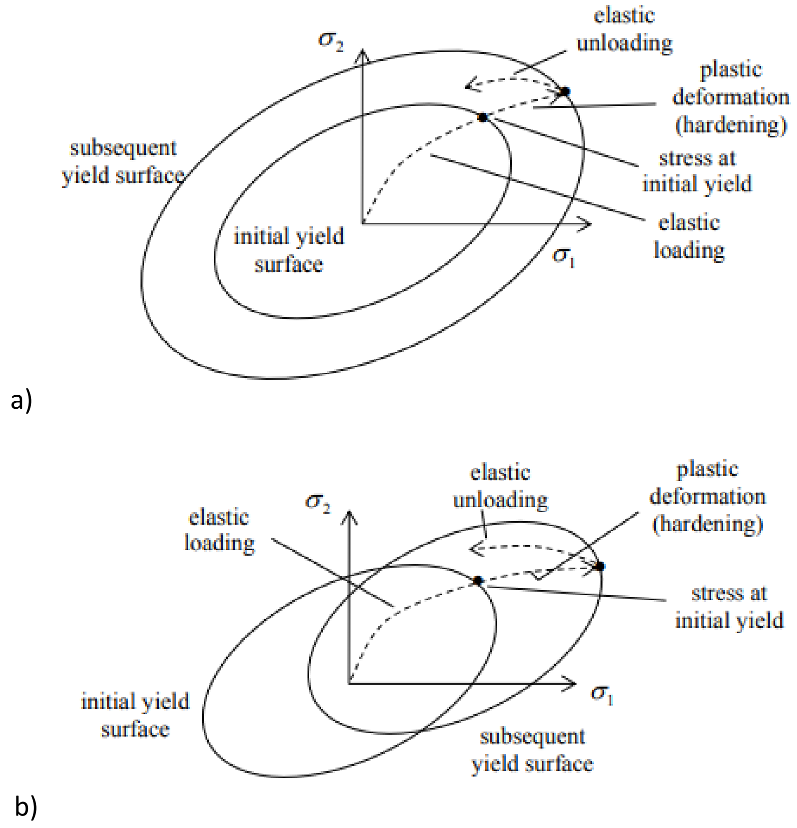

Figure 88: Visualisation of two main hardening models: a) Isotropic hardening. b) Kinematic hardening. [98]

4.2.3 Definition of Simulation Time

The selection of an adequate step size and total time of the simulation is essential to avoid convergence issues and to reduce the solving times of the simulation as much as possible, especially when working on processes like shear forming where its incremental nature implicates a constantly moving contact area at high speed. This basically means that a small element size is needed, hence the large number of elements in the mesh mentioned in section 4.2.1, and as a consequence a small step size was also required for this model. Knowing this the step size used for the simulation controls was 0.001 s/step, and this was selected based on the speed of the dies and the element size. According to Deform's documentation [57], the time per step should be selected so that no nodes move more than a third of the length of their corresponding element edge in a single step to prevent distortion of the mesh.

The effective strain in three different points along the thickness of the workpiece (where the roller roller was initially positioned) was monitored during the simulation to select the minimum number of *steps required for the results to be reliable.*

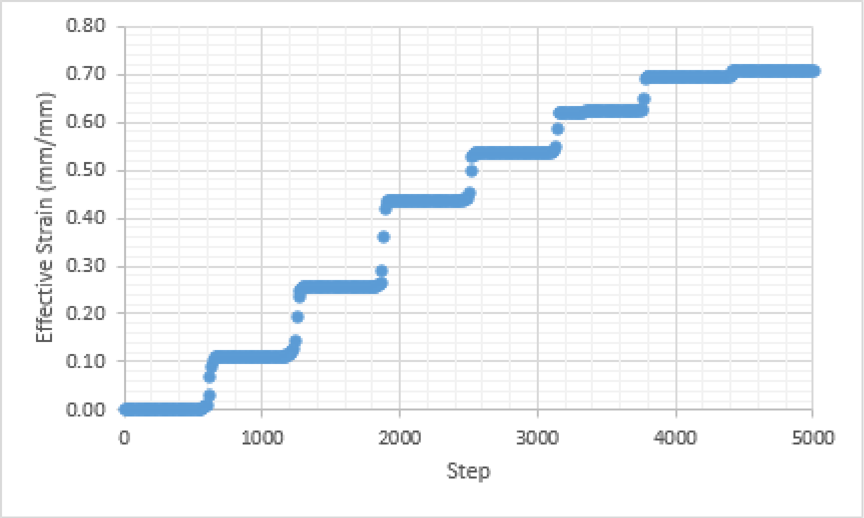

a)

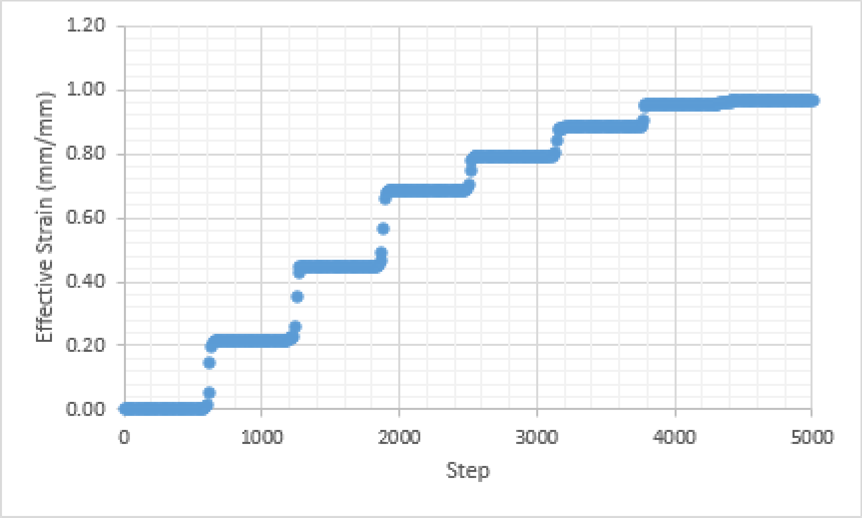

b)

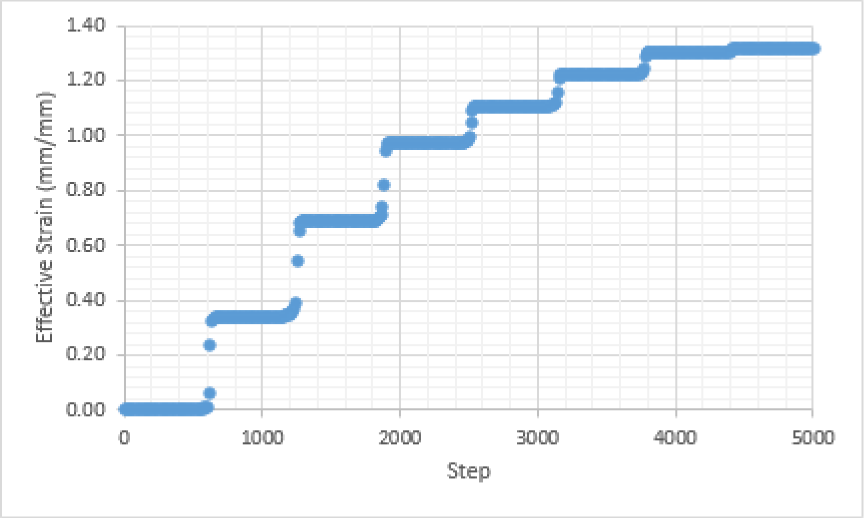

c)

Figure 89 shows how the effective strain accumulates during the process at the mandrel, centre and roller zones. Three observations can be remarked:

1. The accumulated effective strain in all three points follows the same behaviour. It basically accumulates in gradual steps, in this case seven steps. These steps represent the number of revolutions occurring in the process. The beginning of each revolution is basically when the roller comes into contact with the area of interest, which in this case is where the selected points are. When the roller touches this area, a sudden increase of the effective strain value is seen and then it remains stable until the next revolution, this is because during the rest of the revolution the roller no longer deforms that certain area because it is no longer in contact with it.
2. After 7 revolutions the effective strain showed no significant increment. This means that the workpiece in this area has entered the final stage of the process defined by Sellin [12], so no more deformation will occur here and it is safe to analyse the data in this area.
3. The accumulated effective strain is higher in the roller zone and gradually decreasing towards the mandrel, a behaviour that was expected based on the results of Chapter 3.

Finally, based on these observations, the total amount of steps for this model was set at 5000. It is important to note, that this means that the total time of the process would be only 5 s in real life. This time is considerably lower than usual shear forming processes conducted in industry. The main reason for this is that in order to reduce the total time needed to solve the simulations, the dimension of the workpiece and tools were scaled so the actual size of the model is quite small geometrically speaking (See Figure 90). This should not represent a problem for the modelling of real life shear spinning operations, because once the initial deformation area of the workpiece reaches the final stage of the process with no complications (like in this case), it is safe to assume the same will happen for the rest of the workpiece as long as the deformation conditions remain the same, i.e. no process parameters or conditions are changed.

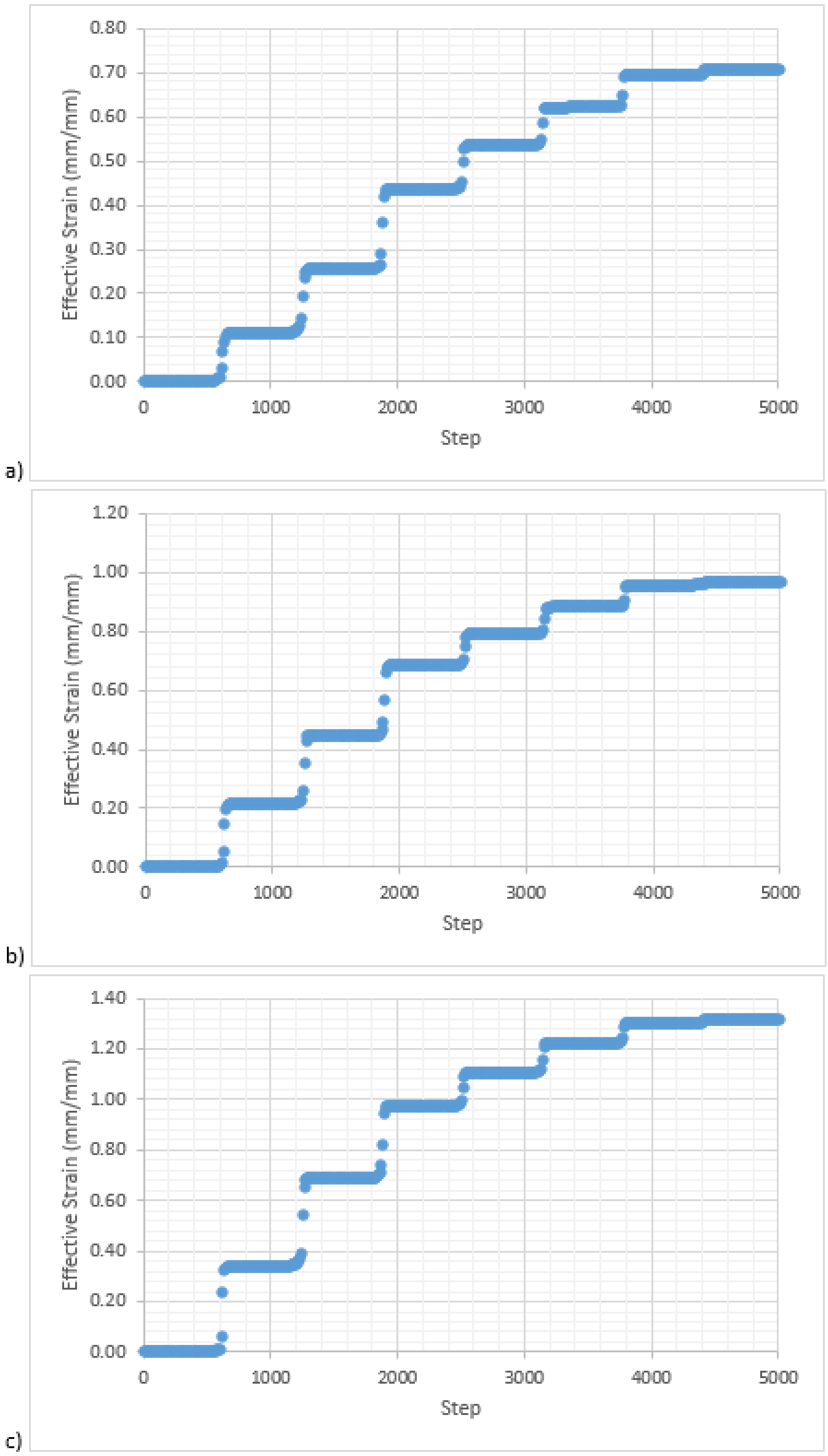

Figure 89: Effective strain vs step measured at three different points in the simulation. a) Near mandrel, b) Centre, c) Near roller.

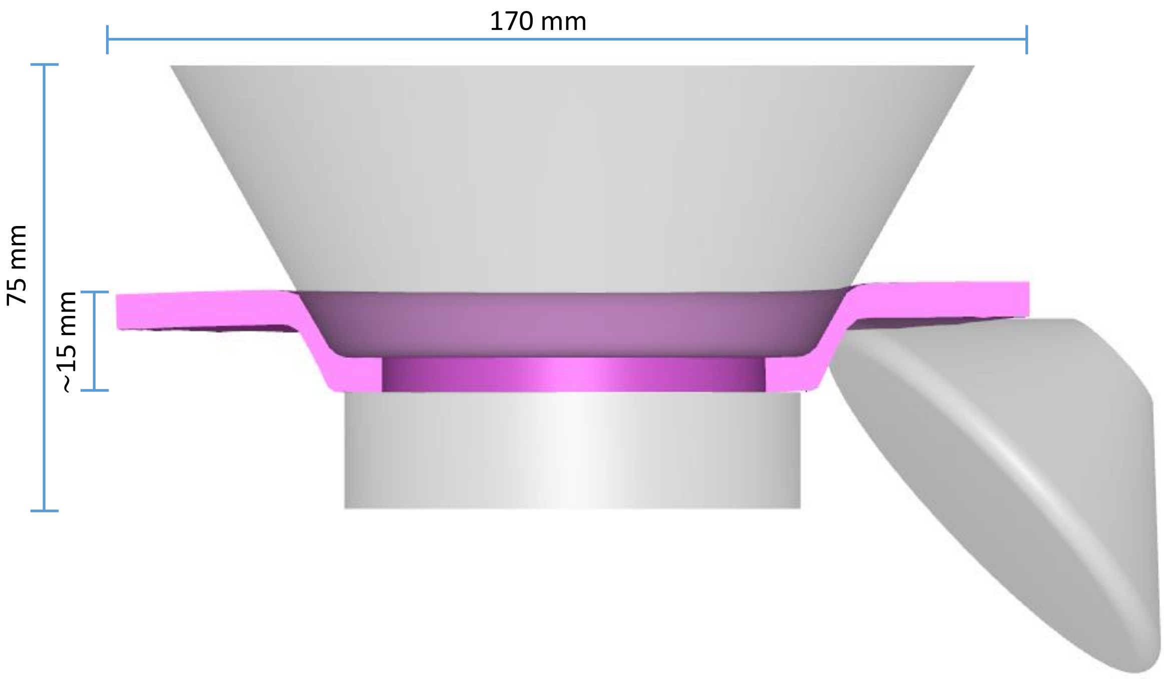

Figure 90: General dimensions of model and deformed zone in mm.

4.2.4 Initial Results

From this model two main results were obtained: the material flow behaviour and the strains distribution along the workpiece.

The material flow behaviour was obtained by adding a flow-net in the transversal direction and the inner and outer[3] surface of the workpiece that allowed to see how the material is displacing throughout the thickness of the blank and in both surfaces during the forming process. This can be seen in the following figures.

---

[3] For practical terms the inner surface refers to the surface that is in contact with the mandrel and the outer surface is the one in contact with the roller.

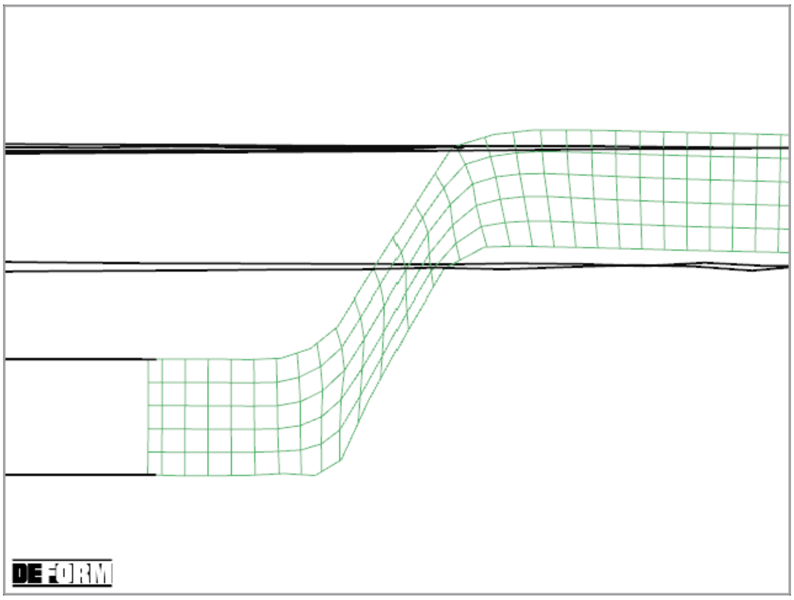

Figure 91: Deformed flow-net in the transversal direction of the blank at step 5000.

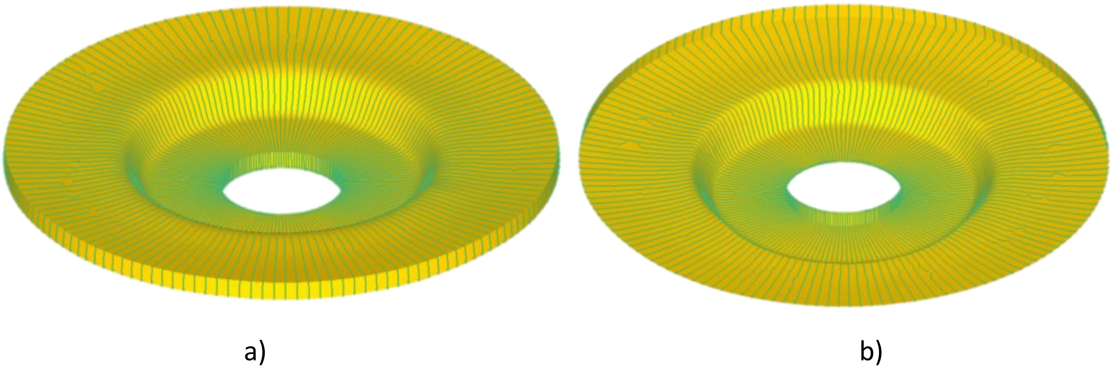

Figure 92: Deformed flow-net at step 5000: a) Inner surface. b) Outer surface

Regarding the principal strains' distribution obtained in the model, both major and minor strains show a consistent behaviour along all the mandrel (See Figure 93 and Figure 94). In both cases, higher values of the principal strains are present in the outer surface, where the roller is in contact and in the transversal section near it. This behaviour has been observed in the experimental work described in Chapter 3 and in previous works found in the literature. Zhan et al. [19] explained that this non-uniform deformation is mainly caused by the following reasons:

- The different friction directions caused by the roller and mandrel: The flow of the material has the same direction as the friction caused by roller, which allows the material to flow easily and resulting in a large level of deformation. The opposite happens to the blank's side, where the friction inhibits the materials flow and reduces the level of deformation achieved.

- The non-uniform deforming area under the roller: As the roller starts deforming the outer surface, the material starts to move along the thickness direction. This progressively increases the deforming area under the roller and reduces the stress and strain concentrations towards the inner surface.

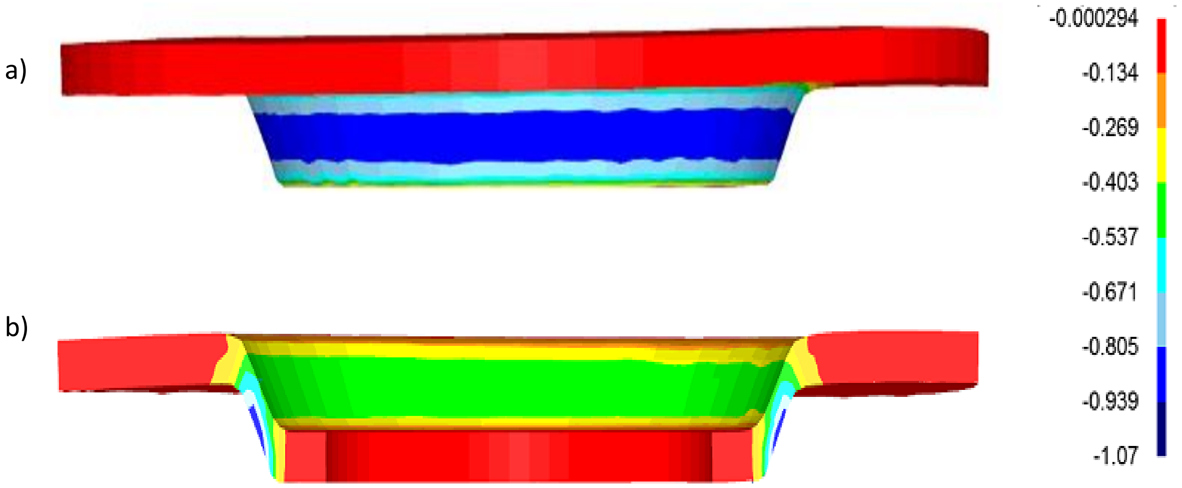

Figure 93: Distribution of Minimum Principal Strain or Minor Strain (mm/mm) along the workpiece at step 5000: a) Outer. b) Inner surface

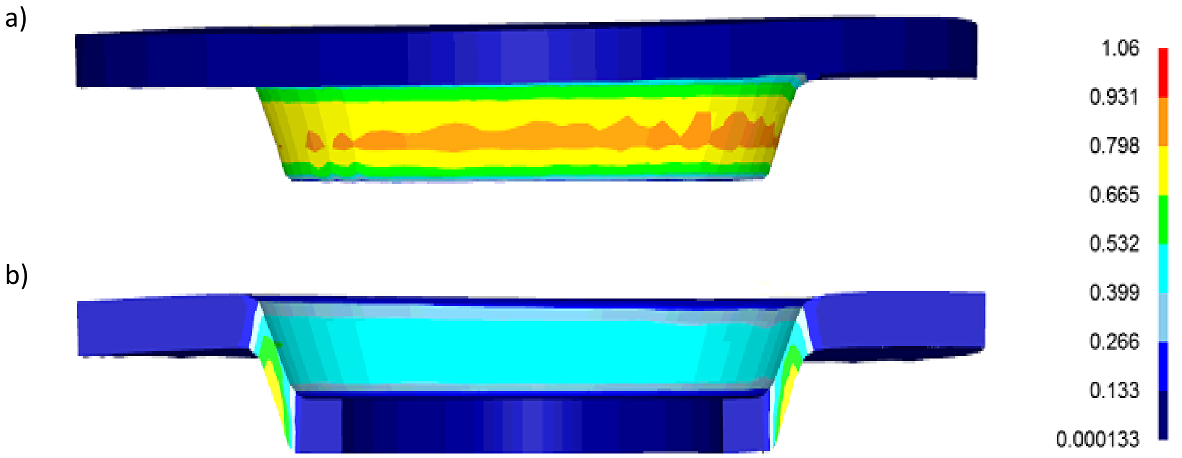

Figure 94: Distribution of Maximum Principal Strain or Major Strain (mm/mm) along the workpiece at step 5000: a) Outer. b) Inner surface

The principal strains values can be compared against the expected values in ideal in-plane simple shear, where the only deformation component that is not zero is the shear strain (See Figure 95) and can be calculated with the following equation [100]:

$$\gamma = \tan\theta$$

Equation 18

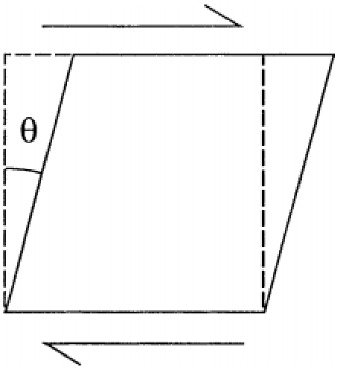

Figure 95: Deformed element by simple shear. [100]

As shown in Figure 96, in shear forming the mandrel angle α is the complementary of the shear angle θ defined in Equation 18, i.e. $\alpha + \theta = 90°$. This means that the shear strain in the process can be expressed as follows:

$$\gamma = \cot\alpha$$

Equation 19

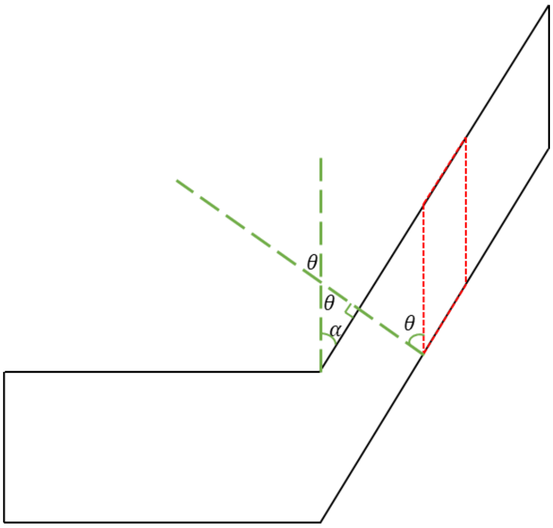

Figure 96: Representation of the mandrel angle α and the shear angle θ in shear forming.

Finally, the in-plane principal strains can be calculated using Equation 20 [101] as shown below:

$$\varepsilon_{12} = \frac{\varepsilon_x + \varepsilon_y}{2} \pm \sqrt{\left(\frac{\varepsilon_x - \varepsilon_y}{2}\right)^2 + \left(\frac{\gamma_{xy}}{2}\right)^2}$$

Equation 20

$$\varepsilon_{12} = 0 \pm \sqrt{(0)^2 + \left(\frac{\cot\alpha}{2}\right)^2}$$

Equation 21

$$\varepsilon_{12} = \pm\frac{\cot\alpha}{2}$$

Equation 22

Using Equation 22, the principal strains for ideal simple in-plane simple shear with an angle $\alpha = 31.5°$ were calculated and are shown in Table 14 along with the values obtained in the FEM model. Even though the principal strains obtained in the model were not exactly the same as the expected in simple shear, the values were very similar. This could be caused for several factors, like:

1. In shear forming, the workpiece is rotating. Even though it has been proven that this rotation does not cause substantial circumferential flow, this does not mean that a small deformation occurs in this direction due to the friction effects of the roller. This could increase the principal strains values.
2. The process parameters, like rotational speed and feed rate were not controlled in this first attempt of modelling which could have prevented the material from flowing in optimal conditions and caused deviations from the sine law.

Additionally in the model, the minimum and maximum principal strains had almost the same magnitude, indicating that their behaviour is consistent with the expected in simple shear.

Table 14: Principal Strains' values calculated for a mandrel angle $\alpha = 31.5°$

Ideal Simple Shear	FEM Model
$\varepsilon_1 = 0.816$	$\varepsilon_1 = 0.865$
$\varepsilon_2 = -0.816$	$\varepsilon_2 = -0.872$

4.2.5 Conclusions

As a first attempt of modelling the shear forming process, the results obtained were promising. The flow paths along the thickness obtained with this model were quite similar to the ones from Kalpakcioglu's work [6]. In both the model and Kalpakcioglu's results, the grid lines parallel to the rotation axis and where the blank was already fully shear spun kept almost the same direction, which is expected to happen in idealised simple shear (See Figure 97). This observation backs up the assumption that in shear forming the deformation mechanism along the thickness is mainly shearing.

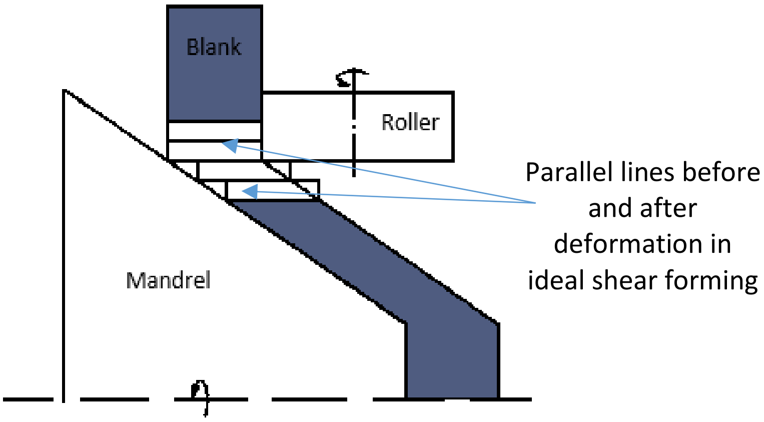

Figure 97: Representation of the idealised shear forming process. Adapted from [6].

Also, the material flow in the circumferential direction is like the one obtained by Mori et al [10]. In both the FEM model and their experimental results no significant deformation was found along the circumferential direction.

When comparing the principal strains' obtained in the FEM model against the calculated for in-plane ideal simple shear, the numerical values were not exactly the same. Even with this numerical difference, the behaviour of the principal strains was as expected in ideal simple shear indicating that this in fact is the main deformation mechanism and that the model is accurately representing it.

Additionally, these first results showed good agreement with the experimental results in terms of level of deformation experienced. When observing the principal strains distribution along the mandrel shown in Figure 93 and Figure 94, larger values were obtained in the outer surface, where the roller is in contact. This suggests that the model is accurately representing the variation of the deformation across the thickness that was observed in the shear spun samples analysed in chapter 3, however texture simulations were conducted in a later stage of the project for further validation of the FEM model.

4.3 Stage 2: Analysis of Process Parameters

4.3.1 Introduction

In Stage 1 a FEM model that could accurately represent the deformation experienced in shear forming was developed, however the effect of the process parameters was not taken into account. In order to understand how these could impact the final geometry and deformation behaviour of the workpiece, a Design of Experiments (DOE) analysis was conducted in this stage. Two main paramenter were selected for this study based on the information found in the literature[24] [22]: feed rate and rotational speed.

Using the software Minitab, an Analysis of Variance (ANOVA) was conducted to determine if any of these process parameters have a significant effect on each of the responses. This technique compares the means of the response selected at the different levels of the factors established to determine if there are significant differences between them [102]. In order to use this technique, the following conditions must be fulfilled [103-106]:

1. The population where the data was taken from must follow a normal distribution.
2. The residuals[4] must have equal variance.
3. The residuals must be independent from each other.
4. The experimental data must not be transformed or manipulated for the ANOVA test

4.3.1 DOE Set-Up

For this study, the model developed in stage 1 was used, but the rotational speed and feed rate were increased slightly so the simulation running time would be reduced due to the time restrictions of this process. The nomial run parameters are shown in Table 15.

The sampling method for this analysis was full factorial and 3 levels for each parameter were established. Factorial designs are a type of DOE that study the effect of many factors on the response selected by varying the levels of all the factors at the same time [107]. The number of runs for this

---

[4] Residual: This is the difference between the observed value and the predicted using the regression model calculated with ANOVA.

[106] D. C. Montgomery, *Design and analysis of experiments*, 5th ed. ed. New York ; Chichester: New York ; Chichester : Wiley, c2001, 2001.

type of designs depends on the number of levels selected for each paramter. In this case 9 runs are needed, the details for each run are shown in Table 16.

Table 15: Nominal run process parameters

Input Parameters	Name/Value
Material	Stainless Steel AISI 316
Workpiece Rotational Speed	10 rad/s
Feed rate	2.5 mm/s
Mandrel Angle	31.5 degrees
Material Thickness	6 mm

Table 16: Feed rate and rotational speed combinations used for the DOE analysis.

	Feed Rate	Rotational Speed
Run 1	2.0 mm/s	7.5 rad/s
Run 2		10.0 rad/s
Run 3		12.5 rad/s
Run 4	2.5 mm/s	7.5 rad/s
Run 5		10.0 rad/s
Run 6		12.5 rad/s
Run 7	3.0 mm/s	7.5 rad/s
Run 8		10.0 rad/s
Run 9		12.5 rad/s

The responses selected were:

1. Principal Strains: Any changes in the level of deformation experienced in the workpiece with different process parameters can be monitored using these values.
2. Principal Strains' ratio ($\varepsilon_2/\varepsilon_1$): By monitoring this ratio, it was possible to determine if the process paramaters had an effect on any deviations from the simple shear deformation mechanism.
3. Final thickness: This response is important because deviations from the sine law ideal thickness would mean that the final workpiece could present another type of failure even if it does not fracture.

The significance level was set at 0.05. This indicates the probability of incorrectly rejecting the null hypothesis (H_0) [108], in this case the null hypothesis would be that the means between the responses at each level are equal. For the ANOVA technique, the significance level is used to reject or accept the null hypothesis by comparing it against the P_value[5] calculated for each fact. If the P_value is lower than the significance level, then the null hypothesis is rejected and it can be concluded that said factor has a significant effect on the response.

Finally, 4 measurements of each response were taken for every run along the circumference of the workpiece. All measurements were taken in the outer surface of the blank, where the roller was in contact, since here is where the largest amount of deformation is experienced during shear forming.

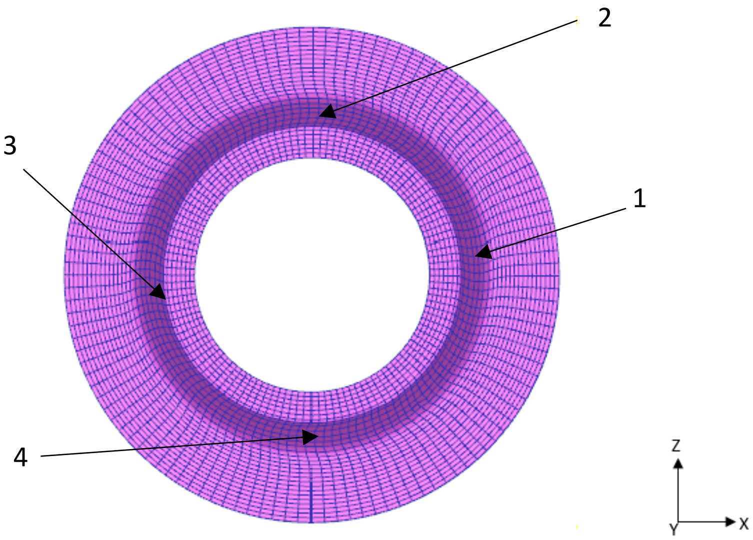

Figure 98: Example of shear formed workpiece. The position of the four measurements taken are indicated with black arrows.

4.3.2 Results and Discussion

The general results of the DOE analysis are summarised in

Table 17. The ANOVA test results for each response, as well as their corresponding residual plots are shown and analysed in the following sections. Additionally, Contour plot charts were also constructed using Minitab. These charts are a way to visualise the relationship between the selected output and two variables, in this case the process parameters [109].

---

[5] P_value: This is the smallest significance level at which the null hypothesis would be rejected. [106] Ibid.

Table 17: Results of DOE Analysis.

Run	Feed Rate (mm/s)	Rotational Speed (rad/s)	ε_2	ε_1	${\varepsilon_2}/{\varepsilon_1}$	Thickness (mm)
1	2.0	7.5	-0.991	0.874	-1.134	3.290
			-0.983	0.878	-1.120	3.419
			-0.979	0.874	-1.120	3.871
			-0.963	0.869	-1.108	3.352
2	2.0	10.0	-0.953	0.857	-1.112	3.395
			-0.928	0.831	-1.117	3.500
			-0.979	0.872	-1.123	3.505
			-0.962	0.867	-1.110	3.365
3	2.0	12.5	-0.982	0.875	-1.122	3.350
			-0.968	0.858	-1.128	3.399
			-0.970	0.863	-1.124	3.407
			-0.962	0.852	-1.129	3.437
4	2.5	7.5	-0.999	0.889	-1.124	3.745
			-1.030	0.931	-1.106	3.837
			-0.908	0.786	-1.155	3.898
			-1.020	0.897	-1.137	4.082
5	2.5	10.0	-0.969	0.872	-1.111	3.425
			-0.979	0.870	-1.125	3.652
			-0.958	0.859	-1.115	3.789
			-0.944	0.849	-1.112	3.486
6	2.5	12.5	-0.894	0.758	-1.179	3.373
			-0.950	0.843	-1.127	3.348
			-0.897	0.767	-1.169	3.359
			-0.997	0.872	-1.143	3.387
7	3.0	7.5	-0.891	0.803	-1.110	3.317
			-0.986	0.849	-1.161	3.670
			-0.910	0.788	-1.155	3.641
			-1.000	0.895	-1.117	3.385
8	3.0	10.0	-0.951	0.847	-1.123	3.435
			-1.020	0.905	-1.127	3.748
			-0.963	0.861	-1.118	3.924
			-0.994	0.871	-1.141	3.580
9	3.0	12.5	-0.983	0.875	-1.123	3.205
			-0.970	0.873	-1.111	3.375
			-0.944	0.841	-1.122	3.543
			-0.961	0.859	-1.119	3.438

4.3.2.1 Principal Strains

Figure 99 shows a summary of the ANOVA results for the Principal strains. It can be seen that the P_values for all parameters and all parameters combinations are higher than 0.05 for both principal strains. This means that there is not enough evidence to reject the null hypothesis for any process parameter, i.e. neither of the process parameters nor their combination have a significant effect on the Principal Strains values. To validate the adequacy of these ANOVA tests, the residual plots for each principal strains are shown in Figure 100. Similar observations can be made for both strains:

1. The normal probability plots and histograms show that the residuals seem to follow a normal distribution.
2. In the Versus Fit plots, the residuals are randomly distributed showing the same amount of points on the positive and negative side of the graph. This suggest that the residuals do have equal variance.
3. No tendencies are visible in the Versus Order plots, which indicates that the data has not been manipulated and that there are no correlations between the residuals.

All these observations indicate that the requirements for the ANOVA test have been met and so the results obtained can be considered reliable. Additionally, when observing the contour plot charts shown in Figure 101, no clear tendencies are visible. This backs up the ANOVA results, since no direct relationship between the parameters and the principal strains values can be determined from these charts.

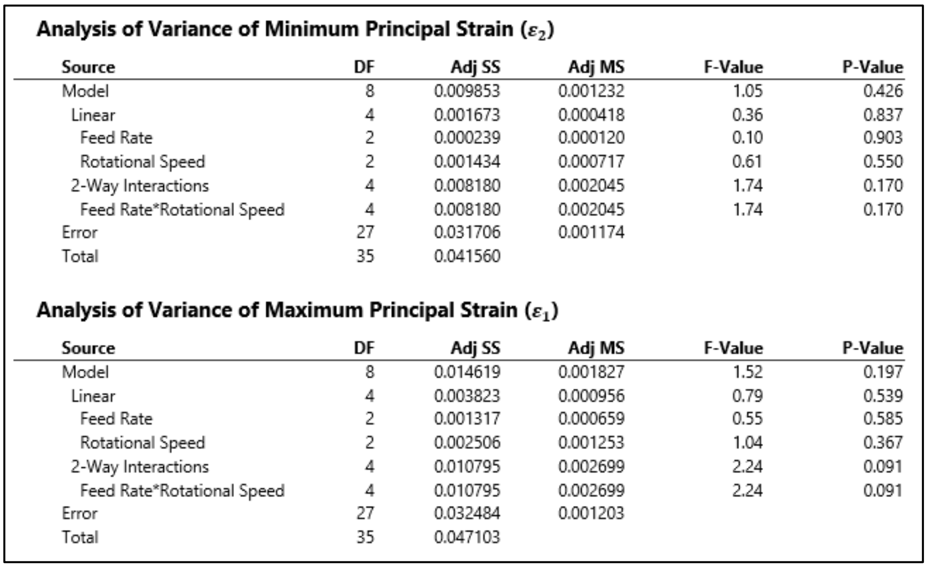

Analysis of Variance of Minimum Principal Strain (ε_2)

Source	DF	Adj SS	Adj MS	F-Value	P-Value
Model	8	0.009853	0.001232	1.05	0.426
Linear	4	0.001673	0.000418	0.36	0.837
Feed Rate	2	0.000239	0.000120	0.10	0.903
Rotational Speed	2	0.001434	0.000717	0.61	0.550
2-Way Interactions	4	0.008180	0.002045	1.74	0.170
Feed Rate*Rotational Speed	4	0.008180	0.002045	1.74	0.170
Error	27	0.031706	0.001174		
Total	35	0.041560			

Analysis of Variance of Maximum Principal Strain (ε_1)

Source	DF	Adj SS	Adj MS	F-Value	P-Value
Model	8	0.014619	0.001827	1.52	0.197
Linear	4	0.003823	0.000956	0.79	0.539
Feed Rate	2	0.001317	0.000659	0.55	0.585
Rotational Speed	2	0.002506	0.001253	1.04	0.367
2-Way Interactions	4	0.010795	0.002699	2.24	0.091
Feed Rate*Rotational Speed	4	0.010795	0.002699	2.24	0.091
Error	27	0.032484	0.001203		
Total	35	0.047103			

Figure 99: Analysis of Variance of Minimum and Maximum Principal Strains vs Feed Rate and Rotational Speed.

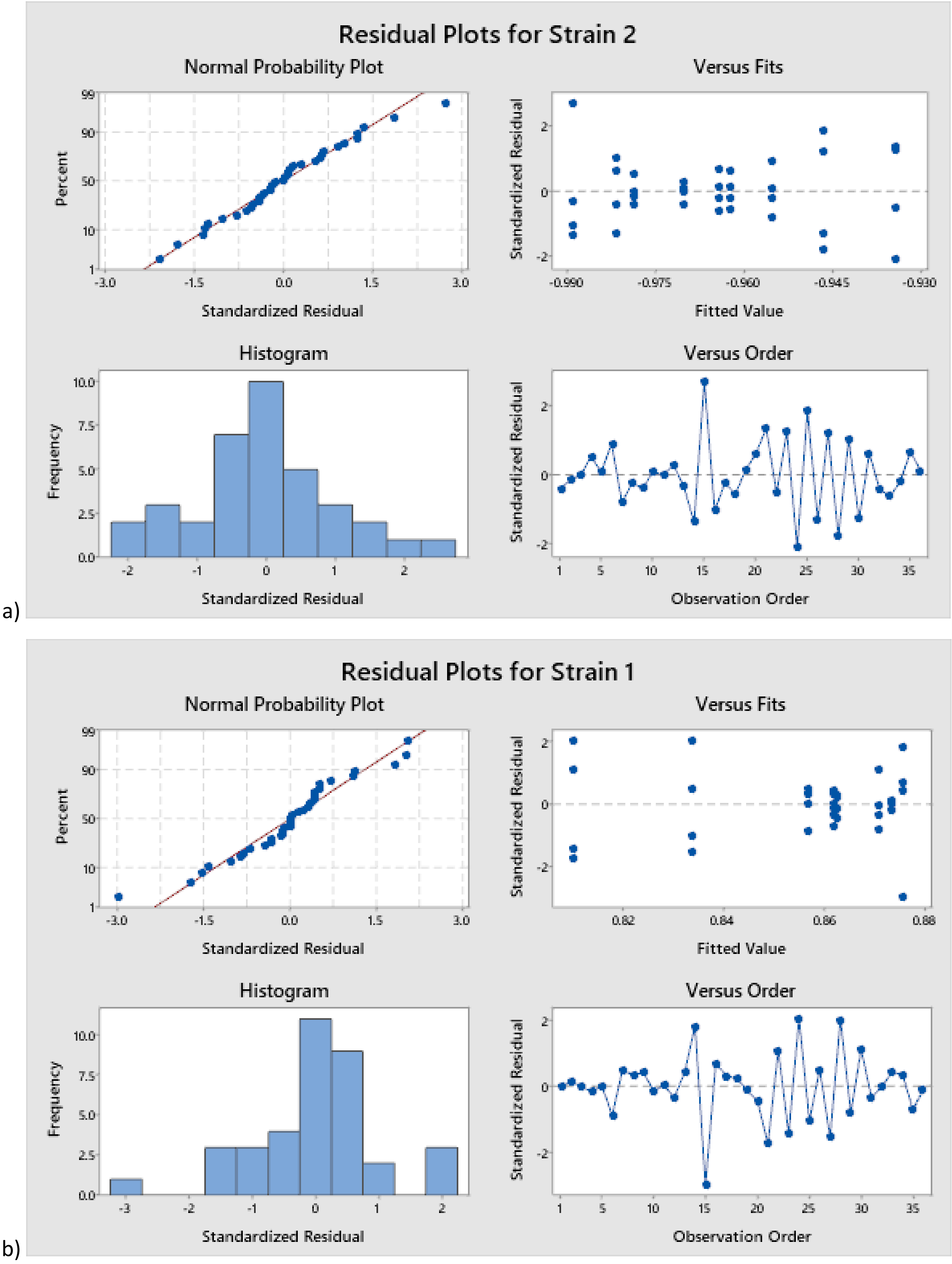

Figure 100: Residual Plots for Principal Strains: a) Minimum Principal Strain (ε_2), b) Maximum Principal Strain (ε_1).

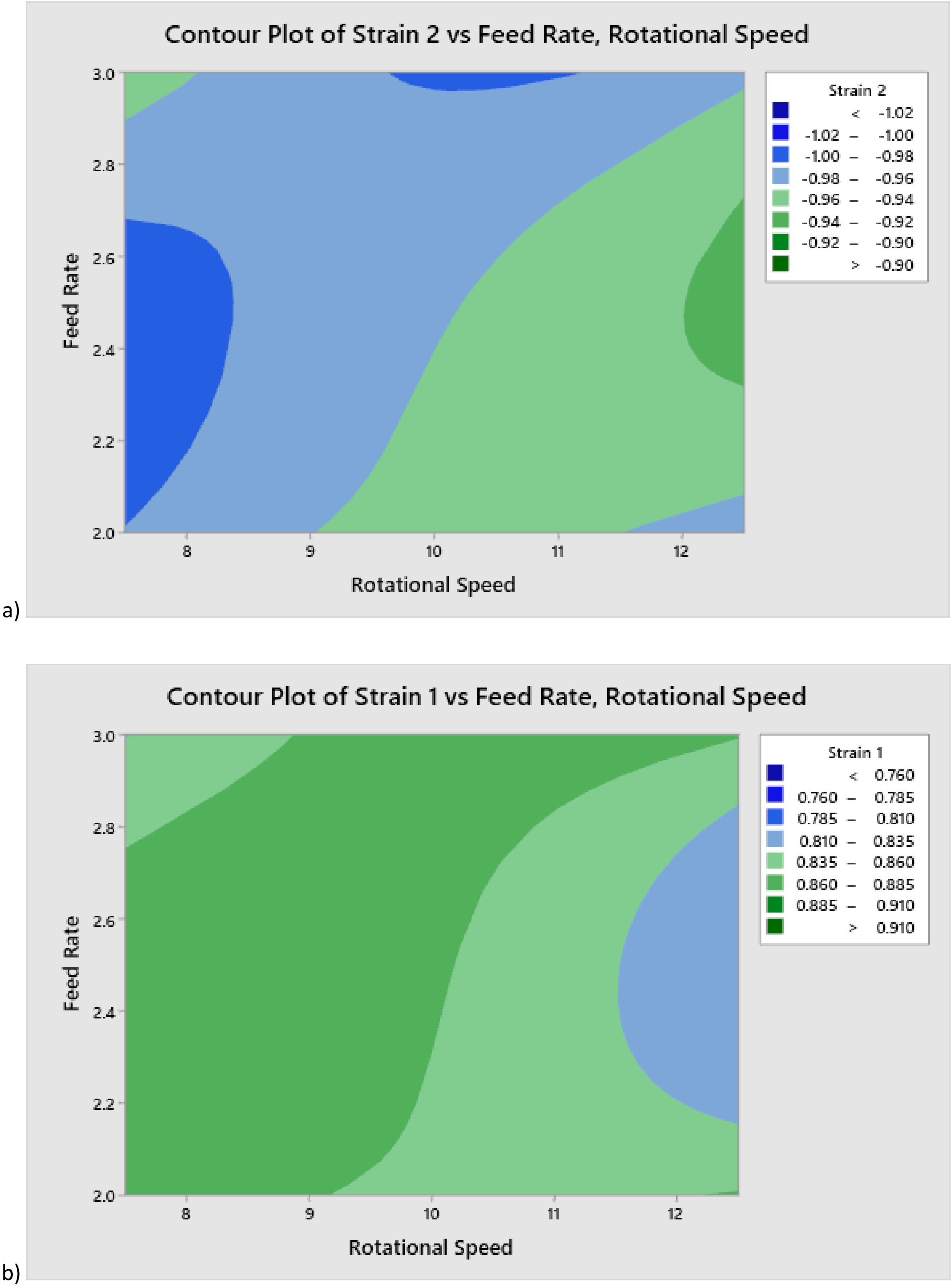

Figure 101: Contour Plots for Principal Strains: a) Minimum Principal Strain (ε_2), b) Maximum Principal Strain (ε_1).

4.3.2.2 Principal Strains’ Ratio

Before any discussion can be made, it is important to note that the principal strain’s ratio was used in this study as a way to measure the level of simple shear deformation experienced in the workpiece. As shown in section 4.2, in simple shear the minimum and maximum principal strains have the same magnitude. This means that in ideal simple shear the following rule applies:

$$\frac{\varepsilon_2}{\varepsilon_1} = -1$$

Equation 23

By comparing the actual values obtained with each set of parameters against this rule, it is possible to establish if any of the parameters affect the deformation behaviour in the workpiece causing deviations from the simple shear mechanism.

The ANOVA results shown in Figure 102 indicate that even though the feed rate and rotational speed on its own do not have a significant effect on the principal strains’ ratio, the combination of both parameters does. Additionally in the Contour Plot chart from Figure 104, it is possible to see that there are not consistent increments or decrements in the strains ratio values obtained when comparing them against each parameter individually. On the other hand, the strain ratios with lower deviation from the simple shear rule (closer to -1) were obtained when the feed rate was lower and the rotational speed was on the intermediate values. This is the combined effect of the parameters deducted in the ANOVA test.

Finally, the same observations described for the principal strains in section 4.3.2.1 can be seen for this response indicating that the ANOVA test results are reliable.

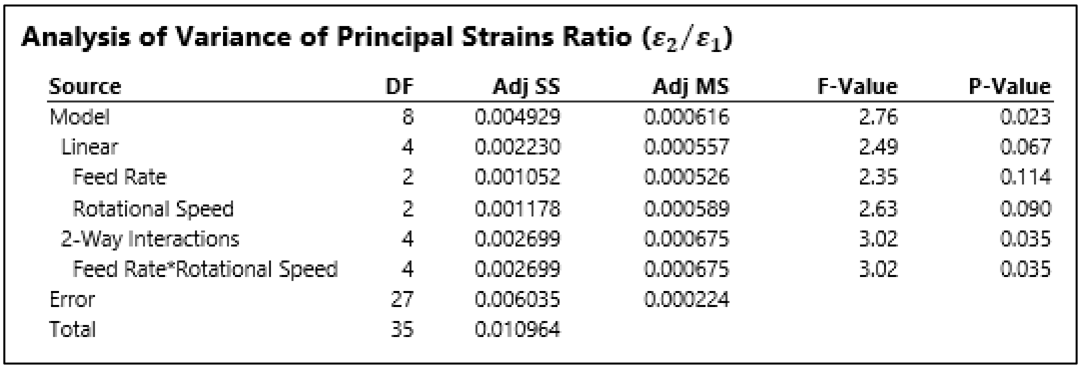

Analysis of Variance of Principal Strains Ratio ($\varepsilon_2/\varepsilon_1$)

Source	DF	Adj SS	Adj MS	F-Value	P-Value
Model	8	0.004929	0.000616	2.76	0.023
Linear	4	0.002230	0.000557	2.49	0.067
Feed Rate	2	0.001052	0.000526	2.35	0.114
Rotational Speed	2	0.001178	0.000589	2.63	0.090
2-Way Interactions	4	0.002699	0.000675	3.02	0.035
Feed Rate*Rotational Speed	4	0.002699	0.000675	3.02	0.035
Error	27	0.006035	0.000224		
Total	35	0.010964			

Figure 102: Analysis of Variance of Principal Strains Ratio ($\varepsilon_2/\varepsilon_1$) vs Feed Rate and Rotational Speed.

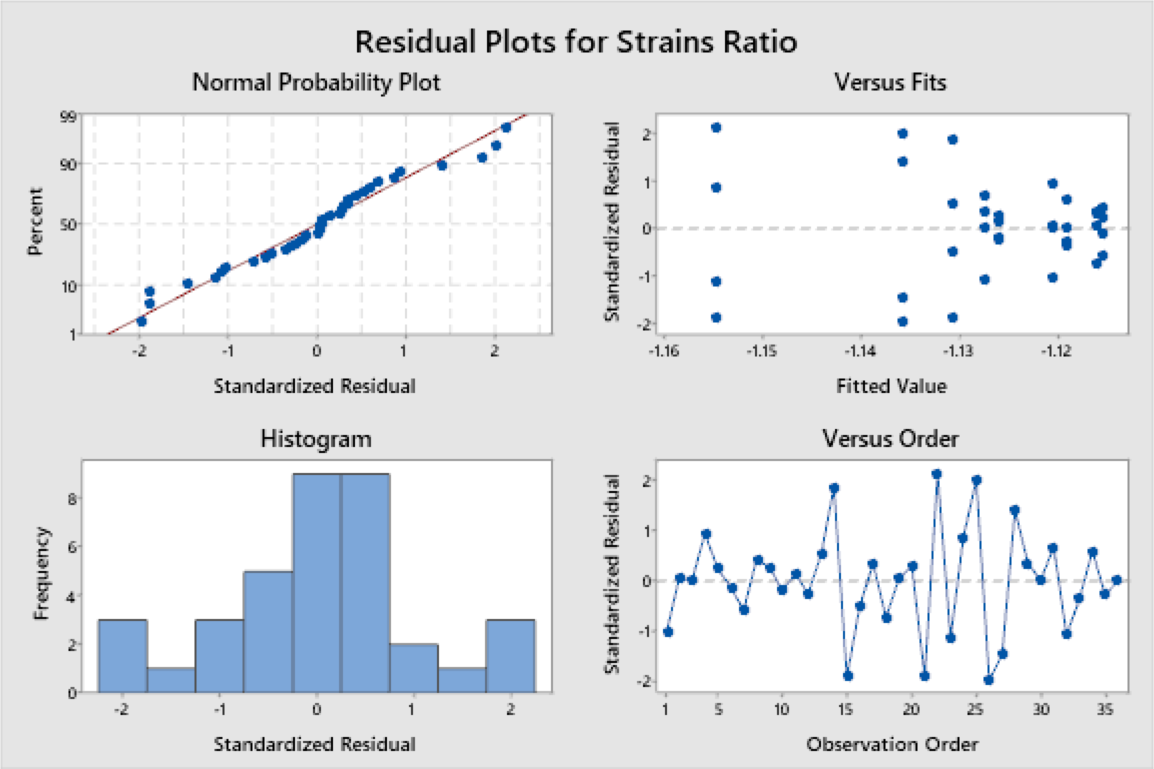

Figure 103: Residual Plots for Principal Strains Ratio ($\varepsilon_2/\varepsilon_1$) vs Feed Rate and Rotational Speed.

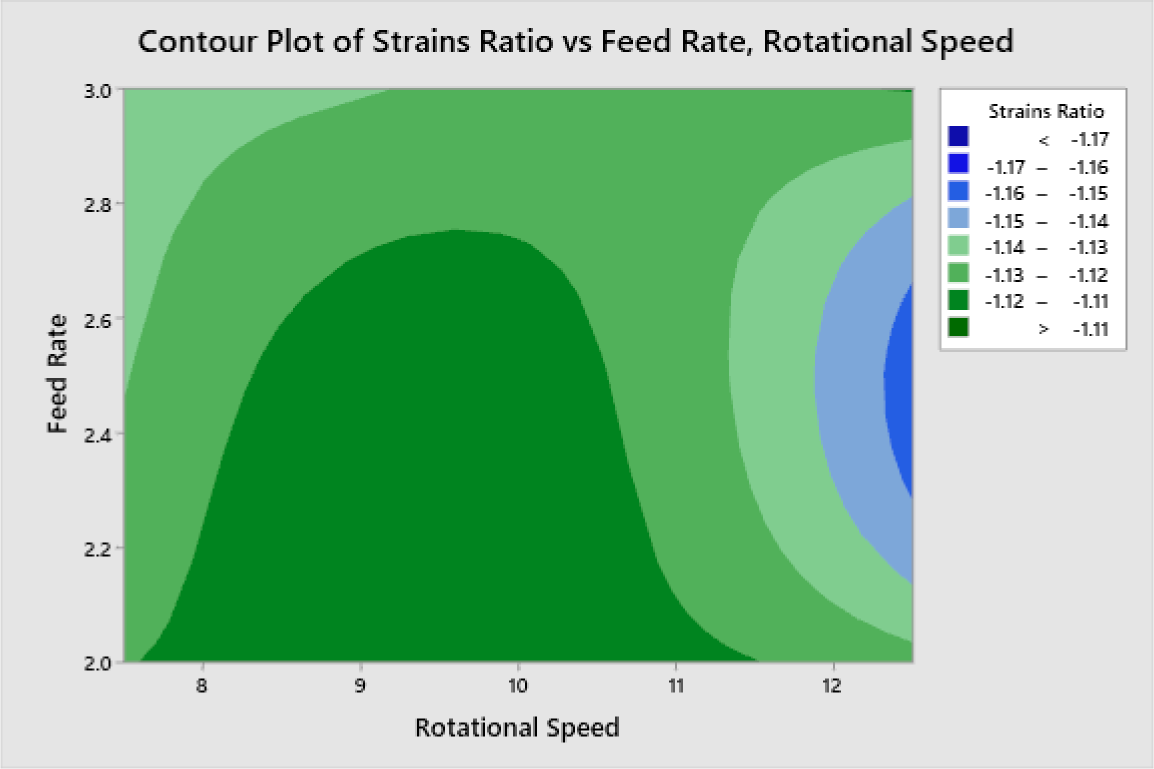

Figure 104: Contour Plot of Principal Strains Ratio ($\varepsilon_2/\varepsilon_1$) vs Feed Rate and Rotational Speed.

4.3.2.3 Thickness

The ANOVA test results for the final thickness of the workpiece are shown in Figure 105. In this case the P_values of all process parameters and all interactions between these are lower than 0.05, which indicates that all parameters have a significant effect on this response. The residual plots again showed behaviours that confirms that the conditions needed for the ANOVA test were fulfilled (See Figure 106).

Finally the contour plot chart shown in Figure 107 show clearly how lower thickness values were obtained with lower feed rates and higher rotational speeds. It is important to note that the ideal thickness should follow the sine law, which is shown in Equation 24. In this DOE all runs resulted in higher thickness than the ideal, but by using this chart this deviation can be minimised.

$$t_1 = t_O \sin(\propto) = 6\, mm \sin(31.5^\circ) = 3.135\, mm$$

Equation 24

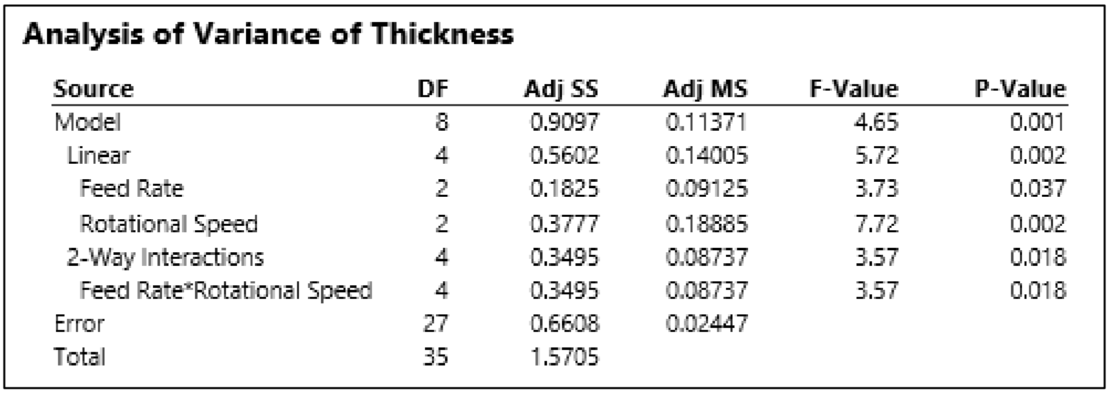

Analysis of Variance of Thickness

Source	DF	Adj SS	Adj MS	F-Value	P-Value
Model	8	0.9097	0.11371	4.65	0.001
Linear	4	0.5602	0.14005	5.72	0.002
Feed Rate	2	0.1825	0.09125	3.73	0.037
Rotational Speed	2	0.3777	0.18885	7.72	0.002
2-Way Interactions	4	0.3495	0.08737	3.57	0.018
Feed Rate*Rotational Speed	4	0.3495	0.08737	3.57	0.018
Error	27	0.6608	0.02447		
Total	35	1.5705			

Figure 105: Analysis of Variance of Thickness vs Feed Rate and Rotational Speed.

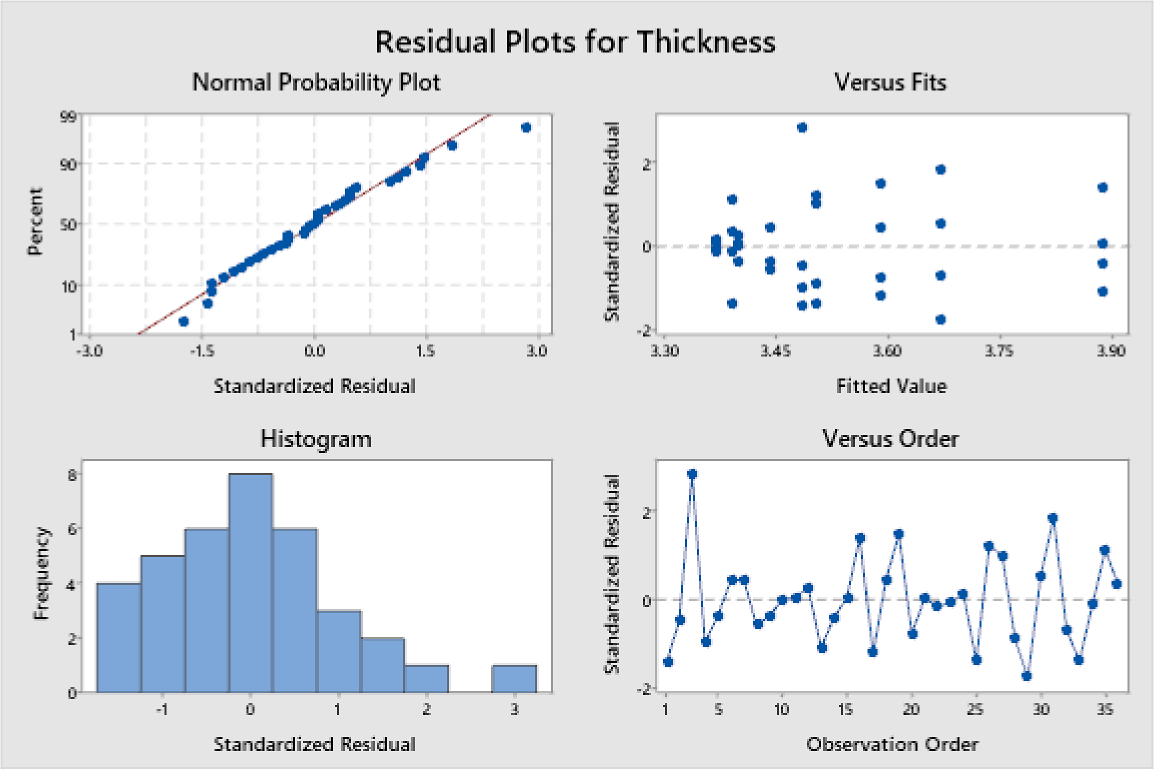

Figure 106: Residual Plots for Thickness vs Feed Rate and Rotational Speed.

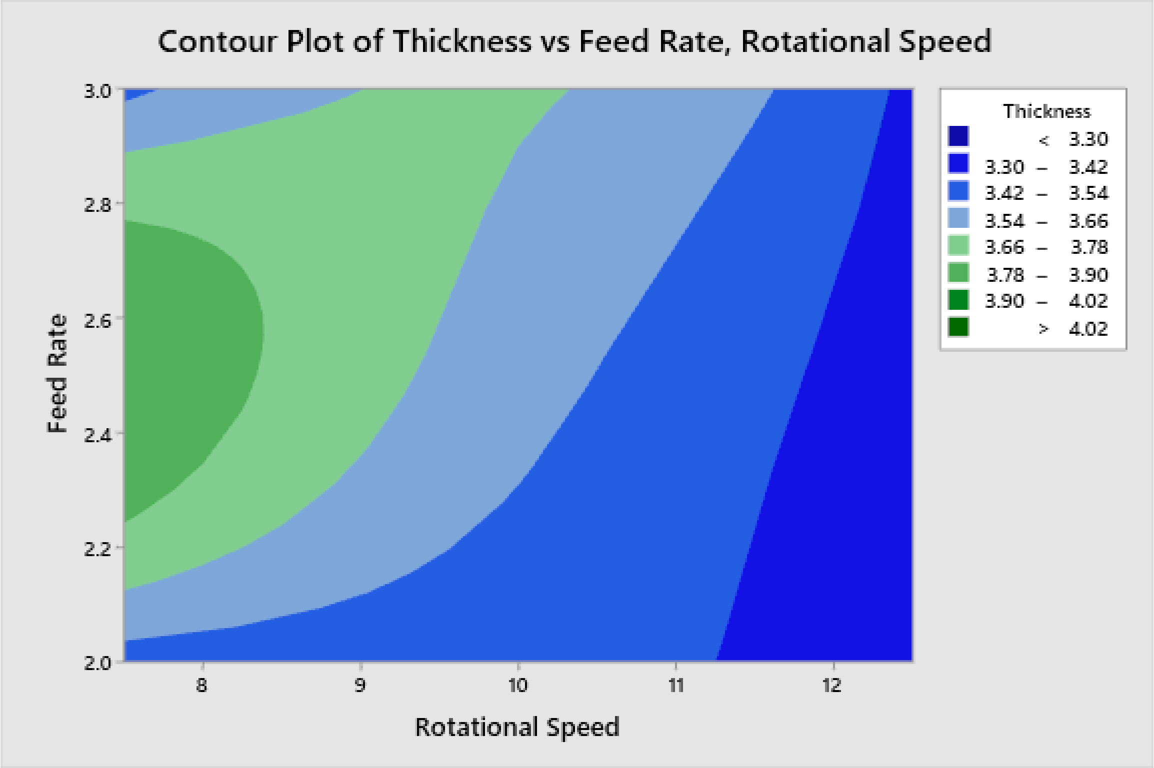

Figure 107: Contour Plot of Thickness vs Feed Rate and Rotational Speed.

4.3.3 Conclusions

Thoroughout this stage, a Design of Experiment analysis was conducted to understand the impact that two key process parameters (feed rate and rotational speed) could have on the deformation behaviour of the workpiece and its final geometry during the process.

The main results from this DOE can be sumarised as follows:

1. Both parameters, including their combinantion have a significant impact on the final geometry of the workpiece (thickness). This means that in order to prevent or reduce deviations from the sine law the adequate set of parameters must be selected when processing a new workpiece.
2. None of the process parameters had a significant effect on the principal strain values of the workpiece. This indicates that the level of deformation itself is not affected by these parameters, however this is not the case for the deformation behaviour. The combination of the feed rate and the rotational speed does have an impact on the deviation from the simple shear deformation mechanism of the material.

From this remarks, it is possible to conclude that a small variation of these process parameters should not have a big impact on the possible failure by fracture of a given material, but if not selected appropriately the final thickness of the workpieces would not obey the sine law and the deformation mechanism could have large deviations from ideal simple shear. These conditions could cause complex stress states that could lead to wrinkling or bending of the workpiece as described in the literature [16].

Finally, it is suggested to run a quick DOE and use contour plot charts for the selection of optimal process parameters when attempting to start a new shear forming operation. Contour plot charts provide a good representation of the response distribution when combining two different variables. For example, if a selection of parameters had to be done from this DOE, it would be suggested to start real-life trials with a feed rate of 2.0 mm/s and a rotational speed of 11.5 rad/s. This selection was done after observing the contour plots of the thickness and the strain’s ratio, since this combination of parameters offers the lower deviations from the sine law and the simple shear rule.

4.4 Stage 3: FEM Model for Texture Prediction

Since the main objective of this stage is to further validate the basic FEM model developed in stage 1 and to prevent further complications with the selection of process parameters, real life data parameters were introduced into this model. This would allow to compare any results obtained with the model against the experimental results obtained in Chapter 3. The material selected for this stage was Jethete M152. It was decided to not use Inconel 718 for texture predictions because the samples provided for the experimental work had already been heat treated causing an impact on its texture, which means comparing against simulated textures that only take into consideration plastic deformation would not be adequate. Also, Timetal 54M was not used for two main reasons; 1. Timetal 54M is an HCP material and the software used in this project only work for FCC and BCC materials, 2. It was not possible to analyse the texture of this material in chapter 3 so there would not be point of comparison even if texture was simulated using any other software.

4.4.1 Model Set-Up

For this model, the same general layout, mesh type, temperature and heat transfer definition, friction values and tool definition were kept and only the material data and process parameters were changed. Table 18 and Table 19 show the input process parameters and material constants according to the power law defined in section 4.2.2, respectively. The material data was taken from a previous work conducted by Perez [63], who studied the impact of several heat treatments on the flow stress behaviour of this alloy at room temperature. As stated by the supplier, the material used in this project was hot rolled and annealed at 780 ˚C plus air cooled. Based on this, the flow stress data from material with the heat treatment with the most similar conditions was selected, which was annealing at 700 ˚C plus air cooling. It is important to note that when this thesis was written, no clear data was found in the literature regarding flow stress behaviour of this alloy at different strain rates or other test temperatures like with stainless steel AISI 316. For this reason strain rate and temperature sensitivity were not taken into consideration for this stage of project.

The step size was changed to be suitable for speed of this model. Since tools are moving faster than in the original model the step size had to be reduced to 2.5 x 10-5 s/step to prevent the model from having convergence and contact issues. The total number of steps performed was 20,000 and this was selected based on the method explained in section 4.2.3. The mesh size of this simulation was 15360 elements with 19800 nodes and the typical solving time was around 139 hours.

Table 18: Shear forming model parameters. This experimental data was provided by the supplier (Refer to Chapter 3)

Input Parameters	**Name/Value**
Material	Jethete M152
Workpiece Surface Speed	300 m/min
Feed rate	0.5 mm/rev
Mandrel Angle	50 degrees
Material Thickness	5 mm

Table 19: Material data for Jethete M152 alloy. Flow stress data constructed from tensile test at room temperature of annealed Jethete M152 specimens [63].

		Jethete M152
Elastic Data	Young's Modulus	213 GPa
	Yield strength (y)	624 MPa
Plastic Data	Strength Coefficient (k)	1175 MPa
	Work-hardening exponent (n)	0.114

4.4.2 Texture Simulation Process

The texture in the mandrel and roller zones was simulated using the software MTMTAY. To do this, the strain values for every step of two points corresponding to each zone were extracted from the Deform database and processed before they could be used in MTMTAY. The strain rate tensors at each of the 20,000 steps were calculated using Equation 25. Later the amount of steps was condensed to 100 using an in-house Matlab code developed by MEng Jan Safranek [110], so that this data could be introduced into MTMTAY which can only perform up to 100 steps per simulation.

The calculated values of the strain rate tensor components at each step defined for the texture simulation are shown in Table 20 and Table 21.

$$\dot{\varepsilon}_{ij} = \frac{\Delta\varepsilon_{ij}}{t} = \frac{\varepsilon_{ij\ at\ step\ n} - \varepsilon_{ij\ at\ step\ n-1}}{Time\ per\ step}$$

Equation 25

$$\dot{\varepsilon}_{ij} = \begin{bmatrix} \dot{\varepsilon}_{xx} & \dot{\varepsilon}_{xy} & \dot{\varepsilon}_{xz} \\ \dot{\varepsilon}_{yx} & \dot{\varepsilon}_{yy} & \dot{\varepsilon}_{yz} \\ \dot{\varepsilon}_{zx} & \dot{\varepsilon}_{zy} & \dot{\varepsilon}_{zz} \end{bmatrix}$$

Equation 26

Two independent .TEN files were created with these data and introduced to MTMTAY as well as the strain step, which was calculated based on the highest accumulated effective plastic strain ($\bar{\varepsilon}$) at the end of the 20,000 steps (see Equation 27). This generated the final texture in each zone after the 100 steps defined. Finally, MTMTAY generated a .SMT file containing the values of the Euler angles of the final texture. This file had to be converted to .CTF using a simple MATLAB code to rearrange the information in a format that could be recognised by the software Channel 5. This software was also used in Chapter 3 to analyse the experimental textures of the materials provided. Using Channel 5 and the files containing the Euler angles, it was possible to generate the pole figures of the textures simulated. Figure 108 shows a summary of the texture simulation process described in this section and a more detailed description of this process can be found in Appendix 1.

$$Strain\ step = \frac{\bar{\varepsilon}}{100\ steps} = \frac{1.18}{100\ steps} = 0.0118\ step^{-1}$$

Equation 27

Table 20: Strain Rate Tensor components for point in the Mandrel zone.

Step	$\dot{\varepsilon}_{xx}$	$\dot{\varepsilon}_{xy}$	$\dot{\varepsilon}_{xz}$	$\dot{\varepsilon}_{yx}$	$\dot{\varepsilon}_{yy}$	$\dot{\varepsilon}_{yz}$	$\dot{\varepsilon}_{zx}$	$\dot{\varepsilon}_{zy}$	$\dot{\varepsilon}_{zz}$
1	-0.010	-0.048	-0.078	0.048	0.039	-0.011	0.078	0.011	-0.029
2	1.197	-9.187	-4.933	9.187	-1.877	-7.285	4.933	7.285	0.680
3	5.084	-14.391	-4.819	14.391	-10.282	-6.307	4.819	6.307	5.198
4	13.821	-21.970	1.101	21.970	-21.596	3.905	-1.101	-3.905	7.776
5	16.520	-31.478	11.593	31.478	-25.838	19.169	-11.593	-19.169	9.318
6	0.008	-0.068	0.052	0.068	0.018	0.063	-0.052	-0.063	-0.026
7	-1.219	-3.216	-3.521	3.216	3.539	0.758	3.521	-0.758	-2.320
8	-0.475	-21.591	-7.076	21.591	6.704	-7.806	7.076	7.806	-6.229
9	1.778	-36.136	-9.298	36.136	1.999	-24.493	9.298	24.493	-3.777
10	-4.595	-25.657	-4.175	25.657	3.357	-9.227	4.175	9.227	1.238
11	-2.072	-50.755	-5.133	50.755	-3.846	-13.640	5.133	13.640	5.918
12	3.041	-36.215	1.021	36.215	-10.228	-10.501	-1.021	10.501	7.187
13	4.743	-42.973	3.461	42.973	-14.407	-2.379	-3.461	2.379	9.664
14	9.007	-54.803	6.880	54.803	-23.397	8.831	-6.880	-8.831	14.391
15	15.035	-68.171	9.998	68.171	-31.365	28.663	-9.998	-28.663	16.331
16	-0.185	-16.751	5.203	16.751	-2.524	11.075	-5.203	-11.075	2.708
17	0.013	-0.061	0.040	0.061	0.036	0.061	-0.040	-0.061	-0.049
18	-2.871	-1.154	-2.729	1.154	4.784	1.502	2.729	-1.502	-1.913
19	-5.613	-12.021	-6.523	12.021	11.481	-1.911	6.523	1.911	-5.868
20	-3.415	-22.709	-8.182	22.709	6.648	-15.910	8.182	15.910	-3.233
21	-8.337	-24.428	-5.426	24.428	7.497	-13.028	5.426	13.028	0.841
22	-6.182	-35.339	-1.340	35.339	1.780	-10.779	1.340	10.779	4.402
23	-0.571	-38.746	0.776	38.746	-7.119	-12.147	-0.776	12.147	7.690
24	-2.341	-46.637	4.442	46.637	-8.511	-7.007	-4.442	7.007	10.852
25	5.642	-55.011	11.316	55.011	-21.108	10.069	-11.316	-10.069	15.466
26	0.448	-29.062	10.738	29.062	-6.088	13.336	-10.738	-13.336	5.640
27	-2.664	-12.829	5.451	12.829	1.840	9.771	-5.451	-9.771	0.823
28	-0.007	-0.011	0.002	0.011	0.067	0.041	-0.002	-0.041	-0.060
29	-4.131	-0.560	-3.867	0.560	7.196	2.036	3.867	-2.036	-3.065
30	-5.631	-15.552	-7.932	15.552	11.804	-10.050	7.932	10.050	-6.173
31	-7.616	-21.576	-9.376	21.576	10.346	-17.352	9.376	17.352	-2.731
32	-8.290	-24.694	0.169	24.694	7.056	-8.107	-0.169	8.107	1.235
33	-3.219	-56.907	5.053	56.907	-1.643	-10.269	-5.053	10.269	4.862
34	-6.236	-111.865	7.484	111.865	-7.310	-10.469	-7.484	10.469	13.546
35	-2.509	-111.196	12.544	111.196	-13.309	-8.883	-12.544	8.883	15.818
36	-3.172	-54.195	14.925	54.195	-4.479	2.782	-14.925	-2.782	7.651
37	-2.780	-62.988	17.653	62.988	-5.674	18.668	-17.653	-18.668	8.454
38	-6.946	-60.985	16.985	60.985	0.055	22.267	-16.985	-22.267	6.891
39	-5.001	-28.184	7.104	28.184	1.865	11.624	-7.104	-11.624	3.137
40	-0.304	-8.829	1.729	8.829	1.549	3.700	-1.729	-3.700	-1.245
41	-0.099	0.008	-0.046	-0.008	0.138	0.037	0.046	-0.037	-0.038

42	-9.143	-13.044	-5.981	13.044	14.098	0.647	5.981	-0.647	-4.955
43	-14.668	-40.565	-9.254	40.565	19.718	-10.998	9.254	10.998	-5.050
44	-15.924	-62.698	-9.496	62.698	19.395	-23.514	9.496	23.514	-3.470
45	-14.330	-36.011	-4.537	36.011	14.576	-11.828	4.537	11.828	-0.246
46	-22.793	-62.665	-3.775	62.665	21.368	-10.272	3.775	10.272	1.426
47	-28.779	-132.269	-2.638	132.269	24.249	-16.786	2.638	16.786	4.530
48	-26.260	-121.116	1.762	121.116	19.634	-18.339	-1.762	18.339	6.626
49	-11.072	-92.659	5.423	92.659	3.474	-16.533	-5.423	16.533	7.597
50	-9.064	-55.085	5.758	55.085	2.763	-5.358	-5.758	5.358	6.301
51	-14.965	-65.170	8.167	65.170	6.906	3.657	-8.167	-3.657	8.060
52	-21.575	-129.943	13.160	129.943	8.769	24.659	-13.160	-24.659	12.806
53	-22.370	-105.540	10.402	105.540	13.492	26.274	-10.402	-26.274	8.878
54	-9.250	-30.194	6.060	30.194	6.168	9.227	-6.060	-9.227	3.082
55	-12.055	-29.068	6.421	29.068	12.475	15.557	-6.421	-15.557	-0.420
56	-0.072	0.046	-0.022	-0.046	0.113	0.036	0.022	-0.036	-0.041
57	-10.120	-1.101	-5.058	1.101	13.323	3.188	5.058	-3.188	-3.202
58	-21.287	-24.981	-11.694	24.981	26.995	-5.566	11.694	5.566	-5.708
59	-16.742	-31.679	-8.844	31.679	17.479	-11.690	8.844	11.690	-0.737
60	-21.991	-27.381	-7.454	27.381	21.847	-7.211	7.454	7.211	0.144
61	-40.607	-74.521	-8.358	74.521	38.342	-12.271	8.358	12.271	2.265
62	-23.618	-72.684	1.235	72.684	19.368	-11.931	-1.235	11.931	4.250
63	-15.498	-50.386	2.913	50.386	10.226	-7.248	-2.913	7.248	5.272
64	-21.015	-52.312	4.573	52.312	13.758	-2.874	-4.573	2.874	7.256
65	-34.536	-112.558	14.278	112.558	20.300	5.662	-14.278	-5.662	14.236
66	-23.546	-50.340	12.906	50.340	16.390	7.516	-12.906	-7.516	7.156
67	-10.950	-18.106	6.699	18.106	8.188	7.066	-6.699	-7.066	2.762
68	-0.061	-0.016	0.025	0.016	0.089	0.053	-0.025	-0.053	-0.028
69	-4.426	1.359	-2.281	-1.359	6.388	0.815	2.281	-0.815	-1.961
70	-7.959	-30.891	-5.549	30.891	12.379	-6.682	5.549	6.682	-4.420
71	-9.402	-43.223	-6.607	43.223	9.934	-8.135	6.607	8.135	-0.532
72	-13.607	-49.559	-4.735	49.559	13.592	-7.865	4.735	7.865	0.015
73	-13.480	-57.479	-1.997	57.479	13.287	-3.739	1.997	3.739	0.193
74	-10.575	-76.505	-3.840	76.505	7.429	-1.099	3.840	1.099	3.146
75	-13.026	-102.472	-4.305	102.472	5.649	0.640	4.305	-0.640	7.377
76	-15.450	-103.047	-1.981	103.047	6.565	0.195	1.981	-0.195	8.885
77	-19.534	-130.215	1.499	130.215	9.240	1.537	-1.499	-1.537	10.294
78	-12.552	-58.429	3.649	58.429	8.569	5.674	-3.649	-5.674	3.982
79	-10.159	-52.453	2.554	52.453	6.483	10.053	-2.554	-10.053	3.677
80	-7.050	-27.263	2.648	27.263	4.700	6.430	-2.648	-6.430	2.351
81	-0.069	0.008	-0.012	-0.008	0.092	0.052	0.012	-0.052	-0.024
82	-6.338	-5.437	-2.742	5.437	8.167	0.806	2.742	-0.806	-1.830
83	-12.931	-38.692	-8.304	38.692	15.409	-3.780	8.304	3.780	-2.478
84	-12.793	-33.619	-5.695	33.619	13.284	-4.638	5.695	4.638	-0.490
85	-15.817	-47.597	-3.308	47.597	14.446	-2.473	3.308	2.473	1.372

86	-21.210	-81.545	-4.659	81.545	18.203	-2.148	4.659	2.148	3.007
87	-19.983	-78.923	-3.352	78.923	16.209	-2.246	3.352	2.246	3.774
88	-16.253	-87.231	1.463	87.231	9.267	-3.875	-1.463	3.875	6.986
89	-14.904	-31.383	3.524	31.383	12.025	2.463	-3.524	-2.463	2.879
90	-17.183	-49.773	3.703	49.773	13.670	7.857	-3.703	-7.857	3.512
91	-5.151	-15.034	3.139	15.034	4.780	3.033	-3.139	-3.033	0.371
92	-0.110	0.094	-0.039	-0.094	0.138	0.048	0.039	-0.048	-0.028
93	-12.961	-20.237	-9.138	20.237	15.501	0.663	9.138	-0.663	-2.540
94	-4.918	-12.935	-2.496	12.935	4.674	0.614	2.496	-0.614	0.244
95	-6.413	-31.528	-1.365	31.528	4.474	3.941	1.365	-3.941	1.939
96	-8.576	-34.589	-0.364	34.589	5.226	9.231	0.364	-9.231	3.350
97	-0.032	-0.106	-0.019	0.106	0.033	0.047	0.019	-0.047	-0.001
98	-1.580	-20.830	-5.261	20.830	1.586	1.323	5.261	-1.323	-0.006
99	-3.150	-23.162	-2.338	23.162	1.825	1.817	2.338	-1.817	1.325
100	0.168	-0.426	-0.010	0.426	-0.180	0.047	0.010	-0.047	0.012

Table 21: Strain Rate Tensor components for point selected in the Roller zone.

Step	$\dot{\varepsilon}_{xx}$	$\dot{\varepsilon}_{xy}$	$\dot{\varepsilon}_{xz}$	$\dot{\varepsilon}_{yx}$	$\dot{\varepsilon}_{yy}$	$\dot{\varepsilon}_{yz}$	$\dot{\varepsilon}_{zx}$	$\dot{\varepsilon}_{zy}$	$\dot{\varepsilon}_{zz}$
1	0.070	-0.195	0.067	0.195	-0.053	-0.035	-0.067	0.035	-0.017
2	4.600	-38.164	-15.645	38.164	5.353	-34.269	15.645	34.269	-9.953
3	16.957	-43.748	-13.204	43.748	-12.899	-30.682	13.204	30.682	-4.058
4	17.453	-66.898	-16.359	66.898	-17.690	-39.050	16.359	39.050	0.236
5	12.359	-50.600	-3.568	50.600	-24.629	-0.547	3.568	0.547	12.270
6	-2.676	-60.721	-1.118	60.721	-8.168	36.083	1.118	-36.083	10.844
7	1.557	-13.732	4.999	13.732	-4.324	27.595	-4.999	-27.595	2.766
8	0.038	-0.105	0.104	0.105	-0.001	0.006	-0.104	-0.006	-0.037
9	2.394	-62.708	-17.819	62.708	15.263	-38.314	17.819	38.314	-17.657
10	16.193	-66.133	-34.216	66.133	5.790	-88.778	34.216	88.778	-21.983
11	13.143	-48.865	-15.872	48.865	1.587	-46.452	15.872	46.452	-14.730
12	7.168	-167.547	-21.959	167.547	-0.121	-69.786	21.959	69.786	-7.047
13	26.818	-150.234	-16.614	150.234	-37.463	-93.853	16.614	93.853	10.645
14	18.357	-93.349	-3.655	93.349	-35.041	-47.950	3.655	47.950	16.684
15	-4.852	-87.248	-0.074	87.248	-11.346	-5.098	0.074	5.098	16.199
16	-11.839	-104.056	10.623	104.056	-4.989	36.846	-10.623	-36.846	16.827
17	2.156	-58.850	26.193	58.850	-20.910	59.297	-26.193	-59.297	18.755
18	0.206	-16.489	9.286	16.489	-2.895	29.070	-9.286	-29.070	2.688
19	0.022	-0.144	0.045	0.144	0.008	0.004	-0.045	-0.004	-0.031
20	-3.535	-59.115	-16.544	59.115	22.720	-25.406	16.544	25.406	-19.185
21	7.983	-57.957	-33.044	57.957	6.451	-54.795	33.044	54.795	-14.434
22	10.287	-71.063	-28.503	71.063	11.895	-64.635	28.503	64.635	-22.182
23	-15.097	-146.089	-33.515	146.089	23.089	-65.850	33.515	65.850	-7.992
24	1.457	-108.746	-15.333	108.746	-12.162	-39.765	15.333	39.765	10.705

25	14.007	-118.277	-6.400	118.277	-31.408	-60.247	6.400	60.247	17.401
26	-2.803	-117.354	-5.139	117.354	-12.697	-43.061	5.139	43.061	15.500
27	-26.541	-100.060	10.337	100.060	1.654	41.378	-10.337	-41.378	24.887
28	-3.701	-57.963	26.834	57.963	-12.197	43.394	-26.834	-43.394	15.898
29	1.213	-34.854	22.717	34.854	-10.627	48.607	-22.717	-48.607	9.414
30	-0.012	-0.172	0.027	0.172	0.038	0.039	-0.027	-0.039	-0.026
31	-6.081	-35.152	-5.392	35.152	24.134	7.908	5.392	-7.908	-18.053
32	-8.482	-82.728	-38.009	82.728	29.190	-41.501	38.009	41.501	-20.709
33	4.263	-72.521	-50.973	72.521	19.611	-68.345	50.973	68.345	-23.874
34	-7.358	-92.570	-32.733	92.570	24.156	-49.880	32.733	49.880	-16.798
35	-38.424	-118.250	-32.463	118.250	33.470	-36.688	32.463	36.688	4.954
36	-31.828	-160.708	-33.559	160.708	20.825	-54.993	33.559	54.993	11.004
37	-0.693	-148.812	-15.793	148.812	-22.850	-76.449	15.793	76.449	23.543
38	-28.917	-130.531	-1.407	130.531	-0.377	-17.804	1.407	17.804	29.294
39	-38.756	-90.283	23.653	90.283	14.302	52.284	-23.653	-52.284	24.454
40	-24.827	-92.331	27.029	92.331	4.663	40.468	-27.029	-40.468	20.164
41	3.420	-66.378	44.969	66.378	-25.871	62.773	-44.969	-62.773	22.451
42	-1.910	-1.020	1.984	1.020	5.739	14.986	-1.984	-14.986	-3.829
43	-0.012	-0.212	0.018	0.212	0.048	0.018	-0.018	-0.018	-0.035
44	-9.946	-38.673	-12.785	38.673	27.221	-1.766	12.785	1.766	-17.274
45	-13.244	-87.880	-48.261	87.880	38.981	-47.334	48.261	47.334	-25.737
46	7.130	-69.929	-47.720	69.929	11.364	-53.798	47.720	53.798	-18.494
47	-26.804	-100.376	-41.223	100.376	37.268	-44.797	41.223	44.797	-10.464
48	-67.651	-156.838	-56.268	156.838	59.691	-54.472	56.268	54.472	7.960
49	-55.749	-197.067	-53.113	197.067	39.674	-71.105	53.113	71.105	16.075
50	-8.175	-127.462	-13.334	127.462	-16.441	-24.362	13.334	24.362	24.616
51	-30.773	-118.094	1.006	118.094	7.346	7.729	-1.006	-7.729	23.427
52	-52.612	-110.379	26.317	110.379	24.142	47.916	-26.317	-47.916	28.470
53	-38.310	-117.720	28.906	117.720	7.709	47.656	-28.906	-47.656	30.601
54	-2.622	-43.879	39.838	43.879	-4.489	51.648	-39.838	-51.648	7.111
55	-0.067	0.025	-0.046	-0.025	0.128	0.079	0.046	-0.079	-0.061
56	-0.215	-11.878	1.618	11.878	2.886	2.387	-1.618	-2.387	-2.671
57	-16.018	-32.980	-16.279	32.980	35.211	-1.679	16.279	1.679	-19.193
58	-12.729	-64.027	-49.993	64.027	30.392	-38.581	49.993	38.581	-17.663
59	-12.059	-77.620	-59.380	77.620	28.962	-39.867	59.380	39.867	-16.903
60	-43.303	-115.576	-65.003	115.576	56.485	-48.922	65.003	48.922	-13.182
61	-66.841	-109.828	-42.097	109.828	48.043	-23.837	42.097	23.837	18.798
62	-54.917	-113.041	-27.343	113.041	41.162	-14.159	27.343	14.159	13.755
63	-38.751	-133.762	-22.264	133.762	23.962	-10.204	22.264	10.204	14.789
64	-49.019	-175.615	-7.551	175.615	27.068	-2.328	7.551	2.328	21.951
65	-55.068	-100.690	37.549	100.690	25.397	43.701	-37.549	-43.701	29.671
66	-29.777	-61.129	27.134	61.129	12.500	32.052	-27.134	-32.052	17.277
67	-14.504	-74.825	53.003	74.825	3.897	51.925	-53.003	-51.925	10.607
68	-0.063	-0.022	-0.049	0.022	0.131	0.010	0.049	-0.010	-0.068

69	-4.160	-17.081	-11.903	17.081	16.632	14.890	11.903	-14.890	-12.472
70	-17.862	-50.883	-62.623	50.883	29.115	-21.890	62.623	21.890	-11.253
71	-23.099	-73.855	-80.754	73.855	41.209	-26.971	80.754	26.971	-18.110
72	-34.710	-69.466	-75.516	69.466	51.604	-15.287	75.516	15.287	-16.894
73	-49.374	-51.729	-38.344	51.729	45.284	-2.709	38.344	2.709	4.090
74	-80.845	-122.972	-55.870	122.972	54.329	-5.341	55.870	5.341	26.516
75	-79.397	-120.962	-50.772	120.962	60.865	1.314	50.772	-1.314	18.531
76	-71.824	-116.446	-31.516	116.446	50.793	16.190	31.516	-16.190	21.031
77	-32.427	-43.127	18.682	43.127	19.085	21.332	-18.682	-21.332	13.342
78	-57.912	-91.956	44.061	91.956	34.010	47.365	-44.061	-47.365	23.901
79	-43.659	-91.853	41.012	91.853	26.977	43.856	-41.012	-43.856	16.682
80	0.002	-0.032	0.028	0.032	0.060	0.058	-0.028	-0.058	-0.061
81	-1.739	-5.755	-2.102	5.755	4.384	0.857	2.102	-0.857	-2.645
82	-11.531	-18.392	-36.407	18.392	24.402	4.777	36.407	-4.777	-12.870
83	-18.275	-41.225	-50.789	41.225	22.930	-17.742	50.789	17.742	-4.656
84	-40.827	-43.481	-35.451	43.481	41.063	-4.298	35.451	4.298	-0.236
85	-62.722	-63.088	-36.161	63.088	46.117	-2.393	36.161	2.393	16.605
86	-34.598	-46.439	3.458	46.439	19.765	21.079	-3.458	-21.079	14.833
87	-43.749	-53.273	6.934	53.273	28.841	12.752	-6.934	-12.752	14.908
88	-31.456	-78.168	52.693	78.168	11.146	34.627	-52.693	-34.627	20.309
89	-0.209	-5.705	12.029	5.705	6.221	10.759	-12.029	-10.759	-6.012
90	-0.065	0.029	-0.082	-0.029	0.117	0.009	0.082	-0.009	-0.051
91	-8.970	-13.582	-23.077	13.582	13.623	1.302	23.077	-1.302	-4.653
92	-30.729	-18.115	-25.199	18.115	28.217	6.400	25.199	-6.400	2.513
93	-19.350	-28.454	-2.270	28.454	12.633	8.706	2.270	-8.706	6.717
94	-30.342	-27.560	7.677	27.560	17.426	13.154	-7.677	-13.154	12.916
95	0.027	-0.021	0.035	0.021	-0.002	0.013	-0.035	-0.013	-0.025
96	-2.706	2.649	-8.030	-2.649	4.965	3.324	8.030	-3.324	-2.259
97	-17.068	1.537	-14.846	-1.537	14.875	7.799	14.846	-7.799	2.193
98	-25.748	-12.339	-10.533	12.339	20.890	10.688	10.533	-10.688	4.857
99	-11.420	-4.413	7.655	4.413	7.825	7.032	-7.655	-7.032	3.595
100	0.345	-0.244	0.071	0.244	-0.302	-0.058	-0.071	0.058	-0.043

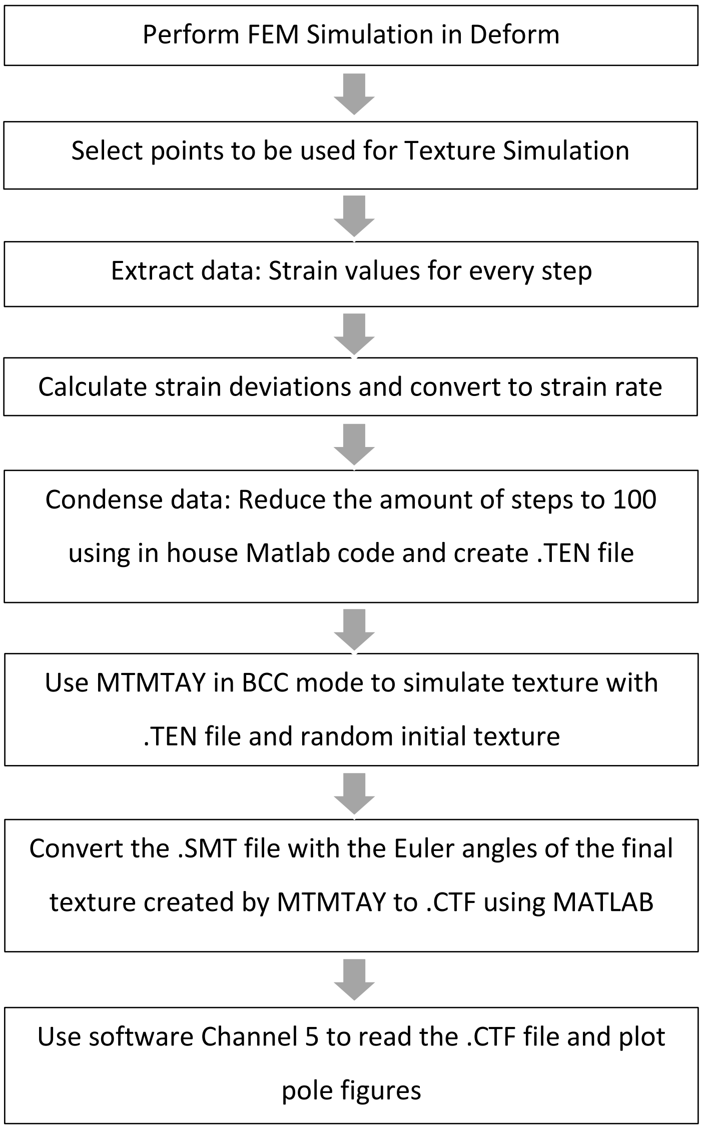

Figure 108: Process for Texture Simulation using Deform and MTMTAY

4.4.3 Results and Discussion

The principal strains' distribution obtained for the Jethete M152 model are shown in Figure 109 and Figure 110. Like in the model shown in stage 1, both principal strains show higher values in the areas near the roller. This means that even though the parameters have changed, the model follows the same behaviour which is an indication that the model set-up has been carried out correctly.

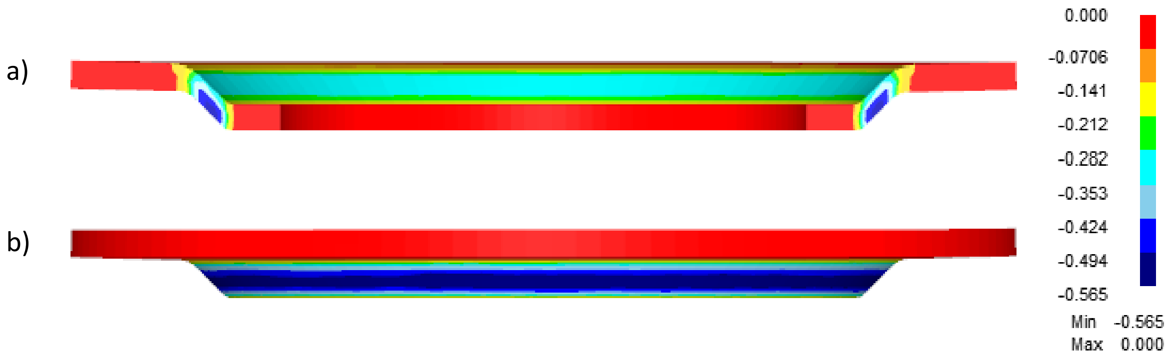

Figure 109: Distribution of Minimum Principal Strain or Minor Strain (mm/mm) along the workpiece at step 30,000: a) Outer. b) Inner surface

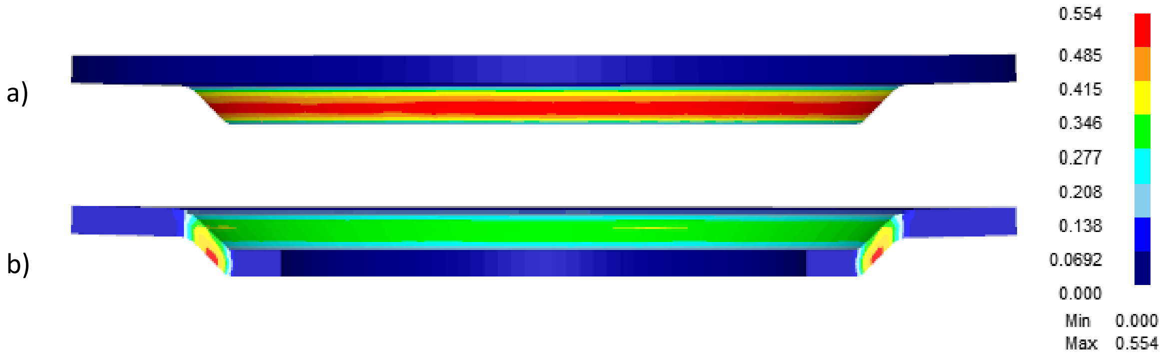

Figure 110: Distribution of Maximum Principal Strain or Major Strain (mm/mm) along the workpiece at step 30,000: a) Outer. b) Inner surface

Using Equation 22 shown in stage 1, the principal strains for ideal simple in-plane simple shear with an angle $\alpha = 50°$ were calculated and are shown in Table 22 along with the values obtained in the FEM model. Like in the initial model, the principal strains' values obtained were higher than ideal simple shear, but the simple shear behaviour was consistent since both principal strains had almost the same magnitude.

Table 22: Principal Strains' values calculated for a mandrel angle $\alpha = 50°$

Ideal Simple Shear	**FEM Model**
$\varepsilon_1 = 0.420$	$\varepsilon_1 = 0.520$
$\varepsilon_2 = -0.420$	$\varepsilon_2 = -0.532$

The poles figures generated with MTMTAY and the initial randomised texture used for the simulations are shown in Figure 111. It is clear that in both the mandrel and the roller zones a visible change in the texture occurred.

As shown in Figure 112, not only the simulated $\{1\ 1\ 0\}$ pole figure of both zones follow the expected pattern after simple shear deformation, they also have similarities with the experimental pole figures obtained in Chapter 3. Like in the experimental results, the pole figures in the roller zone are more intense and the form has better definition than in the mandrel zone. It is also clear that the simulated textures do not have the same level of intensity as the experimental ones and some slight differences can be found between them. This could be caused by several reasons:

1. The number of steps was reduced drastically (from 20,000 to 100 steps) for these simulations leaving little data to analyse with MTMAY.
2. MTMTAY generates an ODF with 1600 orientations, which is very small compared to the ODF obtained with the experimental that had 900,000 orientations each. This small ODF prevents lengthy solving times but could also cause the final pole figures to lack intensity and definition without preventing them from following the correct behaviour.
3. The Taylor-Bishop theory used by MTMTAY makes the assumption that all crystals in the deformed area undergo the same plastic strain [34]. In a process like shear forming, where the deformation is not uniform and larger strains can be found in some areas, this assumption is not correct. Even though this is an important point to take into consideration, it does not represent a major issue for these texture simulations because the analysed areas are very small, meaning that the variation in the plastic strain could be ignored.
4. MTMTAY uses the same strain step for all the 100 steps of the simulation. This does not represent an issue for most forming processes, but for a process like shear forming where the deformation is not continuous and does not have the same level of intensity in every step, this is not an accurate assumption and could cause the shear pattern to lose intensity. Since it is not possible to change this setup in MTMTAY, it is suggested that in the future a software that allows the strain step to be variable is used for more accurate results.

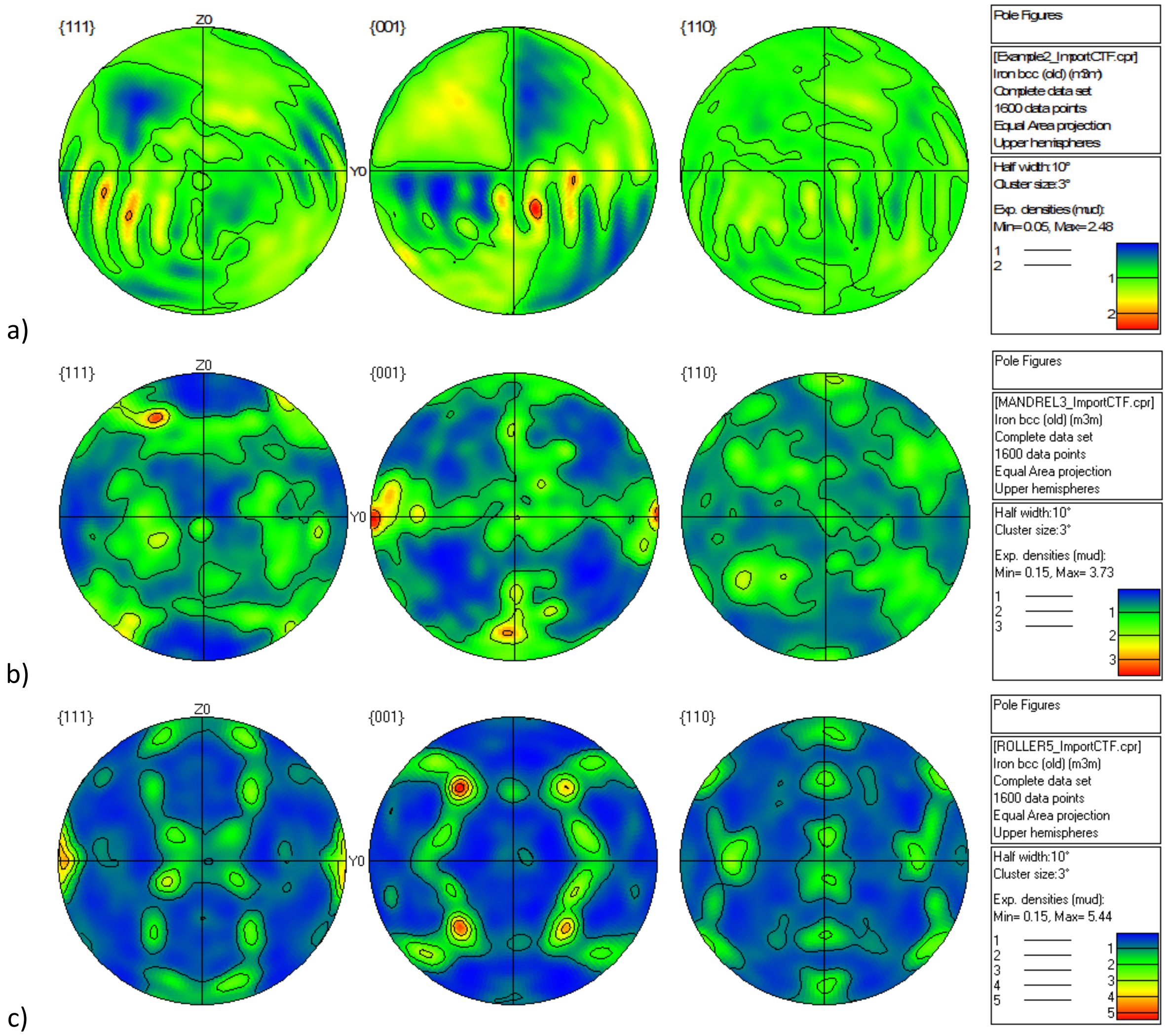

Figure 111: Simulated textures for: a) Initial texture, b) Mandrel zone and c) Roller zone.

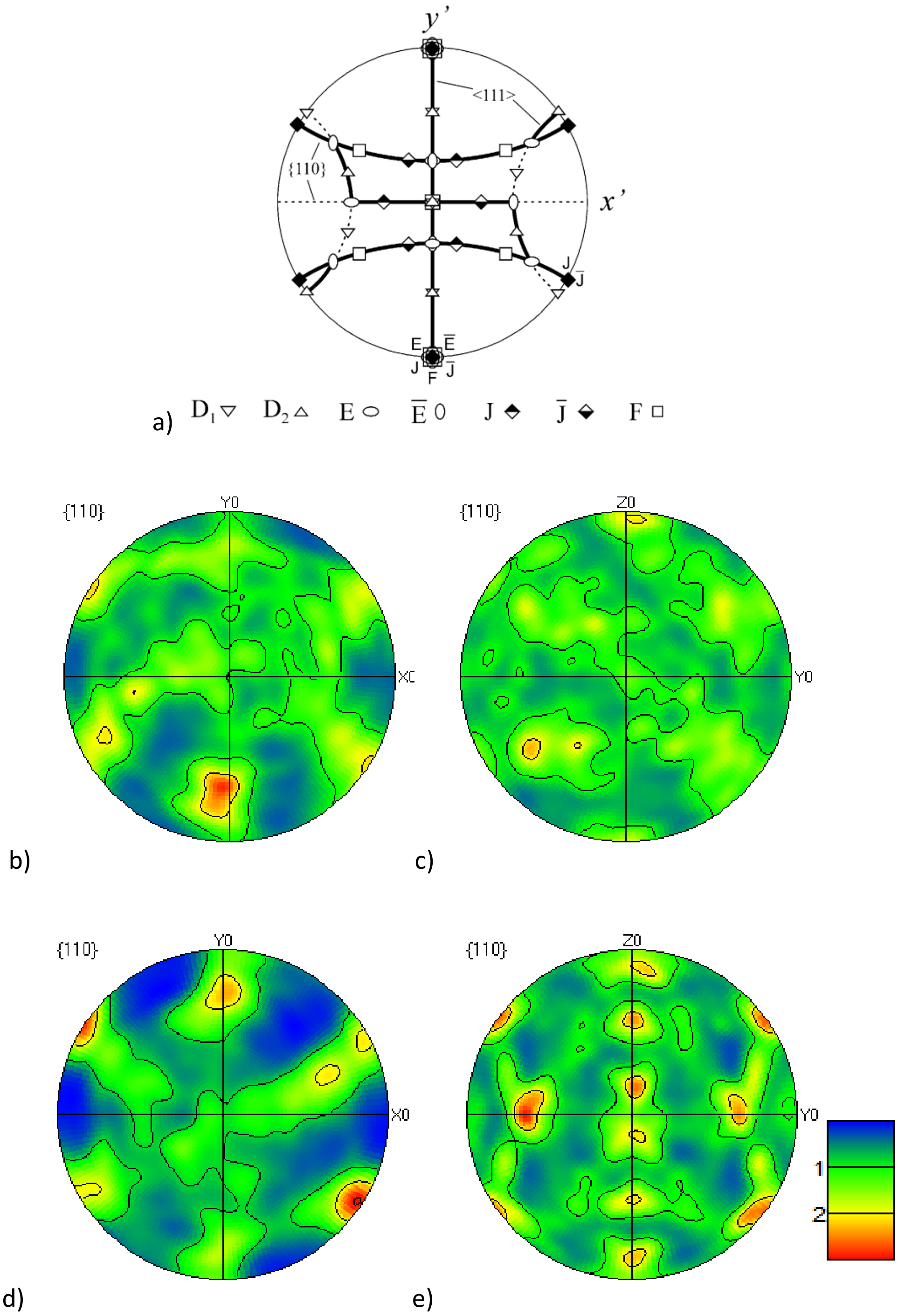

Figure 112: Comparison of simulated textures against ideal theoretical texture and experimental textures. a) Ideal Simple Shear $\{1\ 1\ 0\}$ *pole figure. Mandrel zone textures: b) Experimental, c) Simulated. Roller zone textures: d) Experimental, e) Simulated.*

4.4.4 Conclusions

Throughout this stage, the model developed was tested using experimental parameters for Jethete M152. The initial FEM results were promising, since the strains distribution followed the expected behaviour. The texture was simulated in the two areas of interest investigated in Chapter 3 using the software MTMTAY and the strain rate tensors extracted from the Deform database. The roller and mandrel zone had the expected textures of a material subjected to a deformation mechanism close to simple shear. Like in the experimental results, the simple shear pattern was more defined and intense in the roller zone which indicated that the FEM model does closely resemble the variation in the deformation behaviour throughout the thickness of the workpiece.

Even though the simulated pole figures had the correct behaviour the intensity and pattern definition was lower than in the experimental results. This was caused mainly by the fixed strain step, the reduced number of steps and the small ODF used for the simulations in MTMTAY, due to the limited computational power available for this project and the time restrictions. It is suggested that a different software with the capability to work with larger ODF's, more steps and variable strain steps is used in the future when simulating textures.

An important limitation of this stage is that the flow stress data for this alloy was very limited and does not take into consideration factors like strain rate and temperature sensitivity. It would be ideal to repeat this stage with experimental flow stress data, however due to the time constraints of this research project this was not possible.

Even with the limitations encountered in this stage, it can be concluded that the texture simulations had satisfactory results and the FEM model accurately represents the material deformation behaviour during shear forming.

4.5 Stage 4: Selection of Damage Model

After the model was validated, this stage was designed to study different damage models available in Deform so a method to evaluate a material's shear spinnability could be established based on one of these damage criterions. It is important to mention that for this project's purpose a workpiece is considered to have failed in the simulation after it has started to fracture, so the term damage refers to the accumulated value calculated with the function of each damage model in which any value higher than 1 indicates that the material has initiated fracture.

The Ayada, Normalised Cockcroft & Latham (CL) and the Forming Limit Diagram damage models were initially evaluated using the experimental parameters provided for Timetal 54M. These three damage models were selected because they were readily available in DEFORM and all three are used for the prediction of fracture in metals, however it is suggested that other damage criterions are considered in any future work that are more comprehensible of other types of failure, like bending or wrinkling. This was not done in this project due to time restrictions but is strongly advised to be reviewed if this project is continued.

As mentioned in Chapter 3, the sample provided fractured after 4 revolutions and the main fracture was initially ductile (this means that it is acceptable to use the Ayada and the CL damage models to try to predict this fracture). With this information and the material data provided by the supplier it was possible to evaluate and select the most promising damage model for further studies.

4.5.1 Model Set-Up

The process parameters and material data used for this study are shown in Table 23, Table 24 and Figure 113. All this data was provided by TIMET and all work was conducted at room temperature. No more data is need for the Ayada and Normalised CL models. The Forming Limit Diagram for this alloy is shown in Figure 114 and was provided by TIMET. Due to confidential reasons no information was given by the supplier regarding the construction method of the FLD and the flow stress curve. The mesh size was 24960 elements with 31800 nodes. Finally, the step size was set at 5 x 10^{-5} s/step and a total of 6,650 steps were calculated, which is when 4 complete revolutions have been performed. The typical solving time was 49 hours for these simulations. No additional changes were done to the model set-up described in stage 1.

Table 23: Process Parameters for Timetal 54M shear forming trials.

Parameters	**Name / Value**
Material	Timetal 54M
Rotational speed	300 mm/min
Feed rate	1 mm/rev
Mandrel angle	31.5^o
Blank thickness	4.5 mm

Table 24: Material Data used in Deform, calculated from flow stress curved provided by TIMET.

	Parameters	**Value**
Elastic Data	Young's Modulus	119 GPa
Plastic Data	Yield strength (y)	860 MPa
	Strength Coefficient (k)	950 MPa
	Work-hardening exponent (n)	0.0105

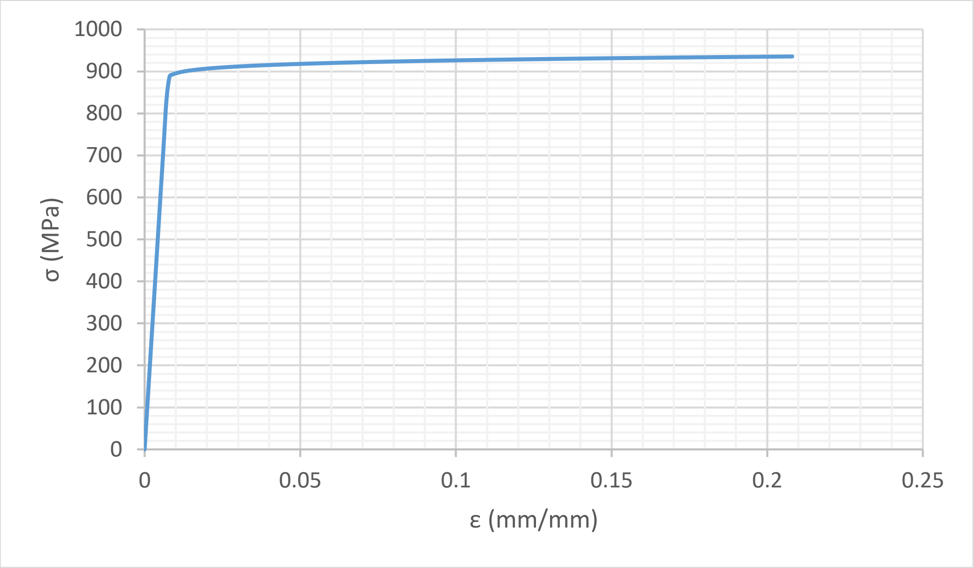

Figure 113: Flow stress curve for Timetal 54M at room temperature provided by TIMET.

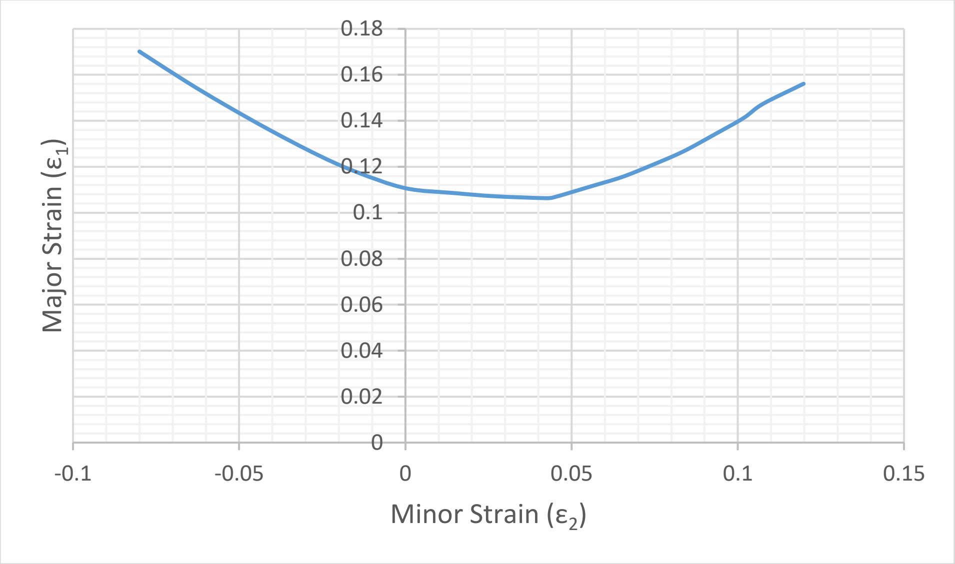

Figure 114: Forming Limit Diagram for Timetal 54M at room temperature provided by TIMET

4.5.2 Results and Discussion

The principal strains distribution obtained after 4 revolutions are shown in Figure 115 and Figure 116. The average strains values in the outer surface were -0.492 for the minimum principal strain and 0.478 for the maximum. For ideal simple shear, the expected principal strain values with $\alpha = 31.5°$ are -0.816 and 0.816 respectively. This means that the sample provided fractured before the workpiece entered the second phase of the process described in the literature, where the initial deformation has been completed and the deformation conditions remain stable and equal during the progress rotation and deformation of the blank [12].

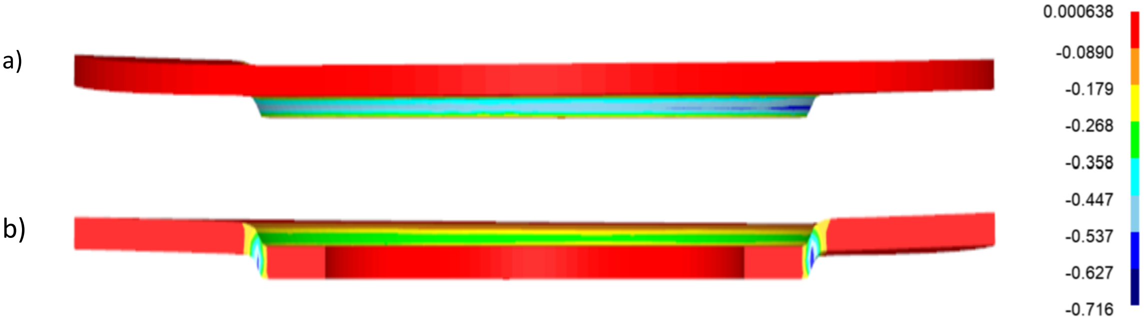

Figure 115: Distribution of Minimum Principal Strain (mm/mm) along the workpiece at step 6,650: a) Outer. b) Inner surface

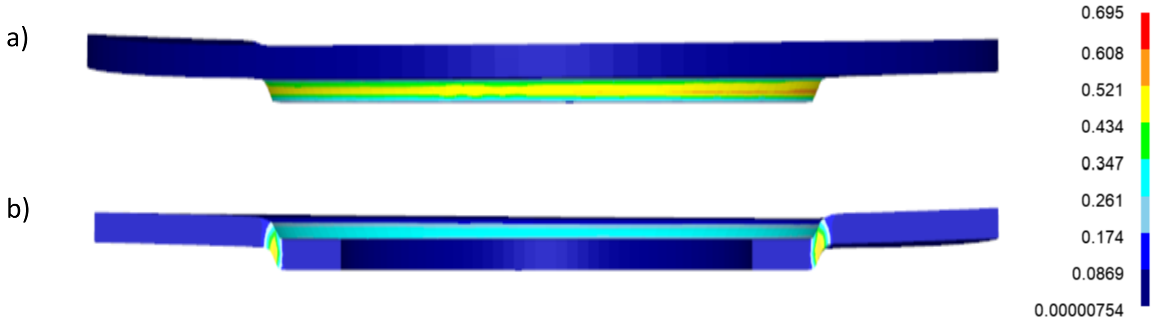

Figure 116: Distribution of Maximum Principal Strain (mm/mm) along the workpiece at step 6,650: a) Outer. b) Inner surface

The damage distributions obtained along the workpiece after 4 revolutions using the three different damage models are shown in Figure 117. As it can be seen, the FLD model was the one that represented the damage distribution more accurately. Both, the normalised CL and Ayada undercalculated the damage with a maximum value of 0.392 and 0.152 respectively, while the FLD was the only one that predicted fracture with a maximum damage factor of 1.14. Additionally the areas with higher damage are those closer to the roller surface, which is in good accordance with the results obtained in the experimental work and the behaviour seen so far in the modelling work shown in stage 1 and 2.

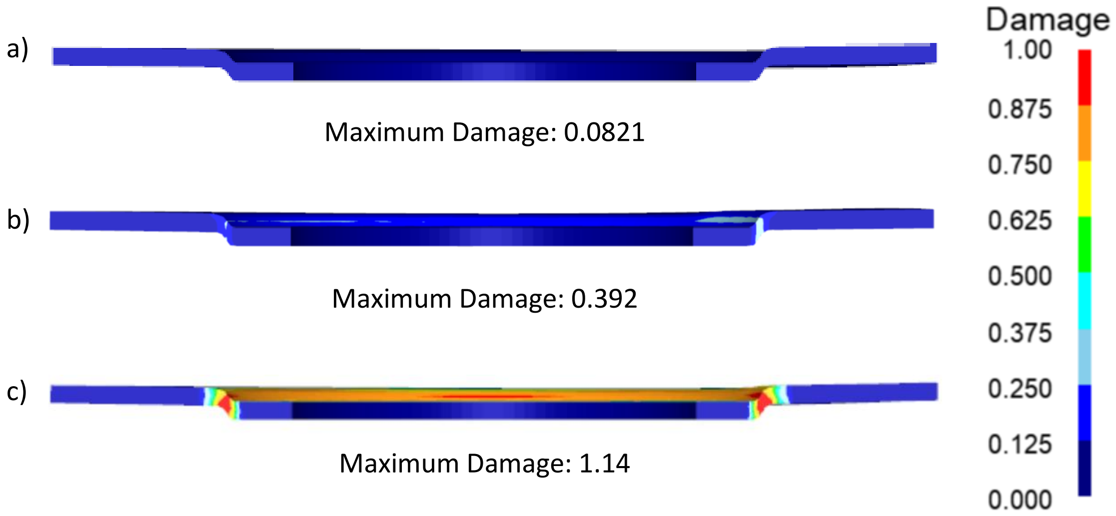

Figure 117: Damage distributions for Timetal 54M model after 4 revolutions. a) Normalised CL, b) Ayada and c) FLD.

Based on these results, the FLD damage criterion was selected for further analysis. Figure 118 shows the principal strains' value obtained compared to the FLD of Timetal 54 M and it is possible to see that this point is far away from the FLD domain. Deform calculates the damage factor with Equation 12 shown in section 2.4.3 and extrapolating the FLD data introduced in the software using a linear equation as follows:

$$\varepsilon_{1Limit} = -0.7521\varepsilon_2 + 0.1074$$

Equation 28

$$\varepsilon_{1Limit} = -0.7521(-0.492) + 0.1074 = 0.477$$

Equation 29

$$D = \frac{\varepsilon_{1Real}}{\varepsilon_{1Limit}} = \frac{0.478}{0.477} = 1.002$$

Equation 30

So the average maximum damage factor in the outer surface of the workpiece is 1.002. Note that even though the maximum damage obtained 1.14, this does not mean that all elements reach this value due to the incremental nature of the process, hence the difference between these two results.

Even though it seems that the damage model is predicting failure accurately since the damage only surpasses the FLD limit after 4 revolutions (See Figure 118), the fact that the strains obtained are way out of the FLD domain indicates that this approach is not entirely adequate. In fact, the correct interpretation of FLD's indicates that any point with a minimum principal strain lower than -0.080 is a failure for this material. This means, that under these conditions according to the FLD data, this material was expected to fail much earlier in the process.

These observations indicate that even though the FLD approach could be used to predict fracture in shear forming, a more adequate construction method must be implemented.

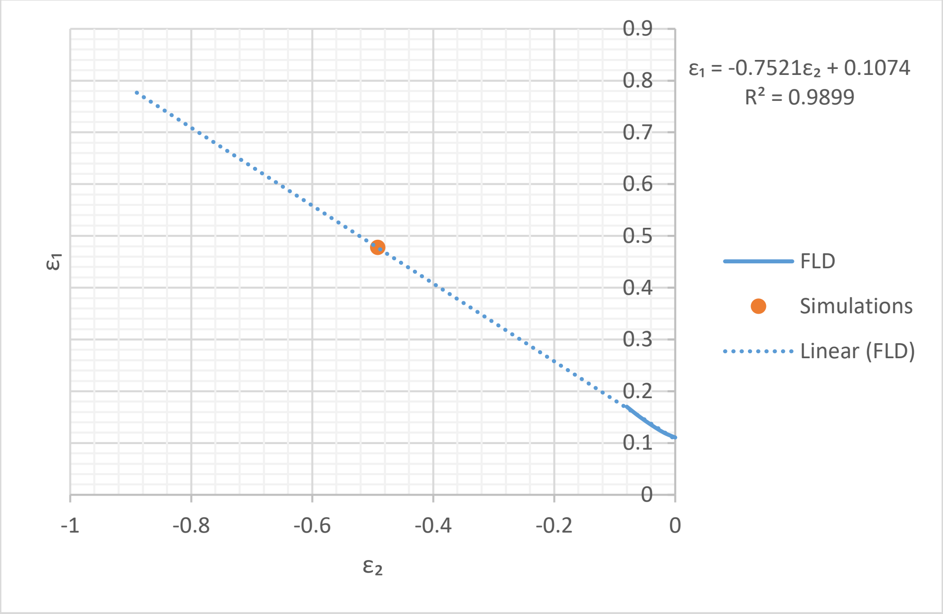

Figure 118: Average Principal Strains obtained in the outer surface of the workpiece against the FLD of Timetal 54M.

4.5.3 Conclusions

Out of the three damage models used in this stage, the FLD model was the one with better results, and it was the only one that predicted that the material would start to fracture after 4 revolutions had been completed. An important remark from this damage model is that the damage factor was calculated using an extrapolation of the FLD curve available, because the strains obtained during the process were all way out of the domain of the FLD. However, this method for calculating damage is not entirely correct since anything than is not under the FLD curve is supposed to indicate failure, which was clearly not the case for this material in shear forming since the workpiece was able to undergo 4 revolutions experimentally and accumulate strain much higher than the limit indicated by the FLD.

Even with these limitations, it was decided to conduct a more detailed analysis of this damage model in the following stage to understand its suitability for incremental forming processes. Since these FLDs are often constructed using conventional forming processes, it may be possible to modify their construction method for its implementation in a methodology for testing shear spinnability of materials. This is discussed in greater detail in stage 5.

The Ayada and normalised CL models were discarded from further analysis since they both undercalculated the damage values by far.

4.6 Stage 5: Evaluation of Damage Criterion

4.6.1 Introduction

In this stage, the accuracy of the damage model selected in stage 4 was tested using the process parameters of the successfully shear formed Inconel 718 workpiece provided for this project and the material data and Forming Limit Diagram of this alloy which are widely available in the literature.

Based on the results obtained, a further analysis of the principal strains' behaviour and the FLD of each material used in this chapter was conducted. Jethete M152 was not included in the analysis because its FLD data was not available. The relationship between the mandrel angle and the maximum principal strain values in the workpiece was compared against the FLD of these materials using the basic FEM model developed in stage 1. Finally, a new concept of FLD and a new alloy was introduced and studied by the end of this stage based on this analysis and a further review of the literature regarding this subject.

4.6.2 Evaluation of FLD damage Criterion

The damage model selected on stage 3 was able to predict failure in Timetal 54M, however it is important to test it with other materials to test its ability to predict correctly when a material can be shear spun or not. Since a fully shear formed sample of Inconel 718 was provided, this was the material selected for the start of this stage.

4.6.2.1 Model Set-Up

The process parameters used for this model are shown in Table 25. In this case the general model set-up was kept as in the other models, however heat transfer was enabled for this simulation. Inconel 718 is an alloy that is well known for its dependency on temperature during deformation [111-113], so dismissing heat transfer during this simulation would mean that important changes during the flow stress behaviour of this material would not be taken into consideration and hence the results would not be as accurate. For this reason, a plastic model that includes the thermal softening of Inconel 718 was selected. It is important to mention, that the main purpose of enabling heat transfer in this stage is to evaluate how temperature could impact the final result of the simulations, however other factors that should also be considered in temperature calculations were not included, like the potential use of coolant during the process and the heat transfer coefficients between the workpiece and tools. This was mainly due to the lack of information provided by the supplier and the funding limitations of this project which meant that even though some missing data could have been obtained experimentally, it was not possible to do it. Even with these limitations, it is expected to gain a general idea of how the temperature changes during the shear forming process of this material. With this information, it can be decided if this variable is relevant for the FE analysis of this specific material and whether it should be considered in any future work.

Table 25: Process parameters used for Inconel 718 FEM model

Input Parameters	Name/Value
Material	Inconel 718
Surface speed	300 m/min
Feed rate	0.5 mm/rev
Mandrel Angle	40 degrees
Material Thickness	6 mm

Initially, the Johnson-Cook constitutive model which defines the flow stress of a material based on its strain hardening, strain rate hardening and thermal softening was considered for this FEM model (see Equation 31) [114]. However, a more comprehensive plastic model developed by Arrazola et al. that also includes the strain softening of the alloy at elevated temperatures (See Equation 32) was selected [113]. The material constants defined by Arrazola et al. for this plastic model for Inconel 718 are shown in Table 26.

$$\sigma = [A + B\varepsilon^n]\left[1 + C\ln\frac{\dot{\varepsilon}}{\dot{\varepsilon}_0}\right]\left[1 - \left(\frac{T - T_0}{T_m - T_0}\right)^m\right]$$

Equation 31

Where, A is the yield stress, B and n represent the effect of the strain hardening, C is the strain rate constant, $\dot{\varepsilon}_0$ is the reference strain rate, T is the work temperature, T_0, is the room temperature, T_m is the melting temperature of the material and m is the effect of the thermal softening.

$$\sigma = \left[A + B\varepsilon^n\left(\frac{1}{e^{\varepsilon^a}}\right)\right]\left[1 + C\ln\frac{\dot{\varepsilon}}{\dot{\varepsilon}_0}\right]\left[1 - \left(\frac{T - T_0}{T_m - T_0}\right)^m\right]\left\{\left[1 - \left(\frac{T}{T_m}\right)^d\right] + \left(\frac{T}{T_m}\right)^d\left[\tanh\frac{1}{\left(\varepsilon + \left(\frac{T}{T_m}\right)^b\right)^r}\right]^s\right\}$$

Equation 32

Where, d, r and s represent the effect of the strain softening.

It is also important to note that the material used by Arrazola et al. to construct this model was also heat treated at around 950 ˚C and water quenched, like the samples used in this project. This makes the selection of this flow stress model even more accurate.

The thermal conductivity coefficient of this alloy is strongly dependant on the temperature of the material, and can be described by Equation 33 [115].

$$k = 11.45 + 1.156x10^{-2}T + 7.272x10^{-6}T^2$$

Equation 33

The elastic data and thermal expansion coefficient was directly taken from the Deform database and it can be seen in Table 27 and Table 28. This data was in accordance to the found in the literature [116-118].

Table 26: Material constants for the modified Johnson-Cook model of Inconel 718 [113]

Parameter	Value
A	1300 MPa
B	1100 MPa
n	0.652
a	50
C	0.0134
$\dot{\varepsilon}_0$	1.000 s^{-1}
T_0	25 ˚C
T_m	1297 ˚C
d	0.450
D	0.110
b	0.100
r	0.200
s	-0.500
m	1.300

Table 27: Elastic data for Inconel 718 [57].

Temperature	Young’s modulus
20 ˚C	217 GPa
870 ˚C	156 GPa

Table 28: Thermal expansion coefficient of Inconel 718 [57].

Temperature Range	Thermal Expansion Coefficient
25 ˚C to 100 ˚C	1.31×10^{-5}/˚C
25 ˚C to 200 ˚C	1.35×10^{-5}/˚C
25 ˚C to 400 ˚C	1.41×10^{-5}/˚C
25 ˚C to 500 ˚C	1.43×10^{-5}/˚C
25 ˚C to 760 ˚C	1.58×10^{-5}/˚C

The Forming Limit Diagram used for this model is shown in Figure 121. It was constructed by Prasad et al. [119] using the stretch forming test with various specimen geometries (see Figure 119) at room temperature. The test parameters and setup are shown in Figure 120. The construction of the FLD was done as follows:

1. A pattern of circles was drawn in all specimens.
2. The specimens were deformed until they failed either by necking or fracture
3. The circles after the test became ellipses and their diagonals were measured.
4. The principal strains were calculated using these diagonals and plotted.
5. The FLD was drawn based on the plot obtained in step 4.

Finally, the mesh size was 11880 elements with 16320 nodes. The step size was set at 1.0×10^{-4} s/step and a total of 20,000 steps were calculated based on the method described in section 4.2.3. The typical solving time of this model was 270 hours.

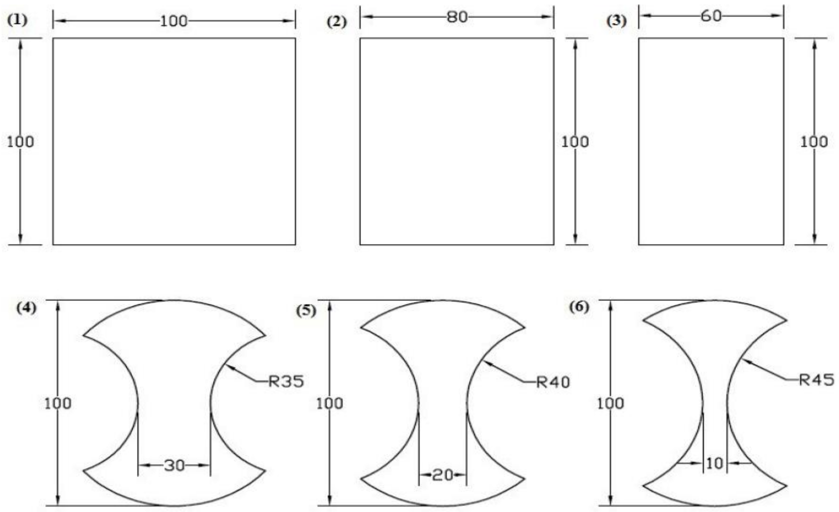

Figure 119: Specimens used by Prasad et al. to construct FLD. (1-3) Specimens for tension-tension domain. (4-6) Specimens for tension-compression domain. Note: All dimensions are in mm. The thickness of all specimens was 1.25 mm and all specimens were cut along the rolling direction. Four specimens were cut for each geometry [119]

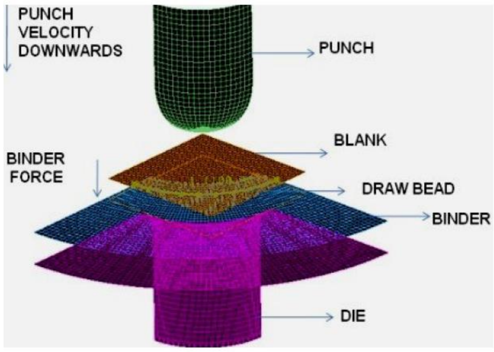

a)

b)

Parameter	Value
Punch diameter	50 mm
Outer die diameter	180 mm
Inner die diameter	54 mm
Binder diameter	72 mm
Punch speed	10 mm/min

Figure 120: Stretch Forming Test. a) Test arrangement. b) Test parameters. [119]

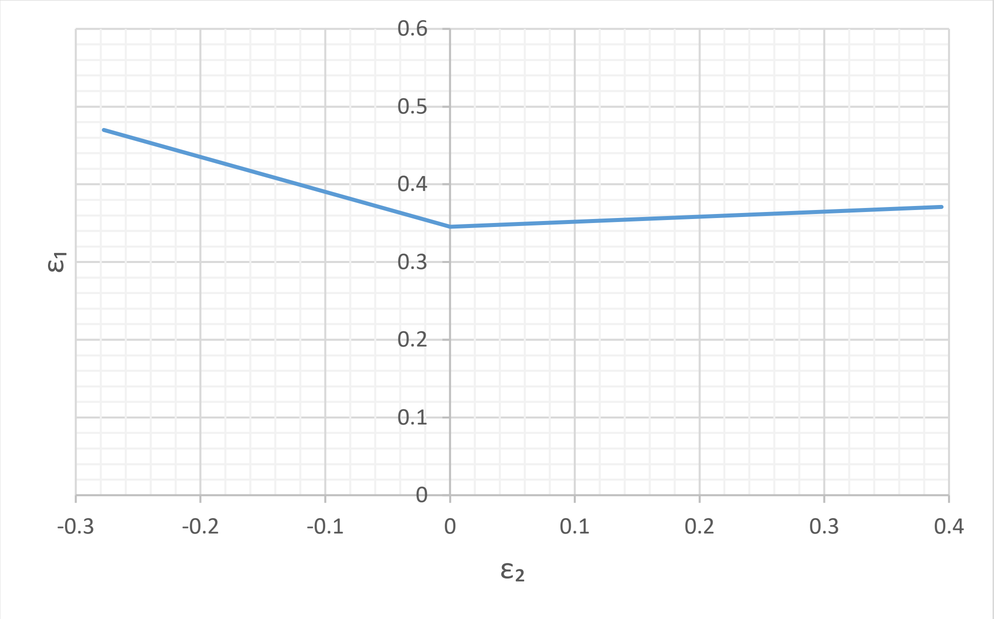

Figure 121: Forming Limit Diagram of Inconel 718. [119]

4.6.2.2 Results and Discussion

The principal strains' distribution obtained in this model are shown in Figure 122 and Figure 123. The average maximum and minimum values in the workpiece compared against ideal simple shear with an angle $\alpha = 40°$ are shown in Table 29 and it is possible to see that for this material both values were very similar indicating that the ideal simple shear condition was fulfilled. The damage distribution obtained with Deform are also shown in Figure 129. The maximum damage factor obtained was 1.42 and in general all the deformed area (including the inner and outer surface) had values higher than 1.07. This result was not expected and a further analysis of the damage calculations is conducted in this section. Finally, the temperature distribution of the workpiece was also included in the results to be able to evaluate the importance of temperature calculations for materials with high temperature sensitivity like Inconel 718 (See Figure 125).

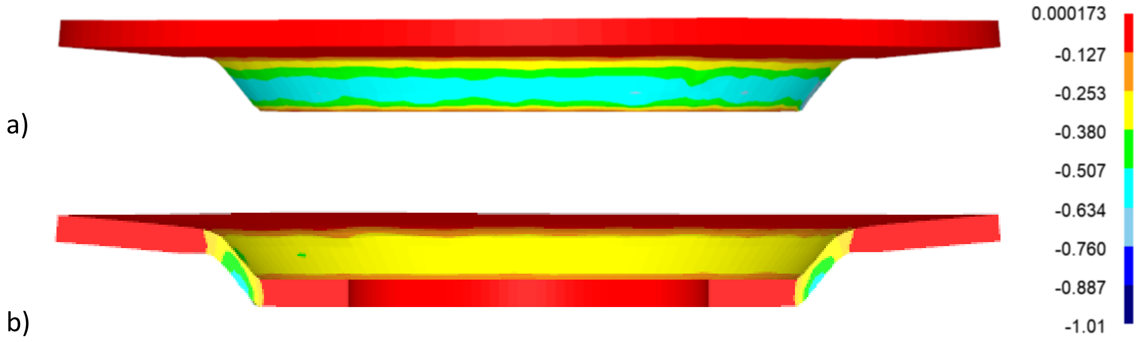

Figure 122: Distribution of Minimum Principal Strain (mm/mm) along the workpiece at step 20,000: a) Outer. b) Inner surface

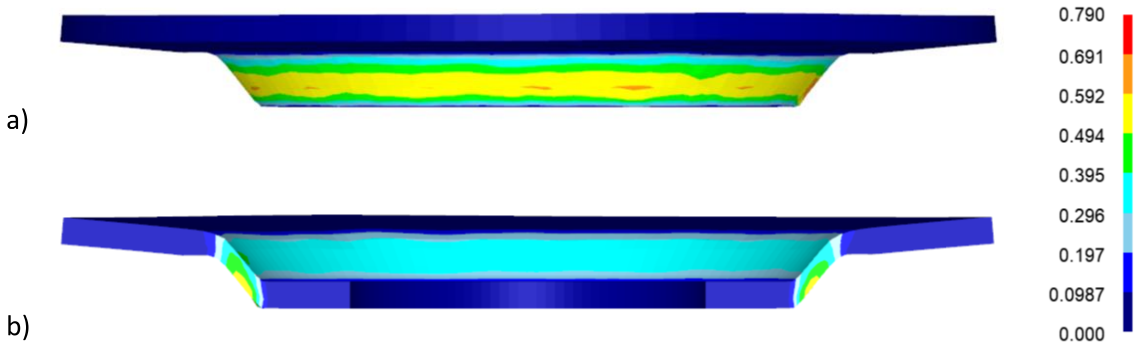

Figure 123: Distribution of Maximum Principal Strain (mm/mm) along the workpiece at step 20,000: a) Outer. b) Inner surface

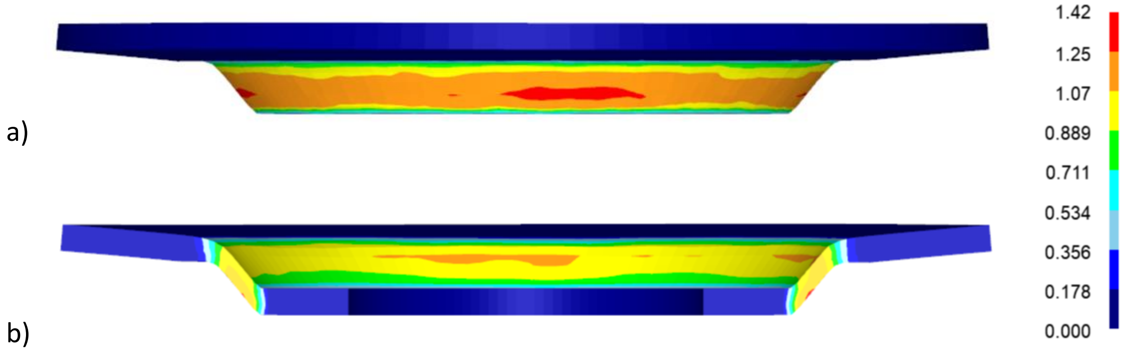

Figure 124: Distribution of Damage along the workpiece at step 20,000: a) Outer. b) Inner surface

a)

b)

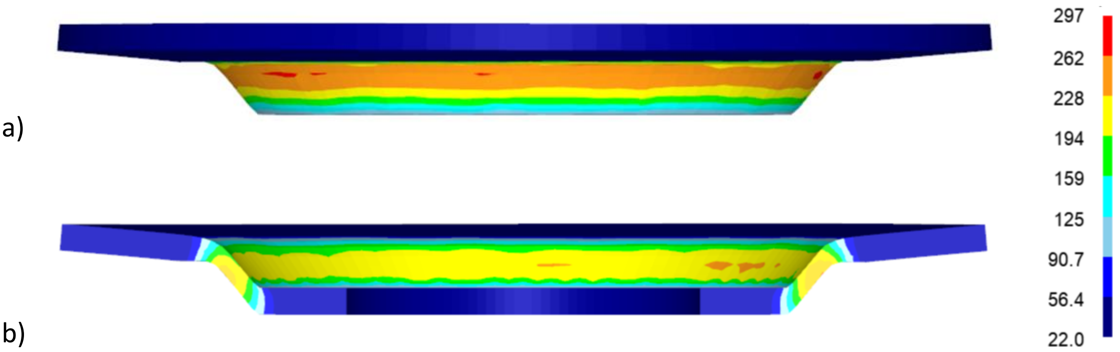

Figure 125: Distribution of Temperature (˚C) along the workpiece at step 20,000: a) Outer. b) Inner surface

Table 29: Principal Strains' values calculated for a mandrel angle $\alpha = 40°$

Ideal Simple Shear	**FEM Model**
$\varepsilon_1 = 0.596$	$\varepsilon_1 = 0.578$
$\varepsilon_2 = -0.596$	$\varepsilon_2 = -0.596$

The principal strains values and behaviour in this Inconel 718 model had good agreement with the observed in the first 4 stages of this chapter, however the damage values obtained across the entire workpiece surpassed 1.0, indicating that the model is predicting failure for this material with these process parameters. Since an experimental workpiece was provided for this project and was studied in Chapter 3, it is already known that failure does not occur with these conditions so the FEM model was supposed to predict a success. Another important remark is that from stage 4, it was concluded that the FLD damage model could possibly be not entirely adequate for the testing of shear spinnability. In order to understand more about this, the same process for calculating damage manually used in stage 4 was repeated with these results and it is shown in Equation 34 to Equation 36.

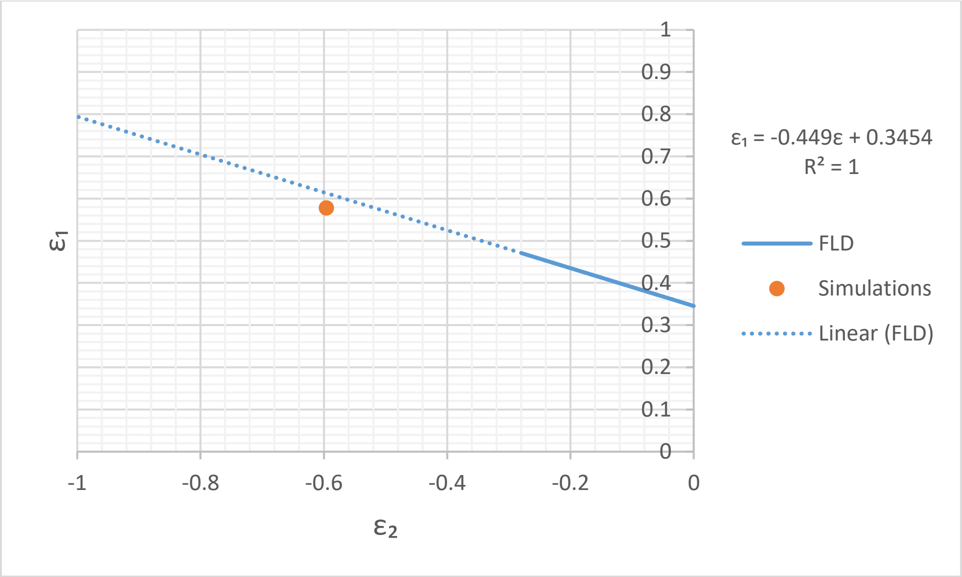

Figure 126: Average Principal Strains obtained in the outer surface of the workpiece against the FLD of Inconel 718.

$$\varepsilon_{1Limit} = -0.449\varepsilon_2 + 0.3454$$

Equation 34

$$\varepsilon_{1Limit} = -0.449(-0.596) + 0.1074 = 0.613$$

Equation 35

$$D = \frac{\varepsilon_{1Real}}{\varepsilon_{1Limit}} = \frac{0.578}{0.613} = 0.943$$

Equation 36

It is possible to see that like with the Timetal 54M case, the principal strain values obtained with Inconel 718 are way outside of the FLD domain. However, even after extrapolating the FLD the damage value calculated was 0.943 and not 1.42 like the FEM simulation. After verifying that all data introduced in Deform was correct and no mistakes were done when setting up the simulation, this result remained unchanged. After speaking to Wilde Analysis[6] (the company in charge of distributing Deform software and giving support to its users in the UK) it was concluded that these discrepancies were likely the result of the FLD damage model just being introduced into the software which means

---

[6] Wilde Analysis Ltd. Whitworth House, 28 Charles St, Stockport, Cheshire, SK1 3JR

t: +44 (0)161 4746886

info@WildeAnalysis.co.uk https://wildeanalysis.co.uk/

that still a lot of errors could be encountered in the damage calculations. For instance, in this model the addition of temperature to the damage calculations could have caused the problem. Even with these negative results the use of FLD can still be implemented if the principal strain values are compared directly against it, instead of extracting the damage value directly from the database but still further analysis need to be conducted to determine if the FLD approach is suitable for this process.

The temperature distributions shown in Figure 125 show that even though the workpiece is not heated by any external means, the temperature in the shear formed areas still reach almost 300 ˚C. For many alloys, these working temperatures do not represent a significant change in the material properties but for Inconel 718 they do, because that this alloy has considerable temperature sensitivity. Figure 127 shows an example of how the material becomes visibly softer as the temperature rises. This means that whenever a new material is introduced into this shear forming FEM model, it is important to consider all material properties and evaluate if said material can be affected by other factors that were not needed to be evaluated for other materials, like the temperature in this case.

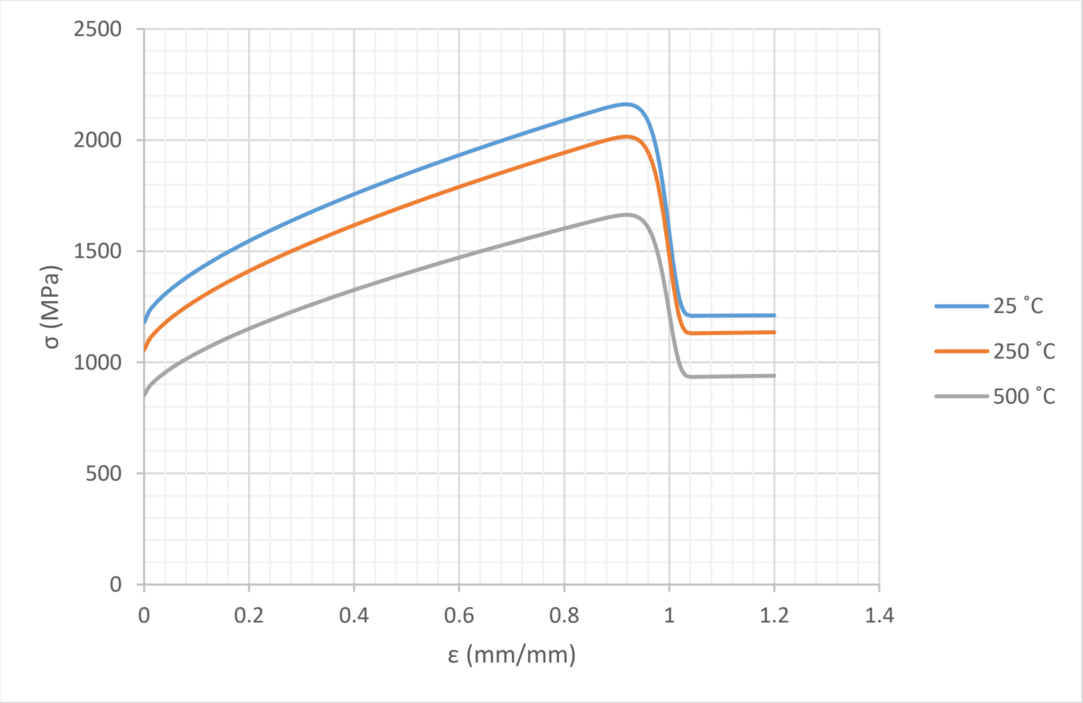

Figure 127: Flow stress curves for Inconel 718 at different temperatures with a strain rate of 1.0 s^{-1}[113].

4.6.2.4 Conclusions

The results obtained in this section indicate that even though damage calculations using the extrapolation of the FLD seem to be in agreement with the experimental results, the principal strain values for Inconel 718 were higher that the allowed by the FLD domain. This means that this approach is not entirely correct. This was also observed in stage 4 using the data for Timetal 54M. However, the fact that this damage model was able to predict fracture and success for two separate materials under their own real-life conditions when the FLD curve was extrapolated is an indicator that the FLD approach could possibly be adapted to incremental forming process like this one, even though it is not suitable as it is now. This can be concluded since the construction methods for FLD that are currently used in industry use conventional forming process, like stretch forming [119], to define the formability limits of materials and these process do not take into account conditions that are often encountered in incremental forming processes that could lead to higher formability limits, like the lack of necking before fracture or the shear deformation limit [53]. Based on this, further analysis were conducted to try and understand how the FLD approach can be modified for shear forming.

Regarding the temperature calculations obtained in this model, it was observed that the temperature in the workpiece could rise up to around 300 ˚C. Like explained in section 4.6.2.1, this calculation does not take into consideration certain factors that could have a significant impact on the result, but it still does provide an insight of how due to the high speeds of this process the temperature could rise considerably. In some materials this temperature rise should not have a significant effect on the model calculations, such is the case of stainless steel AISI 316 [90], but for Inconel 718 it does. This means that for a more accurate FE model, temperature is a variable that should always be considered for temperature sensitive alloys. It is also suggested that all variables that impact heat transfer are also included in the model and if possible determined experimentally for better results.

4.6.3 Analysis of Different Angles vs FLD

Based on the results obtained in section 4.6.2, it was decided to conduct this study to understand how the principal strains behaviour in shear forming compare against the FLD of a given material. To do this, the initial shear forming model was used and the angle of the mandrel was varied from 30˚ to 70˚. The materials selected for this study were stainless steel AISI 316, Timetal 54M and Inconel 718. Jethete M152 was not used because no FLD data could be found in the literature for this alloy.

It was expected that from this brief study, better understanding of the limitations and opportunities of the FLD approach could be gained and a new proposal for the damage criterion to be used in the final shear spinnability methodology could be developed.

4.6.3.1 General Model Set-Up

The same general set up was used as in stage 1 and only the mandrel angle and the materials were changed for each model. A summary of the general process parameters used is shown in Table 30. Figure 128 shows two examples of the modified mandrels. The properties of each materials remain unchanged for this stage and only a forming limit diagram for AISI 316 was added.

Table 30: Process parameters used in this study

Input Parameters	Name/Value
Workpiece Rotational Speed	5 rad/s
Feed rate	1 mm/s
Mandrel Angle	30˚, 40˚, 50˚, 60˚, 70˚
Material Thickness	6 mm

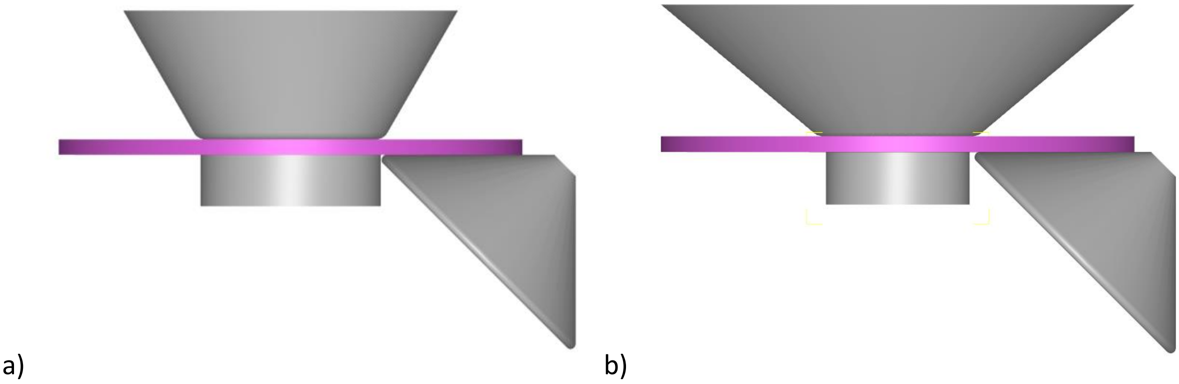

Figure 128: Example of Mandrel modifications. a) 20˚ Mandrel, b) 50˚ Mandrel.

The Forming Limit Diagram of AISI 316 is shown in Figure 129 and was developed for Tourki et al. [120] using the Nakazima formability test. This test had the same arrangement as the stretch forming test described in section 4.6.2.1, but only rectangular specimens with a fixed dimension of 240 mm and widths varying from 20 mm to 240 mm were used.

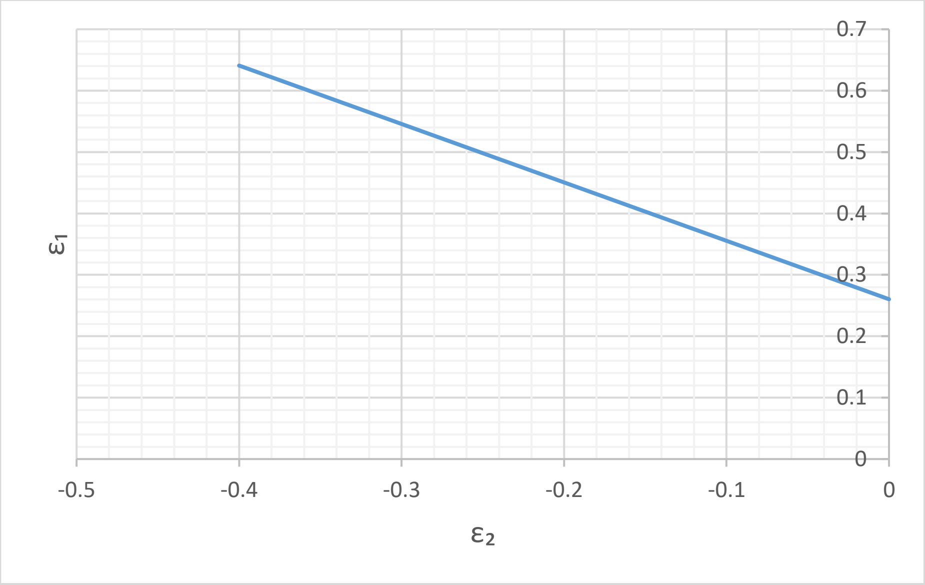

Figure 129: Forming limit diagram for stainless steel AISI 316 [120].

4.6.3.2 General Results and Discussion

The maximum principal strains obtained for every model were extracted and are summarised in Table 31 along with the values calculated for ideal simple shear. It is possible to see that all materials have similar values to ideal simple shear but are not exactly the same. The variation on the strains obtained could be caused by the material flow stress behaviour and the effect of the process parameters. This is a clear evidence of how in order to reduce the variation from the simple shear deformation mechanism it is important to select adequate process parameters using a DOE like in stage 2 of this project. Considering that this variation can be minimised until it is almost negligible, it was concluded that the principal strain values in ideal simple shear can be directly compared to the FLD of any material that needs to be tested as long as the final result is backed up by conducting a DOE to select the adequate process parameters and simulations with the intended real-life parameters to validate that the simple shear condition is being achieved. Based on this, the values of the principal strains in ideal simple shear for the angles used in this study against the FLD of the three materials tested are shown in Figure 130.

Table 31: Maximum principal strains values for each angle and material, including ideal simple shear.

Angle	Ideal Simple Shear		AISI 316		Timetal 54M		Inconel 718	
	ε_2	ε_1	ε_2	ε_1	ε_2	ε_1	ε_2	ε_1
30˚	-0.866	0.866	-0.869	0.834	-0.885	0.852	-0.816	0.837
40 ˚	-0.596	0.596	-0.645	0.582	-0.622	0.601	-0.627	0.614
50 ˚	-0.420	0.420	-0.455	0.446	-0.472	0.453	-0.477	0.461
60 ˚	-0.289	0.289	-0.303	0.302	-0.309	0.298	-0.302	0.297
70 ˚	-0.182	0.182	-0.208	0.204	-0.207	0.203	-0.208	0.196

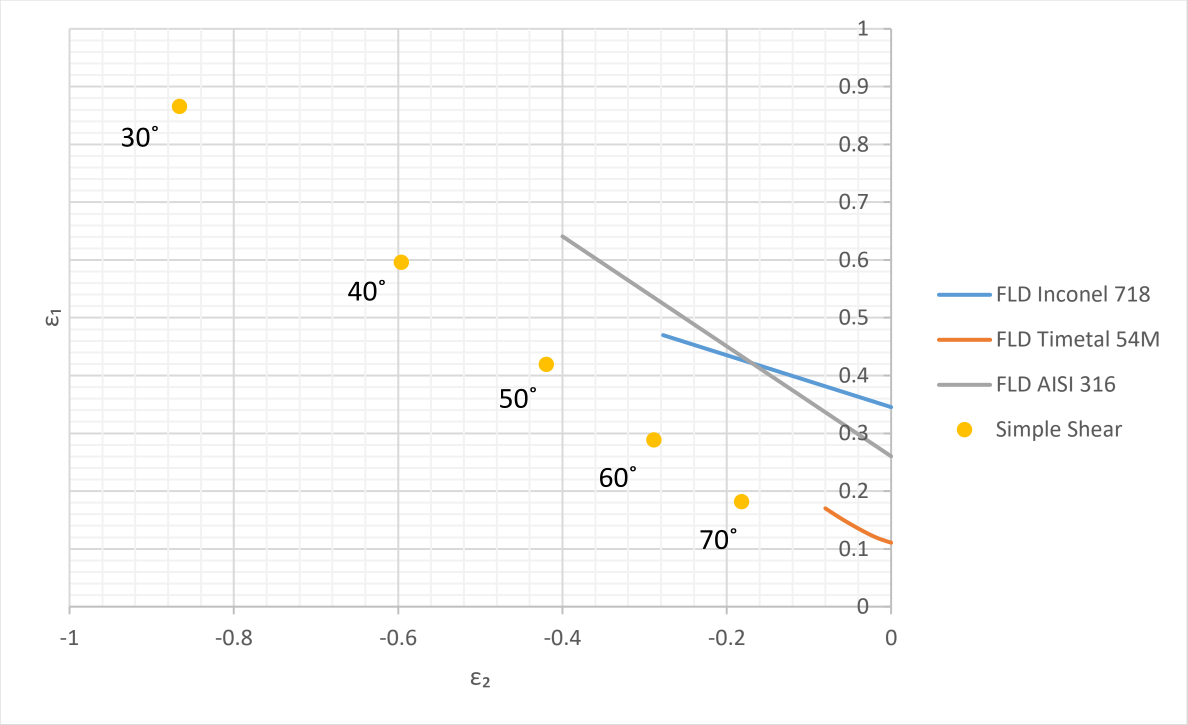

Figure 130: Principal Strains' values with each angle for ideal simple shear against the FLD of AISI 316, Timetal 54M and Inconel 718. [119, 120]

When plotting the principal strains values for each angle and comparing them against the FLD of all materials, two main observations can be made:

1. The principal strains obtained for all angles are on the left side of the FLD domain with smaller angles being more towards the left.
2. The strains obtained during Shear Forming are much higher that the FLD domain for all angles in Timetal 54M and for some angles in AISI 316 and Inconel 718. This is considered an

automatic failure, even if the damage factor says otherwise when extrapolating the FLD curve like it was done in stage 4 and section 4.6.2.

It is also important to note that even though the results for Timetal 54M could be considered correct because there are no records of successfully shear spun parts of this material in the literature, this should not be the case for AISI 316 and Inconel 718. For AISI 316, it was expected that the FLD damage model predicted a success with an angle of 30°, since it is very close to the found in the literature for AISI 304 [24] and both alloys have very similar formability properties. For Inconel 718 success was expected at an angle of 40° considering experimental data shown in Chapter 3. This means that AISI 316 at 30° and Inconel 718 at 40° should still be under the FLD domain.

4.6.3.3 Conclusions

This study allowed to evaluate the performance of the FLD damage criterion selected in stage 3. In two of the materials this criterion had a poor performance, failing to predict success when it was expected. The results for Timetal 54M seemed to be in agreement with the prediction of the FLD, however since no more information was given by the supplier regarding experimental attempts to shear spun parts with other mandrel angles, more testing would be needed to validate them.

Based on these observations, it can be concluded that the FLD approach is not suitable for testing shear spinnability, however the fact that the ideal simple shear deformation mechanism can be applied for the prediction of principal strain values in shear forming means that using a damage model based on these principal strains would be a practical approach.

An important remark from the FLD theory is that, as mentioned in section 4.6.3, currently only conventional forming processes are being used for the construction of this diagram which could explain why they are not adequate for processes like shear forming where the main deformation mechanism is simple shear and hence shear fracture is expected to be the mainly failure mechanism [53, 121, 122] which could result in higher formability limits for this specific process [53, 123].

In conclusion, the principal strains behaviour found in this study offer a promising opportunity to test the shear spinnability of materials without extensive experimental work if a more adequate construction method of FLD’s for shear spinning operations is found.

4.6.4 Analysis of Fracture Forming Limit Diagram Approach

As mentioned at the end of section 4.6.3, a new approach of the FLD needs to be explored so it can be used for shear spinnability testing. A potential solution for this could be to use a modified Fracture Forming Limit Diagram (FFLD) that includes shear fracture limits. A modification of the FLD was proposed by Isik et al. [53], who investigated the fracture limits of aluminium alloy AA1050-H111 sheets for incremental forming processes. The potential of this approach for shear forming operations was studied here using the material and FFLD and SFFLD data for this alloy. From these results it is expected to conclude if this could be used as a damage criterion for the FEM model developed in this project.

4.6.4.1 FFLD construction method

To construct these FFLD, Isik et al [53] used three tests: Single Point Incremental Forming (SPIF), In-plane torsion tests and plane shear tests. The details of each test are described below. All specimens used for all tests were electro-chemically etched to generate a circle pattern that would allow to measure the principal strains after deformation.

Single Point Incremental Forming

A visualisation of the setup and the geometries used with this process is shown in Figure 131. As they explained this process was selected because apart from facilitating the strains measurement, it seems to be more suitable for incremental forming operations that often experience fracture before necking occurs [53, 123]. The forming angle of the workpiece was gradually increased during the process, as shown in Figure 131b and c, so linear strain paths could be obtained from each workpiece fabricated. The process parameters used are shown in Table 32.

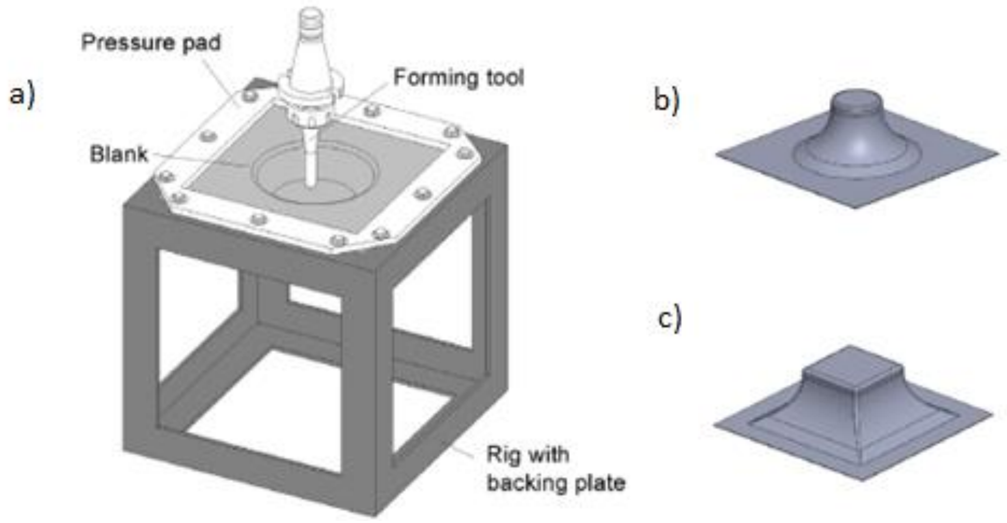

Figure 131: Single Point Incremental Forming and sample geometries used by Isik et al. [53]. a) Process setup, b) Conical

Table 32: Process parameters for the SPIF test. [53]

Parameter	Dimension
Blank geometry	250 mm x 250 mm
Roller diameter	8 mm
Feed rate	1000 mm/min
Step size	0.2 mm/rev
Tool path	Helical

In-plane torsion test

The general setup of the torsion test used is shown in Figure 132. This test was developed by Yin et al. [124] and it consists of a circular specimen with two groves across the circumferential direction (See Figure 132b), attached to an inner and outer clamps. The inner clamp remains stationary during the process and the outer clamp rotates generating the shear deformation. The dimensions of the specimen used by Isik et al. [53] are shown in Figure 132b, however no data was found regarding the velocity of the process.

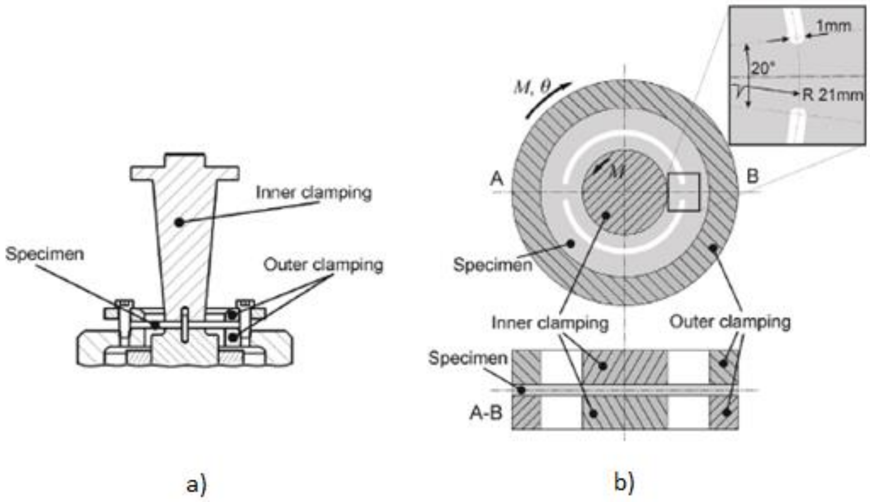

Figure 132: In-plane torsion test. a) General set up, b) Specimen geometry and visualisation of its assembly in the test machine. [53]

In-plane shear test

The geometry of the specimens used by Isik et al. [53] for this test is shown in Figure 133 and it is modified version of the ASTM standard for shear tests in aluminium alloys [125]. This modification was done to prevent buckling during the test [53]. No additional data was found regarding other process parameters of this test.

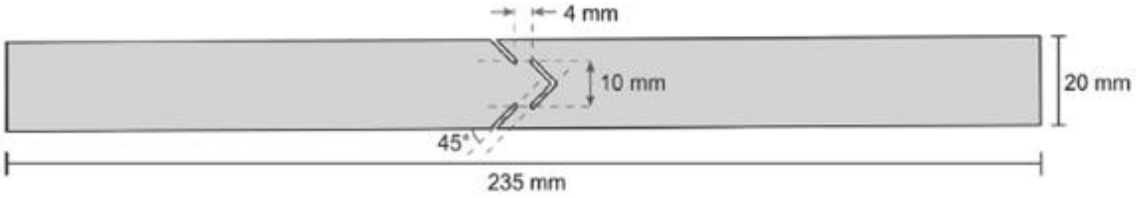

Figure 133: Geometry of the specimen used for the shear tests [53]

4.6.4.2 FFLD of AA1050-H111 aluminium alloy

The final FFLD obtained by Isik et al [53] for this alloy is shown in Figure 134. In here, it is possible to see a comparison between the FLD constructed using conventional stretch forming tests and the FFLD, which can be divided in two main sections:

1. Shear Fracture Forming Limit (SFFL): constructed from the in-plane torsion and shear tests.
2. Fracture Forming Limit (FFL): constructed with the SPIF tests.

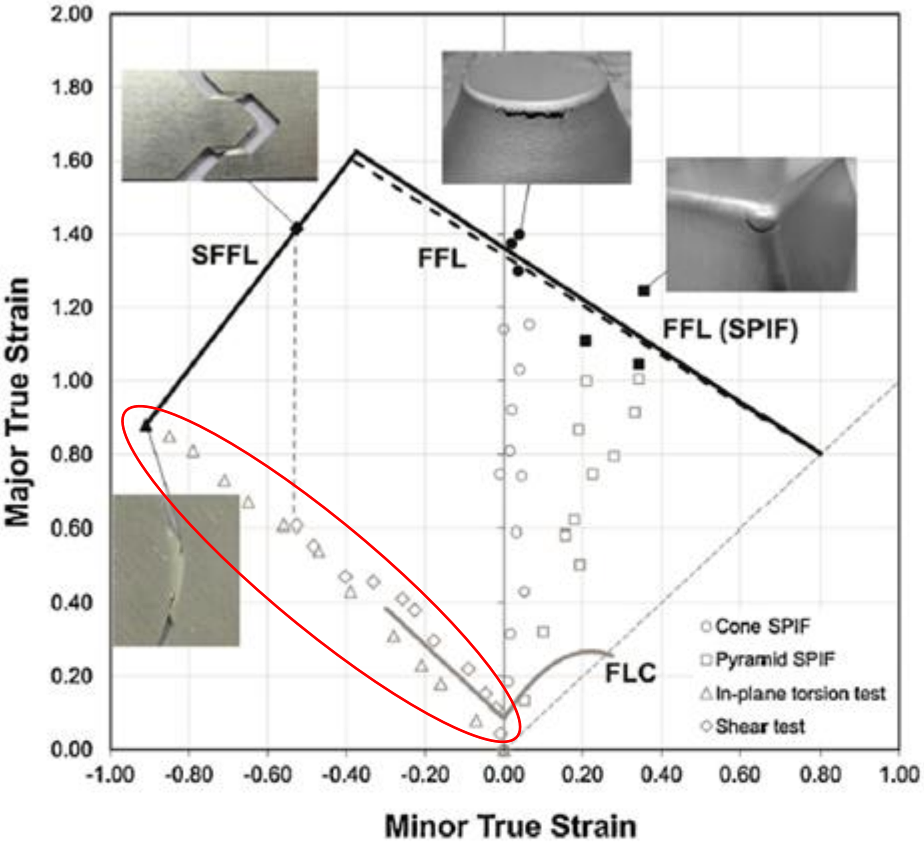

Figure 134: Fracture Forming Limit Diagram (SFFL + FFL) of aluminium alloy AA1050-H111 against Forming Limit Curve (FLC) obtained by conventional stretch forming test. The red circle indicates the data extracted from the shear tests. Adapted from [53]

4.6.4.3 Model Set-Up

Even though it was concluded that the principal strain values of ideal simple shear can be compared against the FLD of the material (FFLD In this case) it was decided to still conduct the simulations for all angles using the material data for this alloy, just to corroborate that the deformation mechanism is still close to ideal simple shear using the material data of this alloy. The analysis of different angles in shear forming conducted in section 4.6.3 was repeated here using this new alloy and the FFLD and FLD data taken from Isik et al. [53]. The process parameters used for these simulations are shown in Table 33 and the material data is in Table 34.

Table 33: Process parameters used for all models in this study

Input Parameters	Name/Value
Workpiece Rotational Speed	5 rad/s
Feed rate	1 mm/s
Mandrel Angle	30˚, 40˚, 50˚, 60˚, 70˚
Material Thickness	6 mm

Table 34: Material data for aluminium alloy AA1050-H111. [53]

	Parameter	Jethete M152
Elastic Data	Young's Modulus	70 GPa
Plastic Data	Yield strength (y)	115.4 MPa
	Strength Coefficient (k)	140 MPa
	Work-hardening exponent (n)	0.04

4.6.4.4 Results and Discussion

The maximum principal strains obtained for every angle are shown in Table 35. Similar values to the expected in ideal simple were obtained, however like explained before if a more accurate model is needed, the adequate process parameters must be selected before so the ideal simple shear condition is achieved. Like in section 4.6.3, the principal strains in ideal simple shear were compared against the FLD and FFLD of AA1050-H111 alloy and are shown in Figure 135. It is possible to see that for this material all angles tested are within the FFLD domain even if they are outside the FLD domain.

It is also important to note, that even though no data is available regarding shear forming of this alloy, it is expected that this alloy has good performance in shear spinning due to its high ductility and the good formability exhibited in other incremental forming processes like SPIF [53]. So these initial results are promising.

Table 35: Maximum principal strains values for each angle of AA1050-H111 aluminium alloy.

Angle	ε_2	ε_1
30˚	-0.893	0.883
40 ˚	-0.642	0.630
50 ˚	-0.496	0.454
60 ˚	-0.313	0.297
70 ˚	-0.224	0.213

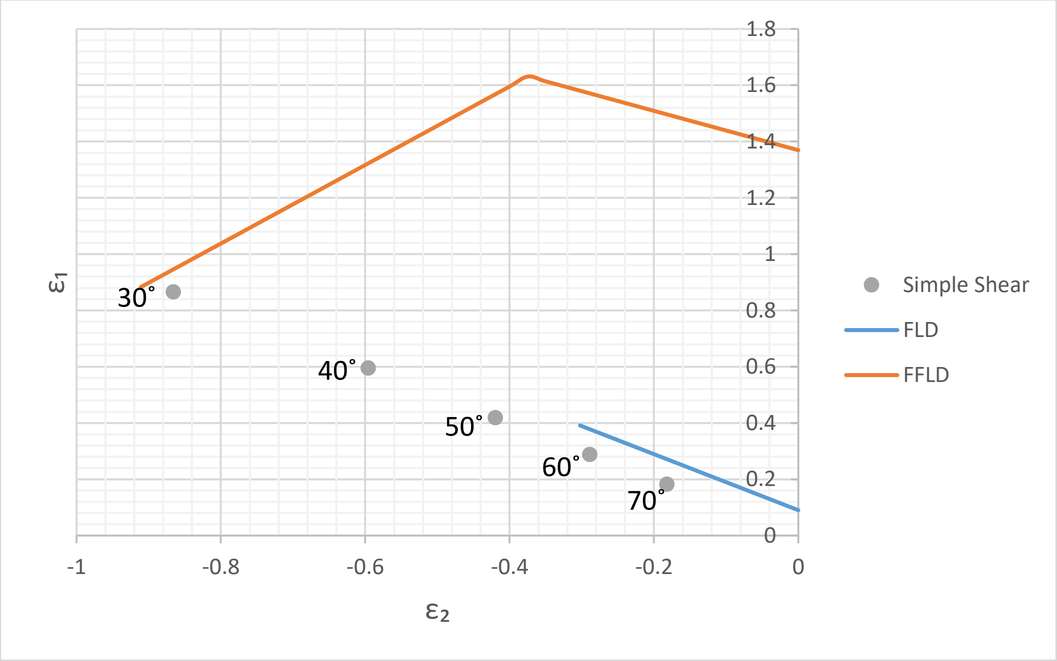

Figure 135: Principal Strains' values with each angle in simple shear against the FLD and FFLD of AA1050-H111 alloy. [53]

With these initial results it would be easy to conclude that the use of FFLD could be a solution for the testing of shear spinnability, however this might not be correct. Even though shear forming is an incremental forming operation, under certain conditions (like high spinning ratios) necking can be experienced in the workpiece [13], so this could lead to under calculation of damage values in some cases and for some materials. Hence, to have an adequate damage criterion for shear forming the formability limits must include all possible simple shear deformation before shear fracture that is within the necking limit.

An important observation from Isik et al work[53], is that the torsion test was able to reproduce simple shear deformation closely until fracture was experienced. Based on this, it could be possible to test materials for shear spinning by simply testing them with the torsion test. For example, this material fractured in the torsion tests at $\varepsilon_2 = -0.9111$, $\varepsilon_1 = 0.8828$, and since ε_1 is the lowest strain value, this can be used to calculate the minimum mandrel angle (α) at which this material is expected to be shear spun as shown below.

$$\varepsilon_{12} = \pm\frac{\cot\alpha}{2}$$

Equation 37

$$0.8828 = \frac{\cot\alpha}{2}$$

Equation 38

$$\alpha = 29.53°$$

Equation 39

By using this method, it could be possible to reduce any real-life trials to basic torsion tests to determine the minimum mandrel angle that could be used in this process for a given specific material and minimum shear forming trials with that angle to corroborate these results after the processing parameters have been selected with the help of this FEM model and a DOE analysis.

4.6.4.5 Conclusions

In this final stage the possibility to modify the FLD damage criterion to an FFLD for incremental forming operations was tested. Even though good results were obtained, it was also observed that the formability limits in the FFLD could under calculate the damage for some materials and some conditions. Finally, after observing that the stretch test conducted by Isik et.al [53] does seem to be able to replicate simple shear deformation, which has been proven to be the main deformation in shear forming throughout this project, it was concluded that using this test could be a more practical and simple solution for the testing of shear spinnability of materials.

4.7 Conclusions

Throughout this chapter, extensive work has been conducted to develop and validate a FEM model for shear forming operations. At the end of stage 1, 2 and 3, a model was completed that was able to simulate the deformation characteristics expected in this process. The material flow-nets and strains distributions obtained with the initial AISI 316 model were in accordance to the observed in the literature [6] and using the maximum principal strain values obtained in the workpieces it was possible to determine that the deformation mechanism is in fact very close to ideal simple shear. Additionally, the texture simulation obtained with the Jethete M152 material and process data showed good agreement with the experimental textures obtained in chapter 3 even though the level of intensity and the definition of the shear pattern in the simulated textures were lower. This was caused by the limitations encountered when using the MTMTAY software which can only work with up to 100 steps and a fixed strain step per simulation and only produces a small ODF. As a first attempt to simulate the texture, these results were satisfactory but it is strongly suggested to tackle all these limitations with a different and more modern software for any future texture simulation work.

The DOE analysis provided key information about how the process parameters affect the shear forming output and it was concluded that in order to have a workpiece with good geometrical characteristics and optimal deformation conditions it is important to select the optimal process parameters. This can be done conducting a quick DOE using the FEM model.

Using the experimental data provided for Timetal 54M, it was possible to evaluate three damage criterions and select the FLD approach as the most promising. However after testing this approach with the Inconel 718 experimental data, the results were unsatisfactory since the damage model was unable to predict a success, like expected.

After studying the principal strains' behaviour with three materials and various shear forming angles, it was concluded that the FLD approach could possibly be used as a damage model if its construction method was changed to a more suitable one for incremental forming operations. An attempt was made to use a FFLD for incremental forming operations, however this too was discarded as damage model since there is a risk of under calculating the damage factors for materials that are more predisposed to necking and for spinning operations with conditions that could lead to necking. Finally, since it has been proven by Isik et al. [53] that the stretch test can reproduce simple shear deformation, this test is proposed as a possible way to evaluate the shear spinnability of materials by calculating the minimum angle at which they can be processed.

In conclusion, all the modelling work done in this chapter enabled the development of a reliable FEM model that can be used to reduce the amount of shear spinning trial and errors needed for testing materials drastically. However a validation of the proposed test method is still needed before this can be used in industry.

Chapter 5: General Conclusions and Future Work

The main goal of this project was to develop a methodology to test the potential of materials to be shear spun. To do so, it was necessary to have a better understanding of the deformation conditions throughout the workpiece and to be able to translate these conditions into and FEM model that could be used to study the potential of a given material to undergo this process without failure. For this reason, the project was divided into two big blocks that were described in Chapter 3 and 4 of this thesis. The first block consisted in all the experimental work that was conducted on three materials that had already been used in shear spinning trials and that was necessary to characterise the deformation behaviour throughout the transversal section of spun parts. The second block comprehended all the modelling work carried out to develop a FEM model that closely resembled the shear forming process conditions and that could be used in a methodology for testing the potential of materials to undergo shear spinning minimising the experimental work needed.

The main conclusions obtained from the experimental work described in Chapter 3 were:

1. The microstructural and texture analysis conducted proved that the main deformation mechanism in shear spinning is in fact very close to simple shear.
2. The deformation in the workpiece during the process is not uniform. The areas closer to the roller have a significant higher level of deformation, however simple shear texture patterns were still found in the mandrel zones but with lower levels of intensity.

Additionally, the experimental results and data from Chapter 3 was fundamental for the development of the modelling work described in Chapter 4 for the following reasons:

- The experimental pole figures obtained for the Jethete M152 alloy allowed the validation of the FEM model by comparing them against the textures simulated using the data extracted from the FEM database.
- It was possible to select a potential damage criterion for the model using the data of the fractured Timetal 54M sample.
- The selected damage model was further analysed using the data from the successfully shear formed Inconel 718 sample.

From all the modelling work described in Chapter 4, the following can be concluded:

1. A reliable FEM model that closely resembles the deformation behaviour in shear spinning has been developed in this project. This model was validated by comparing the flow-nets, strains behaviour and simulated textures against experimental data and information found in the literature. It was also proved that the deformation along the workpiece follow ideal simple shear conditions, by comparing the principal strain values in the model against idealised in-plane simple shear.
2. The DOE analysis suggest that both process parameters studied (feed rate and rotational speed) do have a significant effect on the geometrical characteristics of the workpiece and the deformation mechanism, but not on the level of deformation experienced. This indicates that it is important to select an adequate set of parameters for the process to avoid defects and ensure the optimal deformation conditions are achieved, which can be done using the FEM model.
3. The principal strains in the workpiece after shear forming can be calculated based on the simple shear deformation condition with the following equation: $\varepsilon_{12} = \pm \frac{\cot \alpha}{2}$
4. The Forming Limit Diagram approach was discarded as a damage model for shear spinning since strain states with values much higher that the FLD domain were obtained for both experimental materials (Timetal 54M and Inconel 718) as well as with AISI 316.
5. Based on the work conducted by Isik et al. [53], it was concluded that the shear spinnability of material could be studied using an in-plane torsion test. This test was able to reproduce simple shear deformation closely for an aluminium alloy until fracture was experienced. A possible method for calculating the minimum mandrel angle at which this material can be shear spun was proposed by substituting the principal strains values at fracture obtained with this test in the equation mentioned in point 3.

Finally, even though more work would need to be conducted to validate the reliability of using the in-plane shear test to evaluate shear spinnability, a general methodology can be proposed with the results of this project. This methodology is the main output of this project and is considered to be the novel aspect of this research because it offers an opportunity to expand the understanding of damage development in shear forming operations and the development of a more efficient and reliable testing programme that can be implemented in industry.

5.1 Methodology for Testing Shear Spinnability of Materials

The general methodology proposed for the study of a material's shear spinnability is:

1. Select the material to be studied.
2. Conduct in-plane torsion tests.
    a. Measure Principal Strains at fracture.
    b. Calculate the equivalent mandrel angle α with equation $\varepsilon_{12} = \pm \frac{\cot\alpha}{2}$
3. Prepare shear forming trials
    a. Define material properties for FEM simulations.
        i. Flow stress behaviour (plastic properties).
        ii. Thermal Properties.
    b. Conduct initial simulation using the process parameters suggested by the industrial collaborator and the mandrel angle calculated in point 2.
    c. Use this simulation as a nominal run and conduct DOE analysis. Select adequate process parameters using contour plot charts as shown in section 4.3
4. Conduct shear forming trials with the process parameters selected in point 3, to validate the results from the in-plane torsion test.
5. If successful, this angle is the minimum angle at which the studied material can be shear spun, i.e. any angle higher than this can be used for this process as long the correct process parameters are used.

It is important to note that before using this methodology in industry, more studies must be conducted regarding the in-plane torsion tests. These tests are a promising solution for testing shear spinnability, however due to the time restrictions of this project it was not possible to validate its suitability using the experimental materials available for this project.

5.2 Future Work

Even though the main objectives of this PhD project were fulfilled, some work still remains unfinished before the proposed methodology can be implemented in industry. This work can be divided in two main tasks:

- Validate the suitability of the in-plane torsion tests to evaluate shear spinnability

This can be done by using the materials used in the experimental section of this project (Timetal 54M, Inconel 718 and Jethete M152) in the in-plane torsion test. The minimum mandrel angle for these three materials can be calculated and compared against the experimental data from this project. If first results are satisfactory, then shear forming trials can be conducted for these materials and the minimum mandrel angle calculated to further validate the results of the torsion test.

- Validate the shear spinnability test methodology using new materials.

The proposed methodology was developed using just the data from Inconel 718 and Timetal 54M and the information found in the literature regarding aluminium alloy AA1050-H111. The next step for its validation would be to use this methodology with other material to prove how easily it can be transferred to other materials. Since no shear forming operations have been attempted with AA1050-H111 alloy, shear forming trials with this material should be included as a part of this validation.

Based on the results obtained in these two tasks, any limitations that the proposed methodology could have can be identified and addressed.

APPENDICES

Appendix 1: Data processing for texture simulation of Jethete M152 in section 4.4

The main objective of this appendix is to provide a case study of one of the points used for the texture simulation described in section 4.4, so there can be a better understanding of the process proposed in Figure 108.

Phase 1: Perform FEM Simulation in Deform

In this phase, the simulation was performed in Deform as usual with the adequate shear forming process parameters and simulation parameters described in section 4.4.1. It is important to remember to save every single deformation step conducted. This is mainly because the contact area between the roller and the workpiece is constantly moving, meaning that when selecting a point of study, the steps where the roller is actually deforming this exact point throughout the process is only a small portion of the 20,000 steps. This means that saving every single deformation step was essential to gather enough information for this texture simulation.

Phase 2: Selection of points for Texture Simulation

Once the FE simulation was completed, the points to be used for the texture simulation process were selected. In this appendix, the point representative of the roller zone will be taken as an example for this and all the following phases of the texture simulation, this point will be referred as roller point for practical terms. The selected point is shown in Figure 136. As it can be seen, it was ensured that this point was inside the area that is initially in contact with the roller as well as on the roller edge of the workpiece.

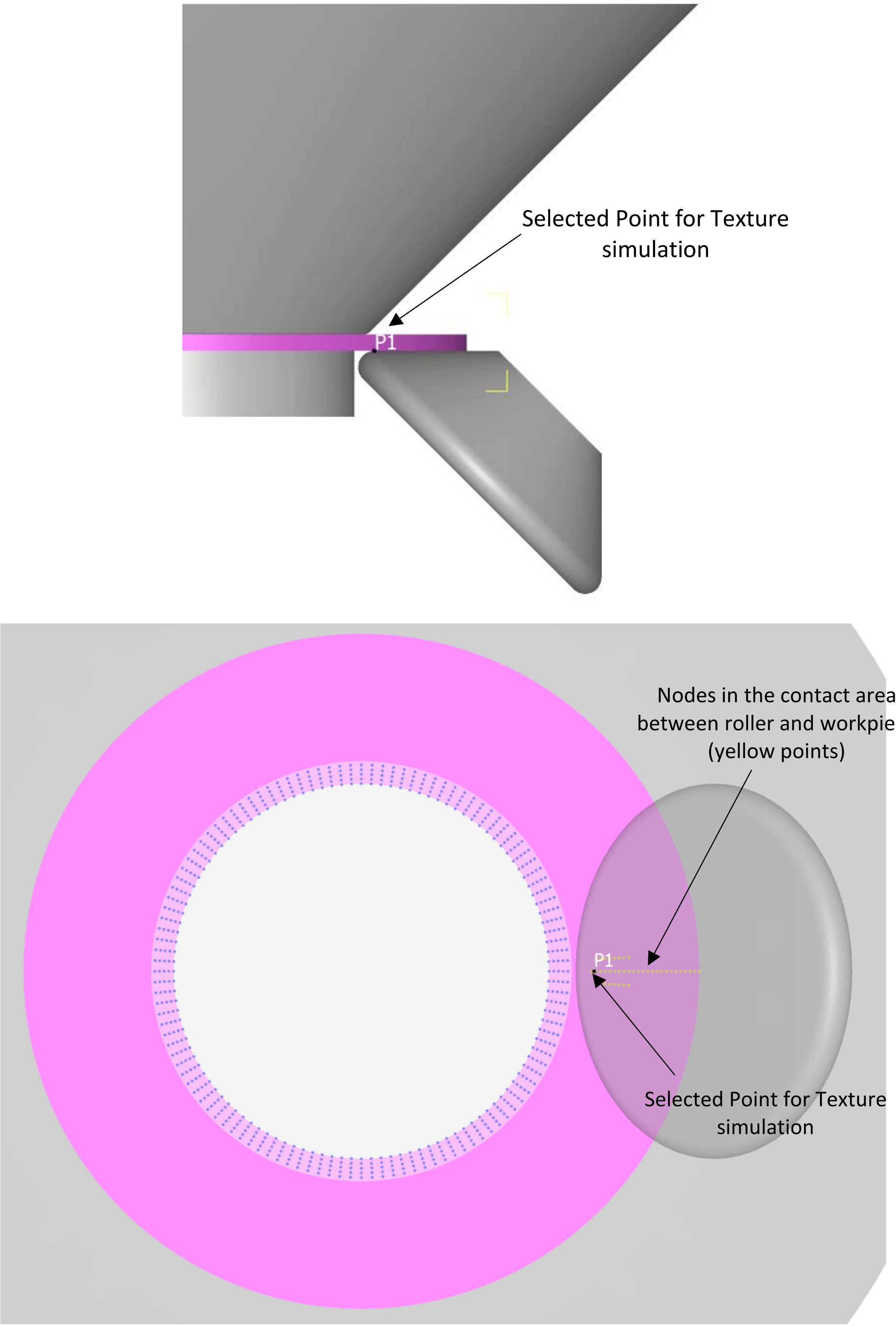

Figure 136: Initial position of the point selected for the texture simulation of the roller area.

Phase 3: Extraction of Data from Deform

In this phase, the strain tensor data at the point selected for every step was extracted and saved to an excel-friendly document with extension .CSV. This document was then converted to .xslx manually. Five steps where a large deformation was experienced at the point selected were chosen and are shown in Table 36. These five steps will be treated in the following phases to show as an example of how all the data was treated. Additionally the effective strain at every step was also extracted and will be used in phase 5.

Table 36: Strain tensor values at roller point for 5 steps with high deformation.

Step	ε_{xx}	ε_{xy}	ε_{xz}	ε_{yx}	ε_{yy}	ε_{yz}	ε_{zx}	ε_{zy}	ε_{zz}
3595	0.0190	0.0985	0.0106	-0.0985	-0.0098	0.0299	-0.0106	-0.0299	-0.0092
3596	0.0192	0.1028	0.0111	-0.1028	-0.0098	0.0317	-0.0111	-0.0317	-0.0094
3597	0.0193	0.1071	0.0117	-0.1071	-0.0099	0.0335	-0.0117	-0.0335	-0.0095
3598	0.0198	0.1099	0.0123	-0.1099	-0.0103	0.0352	-0.0123	-0.0352	-0.0095
3599	0.0206	0.1143	0.0127	-0.1143	-0.0115	0.0379	-0.0127	-0.0379	-0.0091

Phase 4: Calculation of Strain Rate Tensor

To calculate the strain rate tensor, first the strain deviations at every single step were calculated. This was done by subtracting the strain value at the current step minus the strain value at the step before, as shown in Equation 40 (See Table 37). Finally the strain rate tensor was determined by dividing all the strain deviations by the time per step or step size selected for the FE simulation in Deform, which was 2.5 x 10^{-5} s (See Table 38).

$$\Delta\varepsilon_{ij} = \varepsilon_{ij\ at\ step\ n} - \varepsilon_{ij\ at\ step\ n-1}$$

Equation 40

Table 37: Strain deviations values at roller point for 5 steps with high deformation.

Step	ε_{xx}	ε_{xy}	ε_{xz}	ε_{yx}	ε_{yy}	ε_{yz}	ε_{zx}	ε_{zy}	ε_{zz}
3595	0.0002	0.0039	0.0005	-0.0039	0.0001	0.0016	-0.0005	-0.0016	-0.0003
3596	0.0002	0.0043	0.0006	-0.0043	0.0000	0.0018	-0.0006	-0.0018	-0.0002
3597	0.0001	0.0043	0.0006	-0.0043	-0.0001	0.0018	-0.0006	-0.0018	-0.0001
3598	0.0005	0.0027	0.0006	-0.0027	-0.0005	0.0017	-0.0006	-0.0017	0.0000
3599	0.0008	0.0044	0.0004	-0.0044	-0.0012	0.0027	-0.0004	-0.0027	0.0004

Table 38: *Strain rate tensor values at roller point for 5 steps with high deformation.*

Step	ε_{xx}	ε_{xy}	ε_{xz}	ε_{yx}	ε_{yy}	ε_{yz}	ε_{zx}	ε_{zy}	ε_{zz}
3595	7.531	156.991	18.344	-156.991	3.393	63.235	-18.344	-63.235	-10.923
3596	8.128	172.392	23.014	-172.392	-1.351	72.531	-23.014	-72.531	-6.777
3597	5.847	173.259	24.518	-173.259	-2.405	73.592	-24.518	-73.592	-3.442
3598	18.469	109.720	23.753	-109.720	-18.249	66.145	-23.753	-66.145	-0.220
3599	33.713	176.823	15.866	-176.823	-48.923	107.974	-15.866	-107.974	15.209

Phase 5: Condensation of Data and creation of input file for MTMTAY

One of the main limitations of using MTMTAY is that it only accepts up to 100 steps as input for any texture simulation, this means that the 20,000 steps extracted and treated in the first four phases must now be condensed to 100. This was done using an in-house Matlab code developed by MSc Jan Safranek and described in detail in his thesis *"Modelling Crystallographic Texture Evolution in Hot Extruded Titanium for Aerospace Applications"* [110].

This code basically generates a vector of the effective strain with 100 points, using the data extracted of the 20,000 steps and calculates the average strain rate tensor components for each point of the effective strain vector. This is done as follows:

1. The strain step for MTMTAY is defined by dividing the total effective strain accumulated at the end of the Deform simulation by the number of steps in the MTMTAY texture simulation, which is 100 (See Equation 40).
2. The effective strain vector is created with 100 points using the strain step calculated, as shown in Table 39.
3. The strain rate components of all the points contained between each step are extracted and the average is calculated and assigned to each specific point. An example of this is shown in Table 40 using step 2 of the MTMTAY simulation. Note that step 1 was not used as an example because the data of 1761 steps from the Deform database were used for this calculation and would be impractical to show these calculations.
4. Finally, the 100 step matrix is written to a .TEN file, which can be directly uploaded to the MTMTAY software.

$$Strain\ step = \frac{Total\ Effective\ Strain}{100\ steps} = \frac{1.1770}{100} = 0.01177$$

Equation 41

Table 39: Points in the Effective Strain vector created for the roller point MTMTAY simulation. Step 2 (marked in red) is used as an example in Table 40.

Step for MTMTAY	Effective Strain ($\bar{\varepsilon}$)
1	0.01177
2	***0.02354***
3	0.03531
4	0.04711
5	0.05885
…	…
99	1.1652
100	1.1770

Table 40: Example of the averaging of the components of the strain rate tensor for the calculation of the values for step 2 of the MTMTAY simulation. All points that comply with the condition $0.01177 < \bar{\varepsilon} \leq 0.02354$ *are taken for the calculation of this point.*

Step (Deform)	$\bar{\varepsilon}$	$\dot{\varepsilon}_{xx}$	$\dot{\varepsilon}_{xy}$	$\dot{\varepsilon}_{xz}$	$\dot{\varepsilon}_{yx}$	$\dot{\varepsilon}_{yy}$	$\dot{\varepsilon}_{yz}$	$\dot{\varepsilon}_{zx}$	$\dot{\varepsilon}_{zy}$	$\dot{\varepsilon}_{zz}$
1762	0.0122	5.798	42.309	12.226	-42.309	4.959	32.286	-12.226	-32.286	-10.757
1763	0.0133	4.839	42.923	13.303	-42.923	6.535	33.417	-13.303	-33.417	-11.375
1764	0.0146	4.307	44.447	15.023	-44.447	7.183	36.666	-15.023	-36.666	-11.489
1765	0.0158	3.620	44.510	16.187	-44.510	7.415	37.467	-16.187	-37.467	-11.035
1766	0.0169	2.671	41.771	15.377	-41.771	7.321	31.844	-15.377	-31.844	-9.991
1767	0.0180	3.265	40.036	15.418	-40.036	6.550	32.111	-15.418	-32.111	-9.815
1768	0.0191	3.158	38.728	15.549	-38.728	6.343	33.860	-15.549	-33.860	-9.501
1769	0.0202	3.196	37.541	15.913	-37.541	6.068	30.820	-15.913	-30.820	-9.263
1770	0.0212	4.068	37.945	16.185	-37.945	5.153	31.811	-16.185	-31.811	-9.221
1771	0.0224	8.365	26.143	21.294	-26.143	2.474	46.512	-21.294	-46.512	-10.840
1772	0.0233	7.313	23.452	15.620	-23.452	-1.113	30.163	-15.620	-30.163	-6.200
Average		**4.600**	**38.164**	**15.645**	**-38.164**	**5.353**	**34.269**	**-15.645**	**-34.269**	**-9.953**

Phase 6: Calculation of Orientation Distribution Function with MTMTAY

In this phase the .TEN file and the strain step calculated in Phase 5 are uploaded to MTMTAY, as well as a randomised initial texture, which is shown in Figure 137. With these data MTMTAY calculates an ODF with 1600 crystals which corresponds to the final texture. The final texture is written to a .TX1 file and the Euler angles of each crystal in this texture are written to a .SMT file (See Figure 138).

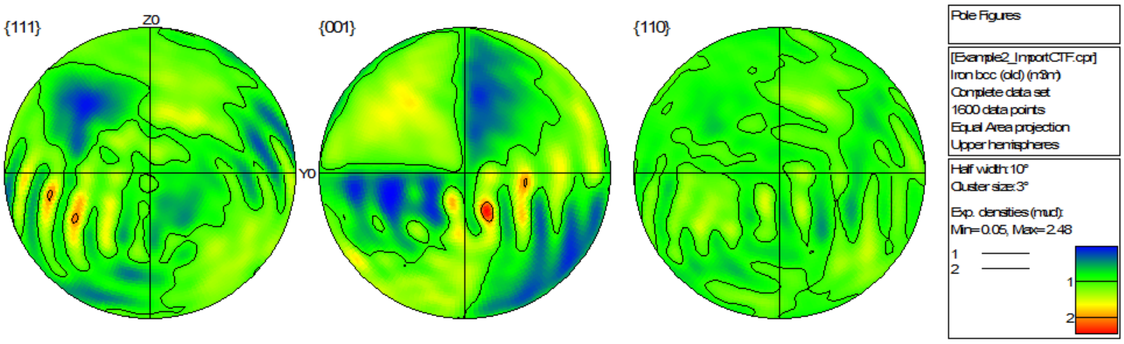

Figure 137: Initial randomised texture used for MTMTAY simulations.

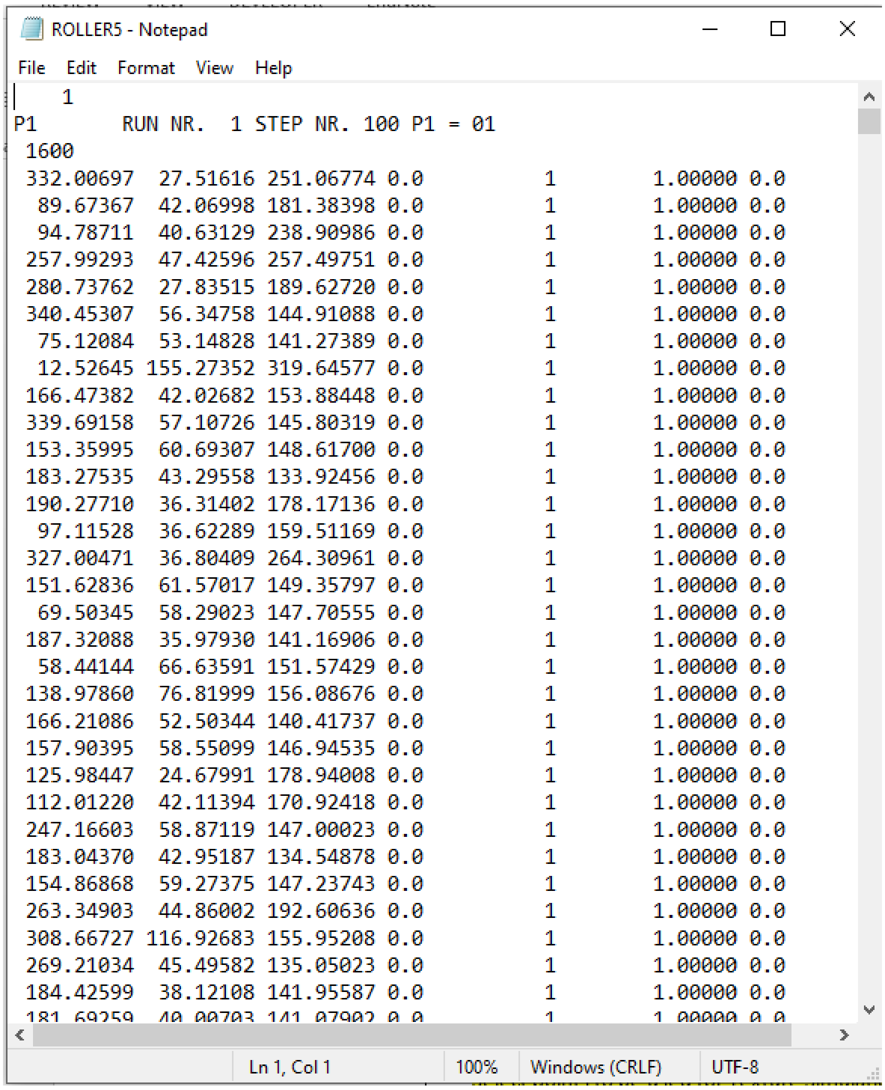

```
     1
P1        RUN NR.  1 STEP NR. 100 P1 = 01
 1600
 332.00697  27.51616 251.06774 0.0         1        1.00000 0.0
  89.67367  42.06998 181.38398 0.0         1        1.00000 0.0
  94.78711  40.63129 238.90986 0.0         1        1.00000 0.0
 257.99293  47.42596 257.49751 0.0         1        1.00000 0.0
 280.73762  27.83515 189.62720 0.0         1        1.00000 0.0
 340.45307  56.34758 144.91088 0.0         1        1.00000 0.0
  75.12084  53.14828 141.27389 0.0         1        1.00000 0.0
  12.52645 155.27352 319.64577 0.0         1        1.00000 0.0
 166.47382  42.02682 153.88448 0.0         1        1.00000 0.0
 339.69158  57.10726 145.80319 0.0         1        1.00000 0.0
 153.35995  60.69307 148.61700 0.0         1        1.00000 0.0
 183.27535  43.29558 133.92456 0.0         1        1.00000 0.0
 190.27710  36.31402 178.17136 0.0         1        1.00000 0.0
  97.11528  36.62289 159.51169 0.0         1        1.00000 0.0
 327.00471  36.80409 264.30961 0.0         1        1.00000 0.0
 151.62836  61.57017 149.35797 0.0         1        1.00000 0.0
  69.50345  58.29023 147.70555 0.0         1        1.00000 0.0
 187.32088  35.97930 141.16906 0.0         1        1.00000 0.0
  58.44144  66.63591 151.57429 0.0         1        1.00000 0.0
 138.97860  76.81999 156.08676 0.0         1        1.00000 0.0
 166.21086  52.50344 140.41737 0.0         1        1.00000 0.0
 157.90395  58.55099 146.94535 0.0         1        1.00000 0.0
 125.98447  24.67991 178.94008 0.0         1        1.00000 0.0
 112.01220  42.11394 170.92418 0.0         1        1.00000 0.0
 247.16603  58.87119 147.00023 0.0         1        1.00000 0.0
 183.04370  42.95187 134.54878 0.0         1        1.00000 0.0
 154.86868  59.27375 147.23743 0.0         1        1.00000 0.0
 263.34903  44.86002 192.60636 0.0         1        1.00000 0.0
 308.66727 116.92683 155.95208 0.0         1        1.00000 0.0
 269.21034  45.49582 135.05023 0.0         1        1.00000 0.0
 184.42599  38.12108 141.95587 0.0         1        1.00000 0.0
 181.69259  40.00703 141.07902 0.0         1        1.00000 0.0
```

Figure 138: Preview of the .SMT file created by MTMTAY

Phase 7: Conversion of .SMT file to a readable format for Channel 5.

Now that the texture simulation is finished, all the information needed to plot the final texture into pole figures is contained in the .SMT file. However this file format is not supported in Channel 5, which is the software used in this project to visualise textures (refer to Chapter 3). For this reason this file is converted using a simple code in MATLAB to a .CTF file, which can be directly uploaded in Channel 5 (See Figure 139).

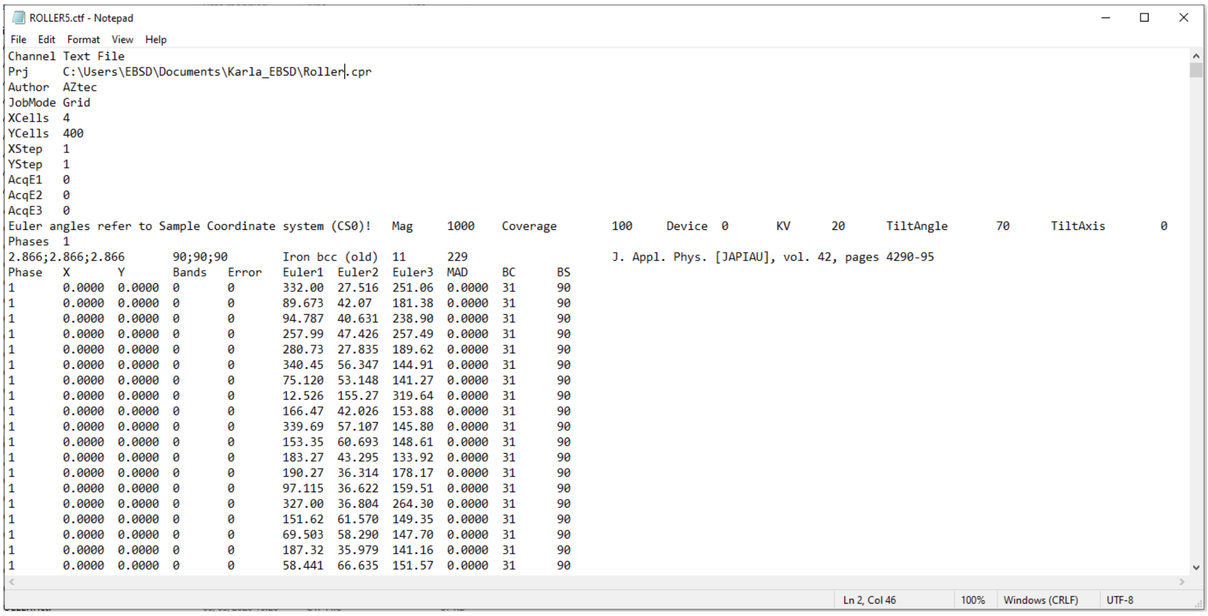

```
Channel Text File
Prj     C:\Users\EBSD\Documents\Karla_EBSD\Roller.cpr
Author  AZtec
JobMode Grid
XCells  4
YCells  400
XStep   1
YStep   1
AcqE1   0
AcqE2   0
AcqE3   0
Euler angles refer to Sample Coordinate system (CS0)!   Mag     1000    Coverage        100     Device  0       KV      20      TiltAngle       70      TiltAxis        0
Phases  1
2.866;2.866;2.866       90;90;90        Iron bcc (old)  11      229                     J. Appl. Phys. [JAPIAU], vol. 42, pages 4290-95
Phase   X       Y       Bands   Error   Euler1  Euler2  Euler3  MAD     BC      BS
1       0.0000  0.0000  0       0       332.00  27.516  251.06  0.0000  31      90
1       0.0000  0.0000  0       0       89.673  42.07   181.38  0.0000  31      90
1       0.0000  0.0000  0       0       94.787  40.631  238.90  0.0000  31      90
1       0.0000  0.0000  0       0       257.99  47.426  257.49  0.0000  31      90
1       0.0000  0.0000  0       0       280.73  27.835  189.62  0.0000  31      90
1       0.0000  0.0000  0       0       340.45  56.347  144.91  0.0000  31      90
1       0.0000  0.0000  0       0       75.120  53.148  141.27  0.0000  31      90
1       0.0000  0.0000  0       0       12.526  155.27  319.64  0.0000  31      90
1       0.0000  0.0000  0       0       166.47  42.026  153.88  0.0000  31      90
1       0.0000  0.0000  0       0       339.69  57.107  145.80  0.0000  31      90
1       0.0000  0.0000  0       0       153.35  60.693  148.61  0.0000  31      90
1       0.0000  0.0000  0       0       183.27  43.295  133.92  0.0000  31      90
1       0.0000  0.0000  0       0       190.27  36.314  178.17  0.0000  31      90
1       0.0000  0.0000  0       0       97.115  36.622  159.51  0.0000  31      90
1       0.0000  0.0000  0       0       327.00  36.804  264.30  0.0000  31      90
1       0.0000  0.0000  0       0       151.62  61.570  149.35  0.0000  31      90
1       0.0000  0.0000  0       0       69.503  58.290  147.70  0.0000  31      90
1       0.0000  0.0000  0       0       187.32  35.979  141.16  0.0000  31      90
1       0.0000  0.0000  0       0       58.441  66.635  151.57  0.0000  31      90
```

Figure 139: Preview of the .CTF file converted using MATLAB.

Phase 8: Plot of pole figures using software Channel 5.

In this final phase, simply upload the .CTF file to channel 5 and use the TANGO module to visualise the pole figure of this final texture, as shown in the following figure.

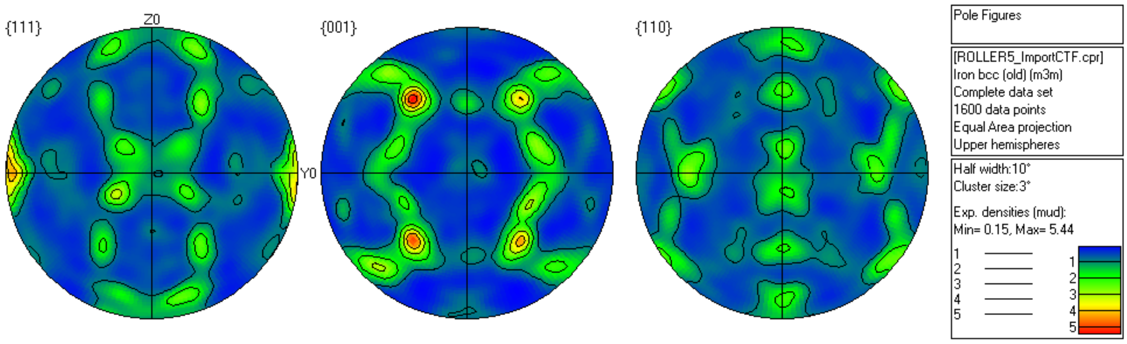

Figure 140: Pole figures of simulated texture of Roller zone.

REFERENCES

[1] Haute Innovation. http://www.haute-innovation.com/en/magazine/innovative-production/incremental-sheet-metal-forming.html (accessed January 26th, 2016).

[2] Metal Spinners. http://www.metal-spinners.net/shear-spinning/ (accessed January 26th, 2016).

[3] "BBS Technology." BBS of America. http://bbs-usa-appguide.com/bbs-technology-expertise.cfm (accessed January 26th, 2016).

[4] C. C. Wong, T. A. Dean, and J. Lin, "A review of spinning, shear forming and flow forming processes," *International Journal of Machine Tools and Manufacture,* vol. 43, no. 14, pp. 1419-1435, 11// 2003, doi: http://dx.doi.org/10.1016/S0890-6955(03)00172-X.

[5] "Spinning and flowing forming," ed. Leico GmbH, 1997.

[6] S. Kalpakcioglu, "On the Mechanics of Shear Spinning," *J. Eng. for Industry,* vol. 83, no. 2, p. 125, 1961, doi: 10.1115/1.3664441.

[7] I. J. Beyerlein and L. S. Tóth, "Texture evolution in equal- channel angular extrusion," *Progress in Materials Science,* vol. 54, no. 4, pp. 427-510, 2009, doi: 10.1016/j.pmatsci.2009.01.001.

[8] B. Avitzur and C. T. Yang, "Analysis of Power Spinning of Cones," *J. Eng. for Industry,* vol. 82, no. 3, p. 231, 1960, doi: 10.1115/1.3663052.

[9] E. Quigley and J. Monaghan, "Metal forming: an analysis of spinning processes," *Journal of Materials Processing Tech.,* vol. 103, no. 1, pp. 114-119, 2000, doi: 10.1016/S0924-0136(00)00394-0.

[10] H. R. Beni, Y. T. Beni, and F. R. Biglari, "An experimental- numerical investigation of a metal spinning process," *Proceedings of the Institution of Mechanical Engineers, Part C: Journal of Mechanical Engineering Science,* vol. 225, no. 3, pp. 509-519, 2011, doi: 10.1243/09544062JMES2133.

[11] M. Hayama and T. Murota, "On the study of metal spinning," vol. 12, ed. Bulletin of the Faculty of Engineering: Yokohama National University, 1963, pp. 53-88.

[12] Sellin, "Metal Spinning," ed. Springer-Verlag, 1955.

[13] O. Music, J. M. Allwood, and K. Kawai, "A review of the mechanics of metal spinning," *Journal of Materials Processing Tech.,* vol. 210, no. 1, pp. 3-23, 2010, doi: 10.1016/j.jmatprotec.2009.08.021.

[14] R. L. Kegg, "A New Test Method for Determination of Spinnability of Metals," *J. Eng. for Industry,* vol. 83, no. 2, p. 119, 1961, doi: 10.1115/1.3664438.

[15] S. Kalpakcioglu, "A Study of Shear- Spinnability of Metals," *J. Eng. for Industry,* vol. 83, no. 4, p. 478, 1961, doi: 10.1115/1.3664570.

[16] B. Avitzur, *Handbook of metal-forming processes*. New York: Wiley (in English), 1983.

[17] K.-i. Mori, M. Ishiguro, and Y. Isomura, "Hot shear spinning of cast aluminium alloy parts," *Journal of Materials Processing Tech.,* vol. 209, no. 7, pp. 3621-3627, 2009, doi: 10.1016/j.jmatprotec.2008.08.018.

[18] L. Radović, L. Nikačević, and L. Jordović, "Deformation behaviour and microstructure evolution of AlMg6Mn alloy during shear spinning," *Transactions of Nonferrous Metals Society of China (English Edition),* vol. 22, no. 5, pp. 991-1000, 2012, doi: 10.1016/S1003-6326(11)61275-2.

[19] M. Zhan, Q.-l. Wang, D. Han, and H. Yang, "Geometric precision and microstructure evolution of TA15 alloy by hot shear spinning," *Transactions of Nonferrous Metals Society of China,* vol. 23, no. 6, pp. 1617-1627, 2013, doi: 10.1016/S1003-6326(13)62639-4.

[20] M. Hayama and A. Tago, "The fracture of walls on shear spinning—study on the spinnability of aluminium plates. ," ed. Bulletin of the Faculty of Engineering, Yokohama National University 1968, pp. 93-103.

[21] K.-i. Mori and T. Nonaka, "Simplified Three- Dimensional Finite Element Simulation of Shear Spinning Process Based on Axisymmetric Modeling," *Journal of Manufacturing Processes,* vol. 7, no. 1, pp. 51-56, 2005, doi: 10.1016/S1526-6125(05)70081-5.

[22] M. M. El-Khabeery, M. Fattouh, M. N. El-Sheikh, and O. A. Hamed, "On the conventional simple spinning of cylindrical aluminium cups," *International Journal of Machine Tools and Manufacture,* vol. 31, no. 2, pp. 203-219, 1991, doi: 10.1016/0890-6955(91)90005-N.

[23] H. Tschaetsch and A. Koth, *Metal forming practise: Processes - Machines - Tools*. 2006, pp. 1-405.

[24] M. Guillot, A. Rosochowski, P. Blackwell, E. Moore, and S. Halliday, "Characterisation and development of the incremental shear forming process for advanced structures.," presented at the 13th International Cold Forming Congress, Glasgow, 2015.

[25] E. Quigley and J. Monaghan, "Enhanced finite element models of metal spinning," *Journal of Materials Processing Tech.,* vol. 121, no. 1, pp. 43-49, 2002, doi: 10.1016/S0924-0136(01)01138-4.

[26] W. T. Qiang, W. and Z. R. Wang, "A study of the working force in conventional spinning," in *International Conference on Rotary Forming*, Beijing, 1989: The Forging and Stamping Institution of CMES.

[27] E. Quigley and J. Monaghan, "The finite element modelling of conventional spinning using multi-domain models," *Journal of Materials Processing Tech.,* vol. 124, no. 3, pp. 360-365, 2002, doi: 10.1016/S0924-0136(02)00259-5.

[28] H. J. Bunge, *Texture analysis in materials science : mathematical methods*. London: London : Butterworths, 1982, 1982.

[29] O. Engler and V. Randle, *Introduction to texture analysis : macrotexture, microtexture, and orientation mapping*, 2nd ed. ed. Boca Raton: Boca Raton : CRC Press, c2010, 2010.

[30] U. F. Kocks, C. N. Tomé, and H.-R. Wenk, *Texture and anisotropy : preferred orientations in polycrystals and their effect on materials properties*. Cambridge: Cambridge : Cambridge University Press, 1998, 1998.

[31] S. I. Robinson, "Modelling The Effect of the α-β Phase Transition on the Microstructure of Extruded Ti-6Al-4V Upon Cooling from Super Transus Temperatures," Master of Engineering, Department of Materials Science and Engineering, The University of Sheffield, 2016.

[32] P. Van Hautte, "MTM-TAYLOR Version 2," Katholieke Universiteit Leuven, Belgium, 1992.

[33] L. S. Tóth and P. Van Houtte, "Discretization techniques for orientation distribution functions.," *Textures and Microstructures,* vol. 19, pp. 229-244, 1992.

[34] P. Van Houtte, "A Comprehensive Mathematical Formulation of an Extended Taylor-Bishop-Hill Model Featuring Relaxed Constraints, the Renouard-Wintenberger Theory and a Strain Rate Sensitivity Model," *Textures and Microstructures,* vol. 8-9, pp. 313-350, 1988.

[35] L. S. Tóth, K. W. Neale, and J. J. Jonas, "Stress response and persistence characteristics of the ideal orientations of shear textures," *Acta Metallurgica,* vol. 37, no. 8, pp. 2197-2210, 1989, doi: 10.1016/0001-6160(89)90145-4.

[36] S. Li, I. J. Beyerlein, and M. A. M. Bourke, "Texture formation during equal channel angular extrusion of fcc and bcc materials: comparison with simple shear," *Materials Science & Engineering A,* vol. 394, no. 1, pp. 66-77, 2005, doi: 10.1016/j.msea.2004.11.032.

[37] V. M. Segal, "Materials processing by simple shear," *Materials Science & Engineering A,* vol. 197, no. 2, pp. 157-164, 1995, doi: 10.1016/0921-5093(95)09705-8.

[38] S. Li, I. J. Beyerlein, and D. J. Alexander, "Characterization of deformation textures in pure copper processed by equal channel angular extrusion via route A," *Materials Science & Engineering A,* vol. 431, no. 1, pp. 339-345, 2006, doi: 10.1016/j.msea.2006.06.022.

[39] S. Li, A. A. Gazder, I. J. Beyerlein, E. V. Pereloma, and C. H. J. Davies, "Effect of processing route on microstructure and texture development in equal channel angular extrusion of interstitial- free steel," *Acta Materialia,* vol. 54, no. 4, pp. 1087-1100, 2006, doi: 10.1016/j.actamat.2005.10.042.

[40] W.-D. Song, M.-L. Hu, H.-S. Zhang, and Y.-X. Jin, "Effects of different heat treatments on the dynamic shear response and shear localization in Inconel 718 alloy," *Materials Science & Engineering A,* vol. 725, pp. 76-87, 2018, doi: 10.1016/j.msea.2018.04.010.

[41] L. Jiang, Y. Yang, Z. Wang, and H. Hu, "Microstructure evolution within adiabatic shear band in peak aged ZK60 magnesium alloy," *Materials Science & Engineering A,* vol. 711, pp. 317-324, 2018, doi: 10.1016/j.msea.2017.10.111.

[42] *Fatigue and fracture [electronic resource] : understanding the basics*. Materials Park, Ohio: Materials Park, Ohio : ASM International, 2012, 2012.

[43] W. D. Callister, *Materials science and engineering : an introduction*, 8th ed., SI version / William D. Callister, Jr., David G. Rethwisch. ed. Hoboken, N.J.: Hoboken, N.J. : Wiley, c2011, 2011.

[44] A. Pineau, A. A. Benzerga, and T. Pardoen, "Failure of metals I: Brittle and ductile fracture," *Acta Materialia,* vol. 107, pp. 424-483, 2016, doi: 10.1016/j.actamat.2015.12.034.

[45] G. Gerstein, B. Klusemann, S. Bargmann, and M. Schaper, "Characterization of the Microstructure Evolution in IF- Steel and AA6016 during Plane- Strain Tension and Simple Shear," *Materials (Basel, Switzerland),* vol. 8, no. 1, pp. 285-301, 2015, doi: 10.3390/ma8010285.

[46] M. Isakov, J. Seidt, K. Östman, A. Gilat, and V. T. Kuokkala, "Characterization of a ferritic stainless sheet steel in simple shear and uniaxial tension at different strain rates," vol. 8, ed, 2011, pp. 101-109.

[47] A. Kacem, A. Jégat, A. Krichen, and P. Y. Manach, "Forming limits in the hole-flanging process by coupled and uncoupled damage models," vol. 1567, ed, 2013, pp. 575-578.

[48] C. Canales and J. P. Ponthot, "Numerical prediction of ductile failure in the blanking process by means of uncoupled and coupled phenomenological damage models," *MATEC Web of Conferences,* vol. 80, p. <xocs:firstpage xmlns:xocs=""/>, 2016, doi: 10.1051/matecconf/20168003006.

[49] M. Ayada, "Central bursting in extrusion of inhomogeneous materials," *Proceedings of 2nd International Conference on Technology for Plasticity, Stuttgart, 1987,* vol. 1, pp. 553-558, 1987 1987.

[50] J. D. Landes, *Fracture Mechanics: Twenty- Fourth Volume*. ASTM International, 1994.

[51] M. Cockcroft and D. Latham, "Ductility and Workability of Metals," *Journal of the Institute of Metals,* no. 96, pp. 33-39, 1968.

[52] S. Oh, C. Chen, and S. Kobayashi "Ductile fracture in axisymmetric extrusion and drawing - part 2: workability in extrusion and drawing," *Journal of Engineering for Industry,* vol. 101, no. 1, pp. 36-44, 1979.

[53] K. Isik, M. B. Silva, A. E. Tekkaya, and P. A. F. Martins, "Formability limits by fracture in sheet metal forming," *Journal of Materials Processing Tech.,* vol. 214, no. 8, pp. 1557-1565, 2014, doi: 10.1016/j.jmatprotec.2014.02.026.

[54] S. P. Keeler, "Circular Grid System — A Valuable Aid for Evaluating Sheet Metal Formability," 1968. [Online]. Available: https://doi.org/10.4271/680092.

[55] G. M. Goodwin, "Application of Strain Analysis to Sheet Metal Forming Problems in the Press Shop," 1968. [Online]. Available: https://doi.org/10.4271/680093.

[56] H. J. Bong, F. Barlat, M.-G. Lee, and D. C. Ahn, "The forming limit diagram of ferritic stainless steel sheets: Experiments and modeling," *International Journal of Mechanical Sciences,* vol. 64, no. 1, pp. 1-10, 2012, doi: 10.1016/j.ijmecsci.2012.08.009.

[57] "DEFORM V11.2 Documentation," ed: Scientific Forming Technologies Corporation, 2017.

[58] A. Andrade, A. Morcelli, and R. Lobo, "DEFORMATION AND FRACTURE OF AN ALPHA/ BETA TITANIUM ALLOY," *Materia,* vol. 15, no. 2, pp. 396-404, 2010.

[59] M. Armendia, A. Garay, L. M. Iriarte, and P. J. Arrazola, "Comparison of the machinabilities of Ti6Al4V and TIMETAL ® 54M using uncoated WC–Co tools," *Journal of Materials Processing Tech.,* vol. 210, no. 2, pp. 197-203, 2010, doi: 10.1016/j.jmatprotec.2009.08.026.

[60] M. Armendia, P. Osborne, A. Garay, J. Belloso, S. Turner, and P. J. Arrazola, "Influence of Heat Treatment on the Machinability of Titanium Alloys," *Materials and Manufacturing Processes,* vol. 27, no. 4, pp. 457-461, 2012, doi: 10.1080/10426914.2011.585499.

[61] H. Al-Khazraji, E. El-Danaf, M. Wollmann, and L. Wagner, "Microstructure, Mechanical, and Fatigue Strength of Ti- 54M Processed by Rotary Swaging," *Journal of Materials Engineering and Performance,* vol. 24, no. 5, pp. 2074-2084, 2015, doi: 10.1007/s11665-014-1283-2.

[62] S. Yang, *Effects of Thermo-mechanical Treatments on Microstructures and Mechanical Properties: TIMETAL-54M vs. Ti-6Al-4V*. 2011.

[63] M. Pérez, "Impact of annealing treatments on the softening and work hardening behaviour of Jethete M152 alloy for subsequent cold forming processes," *Materials Science & Engineering A,* vol. 690, pp. 303-312, 2017, doi: 10.1016/j.msea.2017.03.012.

[64] A. Materials, "Aircraft Stainless Steel Jethete M152 (BS S151/S159)," ed. https://www.aircraftmaterials.com/data/alstst/jetheteM152.html: Aircraft Materials 2013, 2013.

[65] J.-p. Brog, C.-l. Chanez, A. Crochet, and K. M. Fromm, "Polymorphism, what it is and how to identify it: a systematic review," *RSC Adv.,* vol. 3, no. 38, pp. 16905-16931, 2013, doi: 10.1039/c3ra41559g.

[66] "Inspection Certificate," Sildun Manufacturing 2001 Limited, 2012.

[67] Z. Lv, X. Zhang, X. Huang, and N. Hansen, "EBSD characterization of deformed lath martensite in if steel," vol. 219, ed, 2017, p. <xocs:firstpage xmlns:xocs=""/>.

[68] G. Krauss, "Martensite in steel: strength and structure," *Mater. Sci. Eng. A-Struct. Mater. Prop. Microstruct. Process.,* vol. 275, pp. 40-57, 1999.

[69] C. Ghosh, A. Haldar, P. Ghosh, and R. Ray, "Microstructure, Texture, Grain Boundary Characteristics and Mechanical Properties of a Cold Rolled and Annealed Martensitic Steel," *ISIJ International,* vol. 48, no. 11, pp. 1626-1634, 2008, doi: 10.2355/isijinternational.48.1626.

[70] K. V. U. Praveen, G. V. S. Sastry, and V. Singh, "Work- Hardening Behavior of the Ni-Fe Based Superalloy IN718," *Metallurgical and Materials Transactions A,* vol. 39, no. 1, pp. 65-78, 2008, doi: 10.1007/s11661-007-9375-3.

[71] S. Ghosh, S. Yadav, and G. Das, "Study of standard heat treatment on mechanical properties of Inconel 718 using ball indentation technique," *Materials Letters,* vol. 62, no. 17, pp. 2619-2622, 2008, doi: 10.1016/j.matlet.2008.01.001.

[72] C. M. Kuo, Y. T. Yang, H. Y. Bor, C. N. Wei, and C. C. Tai, "Aging effects on the microstructure and creep behavior of Inconel 718 superalloy," *Materials Science & Engineering A,* vol. 510, no. C, pp. 289-294, 2009, doi: 10.1016/j.msea.2008.04.097.

[73] J. Michal, B. Otakar, N. František, T. Libor, and B. Juraj, "Phase Transformations in Nickel base Superalloy Inconel 718 during Cyclic Loading at High Temperature," *Production Engineering Archives,* vol. 15, pp. 15-18, 2017.

[74] M. J. Donachie, *Superalloys : a technical guide*, 2nd ed. ed. Materials Park, Ohio: Materials Park, Ohio : ASM International, 2002, 2002.

[75] S. Azadian, L. Y. Wei, and R. Warren, "Delta phase precipitation in inconel 718," *Materials Characterization,* vol. 53, no. 1, pp. 7-16, 2004, doi: 10.1016/j.matchar.2004.07.004.

[76] A. Thomas, M. El-Wahabi, J. M. Cabrera, and J. M. Prado, "High temperature deformation of Inconel 718," *Journal of Materials Processing Tech.,* vol. 177, no. 1-3, pp. 469-472, 2006, doi: 10.1016/j.jmatprotec.2006.04.072.

[77] F. Czerwiński and InTech, *Heat Treatment: Conventional and Novel Applications*. InTech, 2012.

[78] F. J. Humphreys, *Recrystallization and related annealing phenomena [electronic resource]*, 2nd ed. ed. Amsterdam ; Boston: Amsterdam ; Boston : Elsevier, 2004, 2004.

[79] H. Zhang *et al.*, "Hot tensile behavior of cold- rolled Inconel 718 alloy at 650 ° C: The role of δ phase," *Materials Science & Engineering A,* vol. 722, pp. 136-146, 2018, doi: 10.1016/j.msea.2018.02.093.

[80] Y. Mei *et al.*, "Effects of cold rolling on the precipitation and the morphology of[...]- phase in Inconel 718 alloy," *Journal of Materials Research,* vol. 31, no. 4, pp. 443-454, 2016, doi: 10.1557/jmr.2016.26.

[81] H.-T. Lee and W.-H. Hou, "Development of fine- grained structure and the mechanical properties of nickel- based Superalloy 718," *Materials Science & Engineering A,* vol. 555, pp. 13-20, 2012, doi: 10.1016/j.msea.2012.06.027.

[82] P. Callahan, S. Singh, M. Echlin, J. Stinville, T. Pollock, and M. De Graef, "Automated Prediction of Pseudo- Symmetry Issues in EBSD," *Microscopy and Microanalysis,* vol. 24, no. S1, pp. 566-567, 2018, doi: 10.1017/S143192761800332X.

[83] S. Yokoshima and M. Yamaguchi, "Fracture behavior and toughness of PST crystals of TiAl," *Acta Materialia,* vol. 44, no. 3, pp. 873-883, 1996, doi: 10.1016/1359-6454(95)00255-3.

[84] P. Wang, N. Bhate, K. S. Chan, and K. S. Kumar, "Colony boundary resistance to crack propagation in lamellar Ti– 46Al," *Acta Materialia,* vol. 51, no. 6, pp. 1573-1591, 2003, doi: 10.1016/S1359-6454(02)00559-1.

[85] A. Sun, J. Liu, and C. Jiang, "Recrystallization, texture evolution, and magnetostriction behavior of rolled (Fe 81 Ga 19) 98 B 2 sheets during low-to-high temperature heat treatments," *Full Set - Includes `Journal of Materials Science Letters',* vol. 49, no. 13, pp. 4565-4575, 2014, doi: 10.1007/s10853-014-8156-9.

[86] M. Azarbarmas, M. Aghaie-Khafri, J. M. Cabrera, and J. Calvo, "Dynamic recrystallization mechanisms and twining evolution during hot deformation of Inconel 718," *Materials Science & Engineering A,* vol. 678, no. C, pp. 137-152, 2016, doi: 10.1016/j.msea.2016.09.100.

[87] S. M. Hussaini, S. K. Singh, and A. K. Gupta, "Formability and fracture studies of austenitic stainless steel 316 at different temperatures," *Journal of King Saud University - Engineering Sciences,* vol. 26, no. 2, pp. 184-190, 2014, doi: 10.1016/j.jksues.2013.05.001.

[88] M. Mahmoudiniya, S. Kheirandish, and M. Asadiasadabad, "The Effect of Cold Rolling on Microstructure and Mechanical Properties of a New Cr–Mn Austenitic Stainless Steel in Comparison with AISI 316 Stainless Steel," *Transactions of the Indian Institute of Metals,* vol. 70, no. 5, pp. 1251-1259, 2017, doi: 10.1007/s12666-016-0921-9.

[89] M. Naghizadeh and H. Mirzadeh, "Microstructural Evolutions During Reversion Annealing of Cold-Rolled AISI 316 Austenitic Stainless Steel," *Metallurgical and Materials Transactions A,* vol. 49, no. 6, pp. 2248-2256, 2018, doi: 10.1007/s11661-018-4583-6.

[90] D. Fahr, "Analysis of Stress-Strain Behaviour of Type 316 Stainless Steel," Oak Ridge National Laboratory, U.S. Department of Energy, Office of Scientific and Technical Information 1973.

[91] L. Figueiredo, A. Ramalho, M. C. Oliveira, and L. F. Menezes, "Experimental study of friction in sheet metal forming," *Wear,* vol. 271, no. 9-10, pp. 1651-1657, 2011, doi: 10.1016/j.wear.2011.02.020.

[92] A. P. Avdeenko *et al.*, "Cold rolling of steel strips with metal-working coolants," *Machines,* vol. 6, no. 3, 2018, doi: 10.3390/machines6030029.

[93] J. H. Hollomon, vol. 162, ed: A.I.M.E. Trans., 1945.

[94] R. H. Wagoner, *Fundamentals of metal forming*. New York ; Chichester: New York ; Chichester : Wiley, 1996, 1996.

[95] A. A. Abduluyahed and K. J. Kurzydłowski, "Tensile properties of a type 316 stainless steel strained in air and vacuum," *Materials Science & Engineering A,* vol. 256, no. 1-2, pp. 34-38, 1998, doi: 10.1016/S0921-5093(98)00841-7.

[96] A. M. Eleiche, C. Albertini, and M. Montagnani, "The influence of strain-rate history on the ambient tensile strength of AISI type 316 stainless steel," *Nuclear Engineering and Design,* vol. 88, no. 2, pp. 131-141, 1985, doi: 10.1016/0029-5493(85)90056-1.

[97] M. Palengat, G. Chagnon, D. Favier, H. Louche, C. Linardon, and C. Plaideau, "Cold drawing of 316L stainless steel thin- walled tubes: Experiments and finite element analysis," *Int. J. Mech. Sci.,* vol. 70, pp. 69-78, 2013, doi: 10.1016/j.ijmecsci.2013.02.003.

[98] P. Kelly. "Mechanics *Lecture Notes: An introduction to Solid Mechanics* . ." http://homepages.engineering.auckland.ac.nz/~pkel015/SolidMechanicsBooks/Part_II/ (accessed May 28, 2019).

[99] J. Lubliner, *Plasticity Theory* (Dover Books on Engineering). Dover Publications, 2013.

[100] K. Xia and J. Wang, "Shear, principal, and equivalent strains in equal- channel angular deformation," *Metallurgical and Materials Transactions A,* vol. 32, no. 10, pp. 2639-2647, 2001, doi: 10.1007/s11661-001-0054-5.

[101] R. C. Hibbeler, *Mechanics of materials*, Ninth edition.; SI edition / contributions by K.S. Vijay Sekar. ed. Singapore: Singapore : Pearson Education South Asia, 2014, 2014.

[102] "What is ANOVA?" Minitab, LLC. https://support.minitab.com/en-us/minitab-express/1/help-and-how-to/modeling-statistics/anova/supporting-topics/basics/what-is-anova/ (accessed April 12th, 2019).

[103] L. St»hle and S. Wold, "Analysis of variance (ANOVA)," *Chemometrics and Intelligent Laboratory Systems,* vol. 6, no. 4, pp. 259-272, 1989/11/01/ 1989, doi: https://doi.org/10.1016/0169-7439(89)80095-4.

[104] "Interpret the key results for One-Way ANOVA." Minitab LLC. https://support.minitab.com/en-us/minitab-express/1/help-and-how-to/modeling-statistics/anova/how-to/one-way-anova/interpret-the-results/key-results/#step-5-determine-whether-your-model-meets-the-assumptions-of-the-analysis (accessed April 12th, 2019).

[105] "Residual plots in Minitab." Minitab, LLC. https://support.minitab.com/en-us/minitab/18/help-and-how-to/modeling-statistics/regression/supporting-topics/residuals-and-residual-plots/residual-plots-in-minitab/ (accessed April 12th, 2019).

[106] D. C. Montgomery, *Design and analysis of experiments*, 5th ed. ed. New York ; Chichester: New York ; Chichester : Wiley, c2001, 2001.

[107] "Factorial and fractional factorial designs." Minitab, LLC. https://support.minitab.com/en-us/minitab/18/help-and-how-to/modeling-statistics/doe/supporting-topics/factorial-and-screening-designs/factorial-and-fractional-factorial-designs/ (accessed May 14th, 2019).

[108] "Understanding Hypothesis Tests: Significance Levels (Alpha) and P values in Statistics." https://blog.minitab.com/blog/adventures-in-statistics-2/understanding-hypothesis-tests-significance-levels-alpha-and-p-values-in-statistics (accessed May 14th, 2019).

[109] "Overview for Contour Plot." Minitab, LLC. https://support.minitab.com/en-us/minitab/18/help-and-how-to/modeling-statistics/using-fitted-models/how-to/contour-plot/before-you-start/overview/ (accessed May 14th, 2019).

[110] J. Safranek, "Modelling Crystallographic Texture Evolution in Hot Extruded Titanium for Aerospace Applications.," Aerospace Engineering MEng, The University of Sheffield, 2018.

[111] K. Sajun Prasad, S. Panda, S. Kar, M. Sen, S. Murty, and S. Sharma, "Microstructures, Forming Limit and Failure Analyses of Inconel 718 Sheets for Fabrication of Aerospace Components," *Journal of Materials Engineering and Performance,* vol. 26, no. 4, pp. 1513-1530, 2017, doi: 10.1007/s11665-017-2547-4.

[112] W.-S. Lee, C.-F. Lin, T.-H. Chen, and H.-W. Chen, "Dynamic mechanical behaviour and dislocation substructure evolution of Inconel 718 over wide temperature range," *Materials Science & Engineering A,* vol. 528, no. 19, pp. 6279-6286, 2011, doi: 10.1016/j.msea.2011.04.079.

[113] P. J. Arrazola *et al.*, "On the machining induced residual stresses in IN718 nickel- based alloy: Experiments and predictions with finite element simulation," *Simulation Modelling Practice and Theory,* vol. 41, pp. 87-103, 2014, doi: 10.1016/j.simpat.2013.11.009.

[114] G. R. Johnson and W. H. Cook, "A Constitutive Model and Data for Metals Subjected to Large Strains, High Strain Rates and High Temperatures," presented at the 7th International Symposium on Ballistics, The Hague, Netherlands, 1983.

[115] J. Sweet, E. Roth, and M. Moss, "Thermal conductivity of Inconel 718 and 304 stainless steel," *Journal of Thermophysical Properties and Thermophysics and Its Applications,* vol. 8, no. 5, pp. 593-606, 1987, doi: 10.1007/BF00503645.

[116] "Special Metals INCONEL® Alloy 718." Matweb, LLC. http://www.matweb.com/search/DataSheet.aspx?MatGUID=94950a2d209040a09b89952d45086134&ckck=1 (accessed June 28th, 2018).

[117] P. Hindert, "Thermal Expansion of Some Nickel Alloys," *Journal of Research of the National Bureau of Standards,* vol. 58, no. 2, p. 4, 1957.

[118] "Inconel 718 Technical Data." High Temp Metals. https://www.hightempmetals.com/techdata/hitempInconel718data.php (accessed June 25th, 2018).

[119] K. S. Prasad, T. Kamal, S. K. Panda, S. Kar, S. V. S. N. Murty, and S. C. Sharma, "Finite Element Validation of Forming Limit Diagram of IN- 718 Sheet Metal," *Materials Today: Proceedings,* vol. 2, no. 4-5, pp. 2037-2045, 2015, doi: 10.1016/j.matpr.2015.07.174.

[120] Z. Tourki, H. Bargui, and H. Sidhom, "The kinetic of induced martensitic formation and its effect on forming limit curves in the AISI 304 stainless steel," *Journal of Materials Processing Tech.,* vol. 166, no. 3, pp. 330-336, 2005, doi: 10.1016/j.jmatprotec.2003.08.010.

[121] X. H. An, Q. Y. Lin, S. D. Wu, and Z. F. Zhang, "Microstructural evolution and shear fracture of Cu–16 at.% Al alloy induced by equal channel angular pressing," *Materials Science & Engineering A,* vol. 527, no. 16, pp. 4510-4514, 2010, doi: 10.1016/j.msea.2010.03.101.

[122] C. C. Roth and D. Mohr, "Determining the strain to fracture for simple shear for a wide range of sheet metals," *International Journal of Mechanical Sciences,* vol. 149, pp. 224-240, 2018, doi: 10.1016/j.ijmecsci.2018.10.007.

[123] M. B. Silva, M. Skjoedt, A. G. Atkins, N. Bay, and P. A. F. Martins, "Single- point incremental forming and formability— failure diagrams," *The Journal of Strain Analysis for Engineering Design,* vol. 43, no. 1, pp. 15-35, 2008, doi: 10.1243/03093247JSA340.

[124] Q. Yin, A. Brosius, and A. Tekkaya, *Modified Plane Torsion Tests for Sheet Metal Characterization*. 2011, pp. 696-701.

[125] "ASTM B831-05 Standard Test Method for Shear Testing of Thin Aluminum Alloy Products," ed: ASTM International, 2005.